Roger Urquhart M.Eng. Metallurgical Engineering.

Importance of Metal/Slag Emulsions in Oxygen Steelmaking

ABSTRACT

Reaction rates in Basic Oxygen Steelmaking have been studied by low and high temperature models. Modified Froude Number similarity was maintained in the model systems.

Emulsification of the lower layer into the upper layer by the gas jet was observed in all systems. High speed photography revealed a gas cavity which penetrates through the upper layer into the lower liquid layer.

The cavity is unstable in both the horizontal and the vertical plane and was observed to oscillate between a maximum and minimum penetration, the minimum penetration terminating with ejection of the lower liquid in the form of drops.

A chemical analysis technique has been developed to accurately determine the carbon content of iron droplets emulsified in slag.

The rate of decarburization of emulsified iron droplets was observed in all cases to be more rapid than in the iron bath. Calculations have shown that reactions between metal droplets and oxidized slag and with the gas of slag foams are extremely important in the decarburization process.

It is shown that metal turnover through the slag in the order of 6% of the bath per minute is sufficient to account for the observed industrial decarburization rates.

THE IMPORTANCE OF METAL/SLAG EMULSIONS IN OXYGEN STEELMAKING

by

Roger C. Urquhart

A thesis submitted to the Faculty of Graduate Studies and Research in partial fulfilment of the requirements for the degree of Master of Engineering in Metallurgical Engineering.

McGill University
Montreal
April 1970

- The cruel crawling foam -

Charles Kingsley

The Sands of Dee Stanza 4

TABLE OF CONTENTS

CHAPTER 1

1.0 INTRODUCTION

Improvements in the commercial methods of production of oxygen have made pure oxygen available in quantity and at low cost. The availability of low-cost oxygen has led to the development of steelmaking processes in which pure oxygen is used to remove impurities from steel.

Blowing with oxygen was investigated by R. Durrer and C.V. Schwarz in Germany and by Durrer and H. Hellbrugge in Switzerland. Bottom-blown vessels proved unsuitable because the high temperature attained near the tuyères caused rapid deterioration of the refractory tuyère bottom. The difficulty was overcome in the basic oxygen furnace by blowing oxygen through a supersonic jet suspended above the metal surface. It has been found that this process converted the liquid iron charge to steel with a high degree of thermal and chemical efficiency. Plants utilizing top blowing with oxygen have been in operation since 1952-1953 at Linz and Donawitz in Austria.

Reaction rates in oxygen steelmaking processes are much faster than in the open hearth processes. Oxygen steelmaking decarburization rates of 8-12%C per hour are a full order of magnitude higher than basic open hearth decarburization rates of .5-.6%C per hour.

Processes involving top blowing with oxygen have evolved into three different categories. The Swedish Kaldo process uses a slowly rotating vessel to assist mixing. The Kaldo vessel is generally not vertical but at an angle. The high phosphorous content of the European iron ores prompted the injection of powdered lime with the oxygen jet to facilitate phosphorous removal. The French Oxygen Lime Powder Process or OLP uses this technique while the Benelux LD-AC process not only injects lime with oxygen but also uses a two slag procedure. No additional lime is needed for the low phosphorous North American ores.

With the exception of the Kaldo Process, in which the gas jet impinges at an angle on the liquid surface, the oxygen is introduced via a vertical lance.

1.1 Existing Mechanisms Explaining High Reaction Rates

The reason for the high decarburization rates in the basic oxygen steelmaking process has not yet been satisfactorily determined. Three theories to explain the high reaction rates have evolved.

Focus Point Theory This theory which was first proposed by Kosmider[1], states that the vast majority of the oxygen is reacted at the point of impingement. The optimum condition for the reaction by this theory would be the maximum area of penetration of the oxygen jet.

Droplet Oxidation Theory Rellermeyer[2] agrees that there will be some oxygen reaction at the focus point. However, he maintains that the major portion of the reaction is in the oxidizing atmosphere above the bath, the iron droplets being oxidized and dropping back to the bath, where the reaction continues as with solid oxide.

Slag Emulsion Theory Meyer et al[3] postulated the formation of a metal-slag emulsion. According to this theory small droplets of iron are dispersed into the upper slag layer where decarburization takes place by reaction with the slag. The large surface areas involved are thought to explain the high rate of decarburization. Kozakevitch[4] supports this theory and in addition has shown that gas/slag foams are stable during the best part of an OLP blow.

In order to evaluate the applicability of each of these theories, the rates of reaction in each case have been calculated as described below. The size of the vessel considered is shown in Figure 1.1.

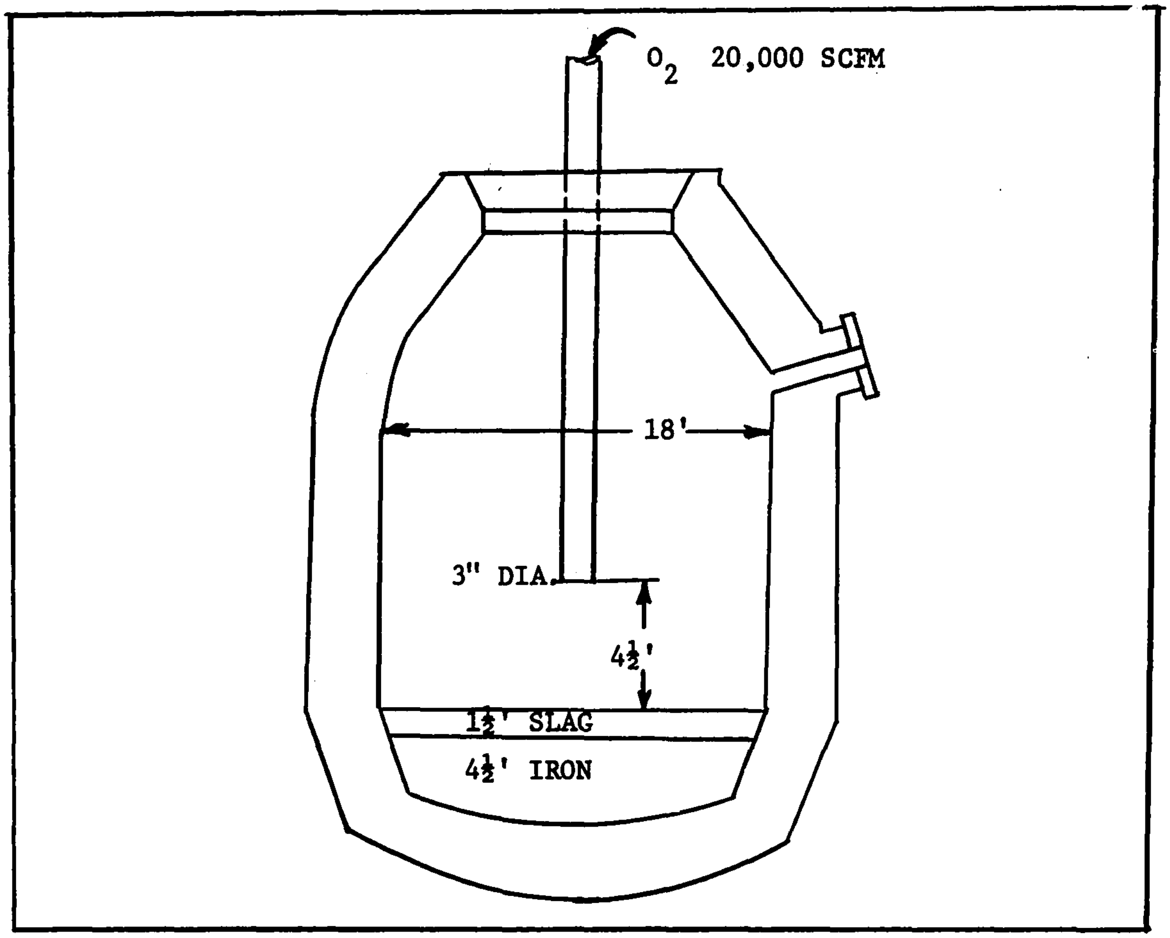

Figure 1.1 Outline of a typical basic oxygen furnace. Capacity 150-200 tons of steel.

Two types of reaction interface are important in the above three theories: metal-gas and metal-slag. In both cases rates of decarburization may be predicted by the mass transfer model suggested by Darken[5], assuming that the rate of decarburization across a metal-slag interface is controlled by the transfer of slag oxygen as FeO across a boundary layer in the slag to the metal-slag interface. In the case of decarburization by pure oxygen gas at a metal-gas interface, the rate can be assumed to be controlled by carbon transfer from the metal bulk across a boundary layer to the gas-metal interface.

The equation governing the steady-state mass transfer of component i across the boundary layer to an interface is given by:

$$\dot{N}_i = k_i A \,\Delta C_i \quad \ldots\ldots\ldots\ldots\ldots 1.1$$

Where: $\dot{N}_i$ - represents the flux of i in moles $\sec^{-1}$

k_i - mass transfer coefficient of i in cm $\sec^{-1}$

ΔC_i - concentration gradient across boundary layer in moles cm^{-3},

A - area of reaction interface cm^2

The rate of change of concentration of i in the bath is given by:

$$\dot{N}_i = \frac{-VdC_i}{dt} \quad \ldots\ldots\ldots\ldots\ldots 1.2$$

Where: V - volume of bath in cm^3

$\frac{dC_i}{dt}$ - rate of change of concentration of i in mole $\frac{cm^{-3}}{\sec^{-1}}$

Combining Equations 1.1 and 1.2 yields an expression relating the rate of reaction to transfer conditions in the system.

$$\frac{-dC_i}{dt} = k_i \frac{A}{V} \Delta C_i \quad \ldots\ldots\ldots\ldots\ldots 1.3$$

To convert carbon concentrations to weight per cent multiply by:

$$\frac{100 \times 7.2}{MWi}$$

Equation 1.3 can be used to find decarburization rates for the three theories explained previously. The mass transfer coefficients for carbon diffusion in molten iron and oxygen diffusion in molten slag are not precisely known, but values of 10^{-2} and 10^{-4} cm sec^{-1} are of the correct order of magnitude according to the results of many researchers [6,7,8,9]. Calculations of reaction rates in the various locations are presented in the following sections.

TABLE 1.1

Variable	Value (weight %)	Value (c.g.s.)
ΔC_c (metal)	2 %C	.012 moles cm^{-3}
ΔC_o (slag)	4 %O(18% FeO)	.009 moles cm^{-3}
k_c (metal)		10^{-2} cm sec^{-1}
k_o (slag)		10^{-4} cm sec^{-1}

Focus Point Theory Application of Equation 1.3 to the cavity created by the oxygen jet will give the rate of decarburization on the basis of mass transfer control. The transfer of carbon in the stirred iron bath to the gas-metal interface to form CO is assumed to be the rate limiting step, while carbon at the gas-metal interface is assumed to be completely reacted, ie $C_c^i = 0$.

The oxygen jet penetration in current steelmaking practice is about one half of the metal depth (limitation, erosion of refractory bottom and excessive slopping)[10]. Assuming the cavity to be in the form of a paraboloid, the area of exposed iron in the present case (Figure 1.1) is about 16.5 ft^2 ($1.53 \times 10^4 cm^2$)[11]. The equivalent volume of 150 tons of steel (density 448 lb ft^{-3}) is 670 ft^3 ($1.9 \times 10^7 cm^3$).

Inserting these area and volume data and the carbon concentration gradient of 2 %C(2 %C in bulk, 0 at gas-metal interface) into Equation 1.3, the decarburization rate predicted by this theory is:

$$-\frac{dC_c}{dt} = 10^{-2} \times \frac{1.5 \times 10^4}{1.9 \times 10^7} \times .012$$

$$= .95 \times 10^{-7} \text{ moles cm}^{-3} \text{ sec}^{-1}$$

$$= 1.6 \times 10^{-5} \text{ \%C sec}^{-1}$$

Droplet Oxidation Theory Calculation of decarburization rates as predicted by the droplet oxidation model have been made on the basis of the oxidation of the iron droplets in an atmosphere of oxygen above the melt. Diffusion of carbon in the droplet is assumed to be the controlling step as for the focus point theory calculation. The Holden and Hogg[12] estimate that droplets ejected from the bath are in the order of .12 inches (.3 cm) diameter has been employed. The surface to volume ratio of a sphere is given by 6/diameter, therefore A/V will equal 20 cm^{-1}. Application of Equation 1·3 to the case of decarburization of a 2 %C iron droplet in oxygen leads to a rate of:

$$-\frac{dC}{dt}_c = 10^{-2} \times 20 \times .012$$

$$= 2.4 \times 10^{-3} \text{ moles cm}^{-3} \text{ sec}^{-1}$$

$$= .4 \text{ \%C sec}$$

Slag Emulsion Theory The reaction of iron droplets which have been dispersed into the slag is treated by considering a 20 % metal in slag emulsion. Meyer et al[3] report that in this type of emulsion the typical iron droplet size would be 1 mm diameter, hence the A/V ratio would be 60 cm^{-1}. In the slag emulsion theory, the rate of decarburization of the droplet is assumed to be controlled by FeO diffusion in the slag phase to the slag-metal interface and an oxygen gradient of 4 %O (18 %FeO) proposed by Darken[9] has been assumed. The rate of decarburization predicted by the transfer of oxygen to the slag-metal interface is:

$$-\frac{dC}{dt}_c = 10^{-4} \times 60 \times .009$$

$$= 5.4 \times 10^{-5} \text{ moles sec}^{-1}$$

$$= .025 \text{ \%C sec}^{-1}$$

Decarburization across the slag-metal interface as occurs in the basic open hearth is common to all three theories and depends on the slag oxygen content. The bath area of an 18 ft. diameter BOF is 254 ft^2 ($2.4 \times 10^5 cm^2$). Inserting these values and Darken's slag oxygen gradient of 4 %O (18 %FeO) into Equation 1.3:

$$-\frac{dC}{dt}_c = 10^{-4} \times \frac{2.4 \times 10^5}{1.9 \times 10^7} \times .009$$

$$= 1.1 \times 10^{-8} \text{ moles cm}^{-3} \text{ sec}^{-1}$$

$$= 3.8 \times 10^{-6} \text{ \%C sec}^{-1}$$

Table 1.2 compares the results of these calculations.

TABLE 1.2

Theory	Rate of Decarburization
Focus Point	1.6×10^{-5} %C sec^{-1}
Droplet Oxidation	.4 %C sec^{-1}
Slag Emulsion	.025 %C sec^{-1}
Slag-metal Reaction (BOH)	3.8×10^{-6} %C sec^{-1}
Industrial Rate	.003 %C sec^{-1}

Table 1.2 shows a very high rate of decarburization for iron droplets that leave the bath. This, however, does not convey how much of the bath is in the form of these droplets, whether they are continually created or how long they are away from the bath. The low rate of decarburization calculated for the Focus Point Theory (two orders of magnitude lower than rates of approximately 10 %C per hour observed in practice) indicates that a simple mass transfer mechanism at the cavity cannot account for the rapid observed rates.

The aim of this research is to investigate further the relative importance of each theory by making use of experimental low and high temperature models.

1.2 Investigation

The investigation has been directed at the simultaneous measurement of the rates of decarburization in the iron bath and in the oxidizing slag and atmosphere of the basic oxygen furnace. The experimental approach was to begin with a transparent room temperature model which could approximate the main features of the process. The second phase of experiments involved a small scale basic oxygen furnace using pig iron, commercially pure oxygen and steelmaking slag.

The reaction which is of most importance in the basic oxygen process can be simply stated as:

$$(C) + 1/2\ O_2 \ = \ CO^*$$

The impurity carbon dissolved in the liquid iron is removed by reaction with oxygen gas thus releasing a second gas, carbon monoxide.

The room temperature reaction chosen to best simulate the basic oxygen furnace was the removal of dissolved sodium bicarbonate salt from water using dry hydrogen chloride gas. The equivalent reaction is:

$$NaHCO_3 + HCl = NaCl + H_2O + CO_2$$

It is immediately apparent that one mole of HCl is needed to react with one mole of $NaHCO_3$ salt to produce one mole of evolved gas whereas, in steelmaking, only one half a mole of oxygen is needed to react with one mole of dissolved carbon. Therefore, for a given molecular rate of reaction the rate of gas evolution in the model is one half the rate of gas evolution in steelmaking processes.

Steelmaking slag was simulated in the model by a mixture of motor

---

* At steelmaking temperatures the equilibrium product gas is > 99%CO[13].

oil and paraffin. This mixture has a suitable density and is immiscible in the aqueous phase.

The effect of the jet characteristics upon foam and emulsion formation and rates of sodium bicarbonate reaction were studied. Liquid properties were varied and their effect on the system was evaluated.

The aim of the high temperature experiments was to investigate each of the three theories presented in the introduction and to study the effects of jet characteristics (flow rate, lance diameter, and lance height*) upon foam and emulsion formation and upon rates of decarburization.

*Lance height represents the distance between the nozzle tip and the upper liquid surface.

CHAPTER 2

2.0 PREVIOUS WORK

2.1 Oxygen Steelmaking Process

With the advent of the pneumatic oxygen processes at Linz and Donawitz in Austria in 1952-53, researchers began investigating the process in efforts to explain the high rates of carbon removal as compared to the basic open hearth process.

Hot model studies were reported by Fuji and Ura[14] who studied the rate of decarburization as a function of oxygen blowing rate and lance height in 30 lb iron melts. Their results indicate that the average decarburization rate is a linear function of the oxygen flow rate. They found that the maximum decarburization rate was obtained with a submerged lance. Laboratory scale experiments were also used by Kun Li, Dukelow and Smith[15] to study the behaviour of a small size basic oxygen furnace with respect to the Jones and Laughlin prototypes. They found oxygen efficiencies (defined as that percentage of input oxygen which combines with bath carbon to form CO) to be comparable with the commercial process (in the order of 60%).

Further work by Smith and Dukelow[16] in a 1/12 linear scale model studied the effect of fluid dynamics on the chemical reaction. It was shown that unless the gas jet penetrated through the slag, large oxygen concentrations could be built up in the slag and that in this event little decarburization occurred. When the over-oxidized slag begins to react with the hot metal and the resultant carbon boil mixes the slag and metal phases, decarburization becomes violent.

Jet penetration into the metal caused the carbon boil to occur earlier and the boil was more uniform. Decreasing the lance height was shown to increase the decarburization rate which varied linearly with oxygen gas flow rate at constant lance height.

The oxygen flow rates in this model were compared to those of the prototype by keeping the volume of gas delivered per unit time per ton of hot metal as being constant. Since Froude Number similarity is a better scale-down criterion[17], the application of their results to the industrial Basic Oxygen Furnaces must be done with care.

G. W. Perbix[18] carried out Basic Oxygen Furnace hot model tests with a 150-200 lb. metal charge in order to investigate the effects of blowing conditions on refining kinetics, oxygen efficiencies and thermodynamic aspects of steelmaking. Perbix also showed that the decarburization reaction is strongly temperature dependent. Scatter in results was attributed to differences in temperature patterns during the course of the heats. The use of induction heating during the process of a blow to off-set heat losses will add the detrimental effect of stirring the metal bath. Like Smith and Dukelow, Perbix used the unit SCFM/TON CHARGED to describe the gas flow rate.

The changes in the degree of oxidation of the slag during the top blowing with oxygen of pig iron in a converter were investigated by Ogryzkin[19]. He found that lowering the lance and increasing the oxygen flow tended to lower the FeO concentration of the slag by increasing the intensity of mixing of the slag and iron. Reduction of the iron oxide content in the slag is, therefore, enhanced by the intense mixing of the upper layer. McBride[20], confirming Ogryzkin's observations, points out that the oxygen content of the relatively calm open hearth slags is high as compared to the oxygen content of the oxygen steelmaking slags which are turbulently mixed with the metal layer.

In the experimental investigations reviewed up to this point the rates of bath decarburization have been measured but no importance has been attached to the formation of slag foams or metal-slag emulsions. The scaling methods used by the above researchers were not well chosen or explained.

2.2 Dynamics of the Blowing Process

Kootz[21] states that in the gas jet impingement area, which is like a concave mirror, the jet itself is directed to all sides and outward. In contact with the liquid surface, the jet transmits part of its impulse to the adjacent layer of fluid and, at higher velocities, entrains liquid droplets from the liquid surface at the periphery of the jet impingement area.

Holden and Hogg[12] suggest that the internal circulation of the splashed droplets is so low, that once the surface has been oxidized, the concentration difference between the droplet and the atmosphere will remain at a low level and hence the rate of mass transfer will be lowered. If, therefore, the turbulence within the bath is maintained at such a level that fresh unoxidized metal is constantly being exposed to the oxygen, then the bath is by far the greater potential absorber. No experimental results were given to support this contention.

Experimental converters of 100, 300, and 4000 lb. capacity were used by Flinn et al[10] to study the depth of penetration of the oxygen jet and the circulatory movement in the bath. Four independent methods were used to determine penetration: the onset of bottom marking, a nitrogen bubbler probe, observation through an optical system built into the lance, and direct viewing of the jet issuing from the bottom of the vessel. The empirical expression defining the depth of penetration of the oxygen jet was:

$$\text{Depth (in.)} = 1.5\,\frac{P_dD_t}{\sqrt{H}} + 1.5$$

Where: P_d - nozzle pressure psia

D_t - nozzle throat diameter in.

H - nozzle height above bath in.

Circulation was investigated by four methods: by direct observation in 200 lb. open baths, by the use of graphite rudders in the 300 lb. and 4000 lb. converters, by direct observation through an optical system in the lance, and by various models at room temperature.

Surface blowing results in low oxygen efficiency and in increased iron oxide content of the slag. Flinn et al report that subsequent reaction between metal and the highly oxidized slag can cause excessive and hazardous splashing from the vessel. Refractory damage at the bottom of the vessel is only encountered when the jet penetrates to the bottom.

Aside from the revealing work of Flinn and co-workers, little has been done to measure gas cavity depressions or shapes. The fluid dynamic behaviour of the cavity has not received any theoretical analysis.

2.3 Model Studies

Experimental work on the Basic Oxygen Process has shown that the important reaction parameters are: the mode of deformation of the surface by the oxygen jet, the circulation imparted to the bath and the formation of metal droplets.

The difficulty of making accurate measurements on a full-scale converter has led many researches to turn to models. The theory and problems involved in establishing similarity have been dealt with by Holmes and Thring[22], while Newby[17] showed, on the basis of experiments using water, mercury and air, that the most useful dimensionless parameter in designing model lancing experiments is the modified Froude Number $\left(\frac{\rho_g v^2}{\rho_1 g d}\right)$.

Qualitative studies of gas flow and liquid circulation have been made by Hasimoto[23], using a submerged water jet impinging on mercury. He noticed changes in liquid flow patterns with angle of lance inclination, as did Holden and Hogg[12], using air on water. The latter also studied the effects of an oil layer on the water surface and concluded that if the oil layer is penetrated by the jet, the circulation patterns in the lower liquid are similar to those in a single liquid system.

Data on the geometry of the depression caused by subsonic gas streams directed on the surface of various liquids were reported by Turkdogan[24] who found that beyond a certain critical axial impact pressure, which depends upon the liquid properties, the depression on the liquid surface becomes unstable and liquid droplets are ejected. Turkdogan found that the most critical liquid properties were surface tension, droplets being ejected more easily at lower surface tensions.

Chedaille and Horvais[25] conducted similar experiments blowing air on water and measured the quantity of liquid splashed from the container.

For a given lance height the amount of liquid splashed out was found to increase with increasing gas flow rate.

J.M. van Langen[26] using a 1/26 linear scale model of an LD converter, qualitatively investigated the absorption of dry HCl gas blown onto a saturated $NaHCO_3$ solution covered with paraffin oil, using methyl orange as indicator. It was shown that the stirring action of the gas jet is very small and that an acid layer is formed which gradually grows until nearly the whole solution is acid. The last of the basic liquid usually mixes suddenly with the acid giving increased gas evolution. Stirring was improved by decreasing the oil thickness, bath depth and lance height, or by increasing the jet momentum.

Models using low temperature liquids and air were used by Red'ko et al[27] to evaluate the relative efficiency of top, bottom and side blowing. They found that the method of introducing the gas has no substantial effect on the gas liquid reaction rate. They also found that foaming and reaction rate increased with increasing gas flow rate. The retardation of the reaction between the gas and the liquid due to an increase in the liquid viscosity was found to be proportional to the sixth root of the kinematic viscosity of the liquid.

Dubrawka[28] studied the absorption of CO_2 blown at 1CFM ($472 cm^3 sec^{-1}$) through a 1/8 inch nozzle onto a bath of NaOH for two minutes. He found that absorption increased with increasing bath diameter up to 15 inches, and for increasing bath depth up to 4 inches for a bath diameter of 5 1/2 inches. Maximum absorption occurred at a lance height of 1 inch.

The size and shape of the depression formed in the liquid surface by subsonic jets of air and CO_2 on water and mercury were measured by

Wakelin[11] for various nozzle heights and jet momenta. The magnitude and direction of the velocities in water were also measured. Wakelin found that the amount of circulation in the liquid increases with increasing jet momentum and decreasing nozzle height especially near the upper surface of the liquid. Rates of mass transfer of CO_2 into water and O_2 into molten silver were shown to be dependent on liquid surface velocity.

Unfortunately quantitative studies on the geometry of the gas depression have been restricted to laminar gas jets usually on a single liquid phase system. Gas cavity behaviour under turbulent conditions is not well known.

2.4 Foams and Emulsions in Steelmaking

Interest in the field of metallurgical foams and emulsions was aroused by the work of Cooper and Kitchener[29] on the foaming of molten silicates. Laboratory experiments on $CaO-SiO_2-P_2O_5$ melts showed that foaming is absent with binary $CaO-SiO_2$ melts but is marked when P_2O_5 is added to melts containing more than 50 mole % SiO_2. The foam stability was shown to increase with (a) the proportion of P_2O_5 (in the range 0-1.8%), (b) the proportion of SiO_2 (50-63%), and (c) a decrease in temperature. The theory of foaming proposed for this system was based on the assumption that P_2O_5 is responsible for a degree of surface elasticity, which, however, is insufficient to sustain foaming unless the melt is viscous (i.e. unless the melt is of low $CaO:SiO_2$ ratio and at relatively low temperatures).

Cooper and McCabe[30] elaborated on the requirements of a surface active oxide in a slag. They suggest that oxides which are believed to be surface active and which are effective as foaming agents have a high value of the ratio of cation valence (Z) to ionic radius (R). The value of Z/R at which the transition from a foaming to non-foaming agent occurs was given as about 5-6, which indicates that P_2O_5, SiO_2, TiO_2 and Al_2O_3 should be effective foaming agents.

Kozakevitch[31] reviewed the conditions favouring foam and emulsion formation. He cited the lowering of interfacial tension by surface active agents as being important while stirring and gas evolution provide the energy necessary to increase the interface. Stabilization of gas and liquid emulsions was favoured by high viscosity of liquid medium and by formation of a viscous or rigid adsorption film at the interface.

The oxides SiO_2, P_2O_5, TiO_2 and Fe_2O_3 were shown by Kozakevitch[4] to lower the surface tension of slags. He suggests that these oxides adsorbed at the surface of steelmaking slags. The stabilization of the metal-in-slag emulsions in the OLP/LDAC process was attributed to crystallization of silicophosphates. Kozakevitch observed that phosphorous and carbon contents of the emulsified iron was lower than that of the iron bath at the same period of the blow. He noted that small droplets were lower in carbon and phosphorous content that big droplets due to the higher surface to volume ratios of the smaller particles.

Samples of slag splashed from an on-line 230 ton BOF at Jones and Laughlin's Cleveland Works were taken by Meyer et al[3] who were able to isolate emulsified iron drops and to determine their carbon content. The carbon content of the iron bath was calculated from the exhaust gas analysis at the same time as each emulsion sample was ejected.

These authors found that the emulsion droplets were lower in % carbon than the bath at each point in the blow and that the smaller droplets contained the least carbon. The authors explain the high reaction rates in the BOF as being due to the "relatively stable slag-metal emulsions formed". Meyer et al[3] were unable to determine the contribution of the metal-slag reaction to the overall rate of reaction because the rate of droplet formation and the residence time of the droplets could not be determined in these experiments.

CHAPTER 3

3.0 DISPERSE METALLURGICAL SYSTEMS

3.1 Definitions of an Emulsion

In general particles of one medium suspended in a second immiscible medium can be referred to as a disperse system. In extractive metallurgy the disperse systems of interest are: small bubbles dispersed in slags (foams) and metal drops emulsified in slags.

The subject of foams and emulsions has been thoroughly investigated by organic chemists using detergent foams and water-oil emulsions. Several different definitions have been postulated by the organic chemists. A listing of the definitions for an emulsion is given below:

1. An emulsion is a very fine dispersion of one liquid in another with which it is immiscible[32].

2. An emulsion is a system containing two liquid phases, one of which is dispersed as globules in the other[33].

3. Emulsions are mechanical mixtures of liquids that are immiscible under ordinary conditions and which may be separated into layers on standing, heating, freezing, by agitation or the addition of other chemicals[34].

4. An emulsion is a two-phase liquid system consisting of fairly coarse dispersions of one liquid in another with which it is not miscible[35].

5. Emulsions are intimate mixtures of two immiscible liquids, one of them being dispersed in the other in the form of fine droplets[36].

6. ......emulsions are finely divided liquid to semi-solid substances[37].

7. Emulsions....are microscopically visible droplets of one liquid suspended in another[38].

8. Emulsions are stable and intimate mixtures of the oil or oily material with water[39].

9. An emulsion....consists of a stable dispersion of one liquid in another liquid[40].

The above definitions all contribute in explaining an emulsion. However, only two refer to stability (8 and 9), while only definition (3) refers to instability. Definition (7) limits the size of the dispersed phase. Surprisingly five definitions (2, 6, 7, 8 and 9) do not mention miscibility while the meaning of definition (6) is not clear. Definition (8) is the only one which stipulates the substances to be oil and water.

This author feels that Becher's[41] definition modified to include dispersed gas bubbles is the most concise definition:

An emulsion is a heterogeneous system, consisting of at least one immiscible liquid or gas intimately dispersed in another in the form of droplets or bubbles, whose diameters, in general, exceed 0.1μ. Such systems possess a minimal stability, which may be accentuated by such additives as surface active agents or finely divided solids.

A dispersion of metal droplets in a slag satisfies all the conditions of the above definition: metal and slag are immiscible by the very nature of pyro-metallurgical separations, the droplet sizes satisfy the 0.1 μ limit[3,4], the emulsion of metal in slag is unstable, and the existance of surface active agents, which tend to stabilize the emulsions, has been postulated by certain researchers.

The dispersion of metal droplets in slag can by this definition be called an emulsion.

3.2 Theory of Emulsions

The theory of emulsions with regard to formation and stability will be discussed on the basis of the water-oil low temperature system then analogies will be given for the metal-slag high temperature system. The accepted terminology describing an emulsion of oil and water is water-in-oil (water is the disperse phase) abbreviated W/O or oil-in-water (oil is the disperse phase) abbreviated O/W. Applying this convention to the metallurgical emulsions gives M/S for a metal-in-slag emulsion and S/M for a slag-in-metal emulsion. These terms will be used throughout as abbreviated forms.

When two immiscible liquids are in contact in a vessel, an interface exists between them. The thermodynamic stability of this interface is a function of the surface forces acting at this interface. Emulsification of one liquid into another is thermodynamically more favourable than the existance of a single interface between the two when the interfacial tension between the two liquids is low, i.e., when the energy needed to create the new surface of an emulsion droplet is low. In exceptional cases[41], the energy is negative and emulsification can occur spontaneously.

The effect of an emulsifying agent on interfacial tension can be readily shown. For example the interfacial tension of olive oil against water at 20°C is 22.9 dynes cm^{-1}. If ten cubic centimetres of this oil is emulsified into droplets having a radius of 0.1 μ, the interfacial area created is 300 square meters. The work of creation of a new surface is given by the product of the interfacial tension by the surface area, therefore work needed to emulsify the 10 cm^3 of olive oil would be 6.86 joules. Since this energy is contained in the system as potential energy, it represents a considerable degree of thermodynamic instability. A suitable soap addition can reduce the interfacial tension to 2 dynes cm^{-1}. This would reduce the equivalent creation energy to .60 joules.

Ross, Chen, Ranouts and Becher[42] were able to show that a correlation exists between the spreading coefficient between the phases and emulsion stability (in the presence of an emulsifying agent). Figure 3.1 illustrates the behaviour of an oil droplet in an O/W emulsion as a function of the spreading coefficient $S = \gamma_{W/A} - \gamma_{O/A} - \gamma_{O/W}$.

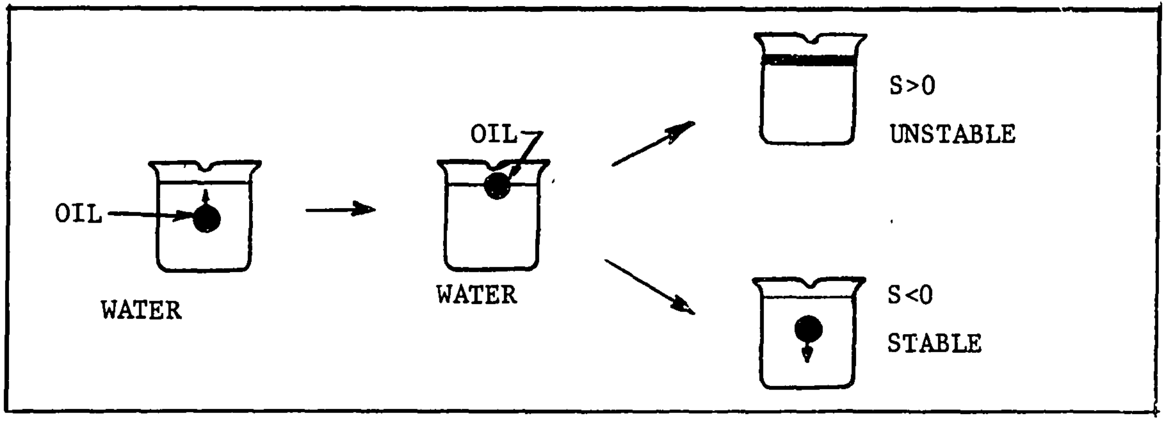

Figure 3.1 Oil droplet in an O/W emulsion, spreading coefficient

$$S = \frac{\partial F}{\partial A} = \gamma_{W/A} - \gamma_{O/A} - \gamma_{O/W}$$

The rising droplet encounters the liquid surface where two things may happen. In the case S<0 the drop will spread on the surface, becoming a film of oil, losing its identity as a droplet. In the other case S>0, the oil will not spread and it will, in due course, return to the body of the emulsion. A negative spreading coefficient between the phases of the emulsion is necessary to ensure stability.

Although the simple correlation of emulsion stability with low interfacial tension is not the complete explanation of stability, a low interfacial tension may be classed in the category of what mathematicians call a "necessary but not sufficient" condition for stability. In terms of the spreading coefficient the most negative spreading coefficient consistent with a low interfacial tension would be the criterion for stability.

Surface and interfacial tension may be explained on a molecular basis by the statement that the Van der Waals field of force acting on a molecule at the surface of a liquid is different from that in the bulk of the liquid (Figure 3.2). In the case of solutions, the molecules whose interaction energy is smallest will tend to accumulate in the surface, thus minimizing the free energy of the system.

Gibbs defined Γ, called the surface excess, which is the concentration of the solute adsorbed at the surface expressed as moles per unit area. The Gibbs' Adsorption Equation is written as:

$$\partial\gamma + \Gamma_1 \partial\mu_1^s + \Gamma_2 \partial\mu_2^s + \ldots\ldots\ldots\ldots\ldots + \Gamma_n \partial\mu_n^s = 0 \ldots\ldots\ldots\ldots 3.1$$

Where: μ_n^s - surface chemical potential of species n

Γ_n - surface excess of species n moles cm^{-2}

γ - surface tension of solution dynes cm^{-1}

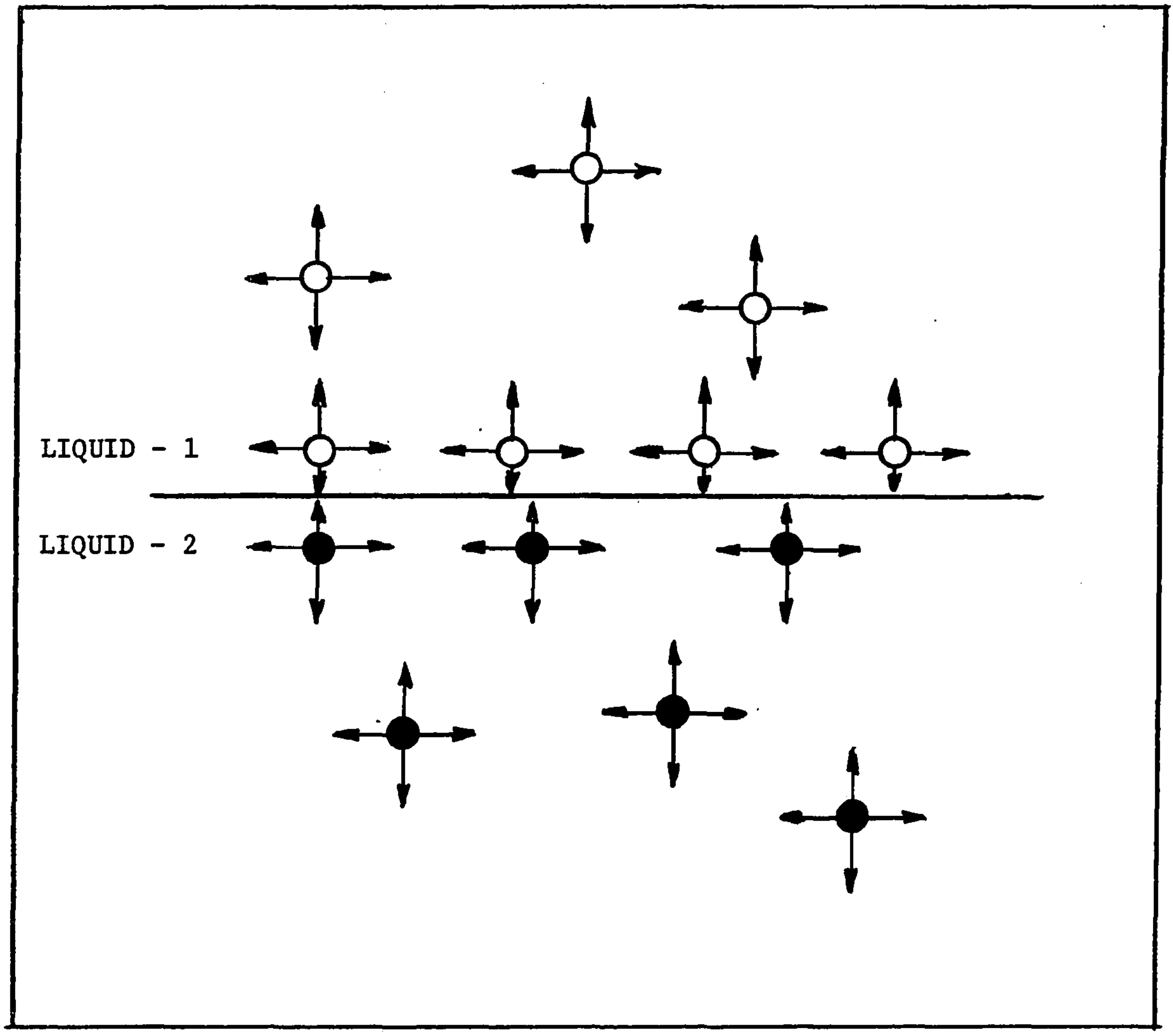

Figure 3.2 Forces acting at the molecules at the interface and in the interior of a pair of liquids.

For a two component dilute system the Gibbs Adsorption Equation can be expressed by using $\mu_i = \mu_i^o + RT \ln a_i$

$$\Gamma_2 = \frac{-a_2}{RT}\left(\frac{d\gamma}{da_2}\right)_T \quad \ldots\ldots\ldots\ldots 3.2$$

create the new surface of an emulsion droplet is low. In exceptional cases[41], the energy is negative and emulsification can occur spontaneously.

The effect of an emulsifying agent on interfacial tension can be readily shown. For example the interfacial tension of olive oil against water at $20^{o}C$ is 22.9 dynes cm^{-1}. If ten cubic centimetres of this oil is emulsified into droplets having a radius of 0.1 μ, the interfacial area created is 300 square meters. The work of creation of a new surface is given by the product of the interfacial tension by the surface area, therefore work needed to emulsify the 10 cm^3 of olive oil would be 6.86 joules. Since this energy is contained in the system as potential energy, it represents a considerable degree of thermodynamic instability. A suitable soap addition can reduce the interfacial tension to 2 dynes cm^{-1}. This would reduce the equivalent creation energy to .60 joules.

Ross, Chen, Ranouts and Becher[42] were able to show that a correlation exists between the spreading coefficient between the phases and emulsion stability (in the presence of an emulsifying agent). Figure 3.1 illustrates the behaviour of an oil droplet in an O/W emulsion as a function of the spreading coefficient $S = \gamma_{W/A} - \gamma_{O/A} - \gamma_{O/W}$.

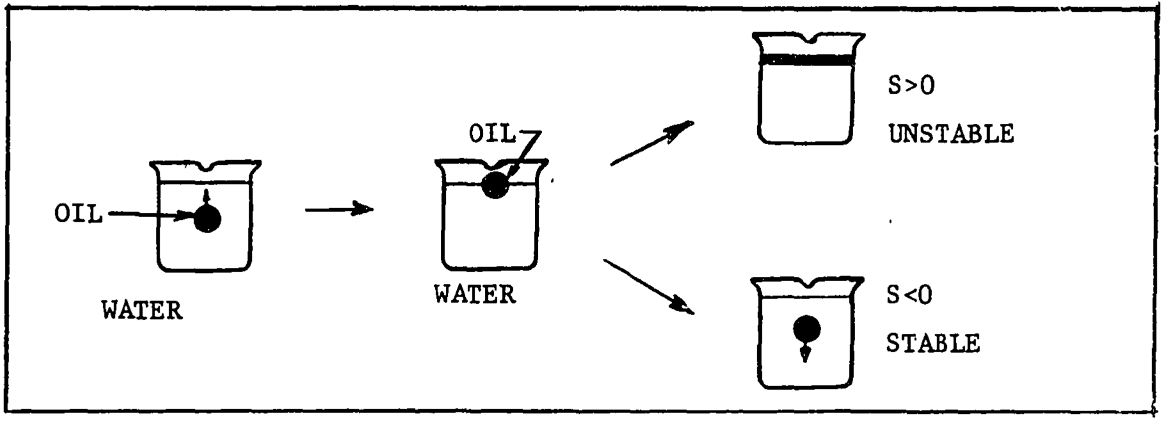

Figure 3.1 Oil droplet in an O/W emulsion, spreading coefficient

$$S = \frac{\partial F}{\partial A} = \gamma_{W/A} - \gamma_{O/A} - \gamma_{O/W}$$

The rising droplet encounters the liquid surface where two things may happen. In the case S<0 the drop will spread on the surface, becoming a film of oil, losing its identity as a droplet. In the other case S>0, the oil will not spread and it will, in due course, return to the body of the emulsion. A negative spreading coefficient between the phases of the emulsion is necessary to ensure stability.

Although the simple correlation of emulsion stability with low interfacial tension is not the complete explanation of stability, a low interfacial tension may be classed in the category of what mathematicians call a "necessary but not sufficient" condition for stability. In terms of the spreading coefficient the most negative spreading coefficient consistent with a low interfacial tension would be the criterion for stability.

Surface and interfacial tension may be explained on a molecular basis by the statement that the Van der Waals field of force acting on a molecule at the surface of a liquid is different from that in the bulk of the liquid (Figure 3.2). In the case of solutions, the molecules whose interaction energy is smallest will tend to accumulate in the surface, thus minimizing the free energy of the system.

Gibbs defined Γ, called the surface excess, which is the concentration of the solute adsorbed at the surface expressed as moles per unit area. The Gibbs' Adsorption Equation is written as:

$$\partial\gamma + \Gamma_1 \partial\mu_1^s + \Gamma_2 \partial\mu_2^s + \ldots\ldots\ldots\ldots + \Gamma_n \partial\mu_n^s = 0 \ldots\ldots\ldots\ldots 3.1$$

Where: μ_n^s - surface chemical potential of species n

Γ_n - surface excess of species n moles cm^{-2}

γ - surface tension of solution dynes cm^{-1}

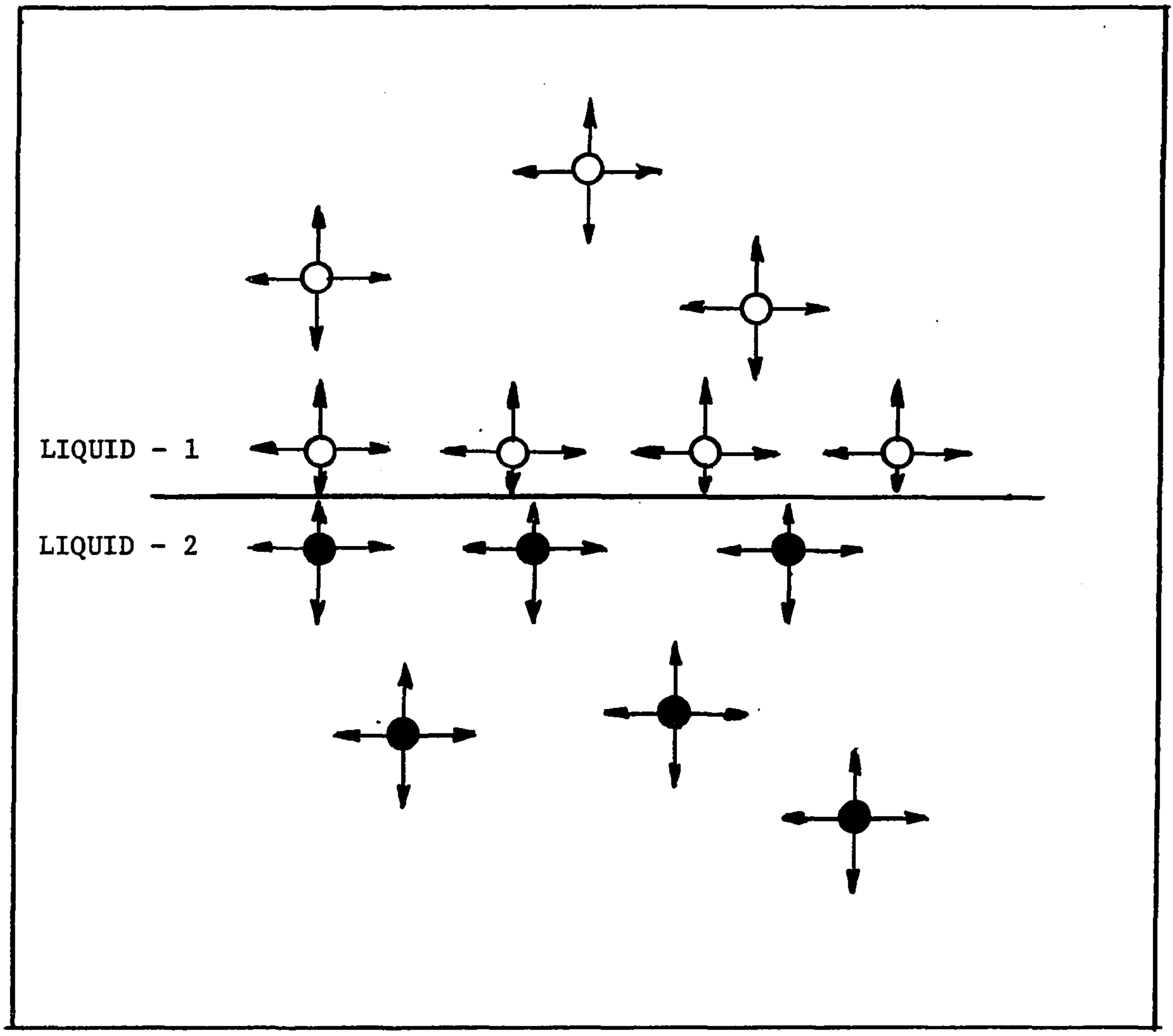

Figure 3.2 Forces acting at the molecules at the interface and in the interior of a pair of liquids.

For a two component dilute system the Gibbs Adsorption Equation can be expressed by using $\mu_i = \mu_i^o + RT \ln a_i$

$$\Gamma_2 = \frac{-a_2}{RT}\left(\frac{d\gamma}{da_2}\right)_T \quad . \; . \; . \; . \; . \; . \; . \; . \; . \quad 3.2$$

Where: R - gas constant

T - temperature in absolute degrees

a_2- activity of species 2

Thus an increase in surface concentration of the surface active agent results in a surface or interfacial tension decrease. The increased concentration per unit area of solute in the surface also tends to oppose the stretching of the liquid surface.

Langmuir and Harkins[43] proposed a theory whereby the polar groups of the emulsifying agent are oriented towards the water phase and the non-polar hydrocarbon chains are oriented towards the oil in water-oil emulsions. A schematic representation of a soap molecule is shown in Figure 3.3.

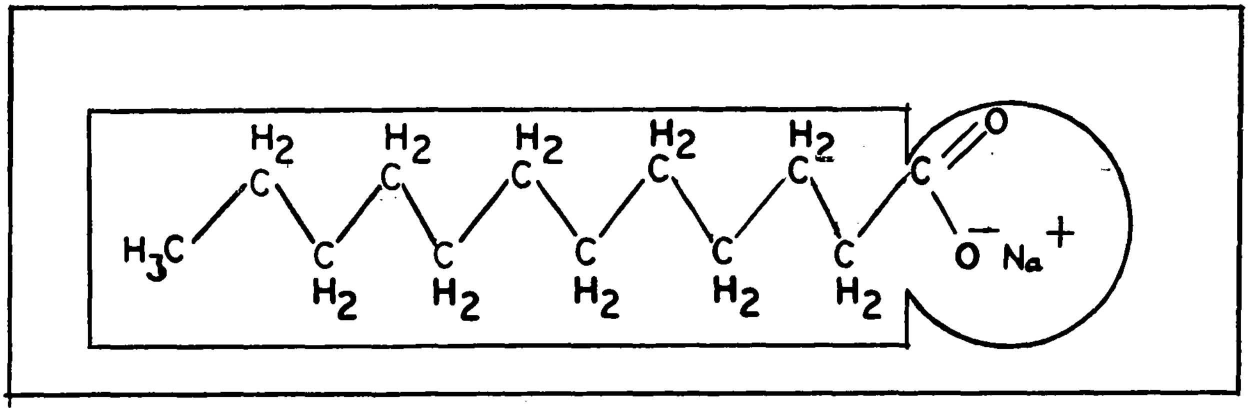

Figure 3.3 The structure of sodium stearate schematically shown as the rectangular non-polar, hydrophobic hydrocarbon tail and the circular polar, hydrophilic, carboxylic head.

Thus an O/W emulsion stabilized by sodium stearate could be schematically shown as in Figure 3.4.

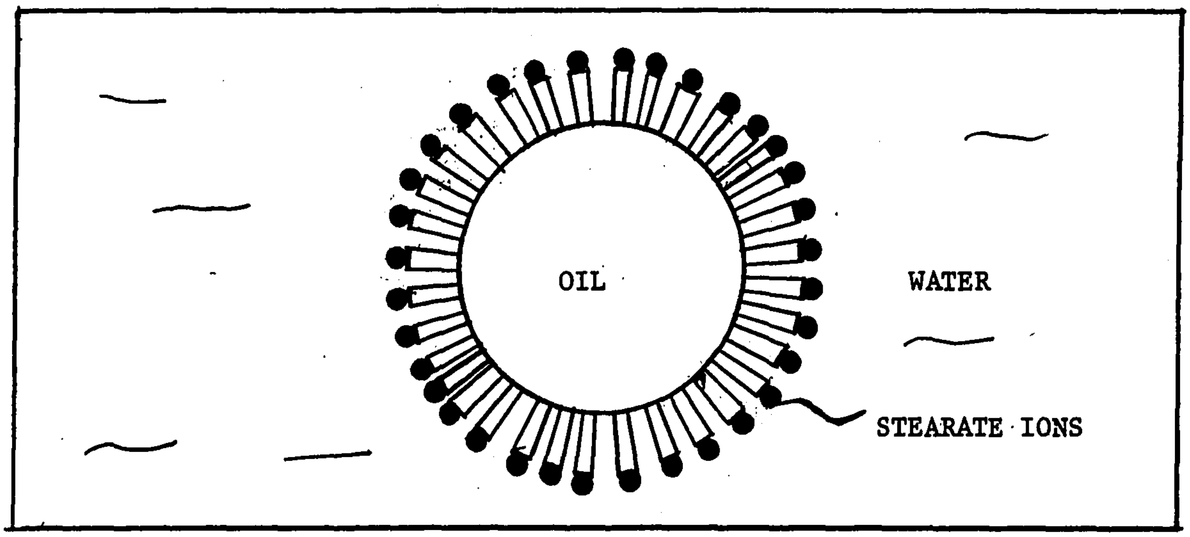

Figure 3.4 Oil droplet covered with stearate ions presents a polar surface to water matrix.

However, where the alkali-metal soaps favour O/W emulsions, alkaline earth soaps, which consist of two non-polar hydrocarbon tails with a metal ion, form W/O emulsions. A W/O emulsion stabilized by magnesium stearate could be schematically shown as in Figure 3.5.

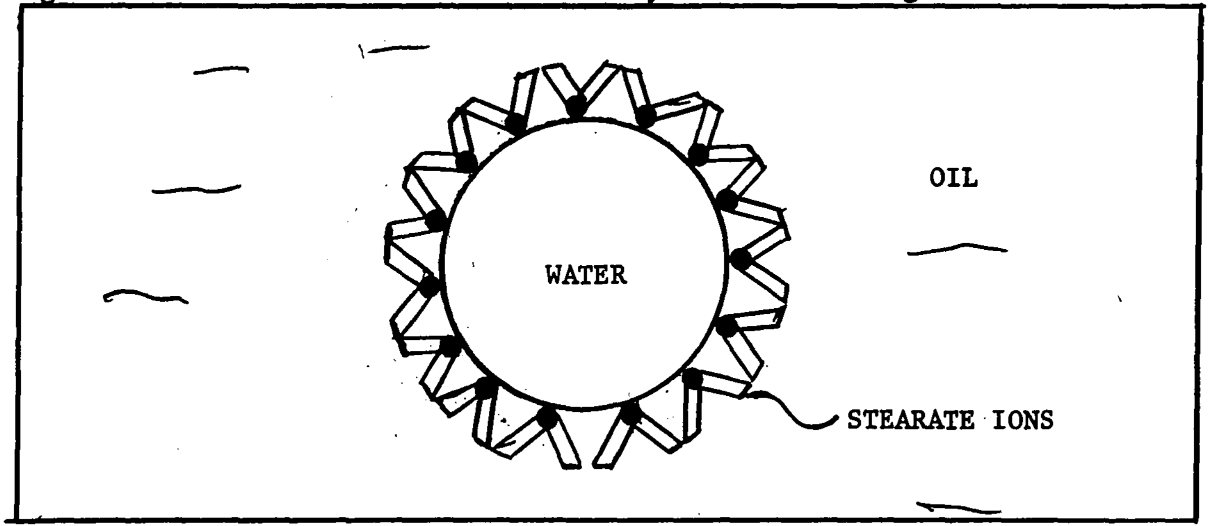

Figure 3.5 Water droplet coated by stearate ions presents a non-polar surface to oil matrix.

It can be seen from Figure 3.4 that an O/W emulsion would not be favoured with alkaline earth soaps as the two tails would be unfavourably crowded on the inside of an oil sphere. The phase in which the emulsifying agent is more soluble will generally be the external one.

The stabilizing effect of these surface active agent coatings is the result of the increase of interfacial viscosity which impedes settling and coalescence, ie., the ionic coating of the oil droplet can participate in the hydrogen bonding of the water media while the non-polar coating of the water droplet in a W/O emulsion exerts Van der Waals attraction forces with the oil matrix. Both cases of bonding contribute to the stability of the liquid-liquid interface and hence to emulsion stability.

Electrical theories of emulsion stability are based on the existance of an electrical double layer at the droplet surface. (Figure 3.6).

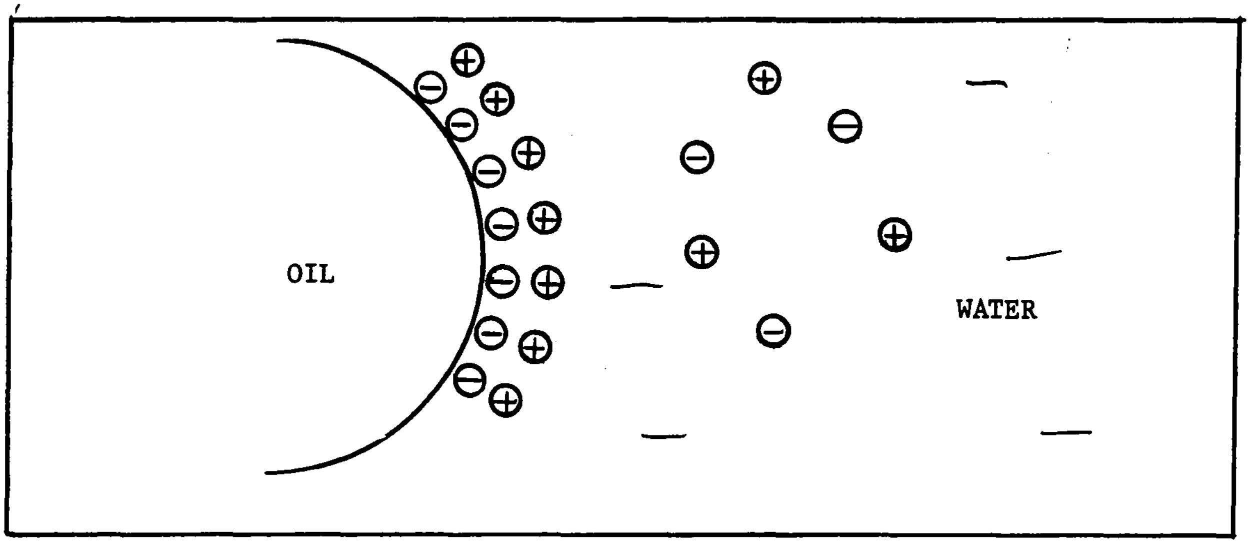

Figure 3.6 The existance of an electrical double layer in an O/W emulsion.

The existance of an electrical double layer at the aqueous side of the oil droplet surface is a result of the ionic charge of the surface active agent (for example the negative charge of the stearate ion) which will tend to attract cations to its surface. The electrical double layer at the surface of a water droplet in a W/O emulsion is a result of the adsorption of charged surface active ions from the aqueous phase. However these charges arise, their presence on the emulsion droplet contributes to the stability of the system, since the mutual repulsion of the charged particles prevents their close approach and coalescence.

Finely divided solids can stabilize foams and emulsions by concentrating at the interface. If the water-oil interfacial tension is greater than the total of the water-solid surface tension plus the oil-solid interfacial tension then the particle will tend to stay at the interface. The following force balance determines the position of the solid particle at the liquid-liquid interface: $\gamma s/o - \gamma s/w = \gamma w/o \cos\theta$ 3.4

Where: $\gamma s/o$ - Solid-oil interfacial tension dynes cm^{-1}

$\gamma s/w$ - Solid-water interfacial tension dynes cm^{-1}

$\gamma w/o$ - Water-oil interfacial tension dynes cm^{-1}

θ - Contact angle between particle and interface.

Figure 3.7 shows the directions of the forces acting on the particle and the three possible situations at the liquid-liquid interface.

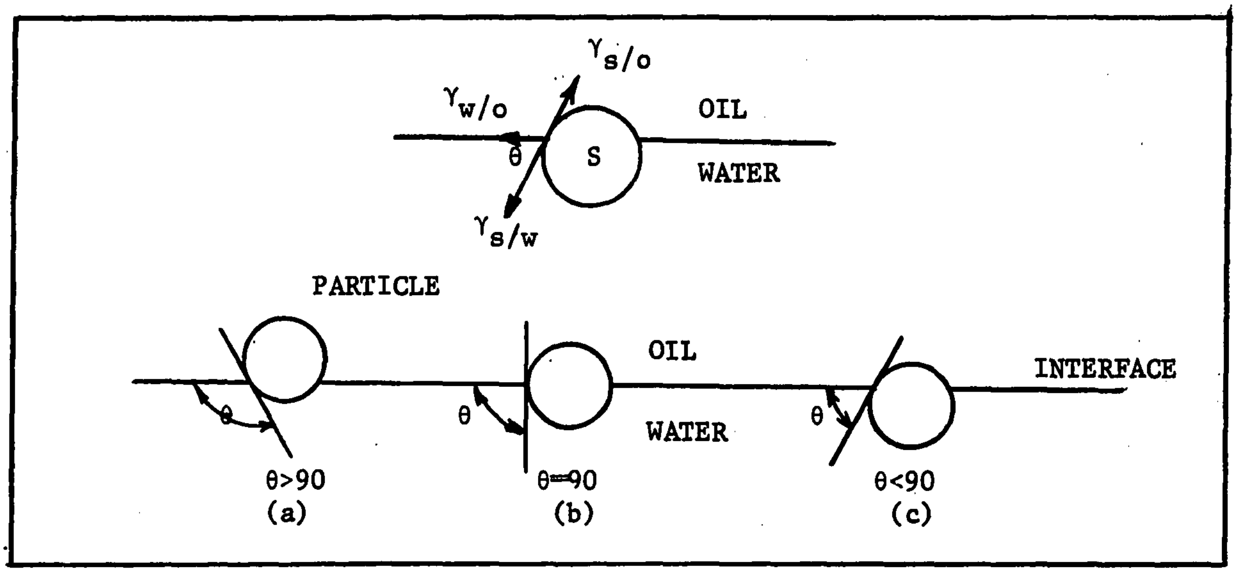

Figure 3.7 Three ways in which solid particles may distribute themselves in an oil-water interface: (a) Particle is wetted by oil so is mainly in the oil, (b) Equal wetting by both phases (c) Particle is better wetted by water so is in water.

According to Schulman and Leja[44] the most stable emulsions are obtained when the contact angle with the solid at the interface is close to 90°. The emulsion which forms is that which contains the solid particles in the disperse phase. A concentration of solids at the interface represents an interfacial "film" of considerable strength and stability, which will serve to stabilize such emulsions.

3.3 Theory of Metal-Slag Emulsions

Some generally accepted facts in metallurgical disperse systems were listed by P. Kozakevitch[31].

a) Emulsion and foam formation is favoured by lowering interfacial tension (liquid-liquid or liquid-gas) by dissolved surface active agents.

b) Stirring and mechanical agitation provides the energy needed to increase the amount of interface.

c) Gas evolution effectively provides stirring and is also important in that it supplies gas to the foam.

d) The stabilization of emulsions and foams is favoured by a high viscosity liquid medium which may stop the normal destruction of the emulsion through coalescence and gravity.

If an analogy is to be drawn between W/O emulsions and M/S emulsions, there is a need for surface active agents to promote stability by producing low interfacial tension and a negative spreading coefficient. Comparing the two systems: the aqueous emulsion involves a polar liquid with a non-polar liquid usually characterized by long hydrocarbon chains. Molecular bonding is covalent in the non-polar oil and no appreciable inter-molecular bonding is present. Water represents the polar liquid characterized by hydrogen bonding and ions in solution.

The metallurgical system involves a liquid composed of mobile atoms having long range disorder. X-ray diffraction has suggested that, in liquid metals, some short range order may temporarily exist; several atoms forming a short-lived crystal lattice. Liquid metals conduct electricity in the same way as solid metals so the presence of a similar electron cloud is thought to exist around the metal nucleii.

Slag properties and structures have been studied by many authors[45, 46,47]. Slag is, very simply, a molten salt, ionic in nature, having short range order (covalent bonding of silica tetrahedra), but long range disorder. Slags conduct electricity[48] by ionic transfer and have much lower conductivity than liquid metals. Figure 3.8 shows a two-dimensional schematic of liquid silicate structures.

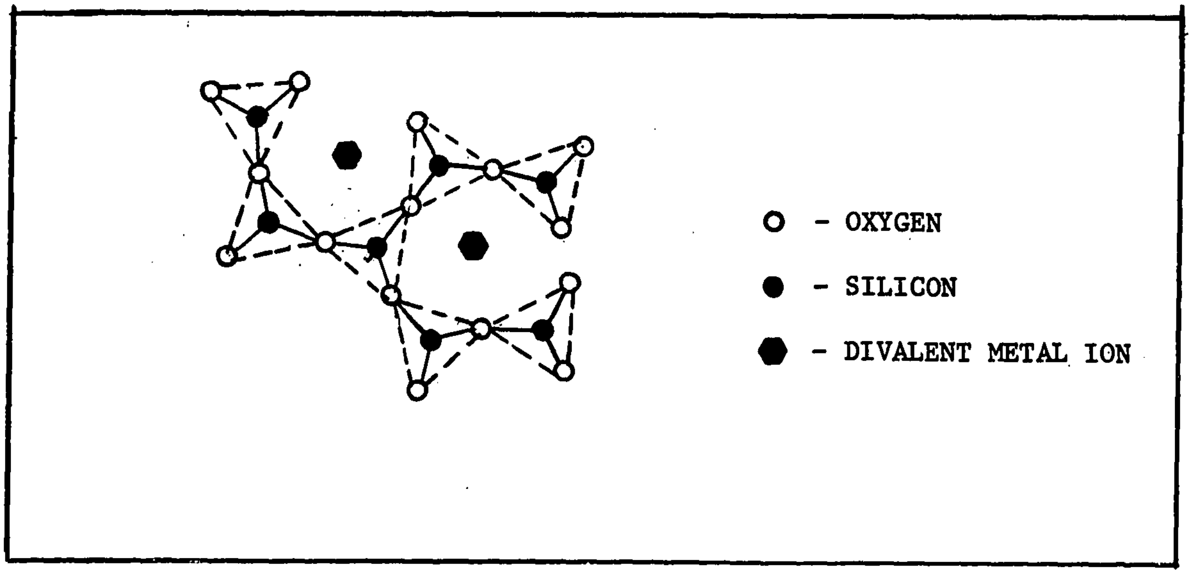

Figure 3.8 Schematic representation of solutions of a divalent metal oxide in molten silica.

Surface active agents in W/O emulsions are characterized by long hydrocarbon chains finally ending with a metallic ion. The ionized soap has a polar end and a non-polar end. In the same way surface active agents in M/S emulsions can be expected to have a chain silicate end and a charged or cationic end. $(FeO.SiO_2)_n$ is an example of a surface active agent in certain metallurgical systems.

According to the Langmuir and Harkins Film Adsorption Theory[43], the $Si_4O_{13}^{-10}$ ions (from a 5 $FeO.4SiO_2$ slag) for example, would align themselves on the metal drop so that the drop surface would have a slag appearance to an external observer. The surface active agent may attach itself to the metal drop in any of three different ways:

1) The iron drop may absorb or dissolve the iron ion leaving the silicate clinging to the droplet surface, due to the excess in charge of the metal drop. The combination of drop and adsorbed ion would be

electrically neutral. This mechanism would rule out the surface active behaviour of any other cation than Fe^{+2} or Fe^{+3} eg. Ca^{+2}, Mg^{+2}.

2) The iron ion may adsorb on the iron droplet surface. This would be a simple physical adsorption and the bonding forces between the drop and adsorbed ion would be of the weak Van der Waals type.

3) The $Si_4O_{13}^{-10}$ ion may chemisorb onto the iron droplet surface. A chemical bond can form between the iron droplet surface and the silicate ion. The combination will have a charge of $-10n$, where n is the number of chemisorbed ions. This mechanism does not require the presence of a cation from the slag, although later association may occur due to charge attraction.

Mechanism 1 and 3 must play the most important roles, the weakness of Van der Waals bonds diminishing the importance of mechanism 2. Figure 3.9 illustrates each mechanism, where for simplicity only one surface active ion is considered.

Drawing a comparison between the metallurgical surface active agents described above and those of the water-oil systems described earlier, it would seem that increasing the size of the adsorbing ion would increase emulsion stability. Examining the typical slag-forming oxides and their structures, according to the model of Toop and Samis [49,50], will help explain the role of the metallurgical surface active agent. Table 3.1 lists various ions present in CaO, SiO_2, P_2O_5 slags.

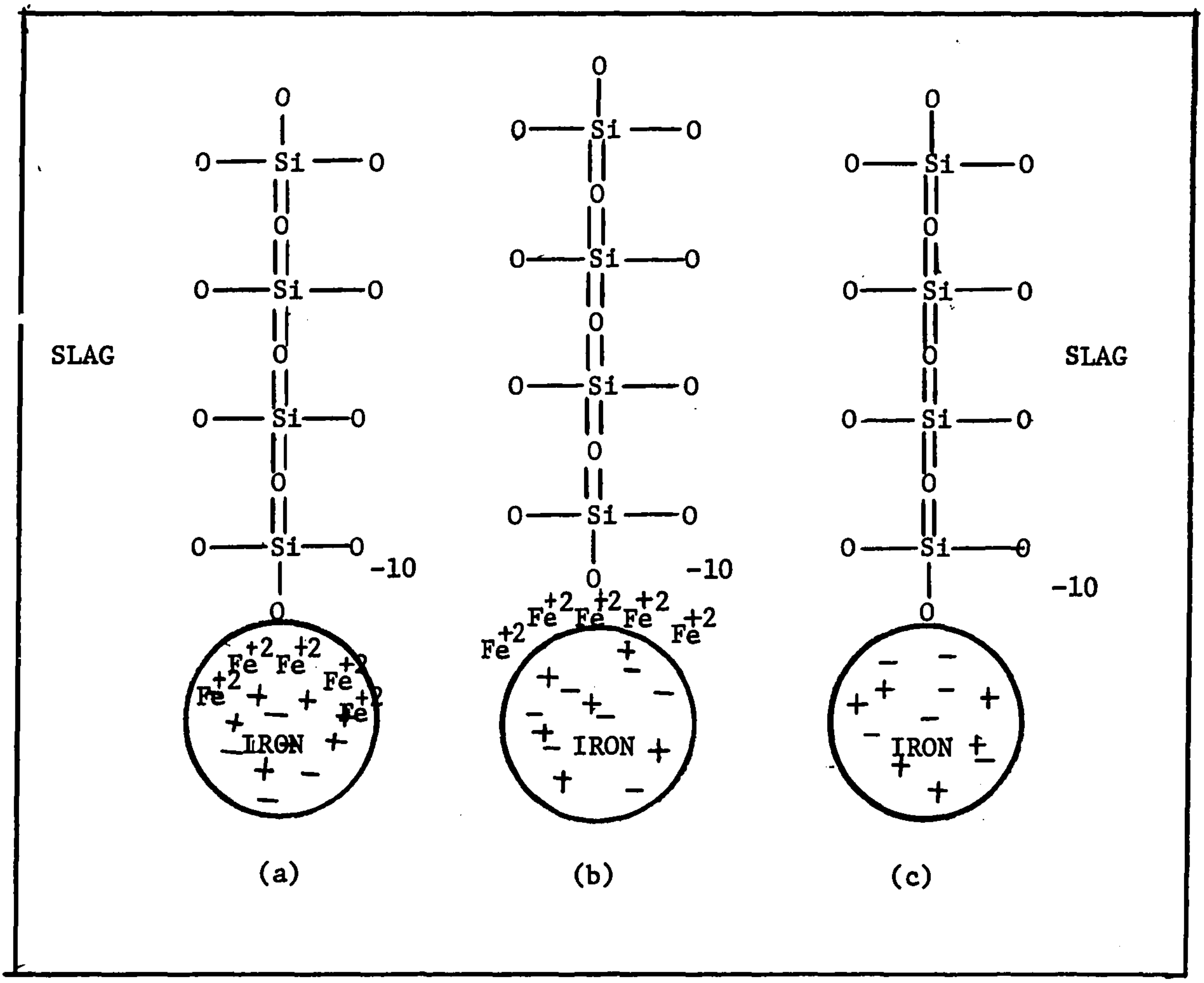

Figure 3.9 Mechanisms of surface active agent attachment (Only one adsorbing ion is shown for simplicity).

a) Iron ion absorption into iron droplet.

b) Iron ion adsorption onto droplet surface.

c) Chemisorption of $Si_4O_{13}^{-10}$ ion onto iron surface.

TABLE 3.1

Slag	Base/Acid Mole ratio	Most Prevalent Ions[49,50]	Probable Structure
$2CaO.SiO_2$	2:1	SiO_4^{-4}	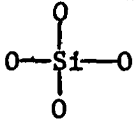 chain
$3CaO:2SiO_2$	3:2	$Si_2O_7^{-6}$	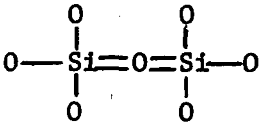 chain
$CaO.SiO_2$	1:1	$Si_4O_{12}^{-8}$	ring (Figure 3.10)
$CaO.2SiO_2$	1:2	$Si_{12}O_{30}^{-12}$	double ring
$CaO.3SiO_2$	1:3	$Si_{24}O_{56}^{-16}$	treble ring
$3CaO.P_2O_5$	1:3	PO_4^{-3}	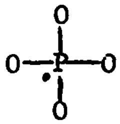

Where . represents an electron free to form a bond

Table 3.1 shows the silicate ions of the acid and neutral slags to be in the form of chains or rings. The silicate chains are negatively charged and can chemisorb at a drop interface according to mechanism 3. Chemisorption of silicate rings at a surface in the form of chains can occur if an oxygen ion is available at the surface to break one of the double bonds of the ring, creating a silicate chain (Figure 3.10).

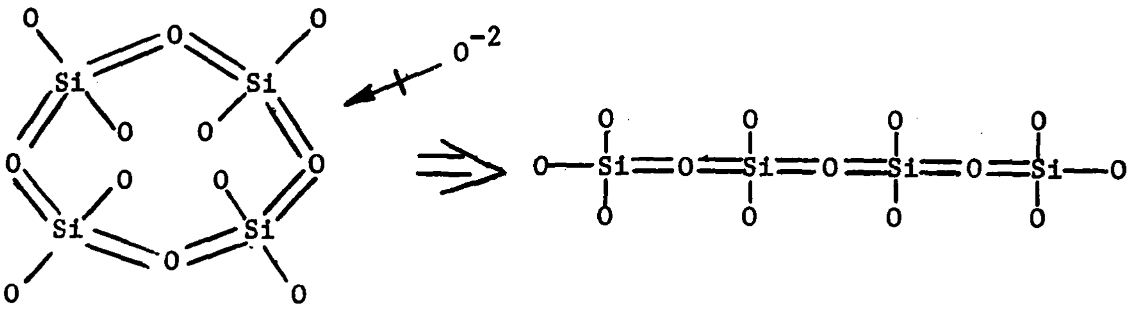

$Si_4O_{12}^{-8}$ + O^{-2} = $Si_4O_{13}^{-10}$

RING CHAIN

Figure 3.10 The conversion of a silicate ring to a chain by addition of one oxygen ion.

In practice the oxygen ion may come from oxygen dissolved in the iron drop.

The surface active behaviour of phosphate ions and chains in silicate slags has been demonstrated by Cooper and Kitchener[29]. The free bonding electron, shown by the dot in Table 3.1, not only aids in the formation of PO_4^{-3} chains but may also be important in the adsorption of this chain at an interface by forming a chemical bond.

The increased viscosity of the high silica slags also aids emulsion and foam stability.

Solid particles are known to stabilize slag foams, Cr_2O_3 being an example. The stabilization of M/S emulsions by suspended particles due to an increase in strength of the interfacial film occurs as in the analogous low temperature systems.

CHAPTER 4

4.0 SCALE-DOWN OF INDUSTRIAL BOF

Several researchers have used models to investigate the basic oxygen process[17,23,24,26,51]. The use of low temperature models enables the study of fluid dynamic parameters in experimentally convenient systems.

In order for a model to be applicable to its prototype, conditions must be the same in both. A particular system described by a finite number of variables will yield a finite number of dimensionless groupings of these variables. If a model system can be devised, that is characterized by the same dimensionless groups as a prototype, the two systems are similar, providing the numerical values of the groups are identical. Under these circumstances the behaviour of a model would give accurate information concerning the performance of the prototype.

It is rarely possible to produce a model that is exactly similar to a particular prototype. However, theoretical considerations of the process under question suggest that certain dimensionless groups are more important to a process than others. Maintaining the important dimensionless groups constant at the expense of the least important ones will give a good approximation to the prototype.

The basic oxygen furnace presents a complicated system of gaseous and liquid flow and it is not possible to build a perfect model with a full application of the laws of physical and chemical symmetry. Newby[17] was the first researcher to make use of the modified Froude number as the most relevant dimensionless group: $\dfrac{\rho_g\, v_m^2}{\rho_l\, l g}$

Where: ρ_g - gas density

ρ_1 - liquid density

V_m - exit velocity of jet

1 - linear dimension (jet diameter)

g - gravity constant

The Froude number (v^2/lg) represents the ratio between the inertial force of the jet disturbing the surface and the force of gravity tending to flatten it out. Full similarity would necessitate that the ratio of gas density to liquid density be the same in the model as in the prototype. However, the inertial force of the gas jet on the liquid is more important than the gravitational force acting on the liquid, thus the ratio of inertial force in the gas to gravity force in the liquid was considered sufficient criterion for similarity.

The experimental BOF's used in the present research were scaled according to geometrical similarity (1:54 linear scale ratio) and according to modified Froude Number similarity. The data characterizing an industrial BOF are listed in table 4.1.

TABLE 4.1

INDUSTRIAL BOF DATA	
Vessel diameter (D)	18 ft.
Lance diameter (d_1)	3 in.
Lance height* (h)	4.5 ft.
Pig iron depth (t_m)	4.5 ft.
Slag layer depth (t_s)	1.5 ft.
Molten metal density (ρ_m)	7.2 gm cm^{-3} (448 lb ft^{-3})
Molten slag density (ρ_s)	$\sim$3.5 gm cm^{-3} (187 lb ft^{-3})
Metal viscosity (μ_m) (η_m)	5 centipoise .69 centistokes
Slag viscosity (μ_s) (η_s)	50 centipoise 14.3 centistokes
Metal surface tension (γ_m)	1200 dynes cm^{-1}
Slag surface tension (γ_s)	500 dynes cm^{-1}
Slag-Metal interfacial tension ($\gamma_{s/m}$)	700 dynes cm^{-1}
Oxygen flow rate (Q)	20,000 SCFM (6.8 x 10^3 ft sec^{-1})
Blow time	20 minutes
Metal temperature	1600°C

*Lance height or lance to bath distance is the distance between the lance tip and the slag surface.

4.1 Room Temperature Model Scale Factors

The data characterizing the room temperature model are listed in Table 4.2. Singly primed variables refer to the room temperature model.

TABLE 4.2

CLEAR ACRYLIC PLASTIC BOF MODEL	
Vessel diameter (D')	10 cm
Lance diameter (d_1')	.15 cm
Lance height (h')	2.5 cm
Sodium bicarbonate solution depth (t_w')	2.5 cm
Oil layer depth (t_o')	.84 cm
$NaHCO_3$ solution density (ρ_w')	1.033 gm cm^{-3}
Oil density (ρ_o')	.8454 gm cm^{-3}
$NaHCO_3$ solution Viscosity (μ_w') (η_w')	1.25 centipoise 1.21 centistokes
Oil viscosity (μ_o') (η_o')	17.9 centipoise 21.2 centistokes
$NaHCO_3$ surface tension (γ_w')	75.4 dynes cm^{-1}
Oil surface tension (γ_o')	29.3 dynes cm^{-1}
$NaHCO_3$ - Oil interfacial tension (γ_{ow}')	49.7 dynes cm^{-1}
Gas flow rate (90%Ar&10%HCl)	100 cm^3 sec^{-1} (5659 cm sec^{-1})
Blow time	5 minutes
Solution temperature	25°C

Gas densities in the two systems are calculated using the ideal gas law:

ρ''_g (oxygen) - .025 lb ft^{-3} at 800°C

ρ''_g (CO) - .020 lb ft^{-3} at 800°C

$\rho'g$ (90%Ar&10%HCl) - .00162 gm cm^{-3} at 25°C

$\rho'g$ (CO_2) - .00180 gm cm^{-3} at 25°C

Gas velocities in the two systems are a function of the nozzle characteristics and flow rate:

v''_g (oxygen) - 6790 ft sec^{-1}

v'_g (90%Ar&10%HCl) - 5659 cm sec^{-1}

The scale-down calculations for the room temperature model were made using the vessel inside diameter and fluid properties as known starting values. The dimensionless groups and their corresponding dimensionless numbers are shown in Table 4.3 for the room temperature model and the prototype.

TABLE 4.3

SIMILARITY CRITERIA			
PROTOTYPE		ROOM TEMPERATURE MODEL	
Dimensionless Group	Dimensionless Number	Dimensionless Group	Dimensionless Number
$\frac{D}{d_1}$	72	$\frac{D'}{d'_1}$	67.7
$\frac{D}{h}$	4	$\frac{D'}{h'}$	4
$\frac{D}{t_s}$	12	$\frac{D'}{t'_o}$	12
$\frac{D}{t_m}$	4	$\frac{D'}{t'_w}$	4
$\frac{\rho_m}{\rho_s}$	2.1-2.5	$\frac{\rho'_w}{\rho'_o}$	1.2-1.3
$\frac{\eta_s}{\eta_m}$	20.6	$\frac{\eta'_o}{\eta'_w}$	17.5
$\frac{\gamma_m}{\gamma}$	2.4	$\frac{\gamma'_w}{\gamma'_o}$	2.6
Modified Froude			
$\frac{\rho_g v^2}{\rho_1 dg}$	320	$\frac{\rho'_g \; v'^2}{\rho'_w \; d'g}$	341
Reynolds of gas jet			
$\frac{d_1 v_g}{\eta_g}$	9.93×10^6	$\frac{d'_w \; v'_g}{\eta'_g}$	2.19×10^4

Table 4.3 shows that most of the important dimensionless groups, including the modified Froude number, have been maintained almost identical. The jet Reynolds number is seen to be considerably lower in the model than the prototype, but both jets are in the turbulent range ($Re > 10^3$)[52].

4.2 High Temperature Model Scale Factors

The constituents of the high temperature model are the same as those of the industrial BOF, only the vessel size is different. Double primed variables represent the high temperature model in Table 4.4.

TABLE 4.4

HIGH TEMPERATURE MODEL	
Inside diameter (D")	6 in.(15 cm) (1:36)
Lance diameter (d_1'')	3/32 in. (.24 cm)
Lance height (h")	1-1/2 in.(3.81 cm)
Iron depth (t_m'')	1-1/2 in.(3.81 cm)
Slag depth (t_s'')	1/2 in.(1.27 cm)
Oxygen flow rate (Q)	1.5 SCFM (709 cm^3 sec^{-1})
Metal temperature	1350°C start
Blow time	10 min

The similarity criteria, in the form of dimensionless numbers are shown for both model and prototype in Table 4.5.

TABLE 4.5

SIMILARITY CRITERIA			
PROTOTYPE		HIGH TEMPERATURE MODEL	
Dimensionless Group	Dimensionless Number	Dimensionless Group	Dimensionless Number
$\frac{D}{d_1}$	72	$\frac{D''}{d''_1}$	64
$\frac{D}{h}$	4	$\frac{D''}{h''}$	4
$\frac{D}{t_s}$	12	$\frac{D''}{t''_s}$	12
$\frac{D}{t_m}$	4	$\frac{D''}{t''_m}$	4
Modified Froude			
$\frac{\rho_g v_g^2}{\rho_1 d_g}$	320	$\frac{\rho''_g v''^2_g}{\rho''_1 d''_g}$	60
Reynolds gas jet			
$\frac{d_1 v_g}{\eta_g}$	9.9×10^6	$\frac{d''_1 v''_g}{\eta''_g}$	2.4×10^4

In the iron-slag system scaled down from the prototype, modified Froude numbers are maintained similar. Gas flow in the jet is turbulent in both cases since the Reynolds numbers are greater than the critical value of 10^3 [52].

4.3 Chemical Similarity

In the high temperature model, where the materials involved in chemical reactions are the same as in the BOF, it is only necessary that thermal conditions be similar to those of the prototype. To achieve perfect thermal similarity, which is a requirement for chemical similarity, absolute temperatures must be comparable and temperature differences must differ by the cube[53] of the pertinent length dimension. However, chemical reaction rates are very fast in steelmaking systems and the predominant rate controlling step is diffusion or mass transfer. In that case equal concentration differences will give a good first approximation for chemical similarity[53].

The low temperature model is based on an instantaneous chemical reaction, since it involves the combination of ions in solution. The following criteria were considered in choosing the most applicable concentration for the sodium bicarbonate solution:

The starting carbon concentration in the pig iron is approximately 4.0 weight % carbon. Expressing this carbon content as a mole fraction yields 16.24 mole % C. In terms of moles of carbon per volume of iron the carbon concentration is 24 moles per litre. The above concentrations of sodium bicarbonate in water would be equivalent to 905 gm l^{-1}(16.24 mole % $NaHCO_3$) and 2016 gm l^{-1} (24 moles $NaHCO_3$ per litre). In both cases the concentration exceeds the solubility of sodium bicarbonate in water[54] which is 69 gm l^{-1} at 0°C and 164 gm l^{-1} at 60°C.

The reaction in the model can be written as:

$$HCO_3^- + H^+ = H_2O + CO_2$$

showing that it is the bicarbonate ion which undergoes change and the sodium ion remains unchanged in solution. The reaction in a basic oxygen furnace can be written as:

$$C + 1/2\ O_2 = CO$$

showing that the dissolved carbon undergoes a similar change to the bicarbonate ion in the low temperature system.

For convenience the initial salt concentration was selected as being 4 weight % HCO_3^- in water as compared to 4 weight % C in iron. The conversion of 4 weight % HCO_3^- to normal concentrations results in 56.9 gm l^{-1}(.68N) sodium bicarbonate, which is within the solubility range at room temperature. A plot showing wt % HCO_3^- as a function of normality concentration is given in Appendix I.

CHAPTER 5

5.0 ROOM TEMPERATURE INVESTIGATION

The room temperature investigation consisted of studies of a reactive gas jet impinging normally upon a two-phase liquid system. The upper liquid phase (inert) was oil and the lower liquid phase was sodium bicarbonate solution. The reactive gas employed was HCl, which reacted with the dissolved sodium bicarbonate to form CO_2 as the reaction product. In all experiments the reactive gas, HCl, was diluted to 10% by volume in order to reduce the HCO_3^- removal rate to a readily measurable value.

Measurements of the cavity formed by the gas jet were made and the amount of lower layer dispersed into the upper layer and the rates of reaction in the upper and lower layers of the system were determined. Liquid properties and lance size, height above liquid surface, and gas flow rate were varied.

5.1 Experimental Apparatus

The room temperature apparatus (Figure 5.2) consisted of a 4" (10 cm) internal diameter perspex cylinder. The internal height of the container and the position of the liquid-liquid interface could be varied by including or excluding 4 perspex discs of various thicknesses in the bottom of the container. A container height of 10 cm was used for most of the tests. The two liquid phases could be separated at any chosen time by pushing a 20 gauge (.0375 inch, 1 mm.) nickel plate across the container thus sealing off everything above the plate. The height of aqueous liquid used in the experiments was 1 inch (2.54 cm) and the height of oil was 1/3 inch (.84 cm). The position of the liquid-liquid interface was adjusted so that the slide was in the oil layer just above the interface.

The mouth of the vessel was flanged to enable a glass cover to be fitted, while a cardboard gasket soaked in oil was used as a seal between the cover and the vessel. The cover was clamped securely to the vessel to prevent any gas leaks. The glass cover was equipped with 4, B24 ground holes, one at the center and three placed at 120^{o} to each other at the perimeter.

A 20 inch (50 cm) length of capillary tubing was fixed into the center hole by using a No. 4 one-holed rubber stopper. The lance was held steady from above by a mobile piece of perspex which could be adjusted to make the lance vertical. The capillary tubing used for the lance varied between .09 cm and .27 cm I.D.

The gas jet consisted of a mixture of 9 parts argon to 1 part hydrogen chloride. The argon (A) was metered by a Gilmont ball-type flowmeter (Figure 5.1) with a capacity of 0-180 (±2) $cm^{3}sec^{-1}$(B). The hydrogen chloride (C) gas flow was metered by a venturi meter with a capacity of

0-30 (±.5) $cm^3 sec^{-1}$(D). The two flows were combined by use of a Y junction (E) and the pressure was measured on a mercury manometer (F). An auxiliary line to waste (G) was used to produce a steady gas flow whereupon the flow was switched to the reaction vessel (H) while a stopwatch was simultaneously activated.

The argon flowmeter was calibrated by measuring the time needed to displace 8 litres from a 4 ft (120 cm) high cylindrical column of water. The hydrogen chloride gas flowmeter could not be calibrated in this way due to the high solubility of HCl in water and most other available liquids. The toxicity of HCl also prevented the use of a soap film meter for the calibration.

The method used, involved bubbling the HCl into a closed flask of distilled water over a timed interval. The acid was then analyzed volumetrically to determine the number of moles of HCl and hence the HCl volume at blowing conditions. An experimental check using argon through the same flowmeter (adjusted for HCl properties) verified the calibration curve.

Exhaust gases from the top of the vessel were directed into a series of gas absorption flasks (I) containing sodium carbonate solutions. Sodium carbonate was chosen because of its availability and its relative efficiency in absorbing hydrogen chloride. This is demonstrated stoichiometrically by considering three possible chemicals NaOH, $NaHCO_3$, $NaCO_3$

$$\begin{aligned} HCl + NaOH &= NaCl + H_2O \\ HCl + NaHCO_3 &= NaCl + CO_2 + H_2O \\ 2HCl + Na_2CO_3 &= NaCl + CO_2 + H_2O \end{aligned}$$

Methyl red indicator was used to warn when the absorbing solution was spent.

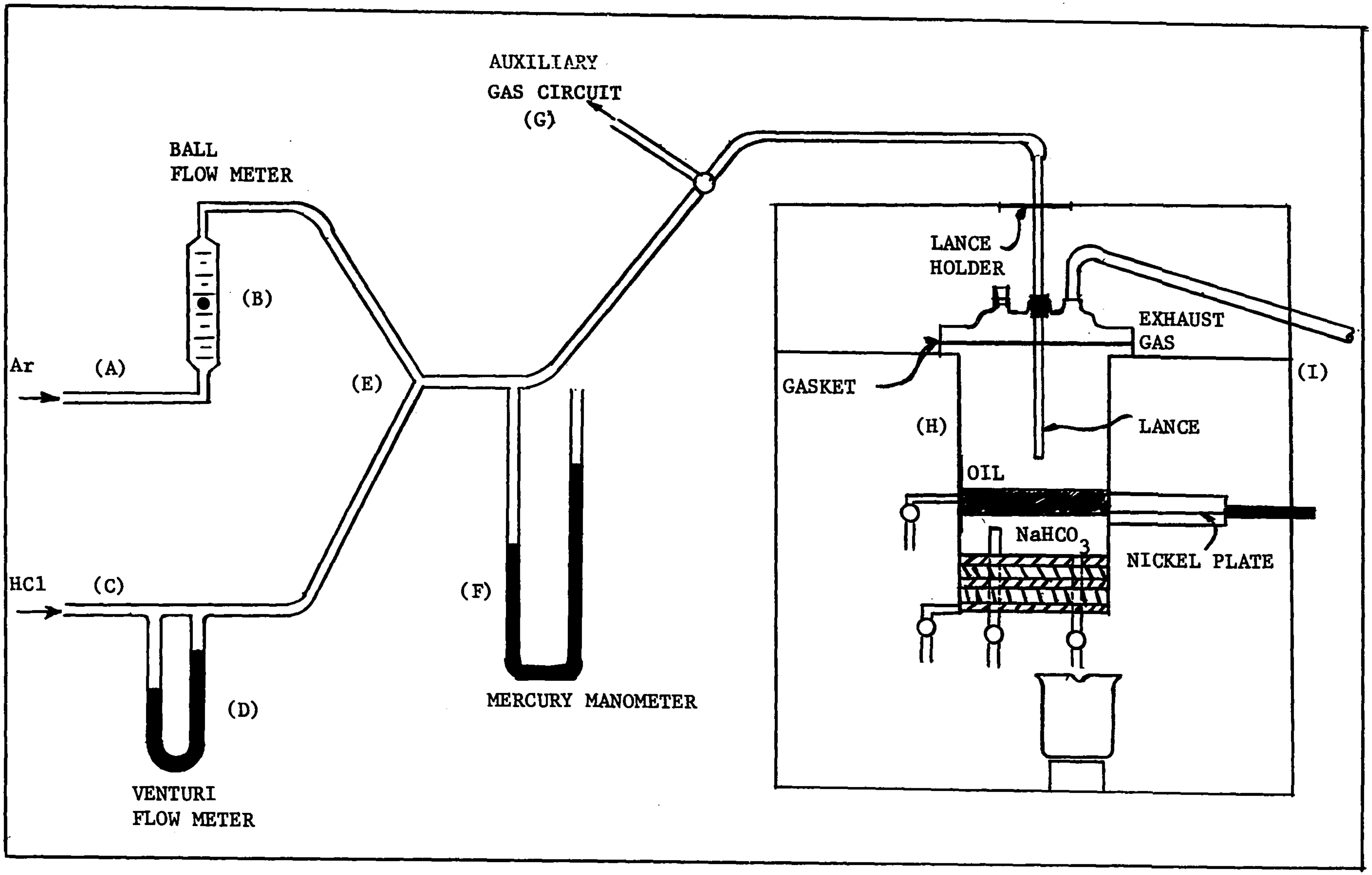

Figure 5.1 Schematic Diagram of Room Temperature Apparatus.

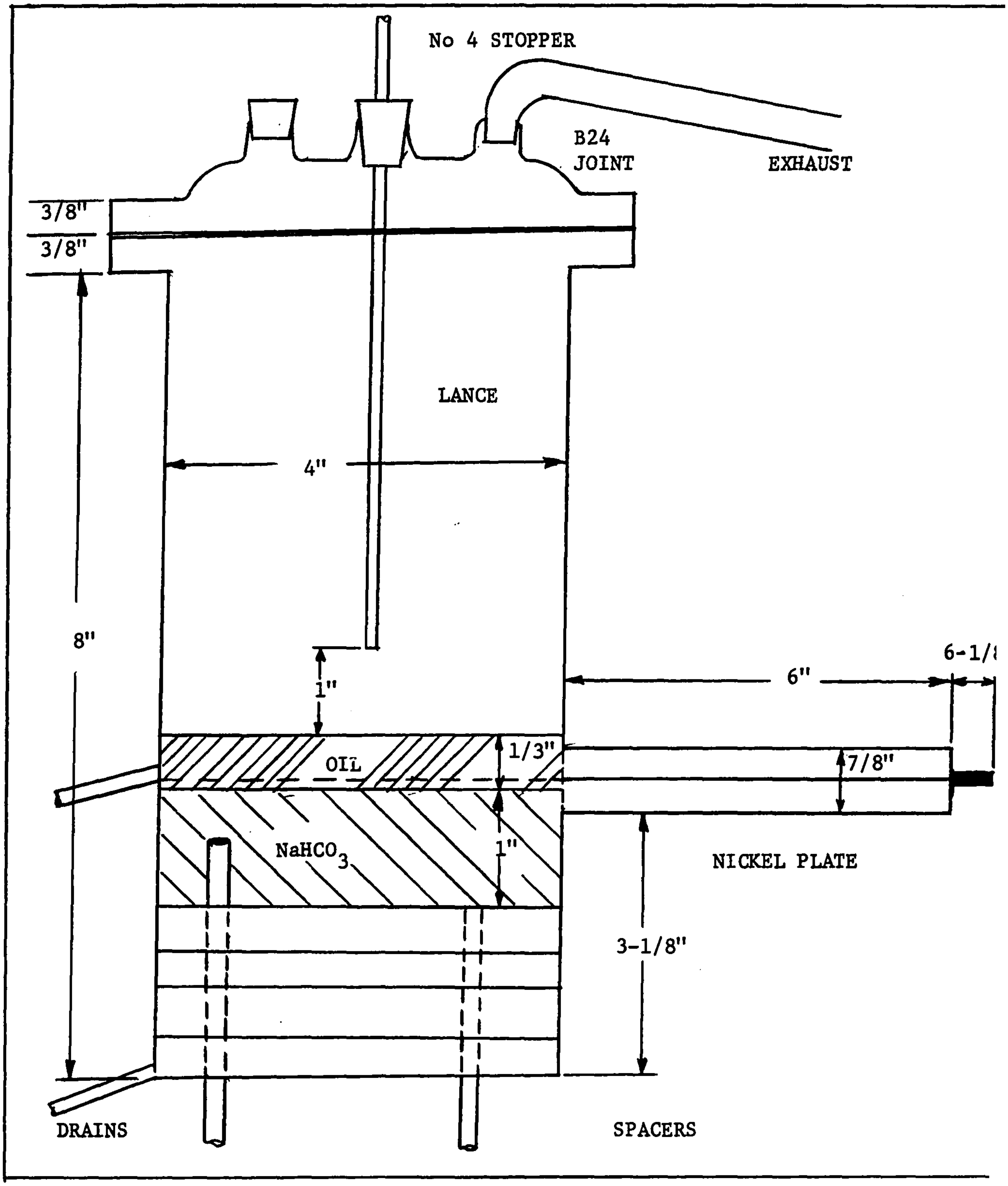

Figure 5.2 Enlarged view of reaction vessel.

5.2 Materials

The purities of the cylinder gases were as follows:

Argon: Canadian Liquid Air
Montreal, Quebec

Pure gas 99.996% purity

Hydrogen Chloride: Matheson of Canada Ltd.
Whitby, Ontario

Technical Grade Purity 99.0% minimum

Water: Single distilled

Sodium bicarbonate: Fisher Scientific Ltd.
Montreal, Quebec

Technical Grade 99.9% pure

Oil (Slag simulation): Mixtures of paraffin

(Shell Pella 911) and Non-detergent Oil

(Shell SAE-10W)

Shell Canada Ltd.
Montreal, Quebec

The properties of the liquids were:

TABLE 5.1

25°C	4%HCO_3 solution	OIL 40P
Density gm cm^{-3}	1.033	.845
Viscosity (cenistokes)	1.21	21.2
Viscosity (centipoise)	1.25	17.9
Diffusivity of HCl $cm^2 sec^{-1}$	4×10^{-5} (54.)	
Surface Tension (dynes cm^{-1})	75.4	29.3
Interfacial Tension (dynes cm^{-1})	32.3	

5.3 Procedure

A .6803N solution of $NaHCO_3$ was prepared by weighing the appropriate amount of dry salt and dissolving it in distilled water in a volumetric flask. The concentration was checked by titration against a standard HCl solution.

The oil was prepared by combining the appropriate amount of the low viscosity and high viscosity oils.

The initial step in each test was to add the bicarbonate solution to the reaction vessel through a funnel. The oil was then carefully added so as not to leave any oil lens' sticking to the bottom of the vessel. The separator slide (Figure 5.2) was then tested to ensure that it passed above the interface. The quantities of liquids used in a typical test are illustrated in Table 5.2

TABLE 5.2

Phase	Volume (cm^3)	Depth (cm)
Aqueous	222	2.54
Oil	70	.84
Liquid above slide	60-65	

When the liquids were in place the lance was moved into position and aligned vertically. The gas recovery connections were checked and the gas flows were activated through the auxiliary waste line and were adjusted to the required rate. After stabilization for about one minute in the auxiliary unit the flow was diverted to the model BOF as the second hand of the stop-watch passed the minute mark.

At the end of the jetting period the nickel slide was pushed across the system thus trapping the foam and emulsion in the upper layer. The gas flows were diverted back to the auxiliary circuit and then stopped. The liquid below the nickel slide was drained into a 250 ml beaker. This aqueous solution had a 1/16" thick covering of oil on its surface, ensuring that the nickel slide passed slightly above the interface. The upper emulsified phase was drained into a 150 ml beaker and the emulsion was allowed to settle.

In most of the tests the emulsion was sufficiently unstable so that the aqueous fraction separated from the oil fraction completely within a few minutes. The accomplishment of complete separation was verified by xylene extraction of the water and distillation, a standard procedure for separating water/oil emulsions.

The procedure is as follows: About 250 ml of xylene is combined with 50 ml of emulsion (Figure 5.3) and the mixture is heated to boiling in a conical flask (A). Xylene and water boil off and condense in the condensing column (B) where the liquids fall back to the graduated collection tube (C). Water is the more dense liquid and settles to the bottom while the xylene forms the top layer. The collection tube is made so that xylene will be returned to the conical flask to be recycled.

This distillation procedure was a necessity in the case of the stable emulsion produced as a result of the addition of surface active agents to the system.

The relative volumes of oil and sodium bicarbonate solution were noted and the sodium bicarbonate concentration of the solution was determined against a standard HCl solution. The lower liquid was also analyzed for sodium

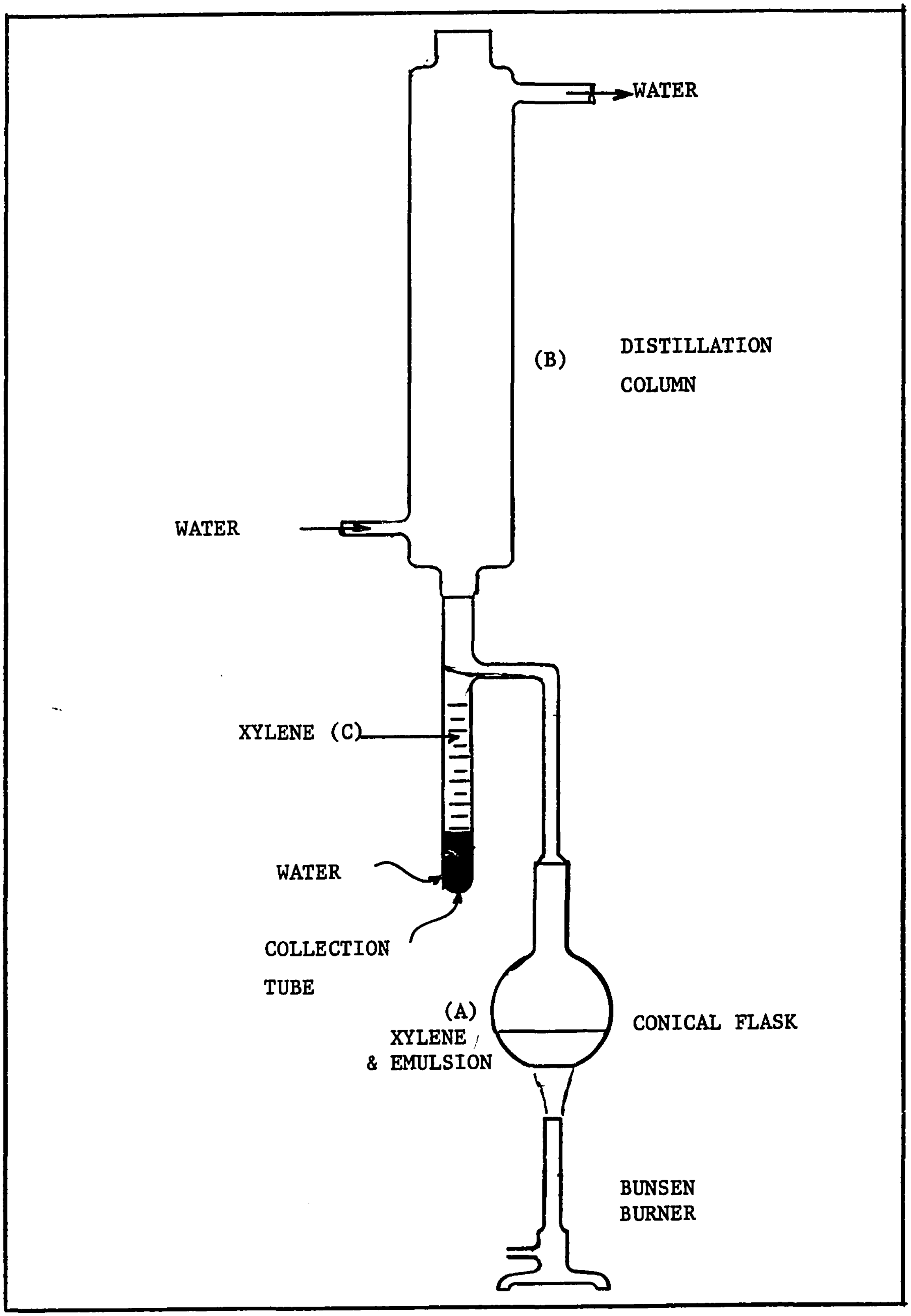

Figure 5.3 Distillation Apparatus for W/O Emulsion.

bicarbonate concentration in the same way. The titration procedure will be discussed in a later section.

The above experimental procedure was followed on fresh liquids for periods of 1 min., 2 min., 3 min., etc. of lancing until the end point of the reaction was reached. Each test yielded one point for the curve of HCO_3^- concentration versus time. This method was necessary due to the difficulty in obtaining adequate emulsion and bath samples without upsetting the system.

The oil viscosity was measured after each run by a gravity method using Cannon-Fenske Routine Viscometers. Surface and interfacial tensions were measured by the drop-weight technique using the empirical correction factors of Harkins and Brown[55].

Titration Procedure: The titration procedure used for the sodium bicarbonate solution was that given by Belcher and Nutten[56]. An approximate .1N standard solution of hydrochloric acid is prepared by diluting concentrated hydrochloric acid (usually between 10N and 11N) 100 times. Standardization is carried out by titrating against primary standard sodium bicarbonate. The indicator proposed by Hoppner[57] consisting of a mixture of dimethyl yellow and bromocresol green was used to signal the end point of the titration. The reaction is as follows:

$$2\ HCl + Na_2CO_3 = 2\ NaCl + H_2O + CO_2$$

The primary standard sodium carbonate solution is prepared by weighing the pure salt which has been dried for one hour at 270-300°C and dissolving it in distilled water. Sodium bicarbonate is not suitable as a primary standard because it decomposes upon heating.

The mixed indicator, which turns yellow in a weakly alkaline solution, is added to a measured volume of standard sodium carbonate solution in a conical flask. The hydrochloric acid to be standardized is added to the solution via a burette until the indicator turns blue.

Dimethyl yellow - bromocresol green gives a colour change to blue in acid solutions, indicating the end-point. The high concentrations of carbon dioxide present in solution do not interfere with the end-point indication of this indicator.

The standard hydrochloric acid solution was used to titrate the sodium bicarbonate solution samples obtained from the model BOF. The calculation of the normality of the sodium bicarbonate solution was based on the fact that for this reaction:

$$HCl + NaHCO_3 = NaCl + H_2O + CO_2$$

acid equivalents must equal basic equivalents.

Normality of $NaHCO_3$ x Volume of $NaHCO_3$

= Normality of HCl x Volume of HCl

or $$N_{NaHCO_3} = N_{HCl} \times \frac{V_{HCl}}{V_{NaHCO_3}}$$

The weight per cent of HCO_3^- ion corresponding to the normal concentration is obtained by referring to Figure A.1 in Appendix I.

5.4 Experimental Results Room Temperature System

The experimental investigation consisted principally of studies of the reaction rate occurring in the upper and lower layer of the model BOF. The degree of foam and emulsion formation by the gas jet was studied in the same experiment.

The specific areas of study in the room temperature (24-26°C) experiments were:

- (a) Geometry of gas cavity at different lance conditions.
    - (i) Rate of reaction and degree of emulsification with varying lance heights.
    - (ii) Rate of reaction and degree of emulsification with varying flow rates.
    - (iii) Rate of reaction with varying lance diameter.
    - (iv) Rate of reaction and degree of emulsification with varying oil viscosity.
    - (v) The effect of a surface active solute in the oil layer upon the degree of emulsification and simultaneously on rate of reaction.
    - (vi) The effect of the oil layer thickness upon the degree of emulsification and rate of reaction.
- (b) Change in behaviour with the use of a reactive upper layer to simulate a reactive slag.

All quantitative results obtained for the room temperature experiments are tabulated in Appendix II and are presented graphically in Figures 5.5 - 5.31. Discussion of all results is reserved for Chapter 7.0.

5.4-1 Qualitative Observations of Cavity Formation & Behaviour

Under all test conditions small CO_2 bubbles were formed on the bottom of the reaction vessel by about the mid-point of the reaction. The bubbles nucleated at a favourable site, often scratches or chips in the perspex, and grew to elongated spheres. The bubbles broke away after several seconds to rise toward the upper surface. Very fine stringers of CO_2 were also observed to rise from various intermediate locations in the bath. The stringers had the appearance of miniature tornados.

As soon as the gas jet was turned on and the crater was formed, a frothiness developed at the O/W interface. As the reaction proceeded, a foam of CO_2 bubbles appeared at the surface surrounding the cavity, while the frothiness at the O/W interface subsided and clouds of small CO_2 bubbles were thrown from the region of the crater into the bulk of the bath. In addition, fine droplets of oil were thrown down into the bath. When the system was viewed through a telescope, these oil droplets were noticed to be the nucleating points for the CO_2 stringers. The lower liquid was murky in appearance suggesting that an O/W emulsion was formed to a small extent.

The important variable with regards to the fluid dynamics of the system was the depth of penetration and size of the gas jet cavity or crater. The conditions which produced a deep cavity were observed to be: low lance height; high flow rate; and a shallow oil layer. The opposite conditions resulted in a poor cavity penetration into the lower liquid.

Under conditions of good cavity penetration, the oil surface soon becomes covered with a stable white foam and the bottom liquid becomes very murky. Near the latter part of the reaction, surface foams leap up higher than the lance tip especially in the case of low lance heights. Drops of the lower liquid are entrained in the gas jet and are continuously thrown into the atmosphere.

Qualitative runs with a few drops of methyl red indicator added to the aqueous layer showed that the drops thrown into the atmosphere were either red in colour when they landed on the perspex wall or turned to red a few seconds later. The red colour of the indicator indicated that the drop had completely lost its dissolved sodium bicarbonate salt and may well have gained a measurable concentration of HCl.

The normal splashing and slopping of oil and aqueous solution at the cavity was apparent with both high and low viscosity oils. However, the higher viscosity oils were noticeably more sluggish in splashing than the low viscosity oils. More fine droplets of oil were thrown into the lower layer and a higher degree of stirring occurred when a low viscosity oil was used.

The addition of a surface active solute to the oil had a very marked effect. Foaming began gradually but since the foam was stable it continued to rise until after a few minutes it had completely passed the lance tip and was reaching the vessel top. After foaming the bath at the bottom of the vessel consisted of a 1/4" aqueous layer covered with 1/8" of oil as compared to the original layer thicknesses of 1" aqueous and 1/3" oil. The normal cavity in the aqueous layer was not visible because the gas flow was not strong enough to reach the aqueous phase in the vessel bottom. The reactive gas left the lance and rose through the foam in a stream of bubbles.

Table 5.3 summarizes qualitative observations in the room temperature investigation.

TABLE 5.3

VARIABLE	VARIABLE RANGE	OBSERVATIONS
Lance Height & Flow Rate	Low lance height or High flow rate	Deep penetration of cavity. Large amount of foam on oil surface. Much splashing and circulation. Tendency to form O/W emulsion.
	High lance height or Low flow rate	Poor penetration of cavity. Small unstable foam in constant motion on surface. Little or no evidence of splashing.
Lance Diameter (constant gas velocity)	Large Dia. lance	A large flow rate is needed to simulate BOF gas velocities A large deep crater is formed with much splashing, foaming and stirring.
	Small Dia. lance	A low flow rate is needed to simulate BOF gas velocities A smaller cavity is produced. The cavity is not so deep as with a large diameter lance and stirring is not so efficient.
Oil Viscosity	High Viscosity oil	Splashing appears to be more sluggish than with lower viscosity oils.
	Low Viscosity oil	A greater amount of fine oil droplets are thrown into the lower layer. Stirring is more pronounced.
Oil layer Thickness	Thick covering of oil	The effective penetration into the aqueous layer is reduced. Foam formation is more difficult and less aqueous phase is splashed into the atmosphere.
	Thin covering of oil	The effective penetration into the aqueous layer is greater. More aqueous phase is splashed into upper atmosphere.

TABLE 5.3(continued)

VARIABLE	VARIABLE RANGE	OBSERVATIONS
Addition of Surface Active Agent	Surface Active Solute in oil	A stable foam developed on surface. The foam continues to grow until the top of the vessel. 75% of the initial liquid is dispersed into foam and emulsion.

High speed motion pictures were taken of the gas cavity using a Locam Camera manufactured by Red Lake Labs, California. Pictures at 500 frames per second show that the depression was very unstable. The depth of the gas cavity changes markedly as the gas jet searches for the path of least resistance. The gas jet dislodges packets of bicarbonate solution during its maximum penetration and flings them into the above atmosphere as it rises to its minimum penetration. Figure 7.2 illustrates this observation.

5.4-1 Geometrical Measurements on Gas Cavity Penetration

The size of the cavity below an impinging gas jet provides a criterion for the effectiveness of gas-liquid contact, hence examination of cavity size and shape were included in the room temperature experiments.

The range of flow rates and lance heights used in the experiments were chosen according to the rules outlined in Chapter 4. The physical limitations of the apparatus were also considered when choosing the range of variables to be used.

The size of the cavity produced under different conditions of lance height and flow rate were measured in the clear perspex apparatus by means of a telescope mounted on a vertical vernier scale. The distance between the oil-water interface and the bottom valley of the cavity was taken as the effective depth of the depression. The diameter of the cavity at the oil-water interface was sighted against a rule through the telescope.

The quantities measured are illustrated in Figure 5.4 and the results are given in Table 5.4. The dimensionless group (n+t)/h is plotted against $\dot{M}/\rho_1 gh^3$ (which combines the important lance parameters) in Figure 5.5. The formulae used to describe the cavity geometry are given in Section 7.2-3.

TABLE 5.4

h (cm)	Q $cm^3 sec$	n cm	m cm	n+t cm	$\frac{n+t}{h}$	A cm^2	$\dot{M}$ $\frac{dyne}{sec}$	$\dot{M}/\rho_1 gh^3$
3.5	100	1.054	1.10	1.894	.541	2.637	922	.0212
3.0	100	1.238	1.20	2.078	.693	3.345	922	.0337
2.5	100	1.408	1.20	2.248	.899	3.748	922	.0583
2.0	100	1.579	1.40	2.419	1.210	4.925	922	.1138
1.5	100	1.789	1.50	2.629	1.753	5.943	922	.2697
2.5	120	1.935	1.50	2.775	1.110	6.380	1328	.0839
2.5	110	1.589	1.30	2.429	.972	4.564	1116	.0705
2.5	100	1.336	1.20	2.176	.870	3.577	922	.0583
2.5	90	0.901	1.10	1.741	.696	2.313	747	.0472

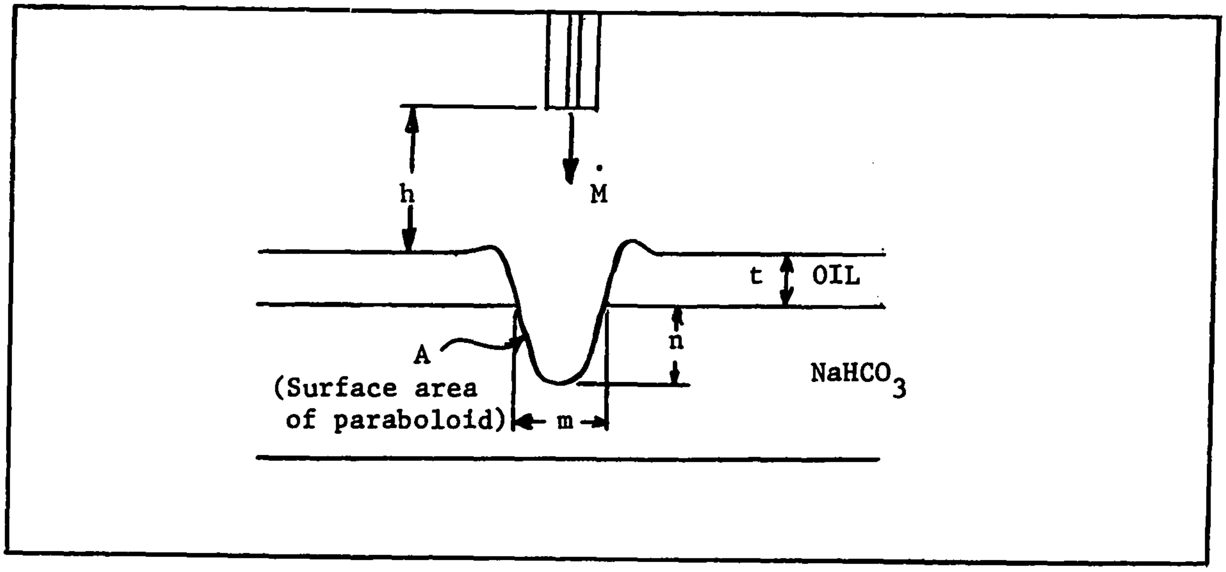

Figure 5.4 Diagram of gas cavity showing important dimensions.

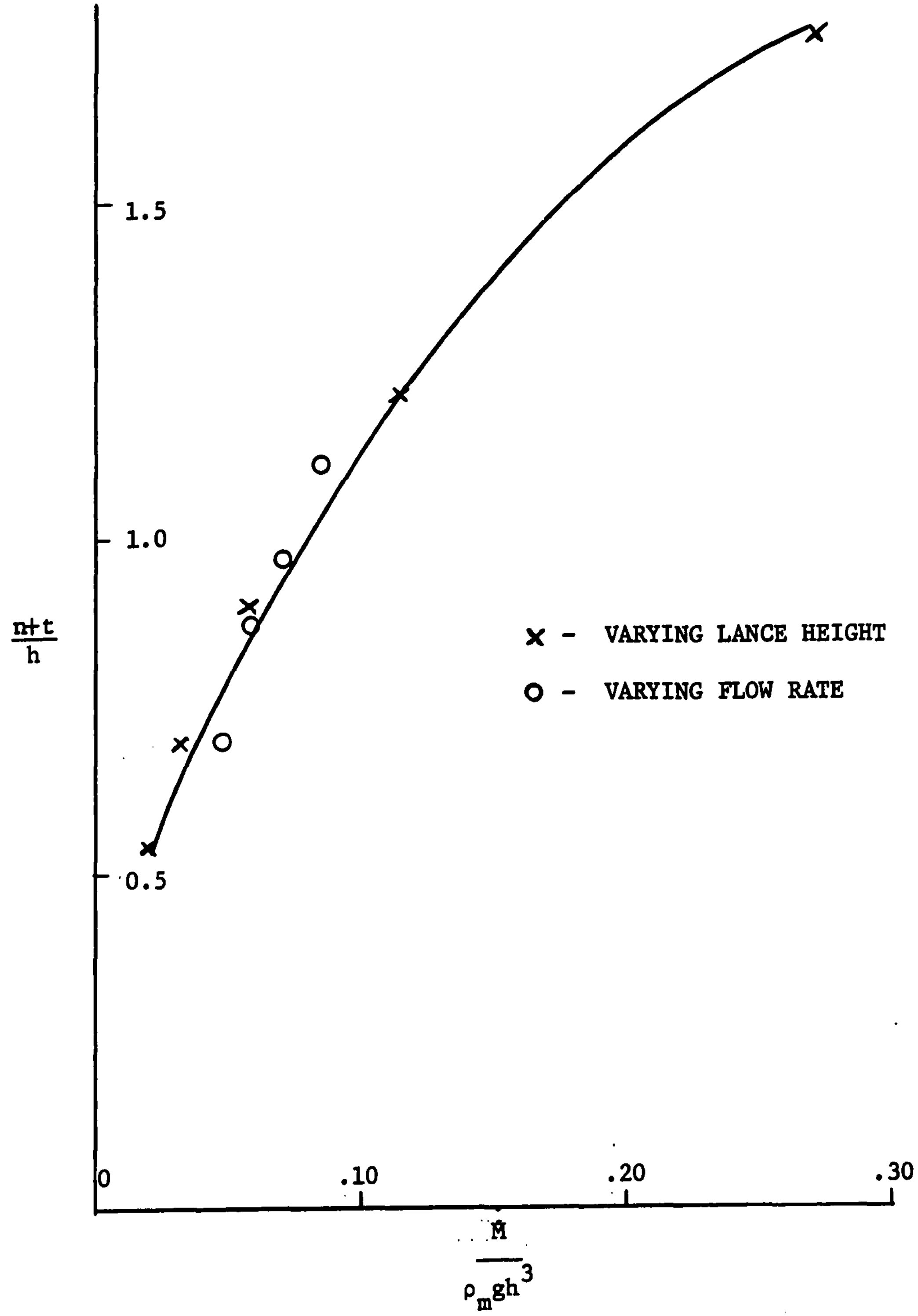

Figure 5.5 Dimensionless Plot Correlating Cavity Depression to jet momentum and lance height.

5.4-3 The Effect of Lance Characteristics on Reaction Rate

The effects of lance height, gas flow rate and lance diameter upon the rate of reaction in the bath and in the emulsified layer were investigated. The concentrations of sodium bicarbonate salt are reported as weight per cent bicarbonate ion to approximate steelmaking practice and figures. The correlation between $\%HCO_3^-$ and normality is given in Appendix I, Figure A.1.

i Lance Height

The lance height was varied between 1.5 cm and 3.5 cm at a constant flow rate of 100 $cm^3 sec^{-1}$ and lance diameter of .15 cm. These conditions were acceptable in terms of modified Froude similarity and yet allowed the widest range of lance heights to be covered without exceeding the physical limits of the apparatus. The gas was always a mixture of 90% Ar - 10 % HCl.

For the tests the variables were as follows:

Lance height - 1.5, 2.0, 2.5, 3.0, 3.5 cm
Flow rate - 100 $cm^3 sec^{-1}$
Lance diameter - .15 cm
Oil depth - .84 cm (volume 70 cm^3, viscosity 21 cstks)
Solution depth -2.5 cm (volume 222 cm^3 4 $\%HCO_3^-$)

A typical HCO_3^- removal curve is plotted in Figure 5.6. The rate of bath reaction versus lance height is shown in Figures 5.7 and 5.8. The rate of reaction in the emulsified solution versus lance height is given in Figures 5.9 and 5.10. Figure 5.11 plots degree of emulsification against lance height.

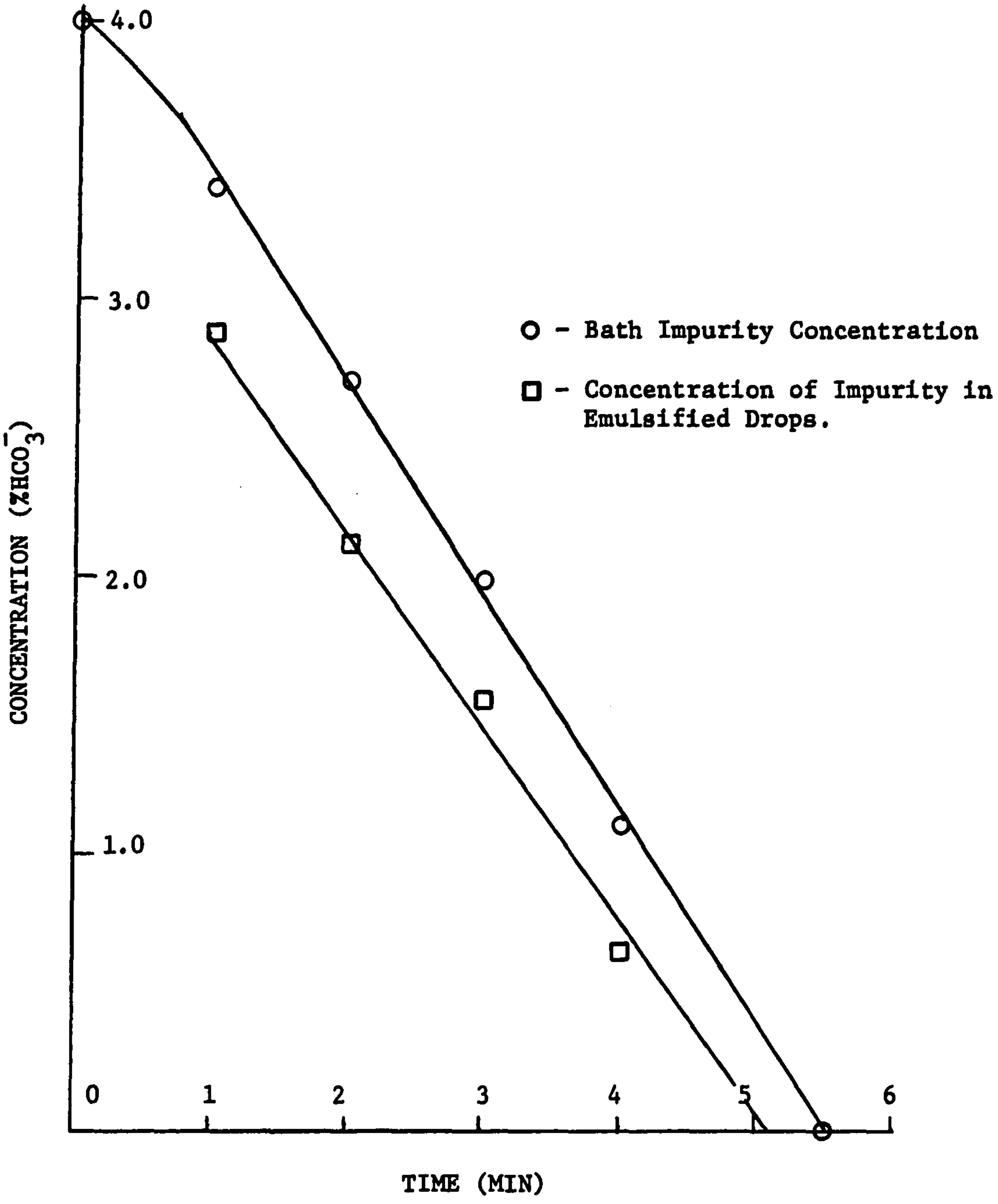

Figure 5.6 Curve of Impurity Concentration vs Time for lance conditions: Q-100 cm^3 sec^{-1}, h-1.5 cm, d-0.15 cm.

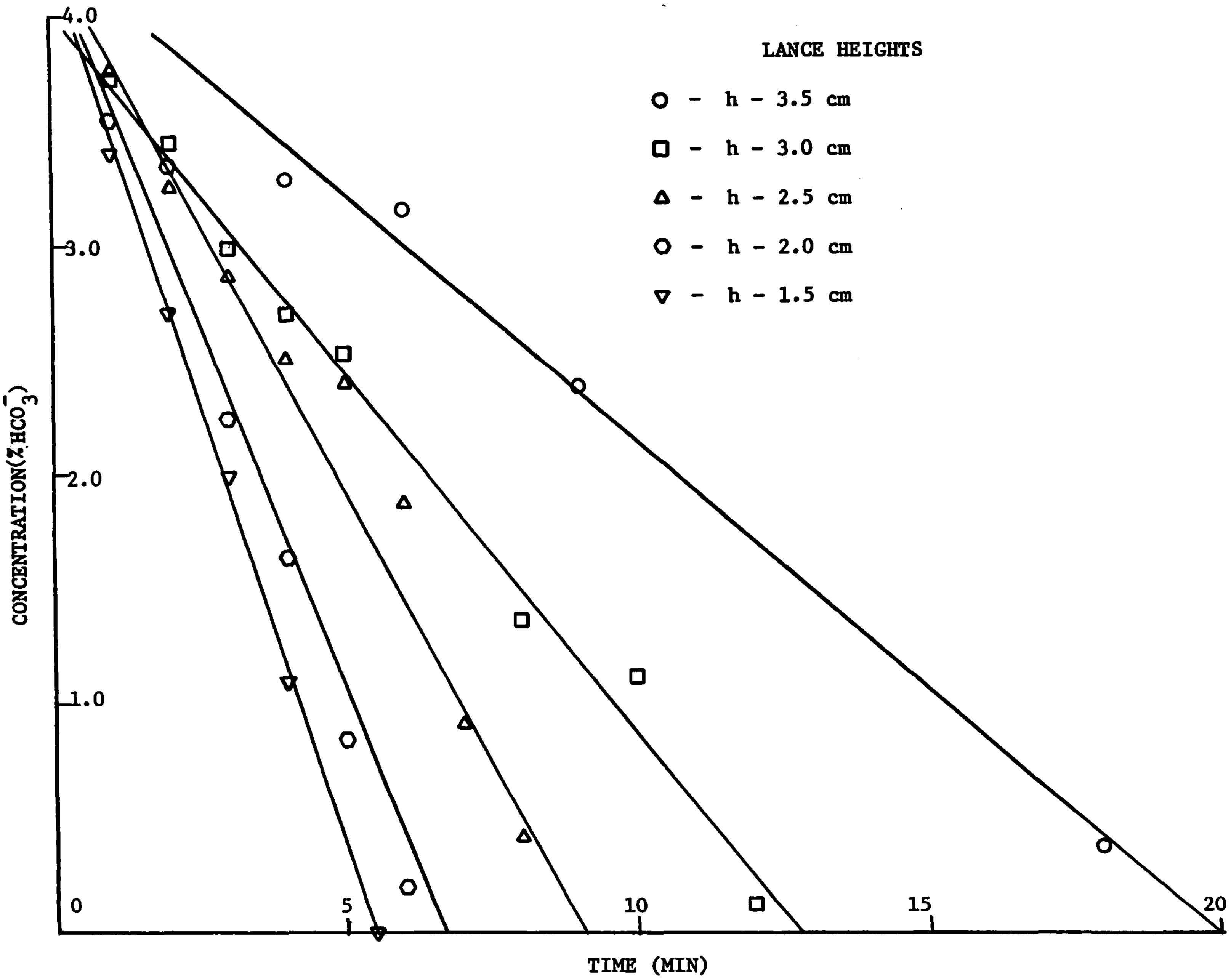

<u>Figure 5.7</u> Rate of Bath Reaction at Varying Lance Heights.

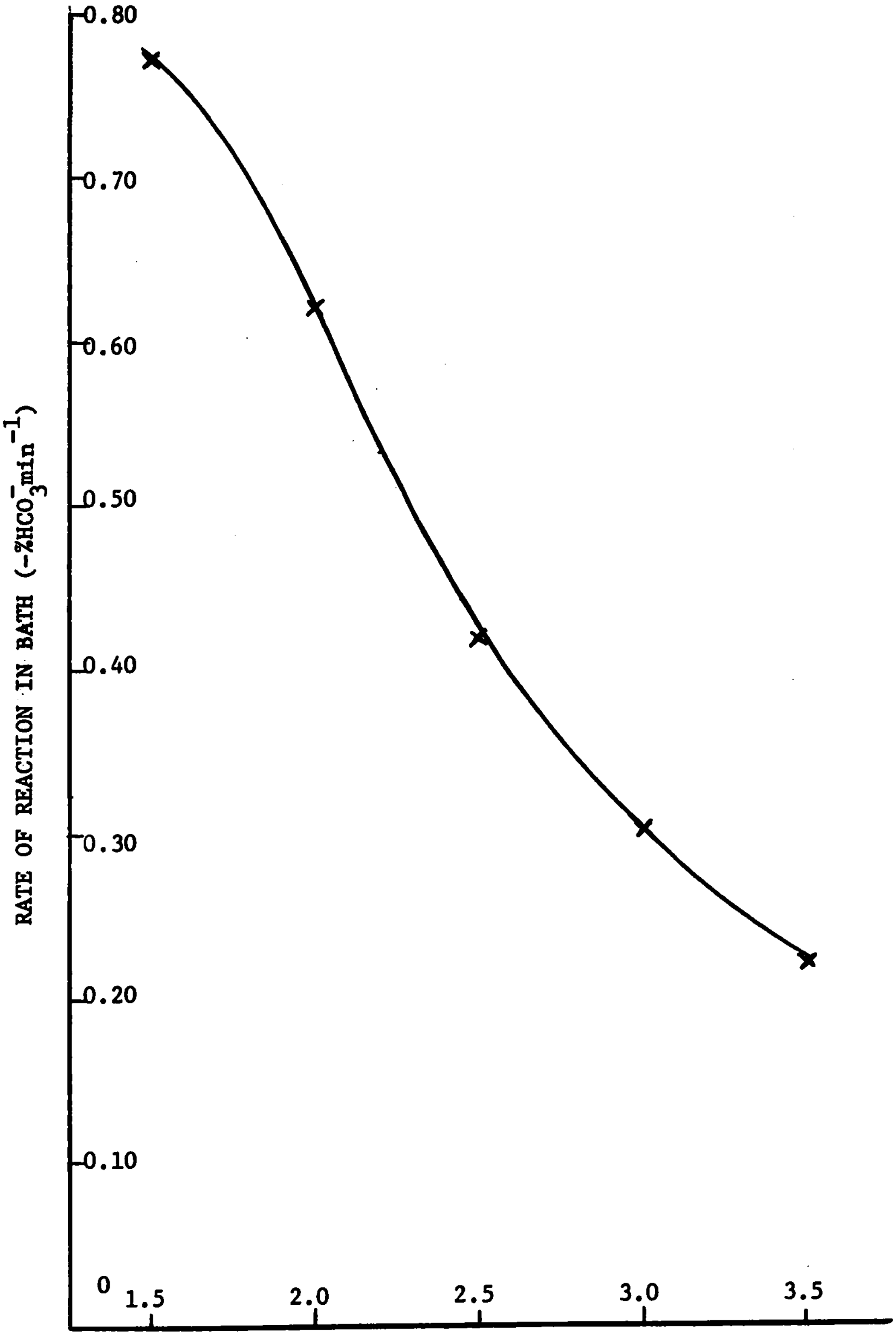

<u>Figure 5.8</u> Plot of Bath Reaction Rate vs Lance Height.

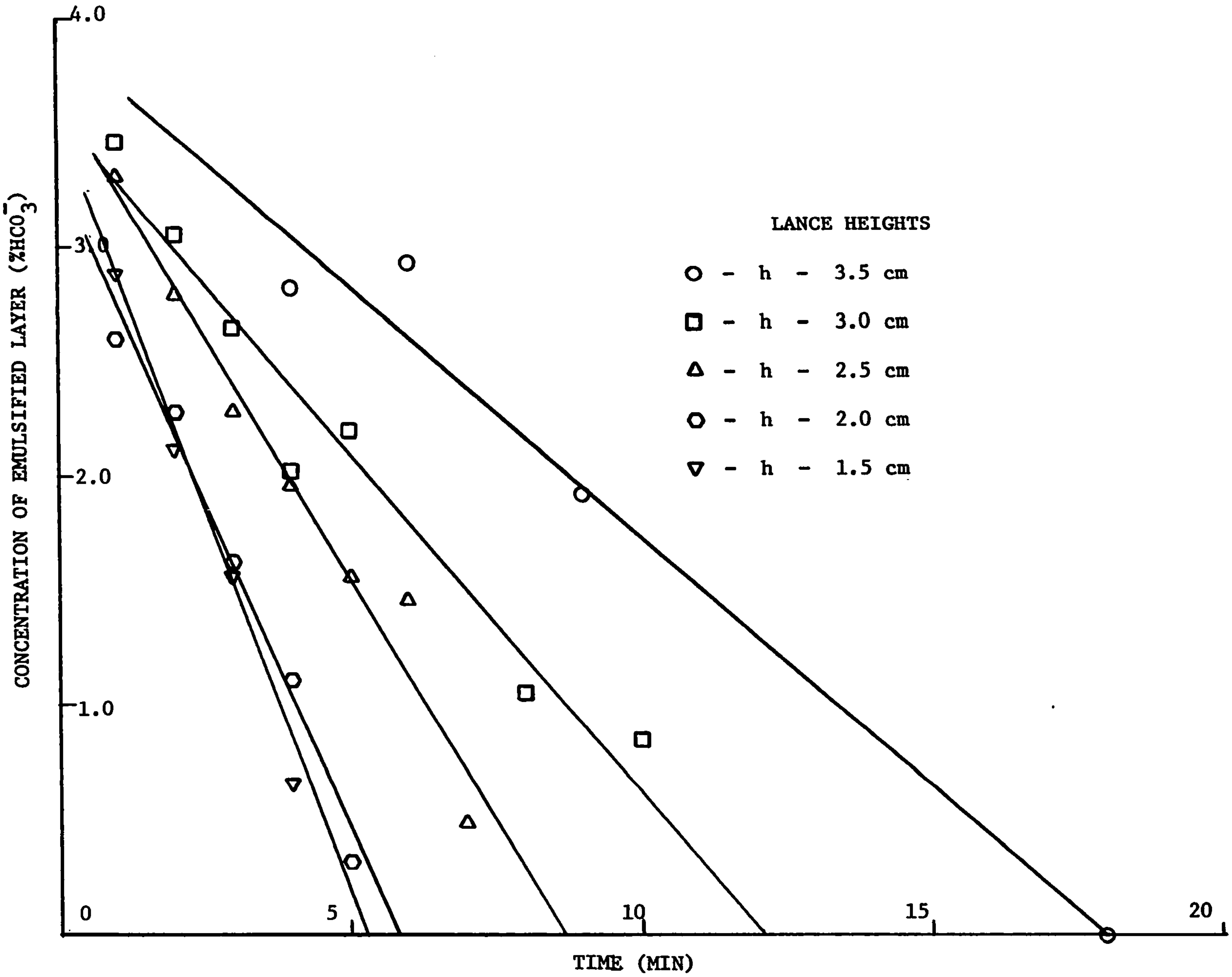

Figure 5.9 Rate of Reaction in Emulsified layer vs Lance Height.

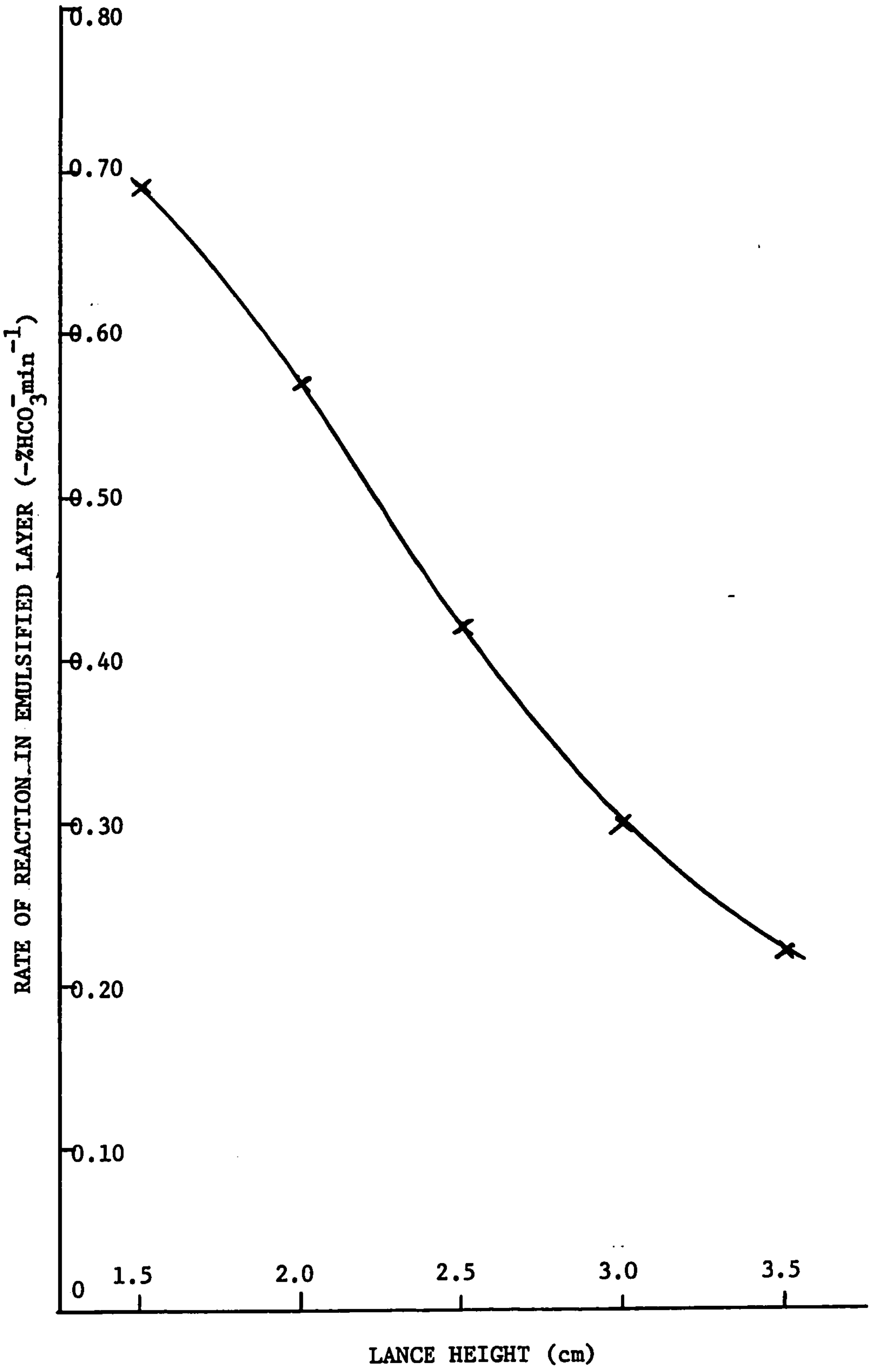

Figure 5.10 Rate of Reaction in Emulsified Layer vs Lance Height.

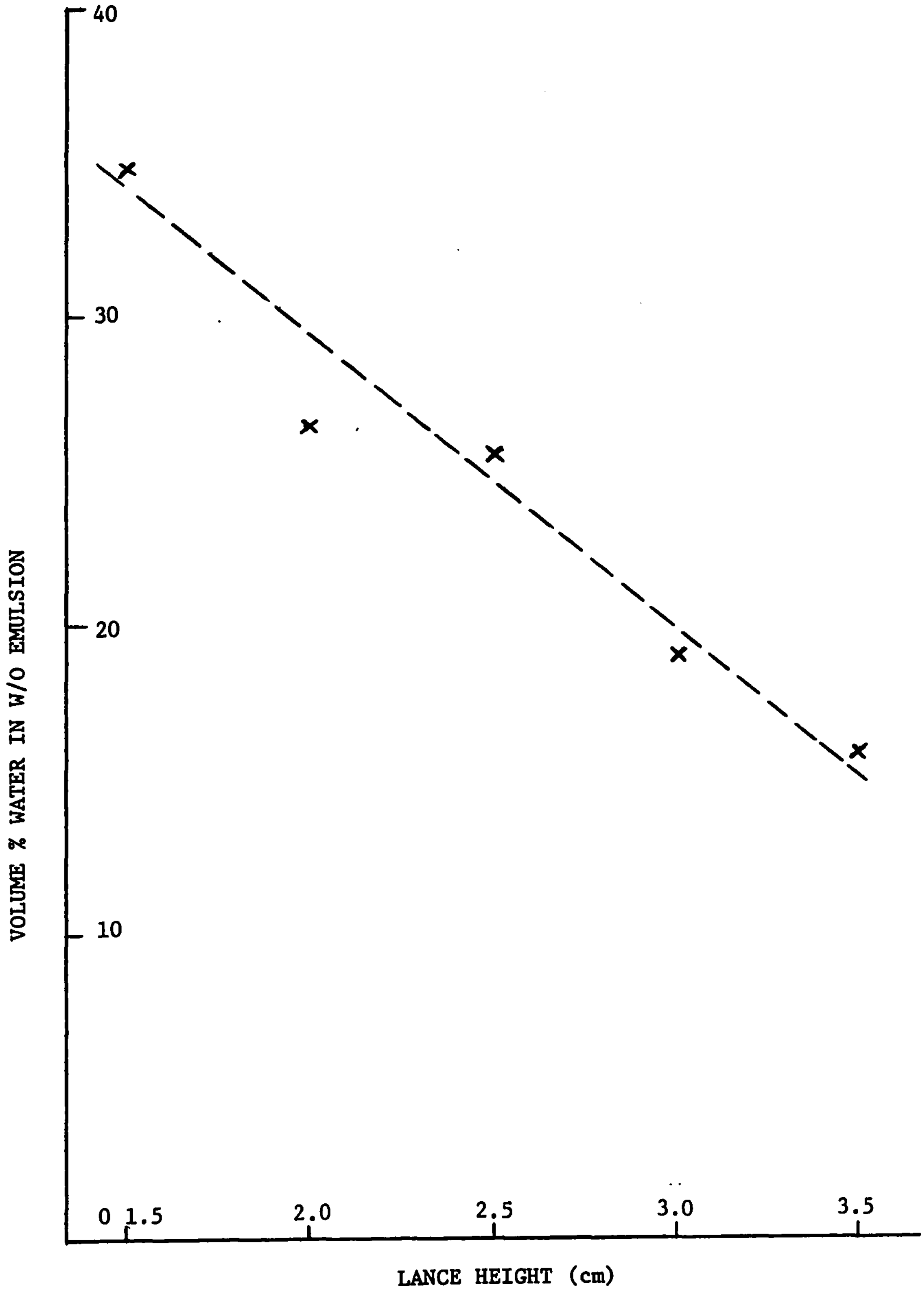

Figure 5.11 Plot of Degree of Emulsification of Water in Oil as a function of Lance Height.

ii Flow Rate

The rate of reaction in bulk liquid and in the emulsified liquid was determined for each flow rate. The gas was always a mixture of 90% Ar - 10% HCl.

For the tests the variables were as follows:

Flow rate Q - 90, 100, 110, 120 $cm^3\ sec^{-1}$
Lance height h - 2.5 cm.
Lance diameter d - .15 cm.
Oil depth t - .84 cm (Volume 70 cm^3,
    viscosity 21 cstks)
Solution depth 2.5 cm (Volume 222 cm^3, 4%HCO_3^-)

A typical HCO_3^- removal curve is shown in Figure 5.12. The rate of bath reaction versus flow rate is shown in Figures 5.13 and 5.14 . The rate of reaction in the emulsion is given by Figures 5.15 and 5.16. The dependence of degree of emulsification upon flow rate appears in Figure 5.17.

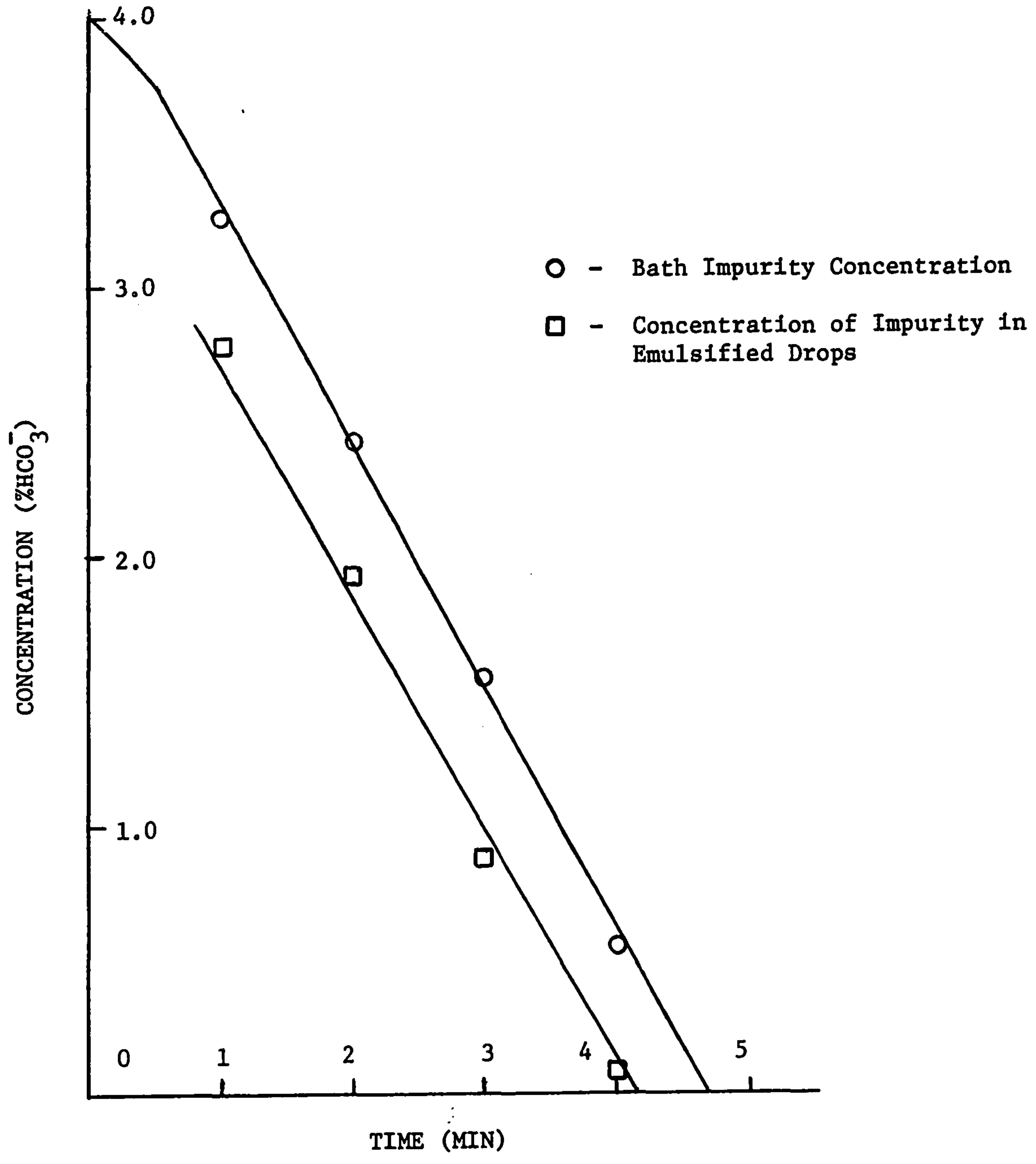

Figure 5.12 Curve of Impurity Concentration vs Time for lance conditions: Q-120 $cm^3 sec^{-1}$, h-2.5 cm, d-0.15 cm.

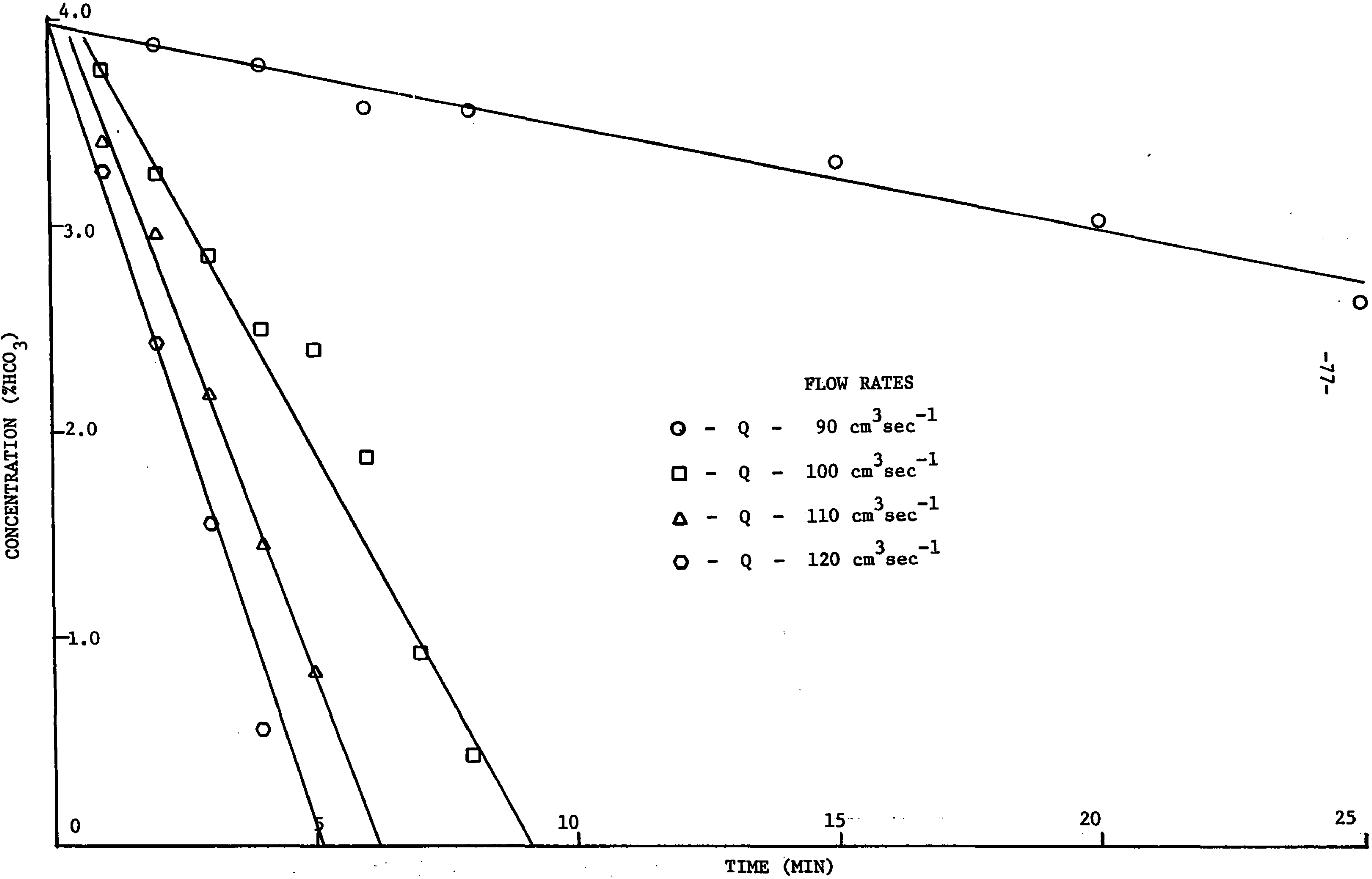

Figure 5.12 Rate of Bath Reaction at Varying Flow Rates

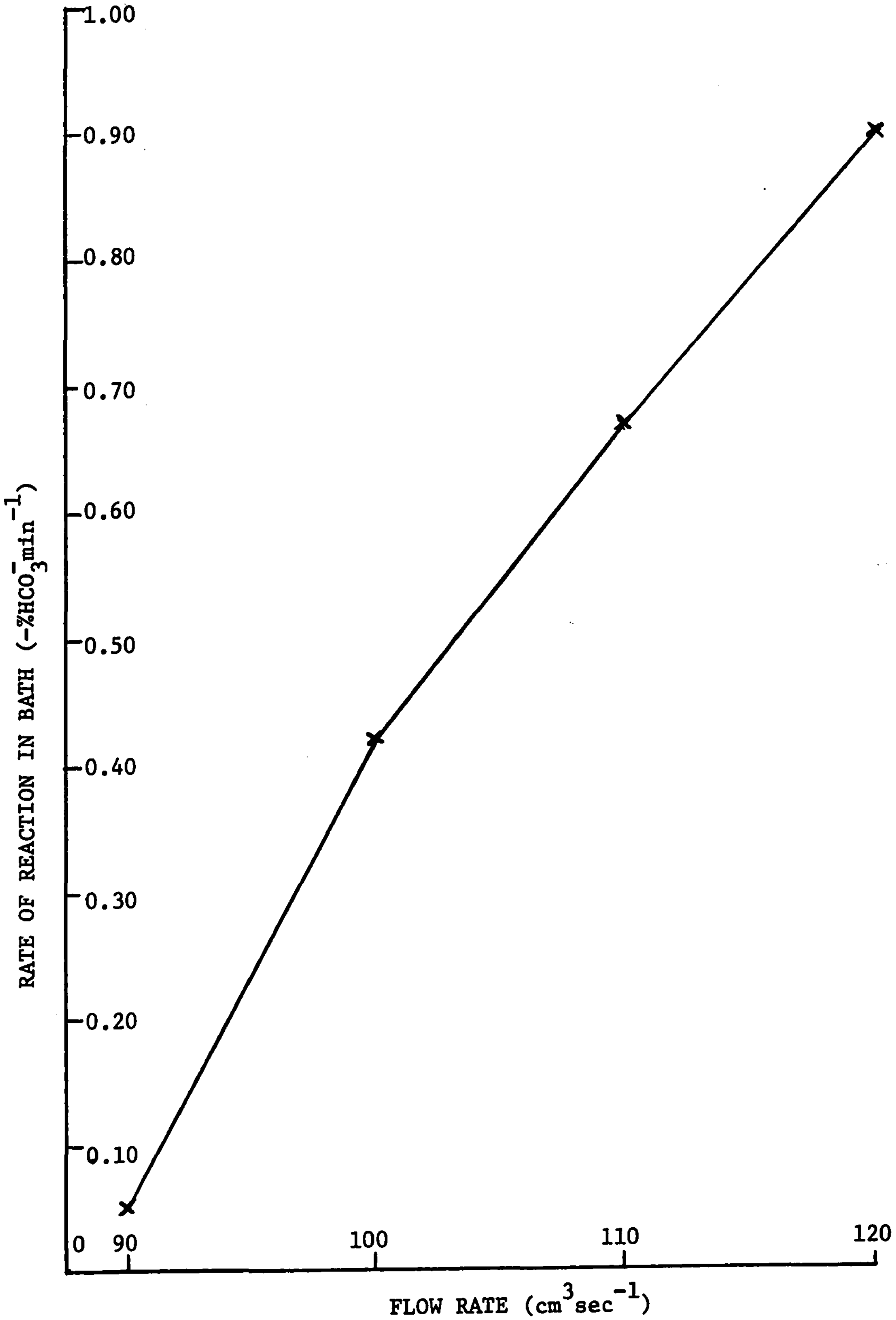

Figure 5.14 Rate of Bath Reaction vs Flow Rate.

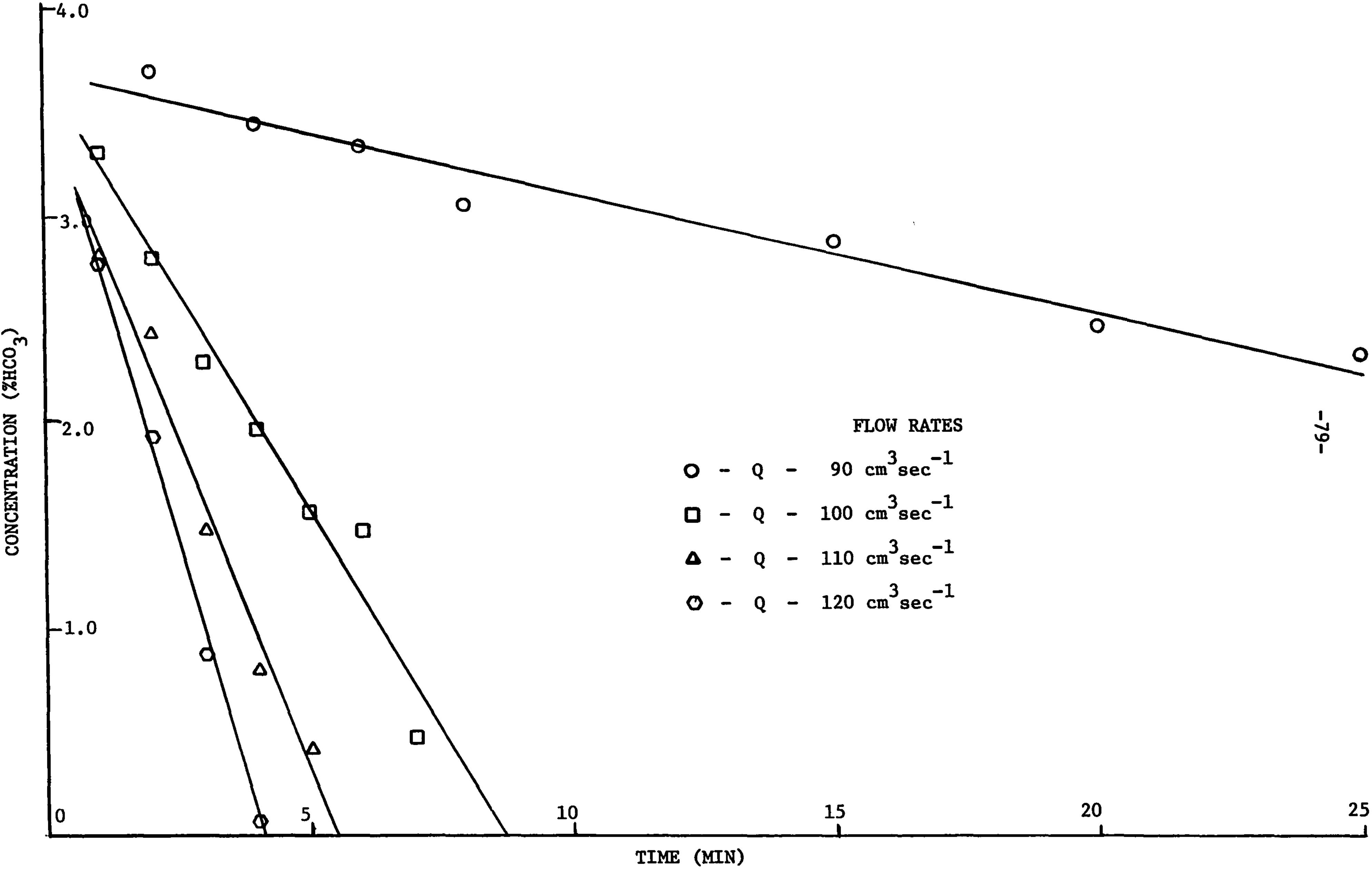

Figure 5.15 Rate of Reaction in Emulsified Layer at various Flow Rates.

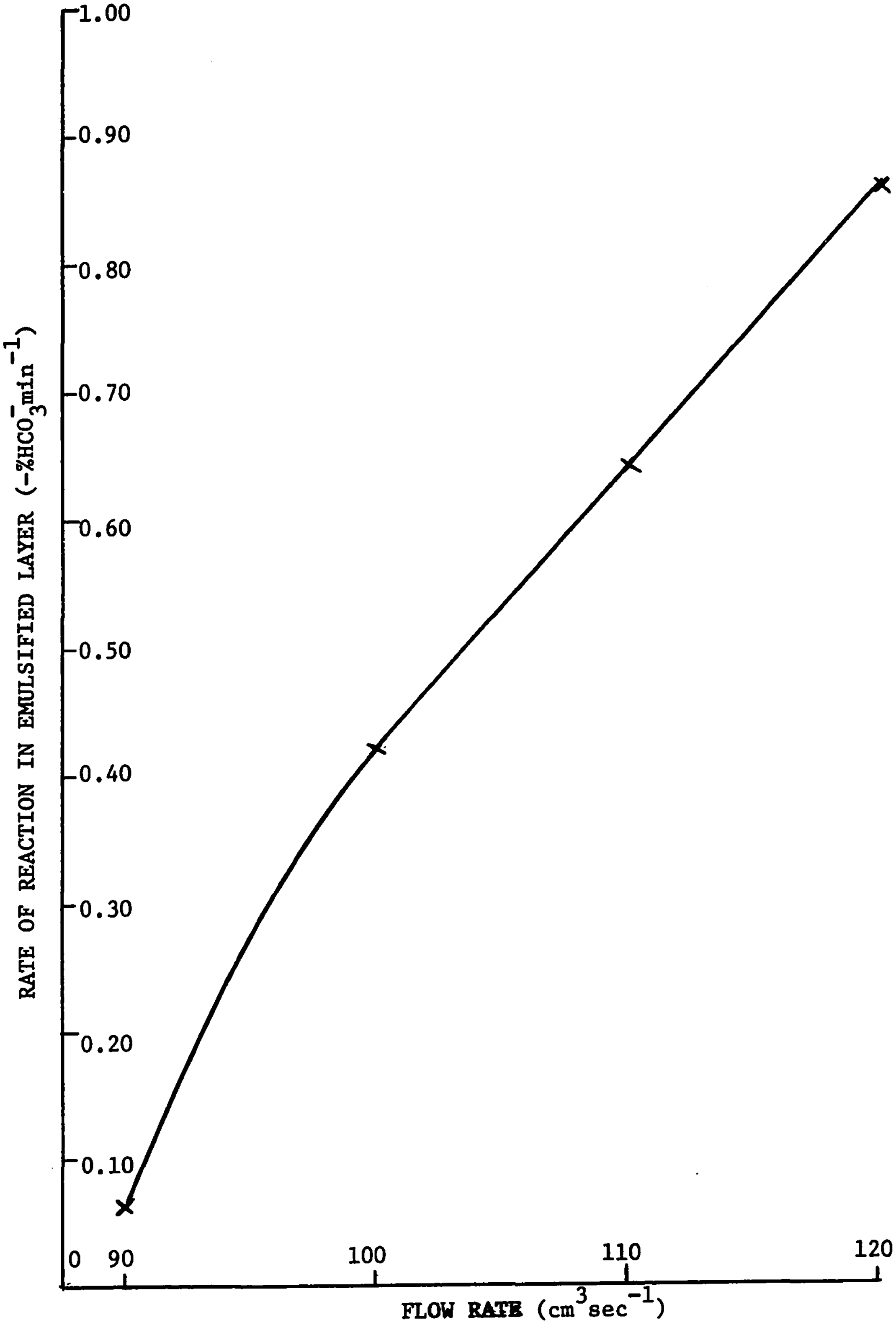

Figure 5.16 Reaction Rate in Emulsified Layer vs Flow Rate.

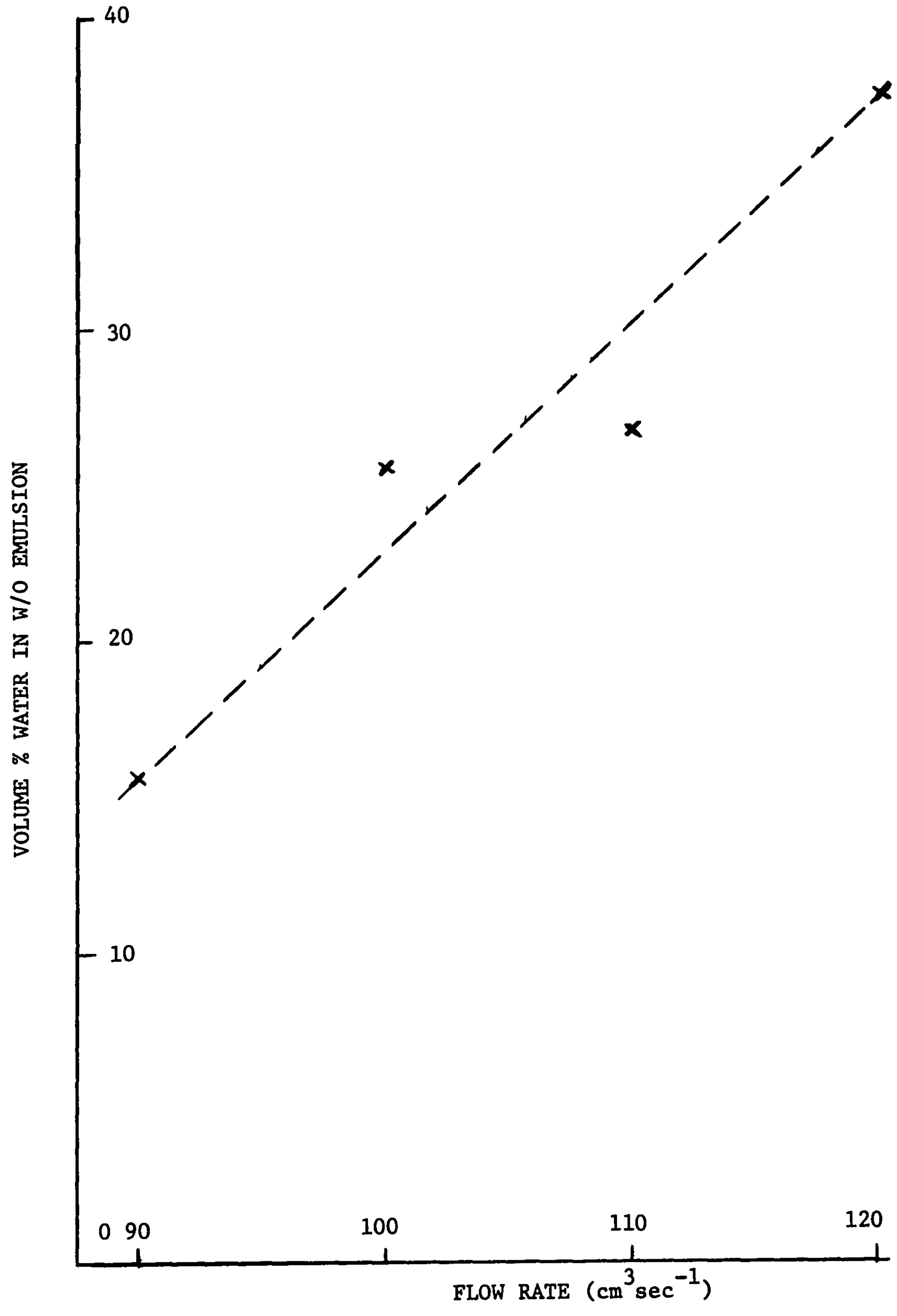

Figure 5.17 Plot of Degree of Emulsification of Water in Oil as a function of Flow Rate.

iii Lance Diameter

In a study of the importance of lance diameter on the reaction rate it was necessary to decide on a flow variable to restrain constant so that a meaningful comparison could be made. Unfortunately this could not be done because of the inability of the gas flow apparatus to cope with the wide range of pressures involved. Keeping the exit velocity constant (5.81×10^3 cm sec^{-1}) by varying the flowrates of the different diameter lances was the method chosen. Lance momentum may have been a better variable to keep constant but the range of pressures restricted this to too small a range of lance diameters.

The basis for comparison of the performance of the different diameter lances was to use a constant gas velocity for each lance and to blow the same total volume of gas for each. The equivalent amount of salt which would stoichiometrically react with the volume of gas used is compared to the actual amount of salt actually reacted in the given time interval. In this way an efficiency for each jet diameter can be computed. Table 5.5 lists the lance sizes and procedure followed and Figure 5.18 shows the relative efficiency of each lance. The remaining variables are held constant at the previous conditions listed on Pages 20, 26.

TABLE 5.5

LANCE DIAMETER cm	FLOWRATE cm^3 sec^{-1}	FLOWTIME sec	TOTAL GAS DEL'D cm^3	HCl DEL'D cm^3	EFF	HCO_3^- %
.093	39.7	755	30,000	3000	19.1	3.58
.148	100	300	30,000	3000	62.1	2.10
.203	189	159	30,000	3000	72.0	1.78

$$*\text{Efficiency} = \frac{\text{Actual measured } \%HCO_3^- - \text{Stoichiometric } \%HCO_3^- \text{ Expected}}{\text{Stoichiometric } \% \; HCO_3^- \text{ Expected}} \times 100$$

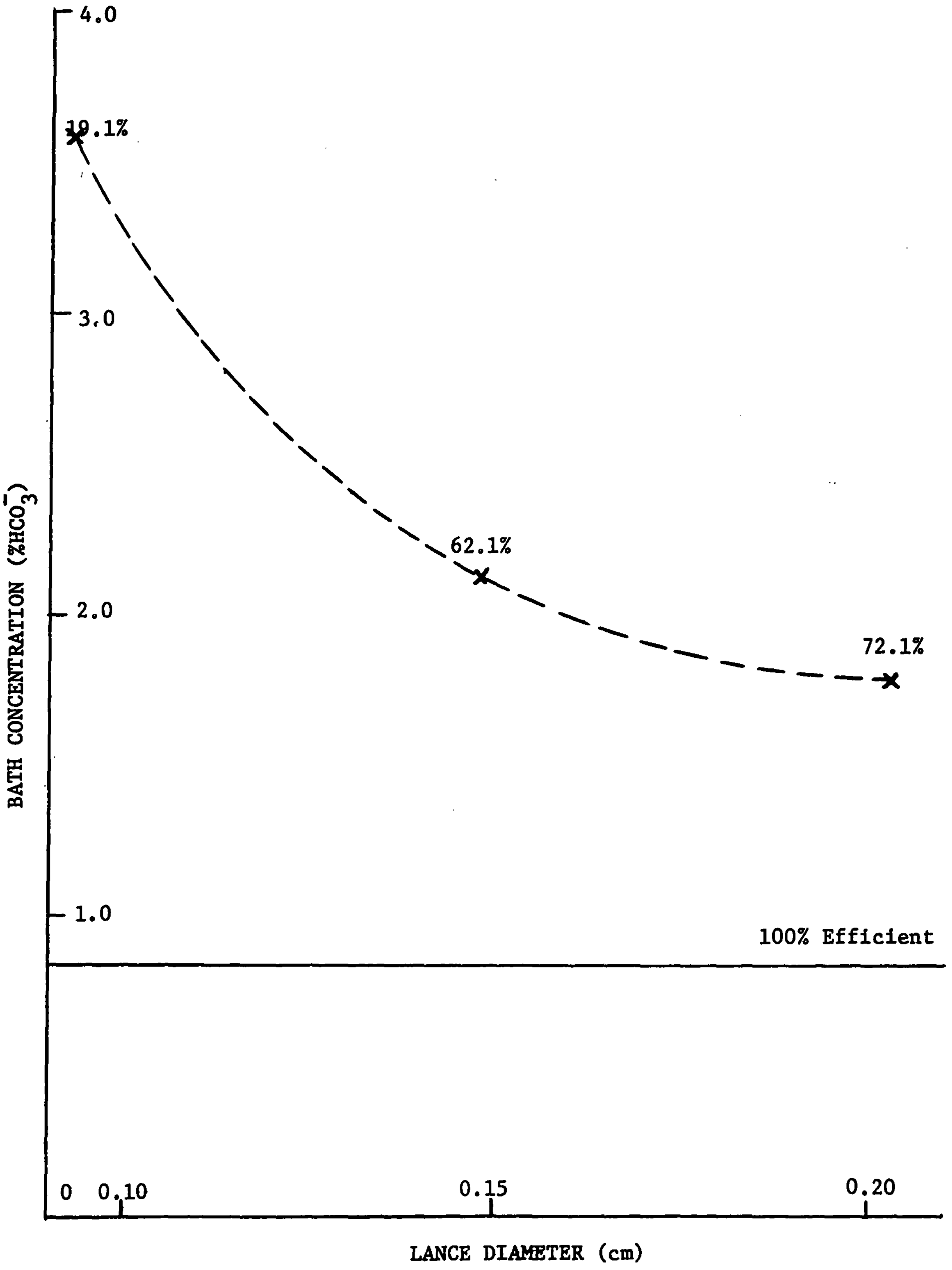

Figure 5.18 Gas Utilization Efficiency vs Lance Diameter.

5.4-4 The Effect of Upper Layer Properties on Reaction Rate

The importance of the oil layer upon reaction rate was studied with reference to oil layer viscosity and the presence of a surface active solute in the oil layer.

i Viscosity

The viscosity of the oil layer could be varied by varying the concentration of Pella and SAE 10W oils in the oil mixture. Figure 5.19 gives the correlation between viscosity and oil composition. The viscosity of the oil was checked after each experiment to eliminate any change due to the corrosive conditions of the vessel.

The experimental conditions were:

Lance height - 2.5 cm
Lance diameter - .15 cm
Flow rate - 120 $cm^3 sec^{-1}$
Oil depth - .84 cm (volume 70 cm^3)
Solution depth - 2.5 cm (volume 222 cm^3, 4 $\%HCO_3^-$)

The rates of reaction as a function of viscosity are shown in Figures 5.20-5.23. A plot of degree of emulsification against viscosity is given in Figure 5.24.

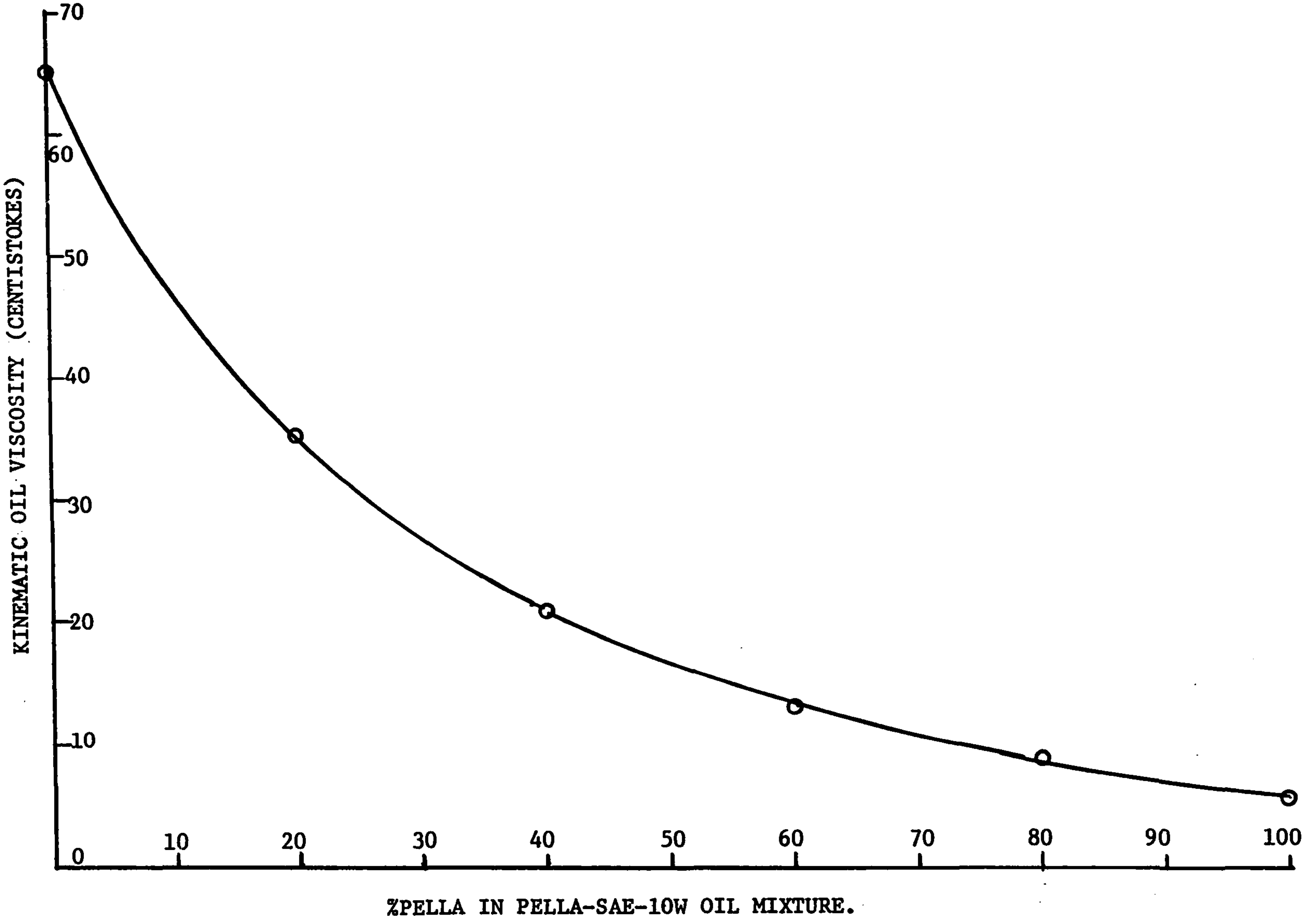

Figure 5.19 Calibration Curve for the Variation of Kinematic Oil Viscosity with Oil Concentration.

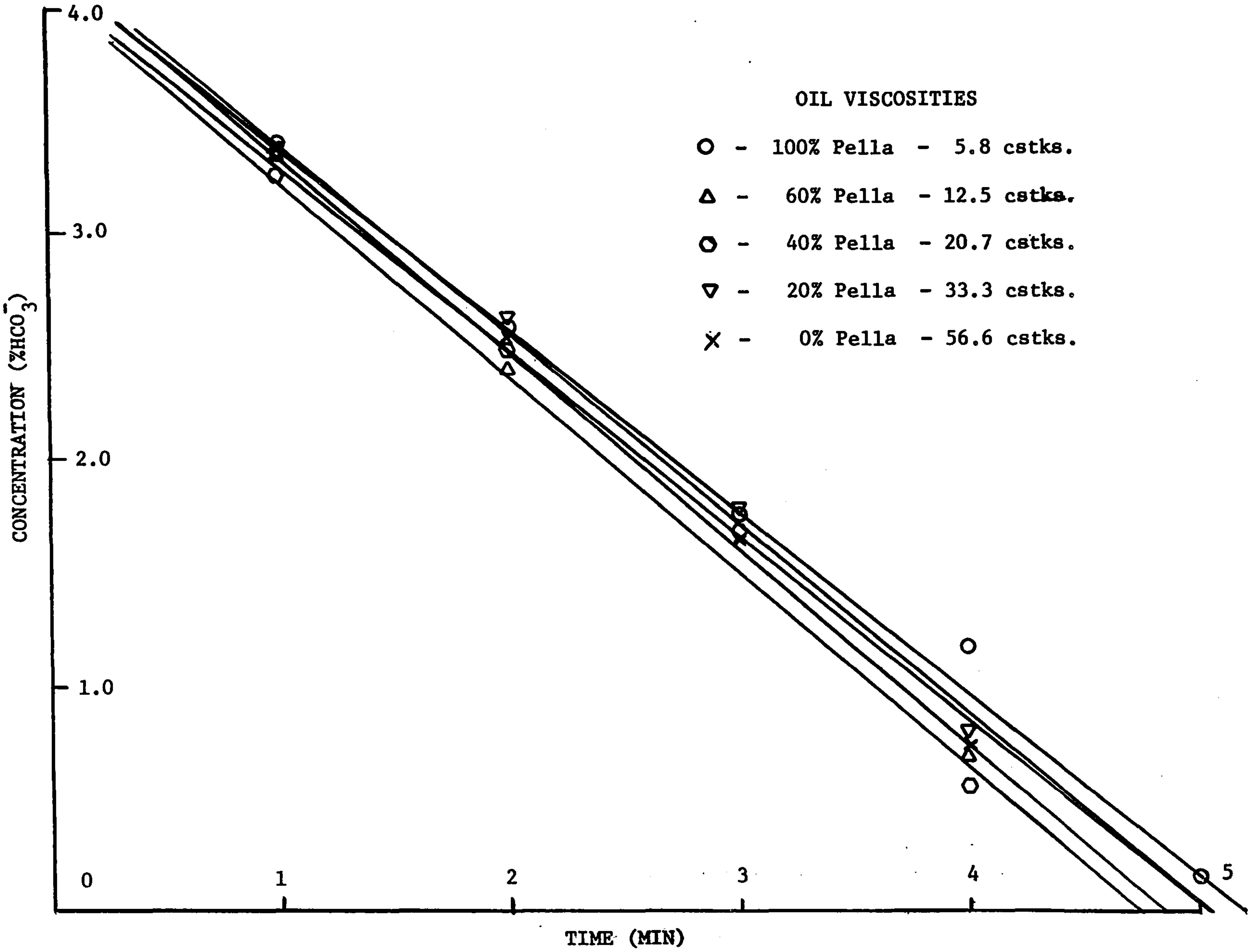

Figure 5.20 Rate of Bath Reaction at Various Oil Viscosities.

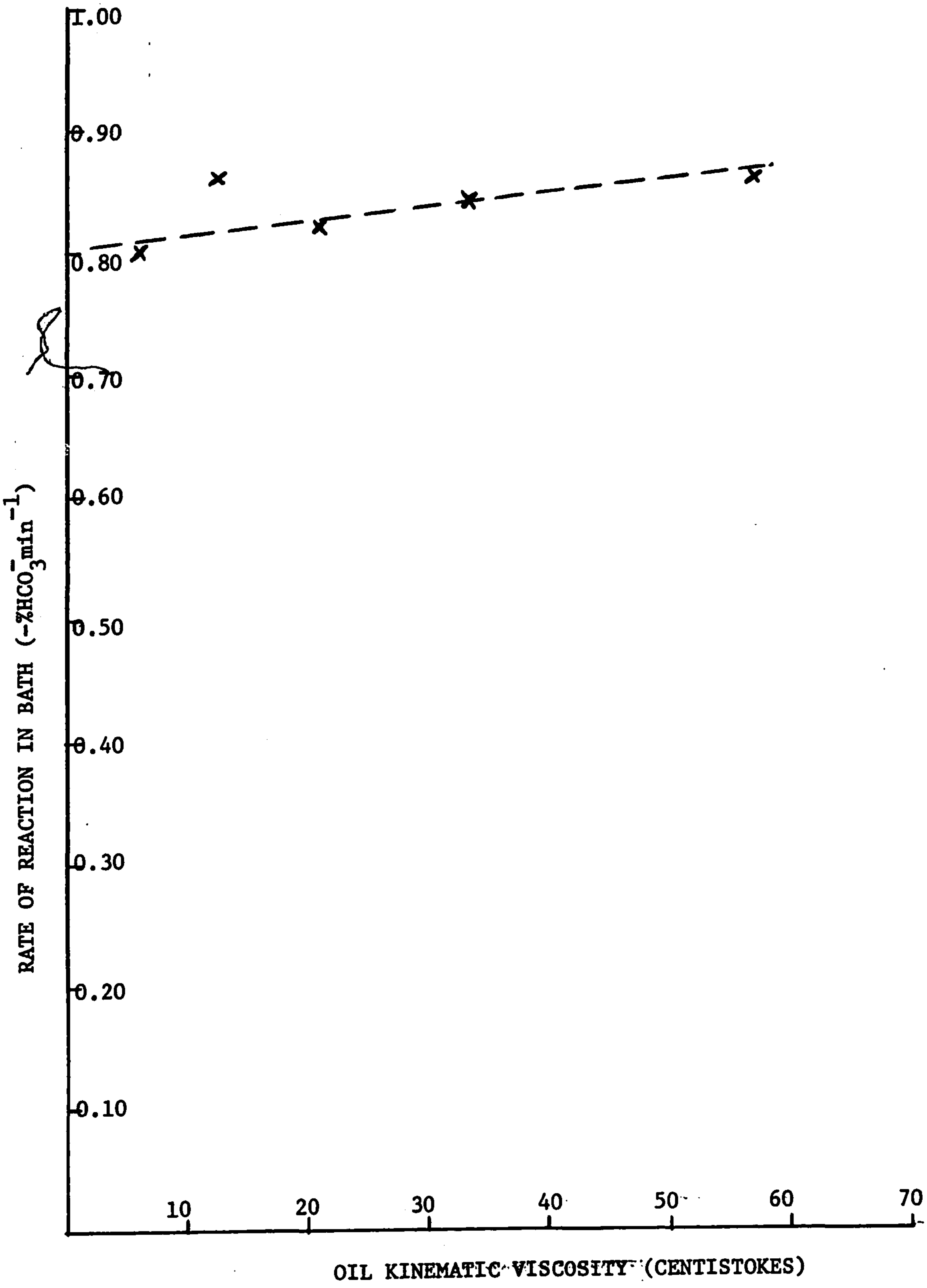

Figure 5.21 Rate of Bath Reaction vs Kinematic Viscosity.

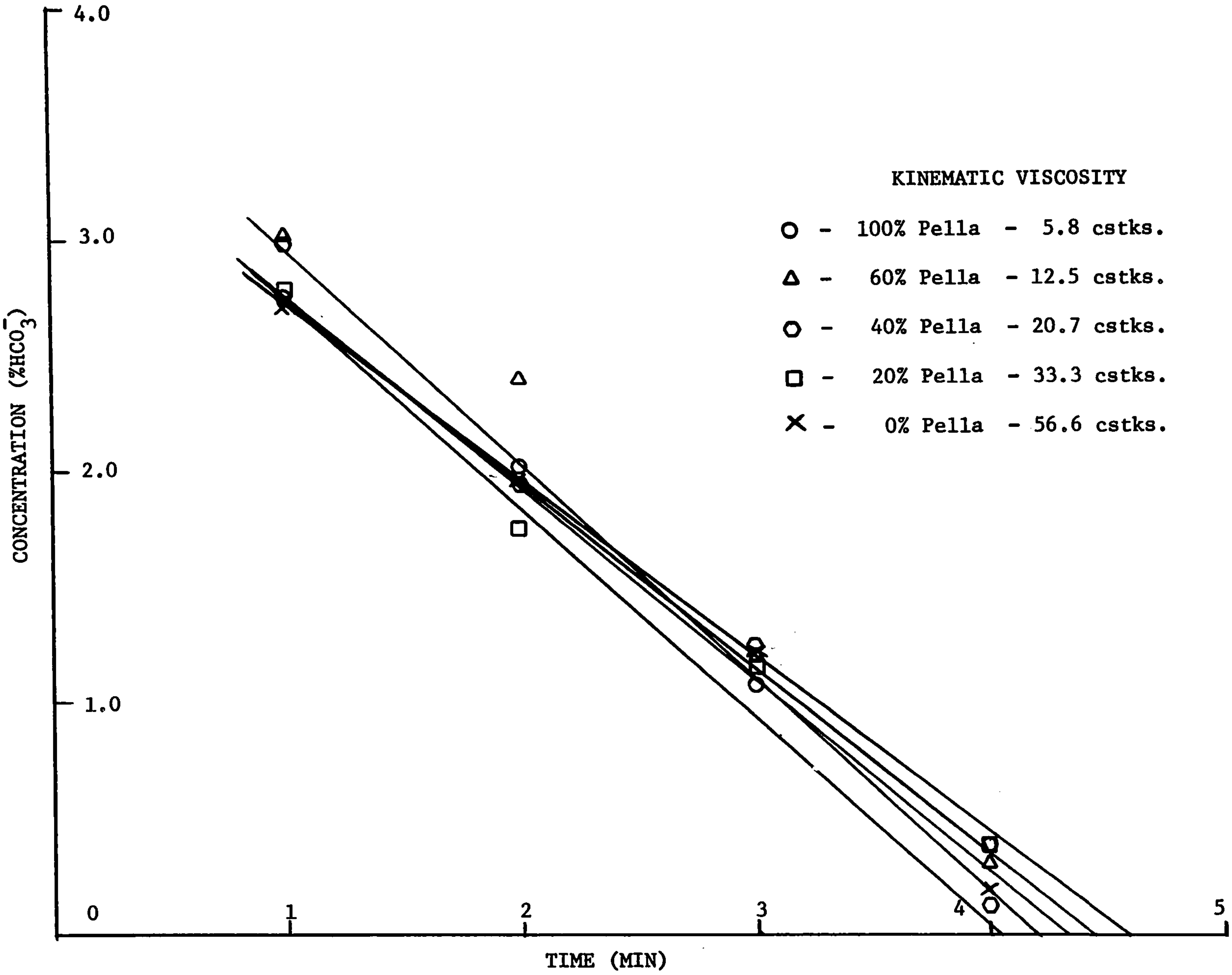

Figure 5.22 Rate of Reaction in Emulsified Layer vs Kinematic Viscosity of Oil.

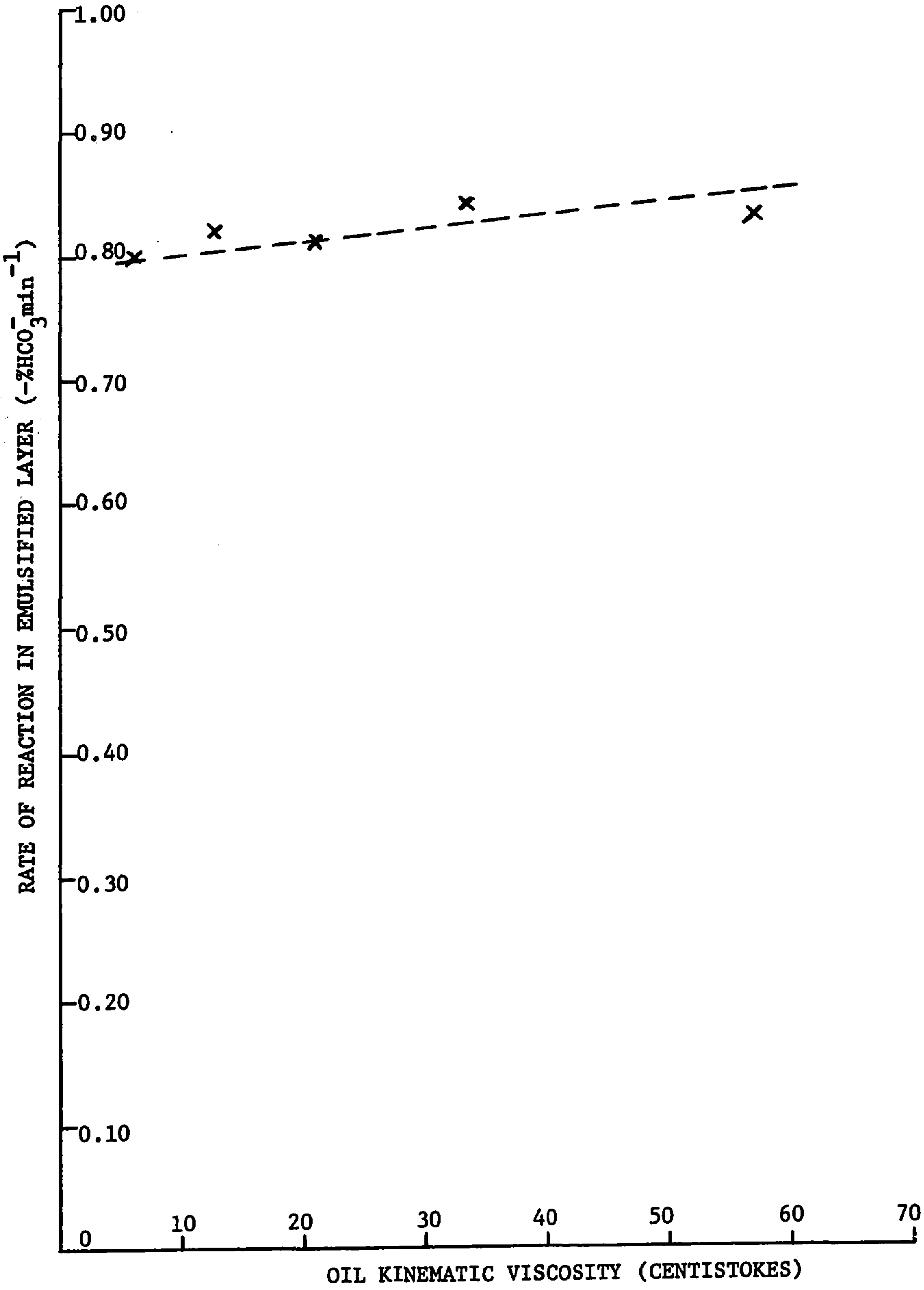

Figure 5.23 Rate of Reaction in Emulsified Layer vs Kinematic Viscosity.

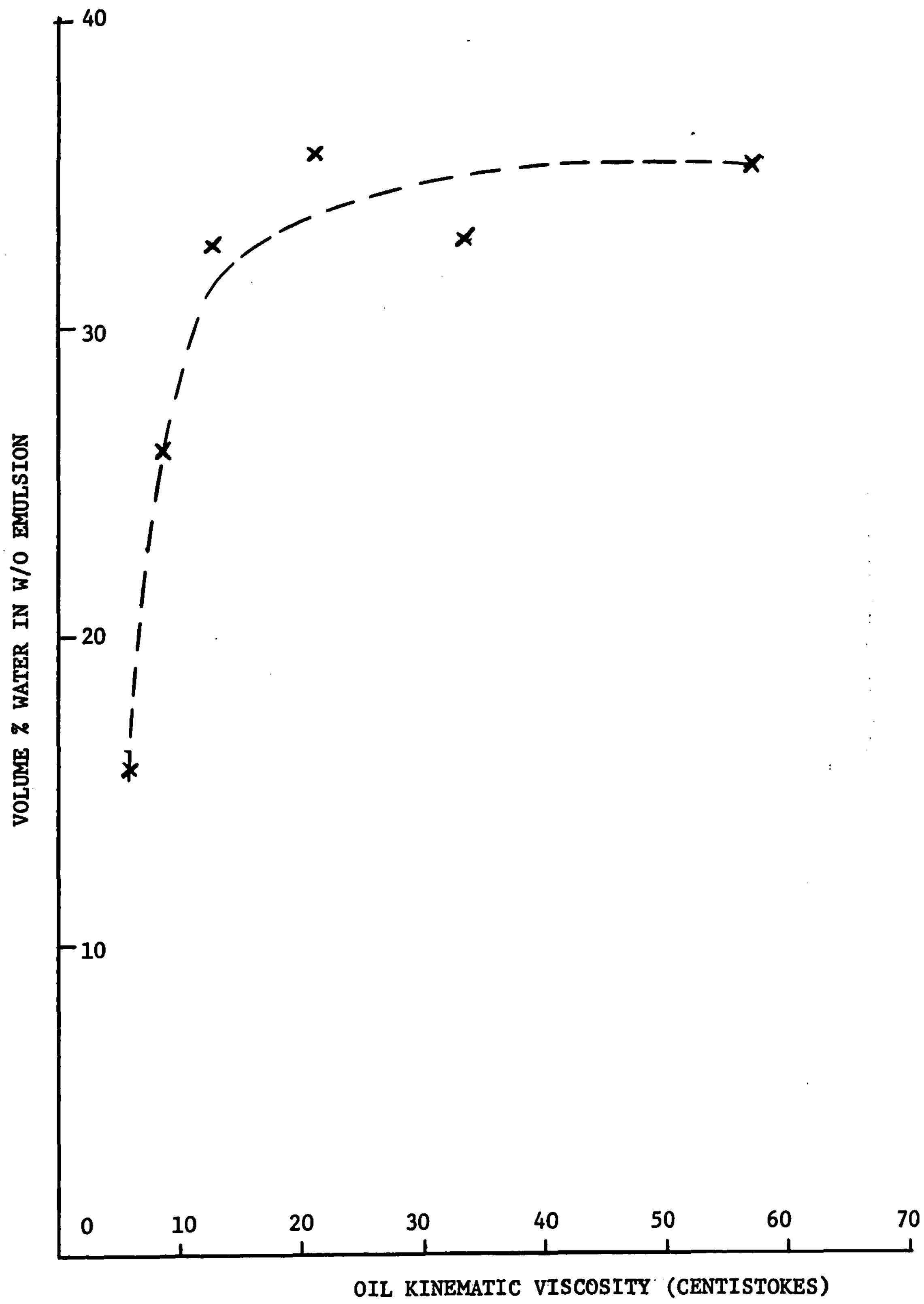

Figure 5.24 Plot of Degree of Emulsification of Water into Oil as a function of Oil Kinematic Viscosity.

ii Surface Activity

The interfacial tension between the sodium bicarbonate solution could be drastically changed by adding a surface active solute called IGEPAL CO-710 (Chemical Developments of Canada Ltd.). This clear syrupy liquid was dissolved in the oil, changing the surface chemistry of the oil layer. It was not possible to cover a range of interfacial tensions due to the high surface activity of the solute.

Two compositions were used:

Oil (Viscosity 21 cstks)

	Interfacial Tension in Contact with 4% HCO_3^-
.2% by volume IGEPAL	∿ 8 dynes cm^{-1}
.4%	< 5 dynes cm^{-1}
0%	50 dynes cm^{-1}

The surface tensions of the oils remained at 30.4 dynes cm^{-1}.

The other variables were fixed constant at:

Flowrate	-120 $cm^3 sec^{-1}$
Lance Height	-2.5 cm
Lance Diameter	- .15 cm
Oil Depth	- .84 cm (70 cm^3 oil, viscosity 21 cstks)
Solution depth	2.5 cm (222 cm^3 4% HCO_3^-)

Figure 5.25 and 5.26 show rate of reaction in bath and in emulsion.

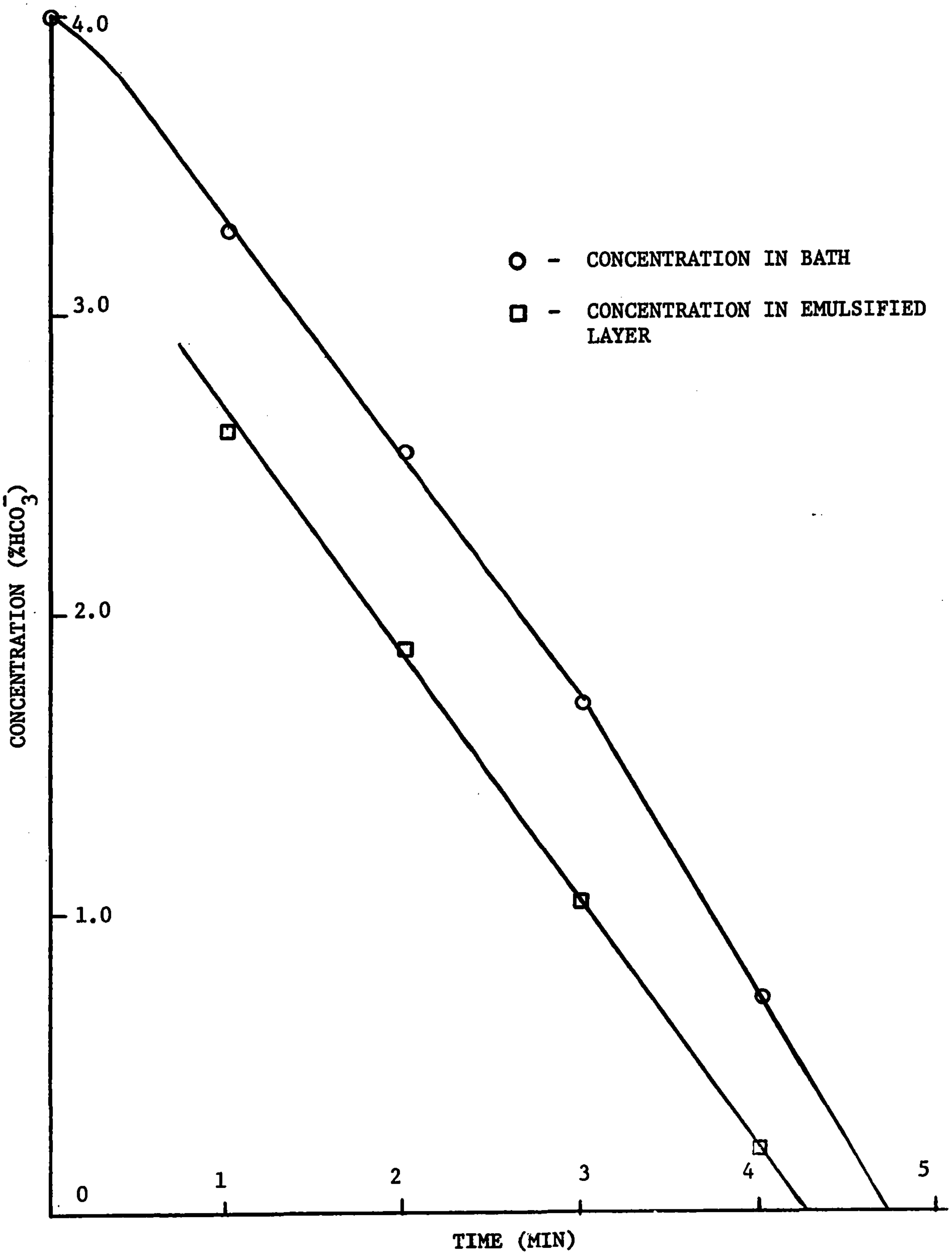

Figure 5.25 Rate of Reaction with Addition of Surface Active Agent to Oil 0.2% IGEPAL CO-710.

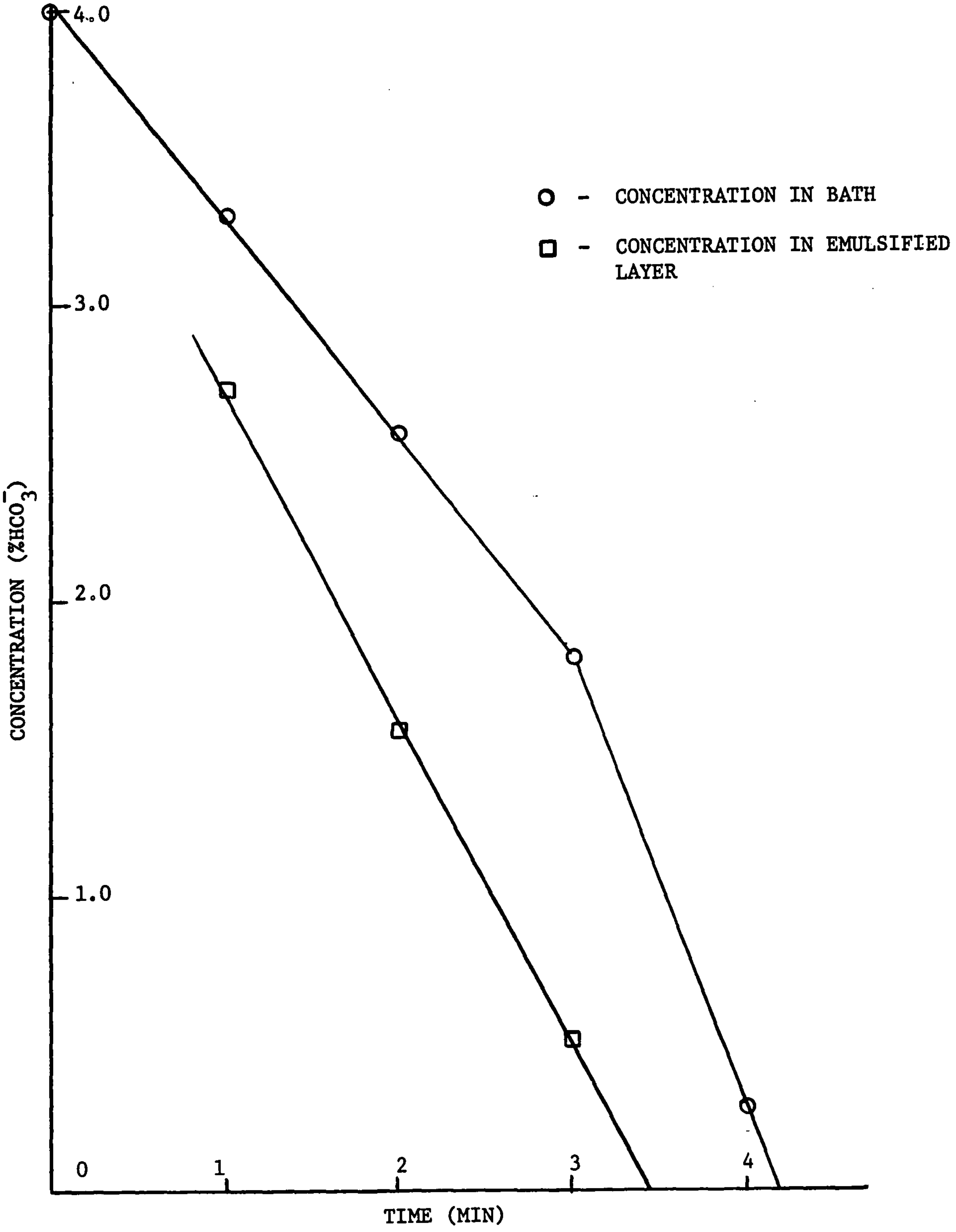

Figure 5.26 Rate of Reaction with Addition of Surface Active Agent 0.4% IGEPAL CO-710.

5.4-5 The effect of Depth of Upper Layer on Reaction Rate

The thickness of the oil layer above the sodium bicarbonate solution was varied to understand its importance in the reaction rates. The depth of the oil and the corresponding volume used is listed below:

TABLE 5.6

Depth 40P Oil	Volume Used (cm^3)
.43 cm	35
.68 cm	55
.86 cm	70
1.11 cm	90
1.30 cm	105

The other variables were kept constant as follows:

Flowrate - 120 cm^3 sec^{-1}
Lance height - 2.5 cm
Lance Diameter - .15 cm
Solution depth - 2.5 cm (Vol. = 222 cm^3 4%HCO_3^-)

Figures 5.27 - 5.30 show the relationship between oil layer thickness and rates of reaction in the bath and the emulsion. Figure 5.31 shows the dependence of degree of emulsification as a function of oil layer depth.

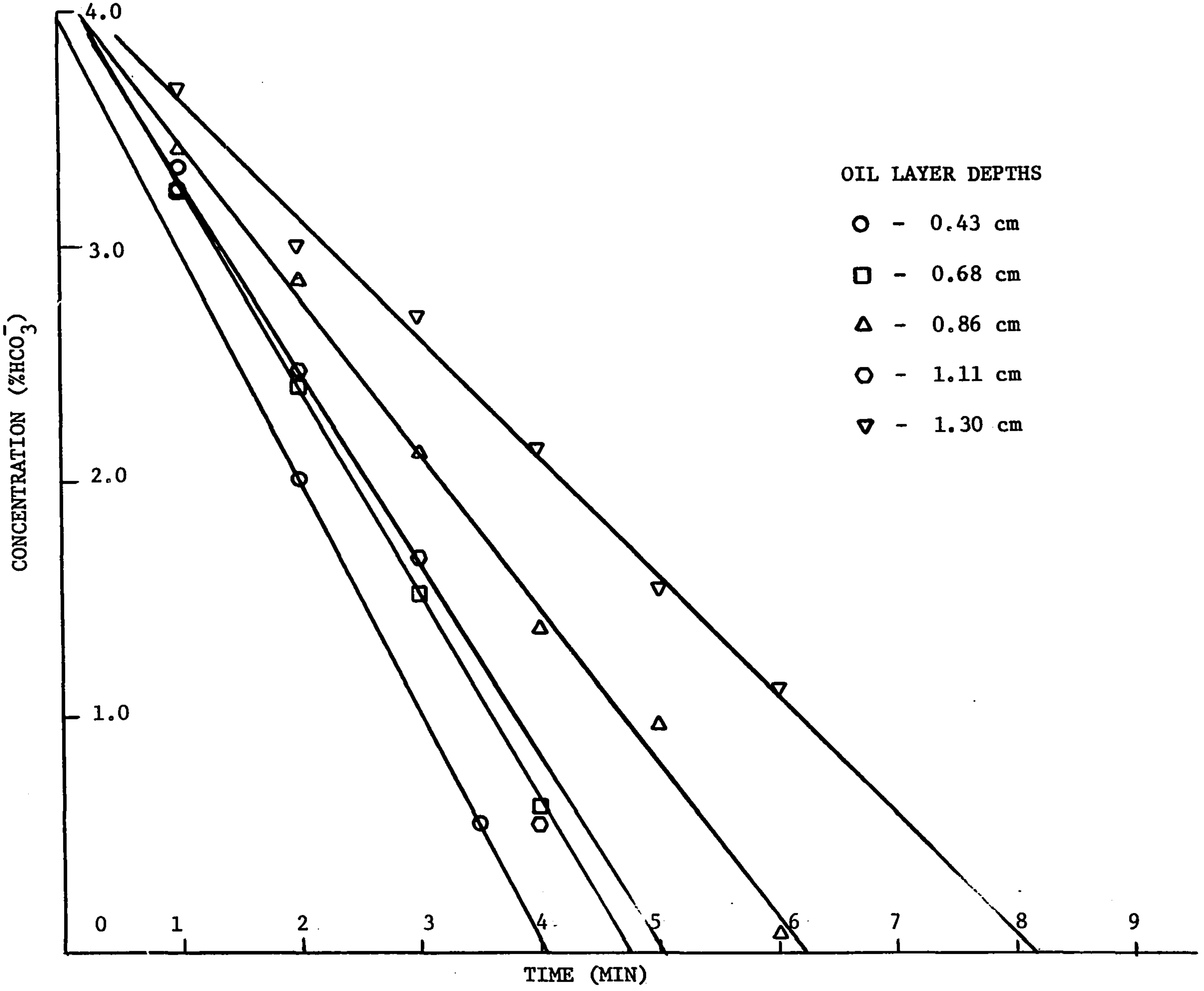

Figure 5.27 Rate of Bath Reaction at Varying Oil Layer Thicknesses.

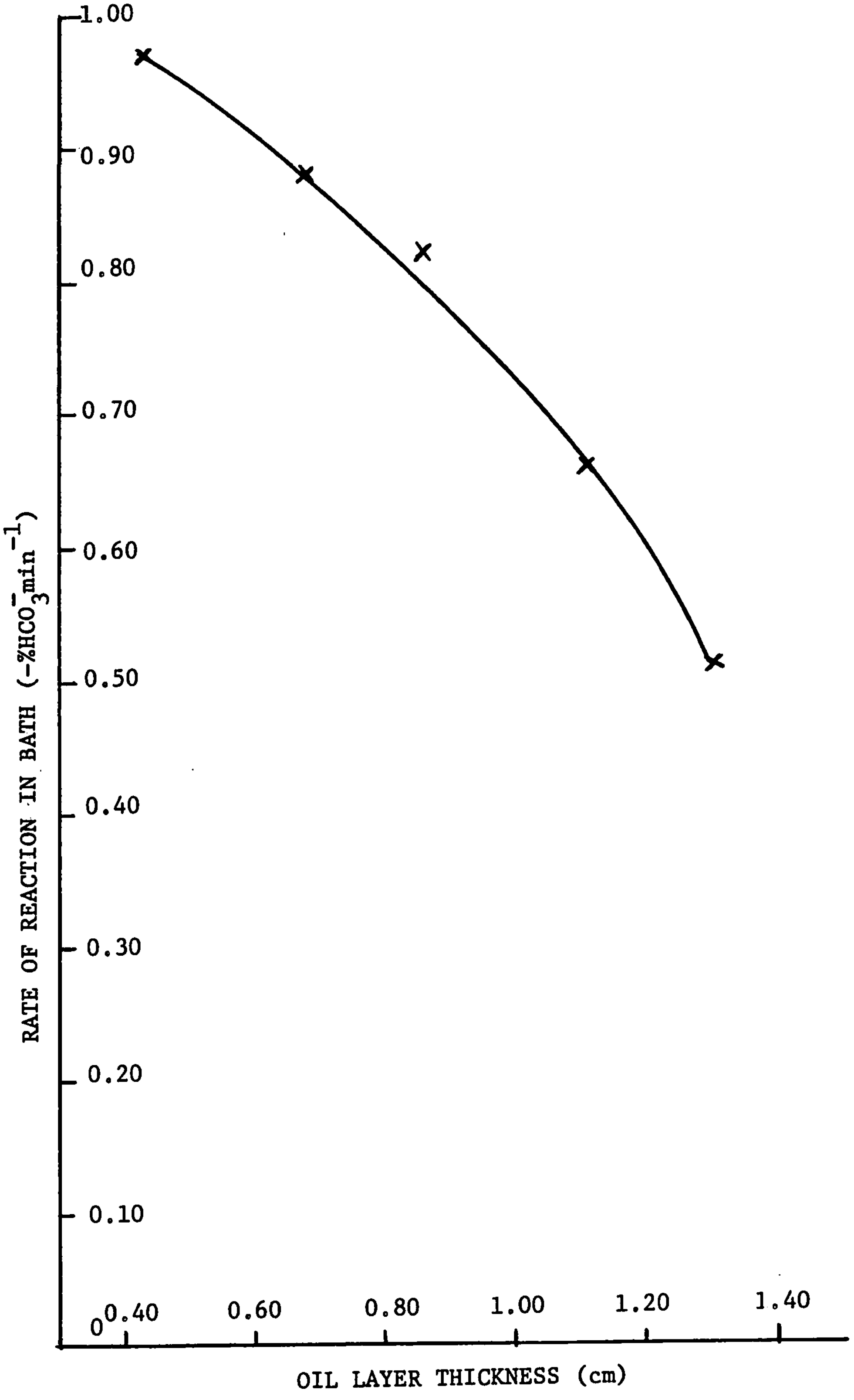

Figure 5.28 Rate of Reaction in Bath vs Depth of Oil Layer.

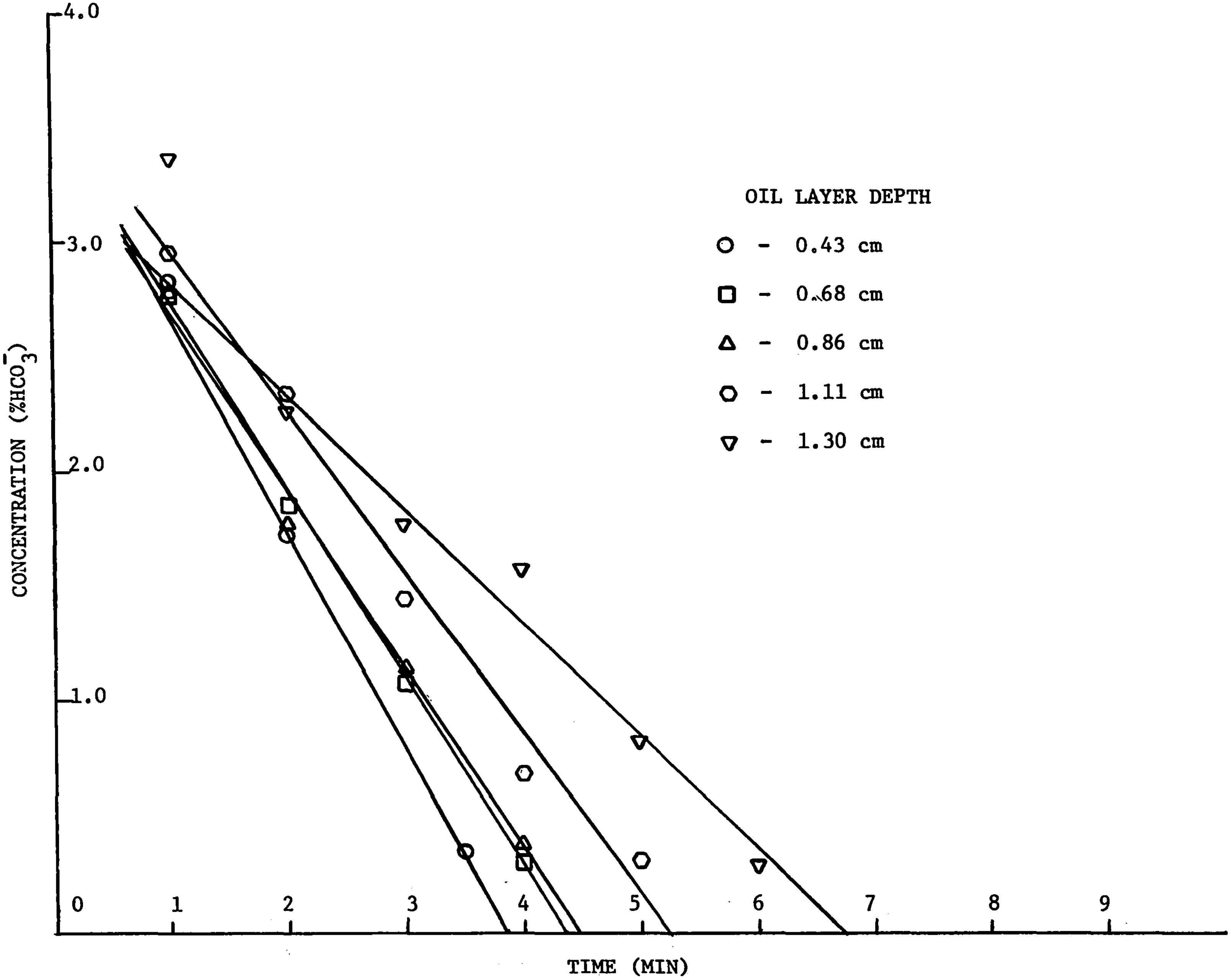

Figure 5.29 Rate of Reaction in Emulsified Layer at Varying Oil Layer Depths.

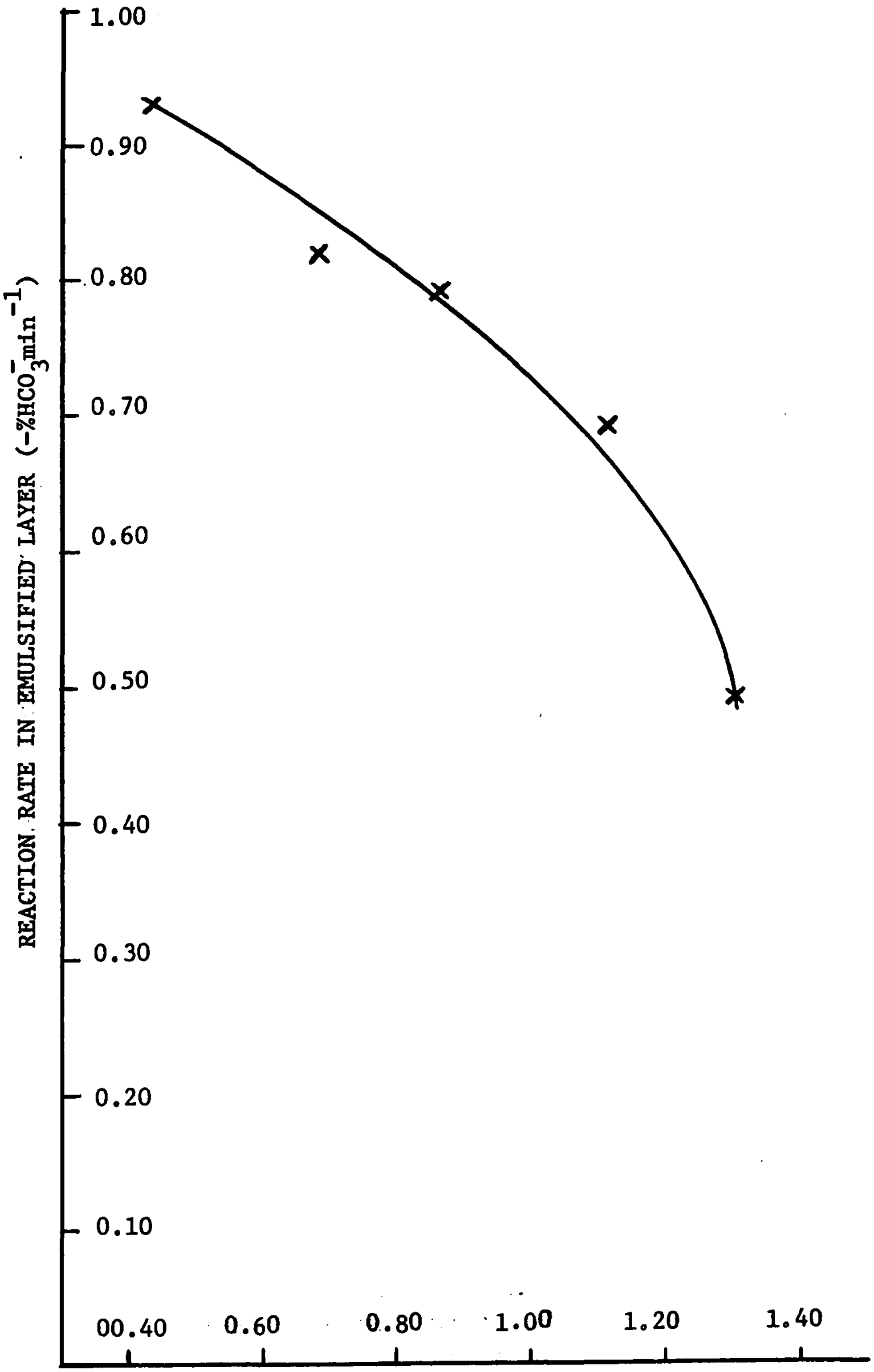

Figure 5.30 Rate of Reaction in Emulsified Layer vs Oil Layer Depth.

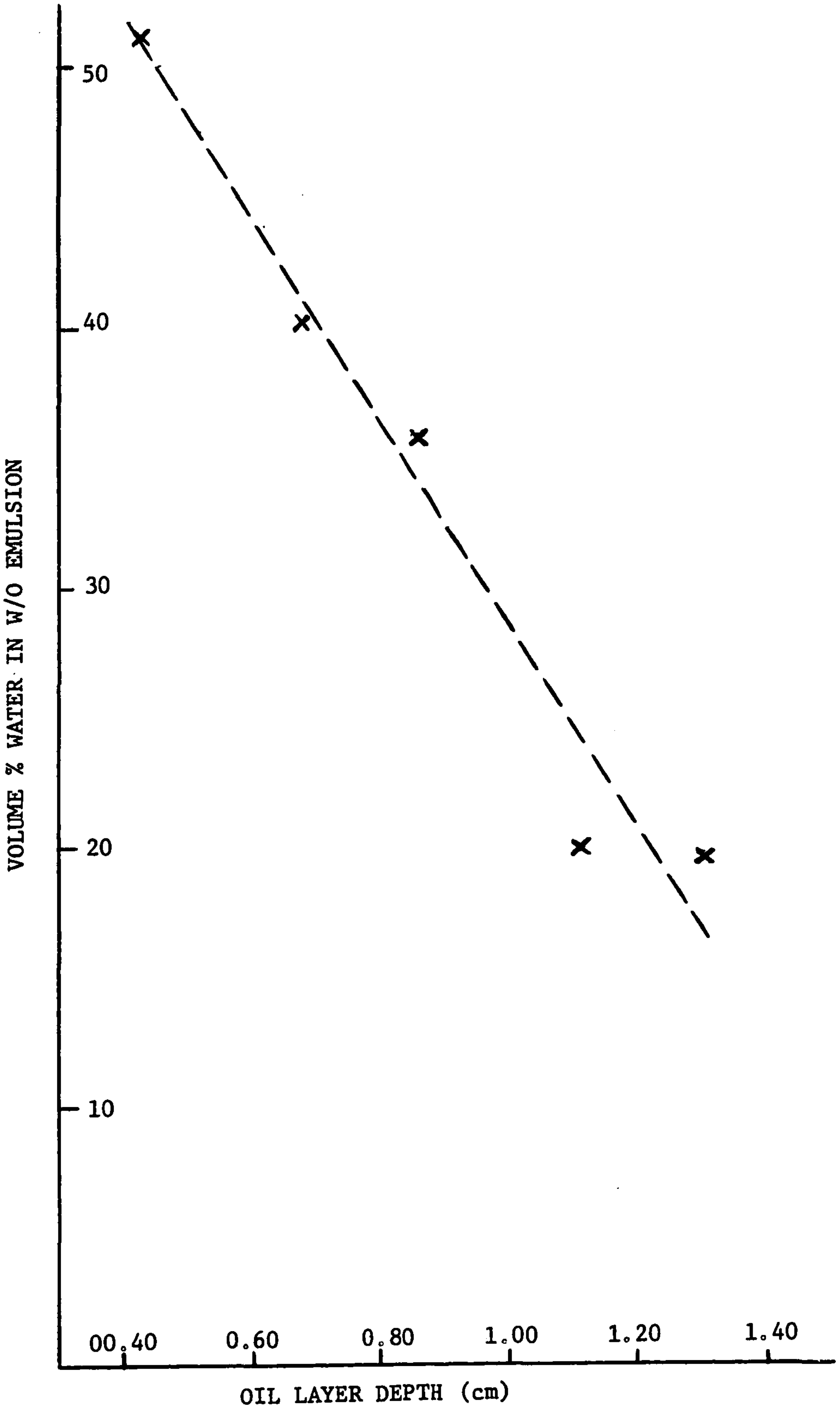

Figure 5.31 Degree of Emulsification of Water into Oil as a function of Oil Layer Thickness.

5.4-6 The Effect of a Reactive Oil on Reaction Rate

The rate of HCO_3^- removal from aqueous solution by HCl dissolved in the oil phase was examined by placing an oil layer which had been exposed to an HCl jet on top of a 4 $\%HCO_3^-$ solution. The oil employed had been reacted with the HCl jet in a usual jetting experiment and hence it had the reactivity of oil which would be found at the end of a jetting experiment.

The measured rate of reaction of $NaHCO_3$ indicated the flux of HCl between the oil and the $4\%HCO_3^-$ layer was 4×10^{-8} moles $cm^{-2}sec^{-1}$. This rate was so small as compared with the observed reaction rates in jet experiments of 10^{-4} moles cm^{-2} sec^{-1}, that the oil-aqueous reaction could be neglected.

An attempt was made to simulate a reactive slag by dissolving ferric chloride in the oil layer. The method used was to first dissolve about 2.4 gm $FeCl_3$ in 150 ml of ether. The ether was then mixed with the Shell SAE-10W oil. The oil turned from a golden colour to a dark green. This was due to the $FeCl_3$ not being in true solution in the oil but probably as a colloidal dispersion. In this system two reactions were of importance:

Gas jet - sodium bicarbonate solution reaction:

$$HCl + NaHCO_3 = NaCl + H_2O + CO_2$$

Since the Na^+ion and the Cl^- ion stay in aqueous solution and undergo no physical change, the reaction may be written in a short form.

$$\text{i.e. } H^+ + HCO_3^- = H_2O + CO_2$$

The oil layer - sodium bicarbonate solution reaction:

$$FeCl_3 + 3NaHCO_3 = Fe(OH)_3 + 3NaCl + CO_2$$

The shorter form of expressing the reaction would be:

$$Fe^{+3} + 3HCO_3^- = Fe\ (OH)_3 + CO_2$$

Ferric hydroxide leaves the solution as a brown precipitate.

5.4-6 The Effect of a Reactive Oil on Reaction Rate

The rate of HCO_3^- removal from aqueous solution by HCl dissolved in the oil phase was examined by placing an oil layer which had been exposed to an HCl jet on top of a 4 $\%HCO_3^-$ solution. The oil employed had been reacted with the HCl jet in a usual jetting experiment and hence it had the reactivity of oil which would be found at the end of a jetting experiment.

The measured rate of reaction of $NaHCO_3$ indicated the flux of HCl between the oil and the $4\%HCO_3^-$ layer was 4×10^{-8} moles $cm^{-2}sec^{-1}$. This rate was so small as compared with the observed reaction rates in jet experiments of 10^{-4} moles cm^{-2} sec^{-1}, that the oil-aqueous reaction could be neglected.

An attempt was made to simulate a reactive slag by dissolving ferric chloride in the oil layer. The method used was to first dissolve about 2.4 gm $FeCl_3$ in 150 ml of ether. The ether was then mixed with the Shell SAE-10W oil. The oil turned from a golden colour to a dark green. This was due to the $FeCl_3$ not being in true solution in the oil but probably as a colloidal dispersion. In this system two reactions were of importance:

Gas jet - sodium bicarbonate solution reaction:

$$HCl + NaHCO_3 = NaCl + H_2O + CO_2$$

Since the Na^+ ion and the Cl^- ion stay in aqueous solution and undergo no physical change, the reaction may be written in a short form.

$$\text{i.e. } H^+ + HCO_3^- = H_2O + CO_2$$

The oil layer - sodium bicarbonate solution reaction:

$$FeCl_3 + 3NaHCO_3 = Fe(OH)_3 + 3NaCl + CO_2$$

The shorter form of expressing the reaction would be:

$$Fe^{+3} + 3HCO_3^- = Fe\ (OH)_3 + CO_2$$

Ferric hydroxide leaves the solution as a brown precipitate.

Quantitative measurements which were obtained were not considered reliable due to the possible influence of the precipitate on the process. Difficulty was experienced in filtering the solutions before volumetric analysis with HCl. Qualitatively a good foam appeared on the oil surface. A large amount of $Fe(OH)_3$ precipitated in the emulsified region.

The interface became covered with the precipitate and the aqueous layer soon became completely clouded with the stirring up of the precipitate by the gas jet.

CHAPTER 6

6.0 HIGH TEMPERATURE INVESTIGATION

The high temperature investigation consisted of a study of carbon removal from the iron in a small scale Basic Oxygen Furnace using a pure high carbon pig iron and an industrial steelmaking slag.

Measurements of the amount of metallic iron dispersed into the slag layer and the rates of reaction in the metal/slag emulsion and the metal layer of the system were made. Lance size and height above the melt were maintained constant, the principle variable being oxygen gas flow rate.

6.1 Experimental Apparatus

The high temperature apparatus consisted of a 5 1/2 - 6 inch (15 cm) internal diameter Norton (Hamilton, Ontario) magnorite crucible. This crucible was cemented into the water-cooled copper coils of an induction furnace (30 kva, 10 kilocycle,motor generator TOCCO MELTMASTER IB-20037-7-63; Tocco Division - The Ohio Crank Shaft Co., Cleveland, Ohio, U.S.A.) A diagram of the induction heating assembly is shown in Figure 6.1.

A moveable trolley was used to house the oxygen lance which was a mullite tube 3/32 inch (.24 cm) inside diameter and 30 inches long. A 1/4 inch inside diameter alumina tube of about 3 or 4 inches length was cemented to the end of the mullite tube to protect the oxygen lance from the slag and high temperatures during a blow. The lance was clamped so as to allow easy vertical adjustment. Pictures of the apparatus assembly are shown in Figure 6.2 - 6.3.

The oxygen gas was metered by a Gilmont ball-type flowmeter with a capacity of 0-2.8 (±.03) SCFM. Gas analysis was not performed on the off gases; the exhaust was collected and discarded through a heavy duty fume hood.

Hot metal temperatures were measured using a Pt - Pt + 13% Rh thermocouple immersed in the melt. The thermocouple sheaths were of mullite and the thermocouple was protected for most of its length by a 1/4 inch diameter alumina tube. The last 3 - 4 inches of the thermocouple were protected by a 1/16" I.D. x 1/8" O.D. graphite sleeve which was cemented to the alumina tube. Graphite was found to be the best protective material due to its high thermal conductivity and its resistance to thermal shock and slag attack.

1. Pouring Spout & Top Seal
2. Top Board
3. Coil Terminals & Water Connections
4. Encapsuled Coil Assembly
5. MgO Crucible
6. Rammed Lining
7. Refractory Base
8. Bottom Board
9. Pouring Handle
10. Release & Safety Switch

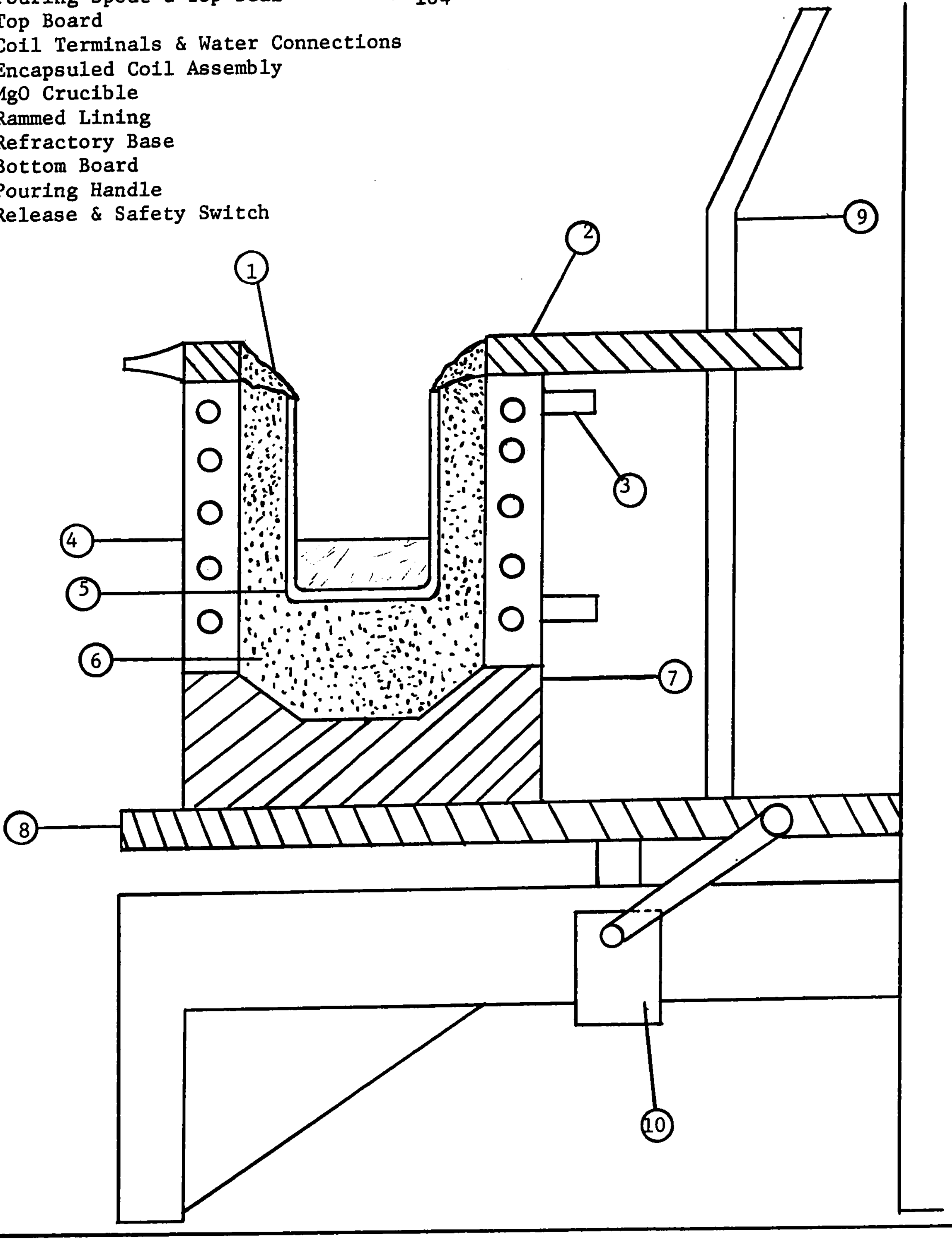

Figure 6.1 Schematic Diagram of the Induction Furnace and Associated Equipment.

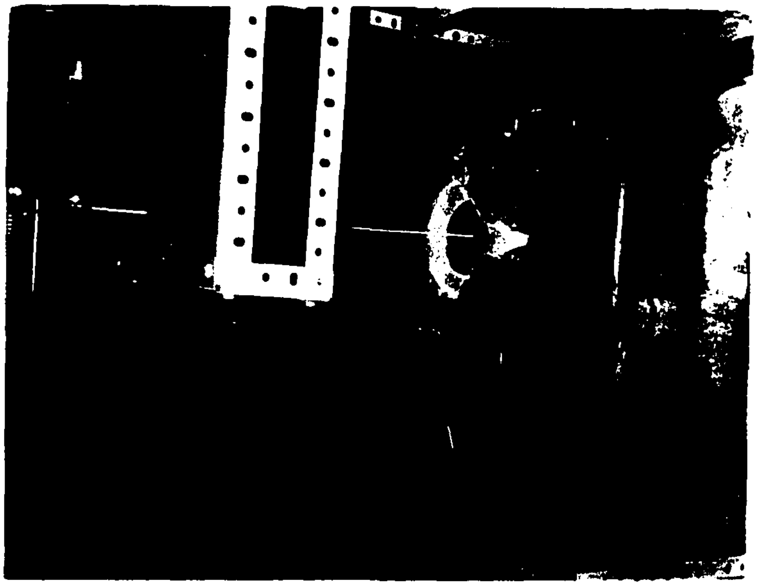

Figure 6.2 Apparatus with crucible in Induction Furnace, moveable trolley and mullite lance.

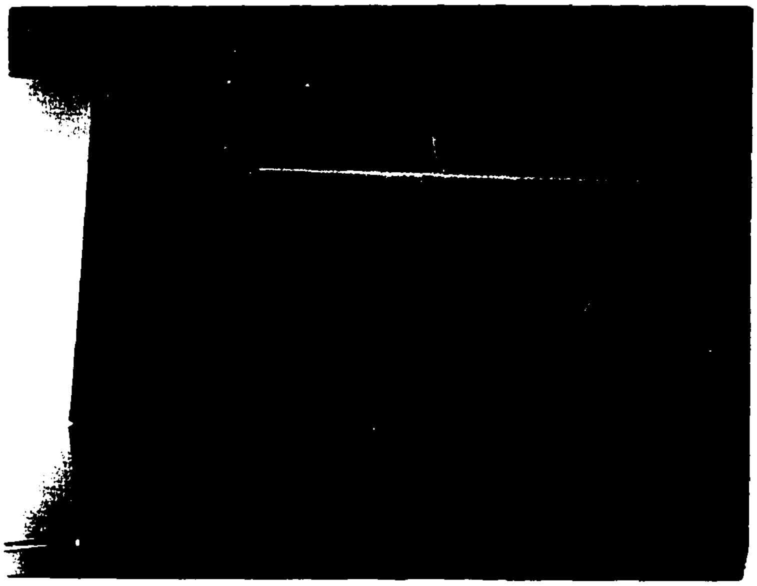

Figure 6.3 Apparatus assembly showing control panel of Induction Furnace.

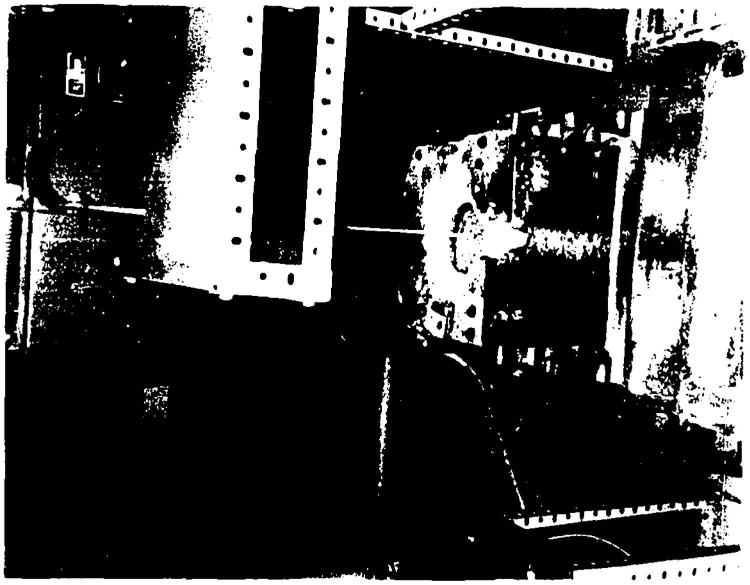

Figure 6.2 Apparatus with crucible in Induction Furnace, moveable trolley and mullite lance.

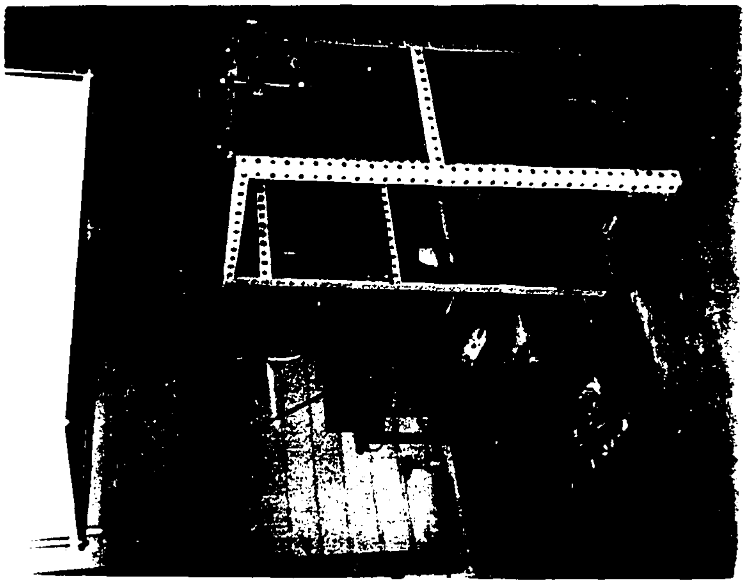

Figure 6.3 Apparatus assembly showing control panel of Induction Furnace.

During the course of an experiment two sets of samples were taken; one from the iron bath and the other from the slag emulsion. The iron sample was obtained in pin form by immersing a piece of 6mm vycor tubing (softening point 1500°C) into the iron layer and applying suction by means of a rubber bulb. The slag sampling instrument was made by fashioning the end of an iron pipe into the form of a wide spoon. Slag samples were taken by scooping out some of the foaming slag with the spoon sampler followed by immediate quenching in water. The iron and slag samplers are shown in Figure 6.4.

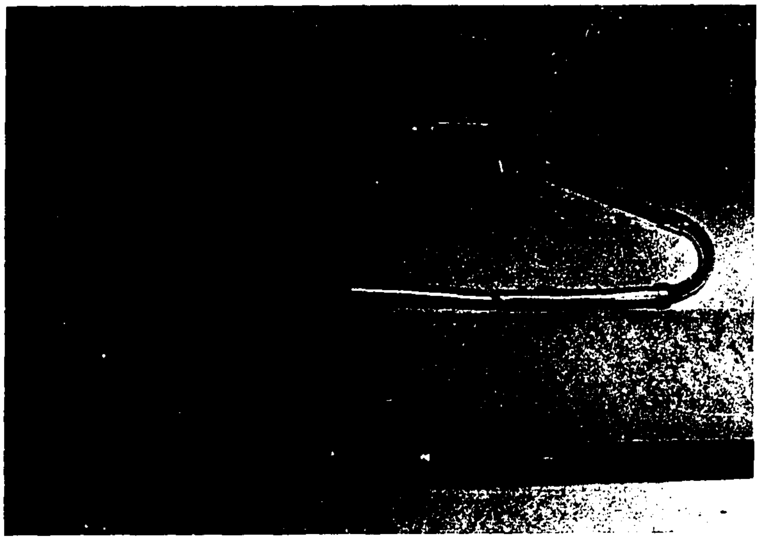

Figure 6.4 The upper half of the photo shows the iron sampler, consisting of a copper tube attached to vycor tubing. The black suction bulb has valves to facilitate quick easy vacuum application.

The lower part of the photo shows the slag sampler with the removable spoon-shaped end.

During the course of an experiment two sets of samples were taken; one from the iron bath and the other from the slag emulsion. The iron sample was obtained in pin form by immersing a piece of 6mm vycor tubing (softening point 1500°C) into the iron layer and applying suction by means of a rubber bulb. The slag sampling instrument was made by fashioning the end of an iron pipe into the form of a wide spoon. Slag samples were taken by scooping out some of the foaming slag with the spoon sampler followed by immediate quenching in water. The iron and slag samplers are shown in Figure 6.4.

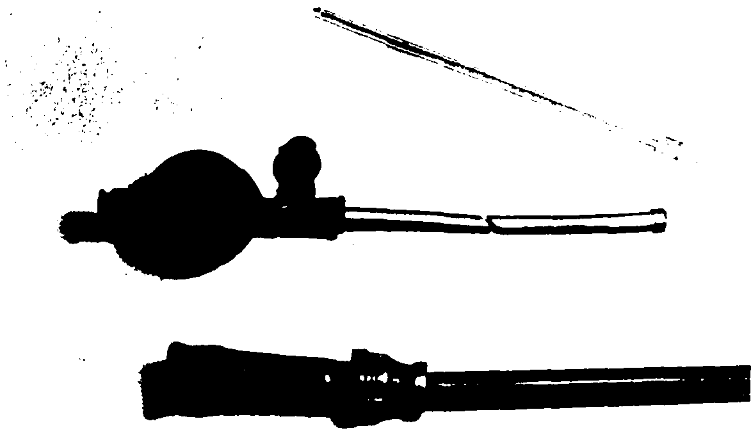

Figure 6.4 The upper half of the photo shows the iron sampler, consisting of a copper tube attached to vycor tubing. The black suction bulb has valves to facilitate quick easy vacuum application.

The lower part of the photo shows the slag sampler with the removable spoon-shaped end.

6.2 Materials

The purities of the cylinder gas is as follows:

Oxygen: Canadian Liquid Air
Montreal, Quebec

99.5% O_2

Pig Iron: Quebec Iron and Titanium Corp.
Sorel, Quebec

Sorelmetal F-3

Typical Analysis

4.5 %C
.015%S
.027%P
.18 %Si
.009%Mn

Steelmaking Slag: Dominion Foundaries and Steel Corp.
Hamilton, Ont.

Slag Analysis

25.5% Fe
25.8% FeO
8.09% Fe_2O_3
0.36% Al_2O_3
36.8 % CaO
9.7 % MgO
4.16% MnO
11.2 % SiO_2
0.037% P_2O_5

6.3 Procedure

Approximately 15-17 lbs of pig iron were weighed out from a broken ingot. The pieces were placed in the MgO crucible and the induction furnace was started. During the heat-up a natural gas burner was trained onto the crucible for the purpose of cutting down heat losses from the top of the crucible and to maintain reducing atmosphere over the molten metal and slag.

When the iron was molten, 300 gm of crushed slag (-14 + 20 mesh) were slowly added to the iron surface. The slag, which is not receptive to induction heating, received all of its heat from the molten iron and the gas burner.

When all of the slag had been added, the thermocouple was immersed into the molten iron and the temperature was recorded. The temperature of the bath was raised to 1350°C and was then maintained constant by regulating the plate voltage of the induction coils. The thermocouple was then removed from the melt, the oxygen lance was positioned and then lowered to 1-1/2 inches above the surface. The power was turned off.

After an initial iron sample was taken and the gas burner was removed, the oxygen gas flow was started and was adjusted to the specified rate as the stopclock was started. Iron and slag samples taken at regular intervals were immediately quenched in water.

Iron Sample Analysis

The iron samples were broken into 1/4 inches lengths weighing about 1 gm and analyzed for per cent carbon using a Leco 70 second carbon analyzer. (Laboratory Equipment Corporation, St. Joseph, Michigan, Mod. 750-100).

The Leco system consists of an oxygen purifying train, a high frequency induction furnace and a 70-second carbon analyzer. A dust trap, sulphur trap, catalyst tube and heater are mounted on the furnace, which also has a raising mechanism fitted with a special cup-locking device to insure leak free operation. The analyzer is composed of a moisture trap, Wheatstone bridge circuit with thermal conductivity cell, weight compensator, oven and a digital voltmeter.

A weighed sample and combustible accelerators are placed in a burned-off ceramic crucible and introduced into the furnace combustion tube by a raising mechanism. Oxygen from the purifying train passes through the combustion tube to rapidly burn the sample which has been heated in the furnace. The oxygen oxidizes carbon to carbon dioxide, sulphur to SO_2 and iron and alloying elements to solid or liquid oxides. Most of these oxides remain in the crucible, but those that are carried out of the crucible are collected in a dust trap. A manganese dioxide trap absorbs the sulphur gases. Moisture is removed in an Anhydrone trap, and any carbon monoxide is converted to CO_2 in a heated catalyst tube.

The carbon dioxide and excess oxygen are collected in a cylinder and their thermal conductivity is measured by a thermal conductivity cell. The cell output is read directly on a special d-c digital voltmeter. With pure oxygen in the cylinder, the thermal conductivity cell is balanced to read zero output as indicated on the digital voltmeter. This means the output of the thermal conductivity cell indicated by the voltmeter is proportional to the cylinder CO_2. The cylinder is housed in an oven above ambient temperature to eliminate temperature variations affecting the thermal conductivity cell. The performance of the Leco Carbon Analyzer is described and evaluated further by J. M. Hathaway[58].

Slag Emulsion Analysis

Samples collected from the foaming slag were crushed in the closed piston-cylinder type crusher depicted in Figure 6.5 The crushed sample was passed over a No. 48 screen and the undersize, which was mostly slag particles, was raked with an electromagnet to remove any small iron droplets. The oversize was also raked with the electromagnet to separate out the iron particles. However, a clean separation of the slag phase from the metallic iron phase could not be adequately achieved.

Clean separation of the metallic iron from slag was an absolute necessity if the carbon concentration in the emulsified metal was to be accurately determined. If, for example, the sample after cleaning contained 20% slag, the carbon content of emulsified iron as recorded by the Leco analyzer would be 20% lower than actual. This is especially significant in this work because the difference in carbon concentration between bath iron and emulsified iron is important. This difference could appear larger than actual if slag is included in the emulsified iron analysis.

It was estimated that the emulsion sample contained 10 - 20% slag after separation with the electromagnet. The reasons for this were that: some slag particles contained magnetite and were attracted to the electromagnet; and that many slag particles were attached and ground into the iron droplets. Further crushing of the iron droplets did not improve the situation. Removing the slag by dissolution in acids such as HCl, HNO_3, H_2SO_4, HF or any combination of these was discarded because of the high rate of iron dissolution in these same acids.

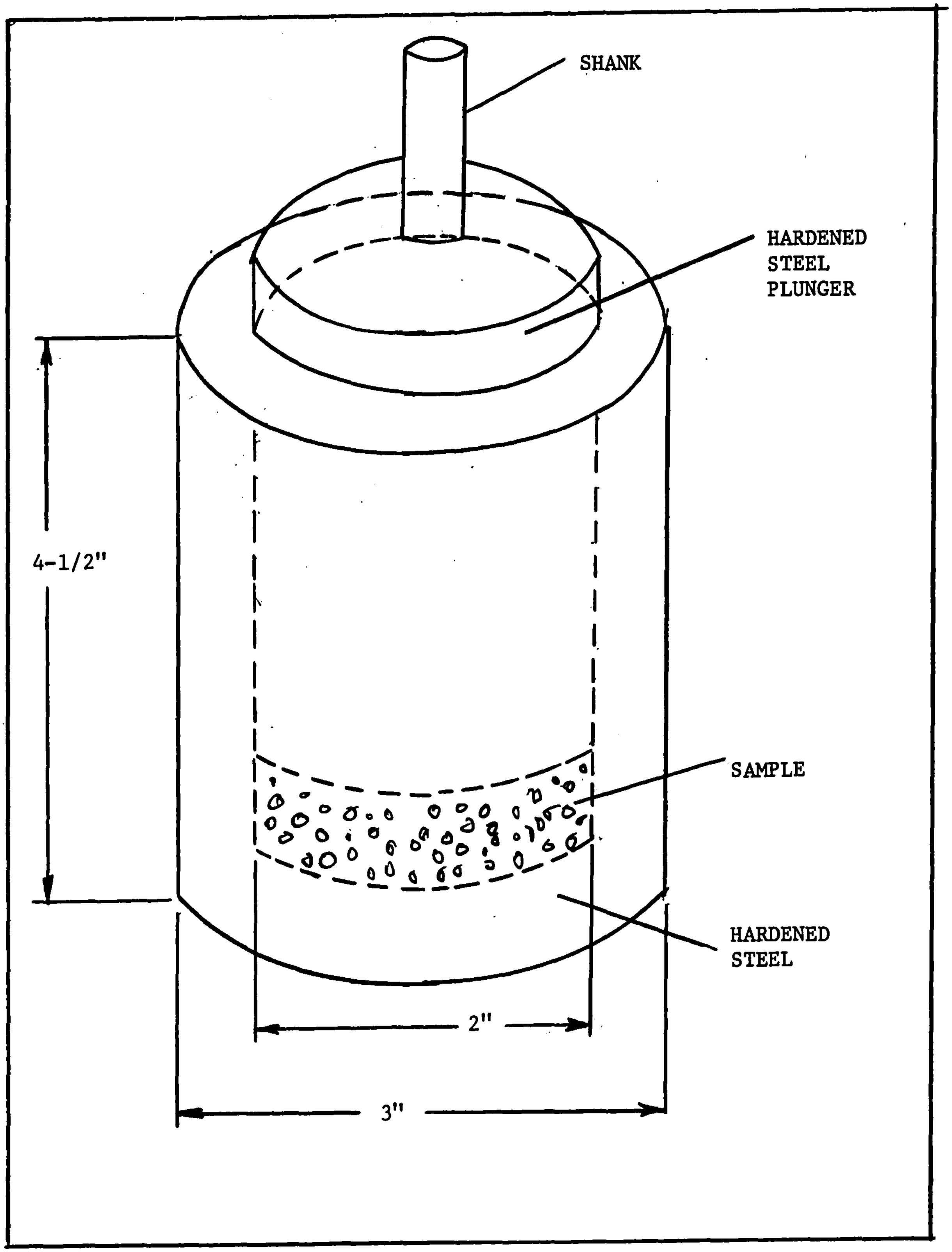

Figure 6.5 Slag Sample Crusher. The sample is crushed by striking the shank with a hammer.

The technique adopted was to determine the amount of metallic iron by dissolution in a bromine and methanol solution, then to analyze the precipitate in the Leco Carbon Analyzer for carbon. The applicability of this chemical analysis method to mixtures of iron and its oxides was investigated by Kinson, Dickeson, and Belcher[59].

A similar procedure to that of Kinson, Dickeson and Belcher was used to analyze the emulsion samples. The crushed sample was first transferred dry to a 250 ml Erlenmeyer flask. A 10% by volume solution of bromine in methanol was prepared by carefully adding the measured amount of methanol to the bromine in a vessel chilled by water. One hundred ml of this solution were added to the Erlenmeyer flask and covered with a watch glass.

The mixture was boiled gently on a hot-plate and then the heat was lowered so that the mixture simmered but vapour losses were low. After 1 1/2 - 2 hours of heating, more bromine solution was added to bring the volume back up to 100 ml and dissolution was continued for an additional 1 1/2-2 hours. After complete dissolution, the solution was cooled and filtered through asbestos fibers in a Gooch crucible into a 250 ml Erlenmeyer flask and the slag particles were washed with methanol.

The filtrate was boiled and the excess bromine was reduced by addition of a solution consisting of a mixture of 80 ml of 5 N hydrochloric acid and 20 ml of 75% hydroxylamine hydrochloride in water. When the reduction of bromine was complete, a 3% hydrogen peroxide solution was added until the straw colour of the chloroferrate complex developed. The solution was boiled to decompose excess hydrogen peroxide, cooled and diluted to 500 ml with distilled water.

The determination of iron was accomplished by reduction of the ferric ion to ferrous using stannous chloride. The ferrous ion was titrated in acid medium using p-Diphenylamine sulphonic acid sodium salt as indicator, which produced a colour change of colourless to purple. The titration procedure followed is according to Belcher and Nutten [56].

Carbon analysis was accomplished by first allowing the asbestos fiber filter pad to dry naturally. The fiber was carefully removed from the Gooch crucible and placed in a Leco refractory crucible. A scoop of Leco carbon free iron chip accelerator and a scoop of tin metal accelerator were added to the crucible. The sample was burned in the Leco Carbon Analyzer and the total carbon present was determined. The average carbon content of the emulsion droplets was calculated using the total carbon value from the Leco and total metallic iron from the titration analysis, i.e.,

$$\%C = \frac{wtC}{wtC + wtFe} \times 100$$

The accuracy of this method was tested on known samples consisting of mixtures of standard iron samples (National Bureau of Standards* and Leco calibration samples) and the same slag as was used in the experiments. The amount of metallic iron and its carbon content was determined according to the above procedure. The results obtained are listed in Table 6.1.

---

* U.S. Department of Commerce
National Bureau of Standards
Washington, D.C.

TABLE 6.1

Known Standard Sample	Analysis Result	Error
4.0901 gm iron	4.343 gm iron	+6.2%
.40%C	.38%C	-5.0%
.8588 gm iron	.784 gm iron	-8.7%
.60%C	.66%C	-10.0%
2.5059 gm iron	2.506 gm iron	0
2.91%C	2.86%C	-1.7%
2.7590 gm iron	2.986 gm iron	+8.2%
2.91%C	2.48%C	-14.8%
1.4301 gm iron	1.227 gm iron	-14.2%
.60%C	.558%C	-7.0%

6.4 Experimental Results High Temperature System

6.4-1 Qualitative Observations of Foam Formation and Behaviour

At the beginning of each decarburization experiment the slag was covered by a solidified crust which was observed to be quickly melted by the heat of reaction between the oxygen jet; and the iron and carbon and the slag. Once melting had occurred, the slag began to foam forming a blanket of considerable elasticity which tended to hold the gases in the bath. When the gas pressure beneath the foam became too high, due to evolution of carbon monoxide gas, the gas burst a large hole in the foam blanket as it escaped. The hole subsequently sealed itself until the gas pressure again built up. This phenomenon was observed through the oxygen jetting period.

At higher flow rates the instability of the gas cavity caused frequent ejections of molten iron and slag into the furnace atmosphere. The bursts of gas and slag cause the lance to move about its axis. The turbulence of the system at high gas flow rates is illustrated by the sequence of 16mm film frames in Figure 7.12.

Though temperature measurements were not taken during the blow it was obvious from the radiation from the crucible that temperatures rose due to the decarburizing reaction. The higher the oxygen flow rate the higher was the bath temperature rise.

The starting temperature of the hot metal was very important. It was absolutely necessary that each blow be begun at the same temperature as the rate of decarburization is temperature dependent. In attempting to find a suitable starting temperature for the range of flow rates under study it was found that a combination of high starting temperature (>1350°C) and high flow rate

6.4 Experimental Results High Temperature System

6.4-1 Qualitative Observations of Foam Formation and Behaviour

At the beginning of each decarburization experiment the slag was covered by a solidified crust which was observed to be quickly melted by the heat of reaction between the oxygen jet; and the iron and carbon and the slag. Once melting had occurred, the slag began to foam forming a blanket of considerable elasticity which tended to hold the gases in the bath. When the gas pressure beneath the foam became too high, due to evolution of carbon monoxide gas, the gas burst a large hole in the foam blanket as it escaped. The hole subsequently sealed itself until the gas pressure again built up. This phenomenon was observed through the oxygen jetting period.

At higher flow rates the instability of the gas cavity caused frequent ejections of molten iron and slag into the furnace atmosphere. The bursts of gas and slag cause the lance to move about its axis. The turbulence of the system at high gas flow rates is illustrated by the sequence of 16mm film frames in Figure 7.12.

Though temperature measurements were not taken during the blow it was obvious from the radiation from the crucible that temperatures rose due to the decarburizing reaction. The higher the oxygen flow rate the higher was the bath temperature rise.

The starting temperature of the hot metal was very important. It was absolutely necessary that each blow be begun at the same temperature as the rate of decarburization is temperature dependent. In attempting to find a suitable starting temperature for the range of flow rates under study it was found that a combination of high starting temperature (>1350°C) and high flow rate

(> 1.0 SCFM) resulted in a hot fluid slag which because of the low viscosity did not foam. However, at low temperatures (<1350 °C) and low flow rate (<1.0 SCFM) the temperature was too low and the slag would not melt nor foam. A starting temperature of 1350 °C was found to best satisfy the range of flow rates between .75 SCFM and 1.25 SCFM.

6.4-2 The Effect of Lance Characteristics on Reaction Rate

Due to severe lance consumption when the lance was positioned near the slag layer, the effect of lance height on the rate of decarburization could not be effectively studied.

The principle variable in the high temperature study was gas flow rate which was varied from 0.75 SCFM to 1.125 SCFM. These flow rates are equivalent to jet velocities (at the lance tip) of 261 and 434 ft $\sec^{-1}$ (STP).

The conditions for the high temperature tests were:

Flow rate Q - .75, .875, 1.00, 1.125, 1.25 SCFM
Lance height h - 1 1/2 inch
Lance diameter - 3/32 inch
Slag depth - 1/2 inch 300 gm DOFASCO slag
Metal depth - 1 1/2 inch 15 - 17lbs Q.I.T. pig iron

The tabulated data for the above tests are given in Appendix II. The curves of carbon concentration as a function of time at varying flow rates are shown in Figures 6.6-6.9. The rate of bath decarburization versus flow rate is given in Figure 6.10. The dependence of degree of emulsification upon flow rate appears in Figure 6.11.

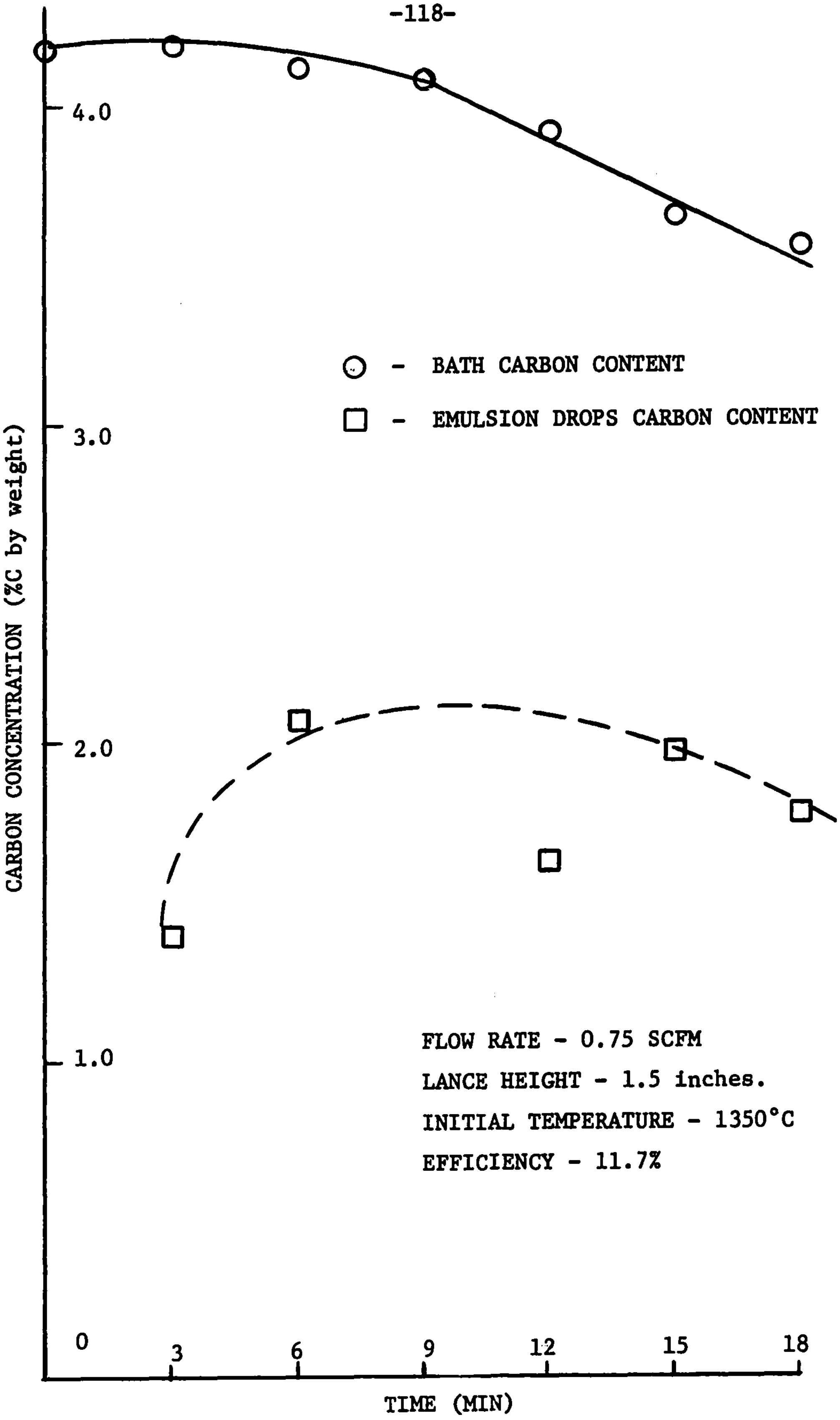

Figure 6.6 Carbon Concentration vs Time at Q=.75 SCFM.

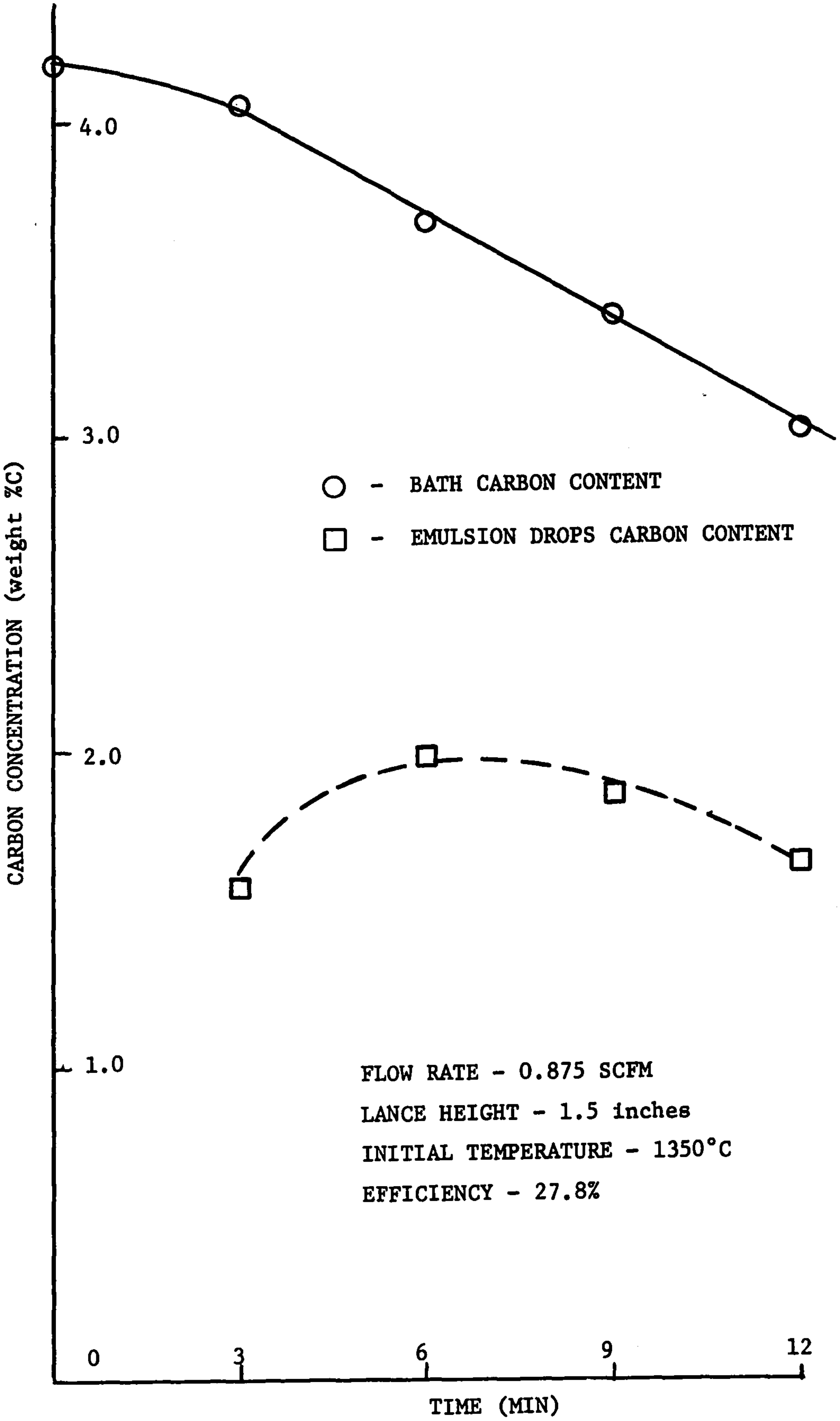

Figure 6.7 Carbon Concentration vs Time at Q=0.875 SCFM.

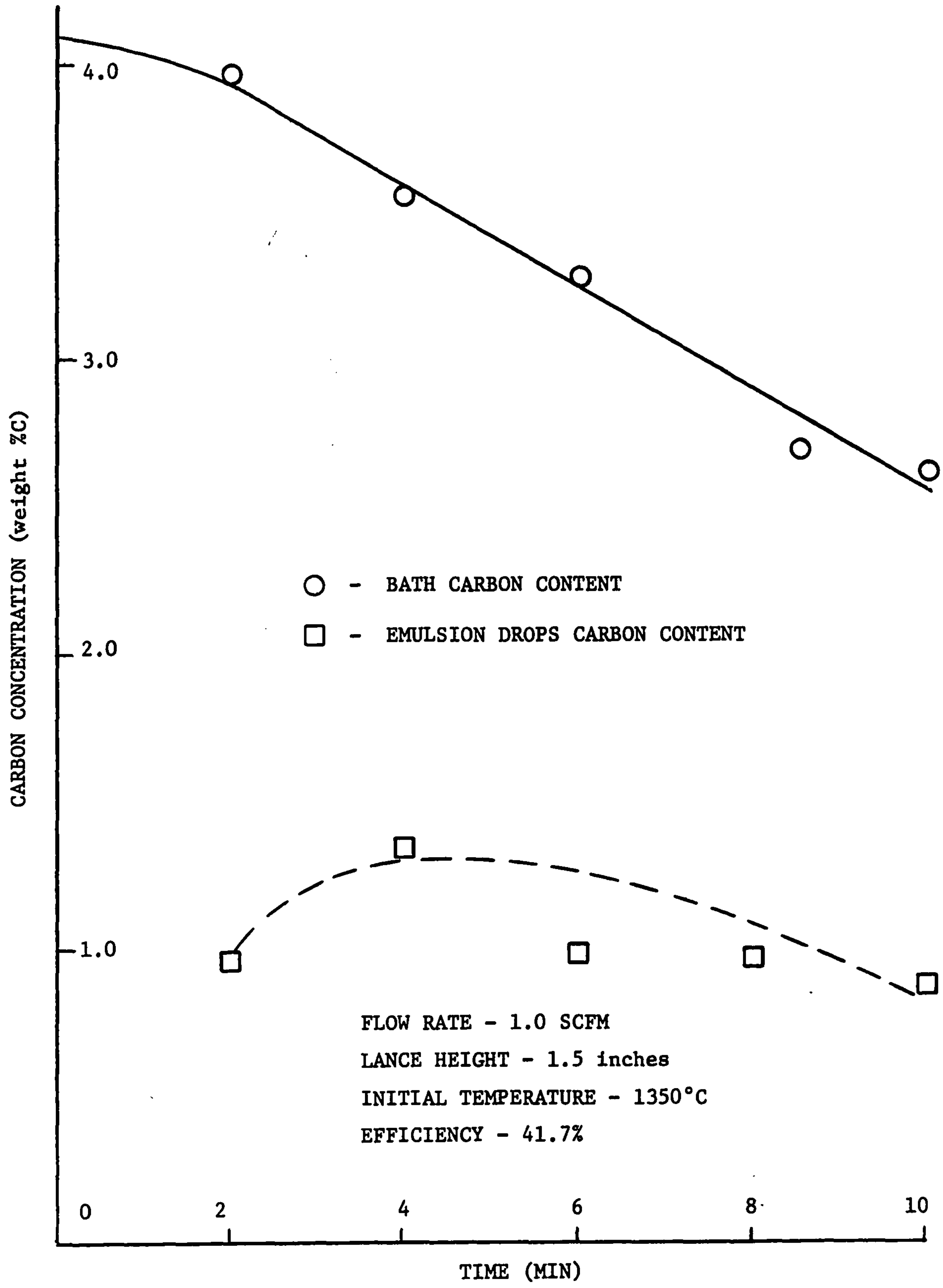

<u>Figure 6.8</u> Carbon Concentration vs Time at Q=1.0 SCFM.

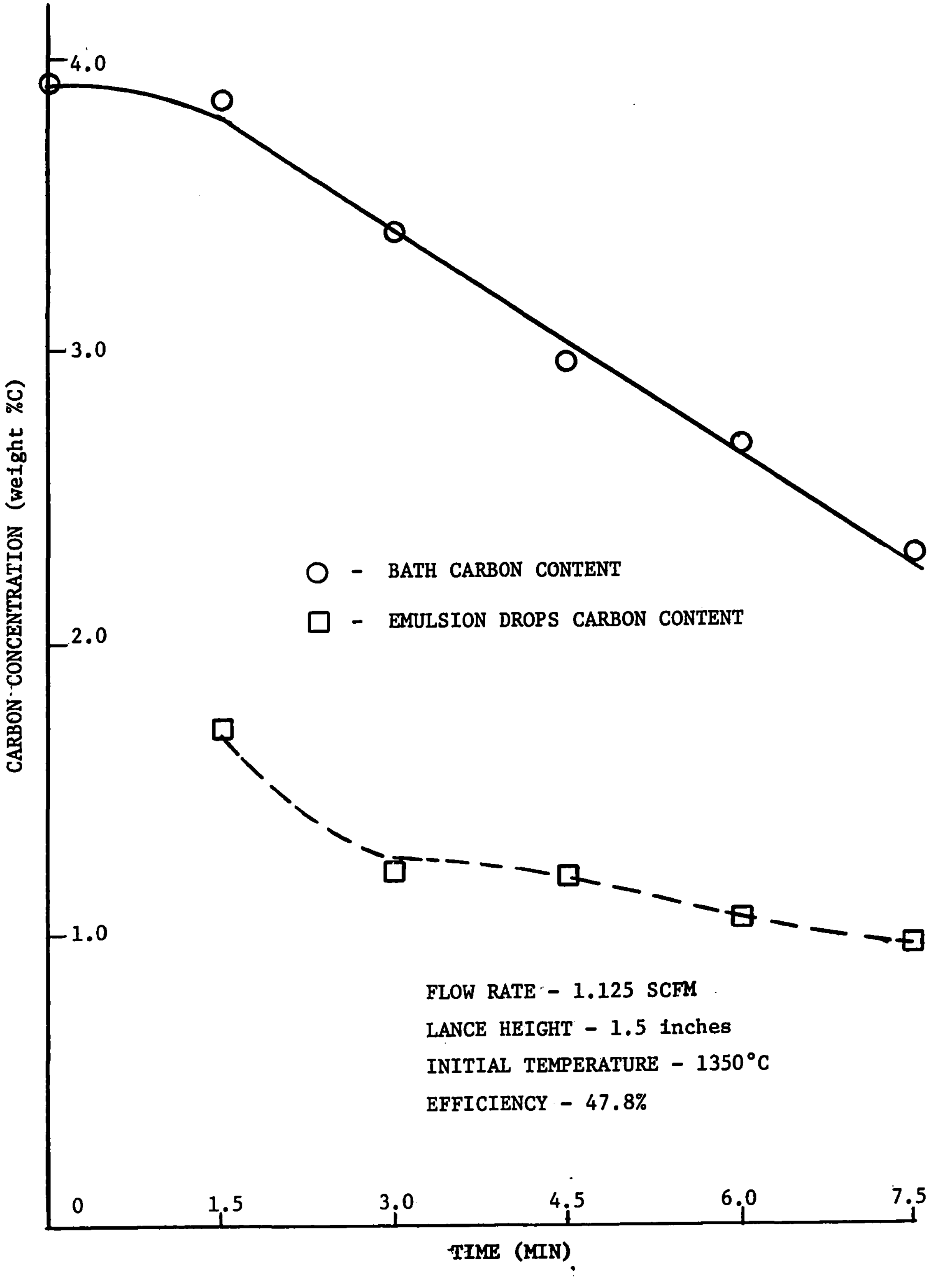

Figure 6.9 Carbon Concentration vs Time at Q=1.125 SCFM.

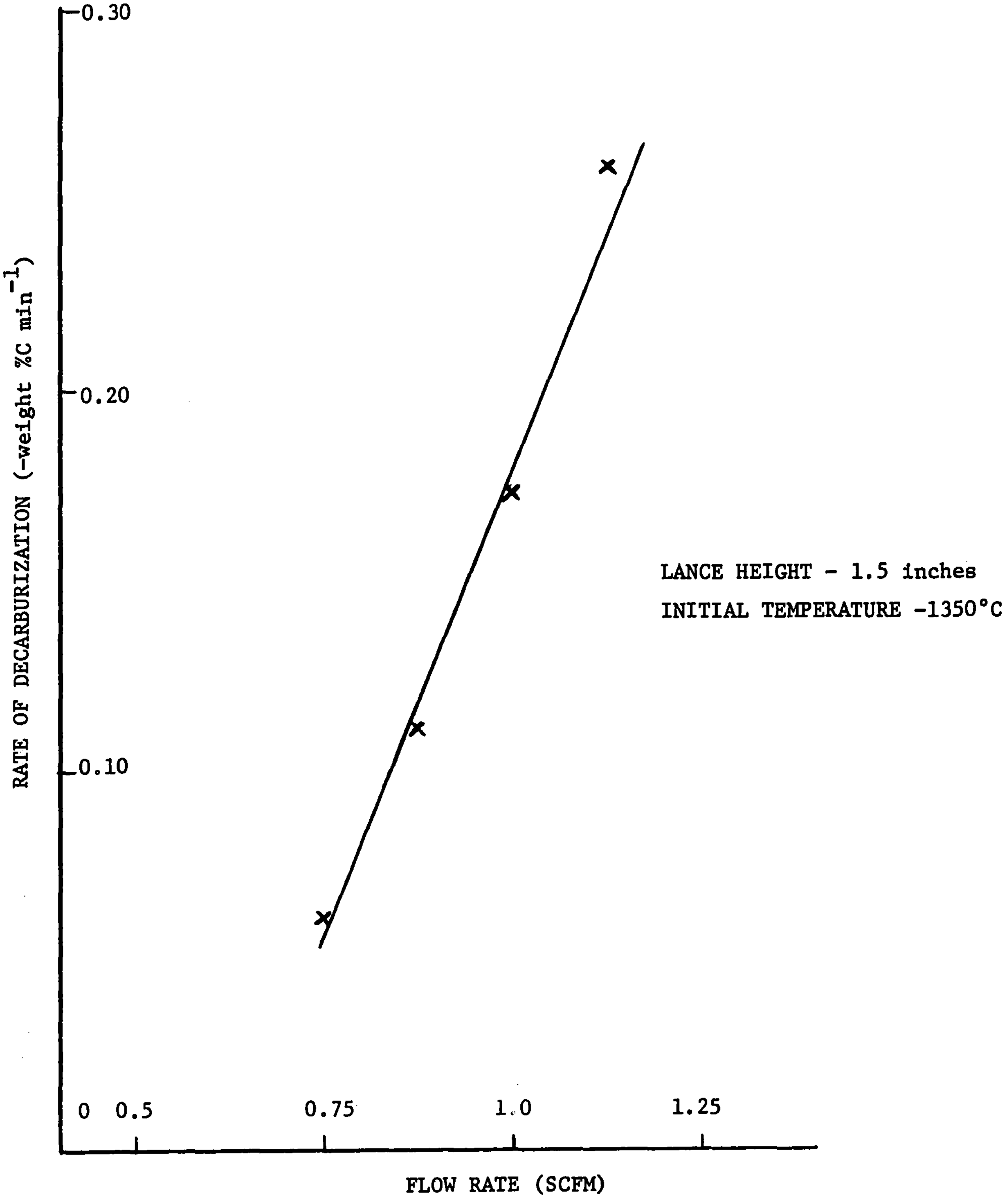

Figure 6.10 Rate of Bath Reaction vs Flow Rate.

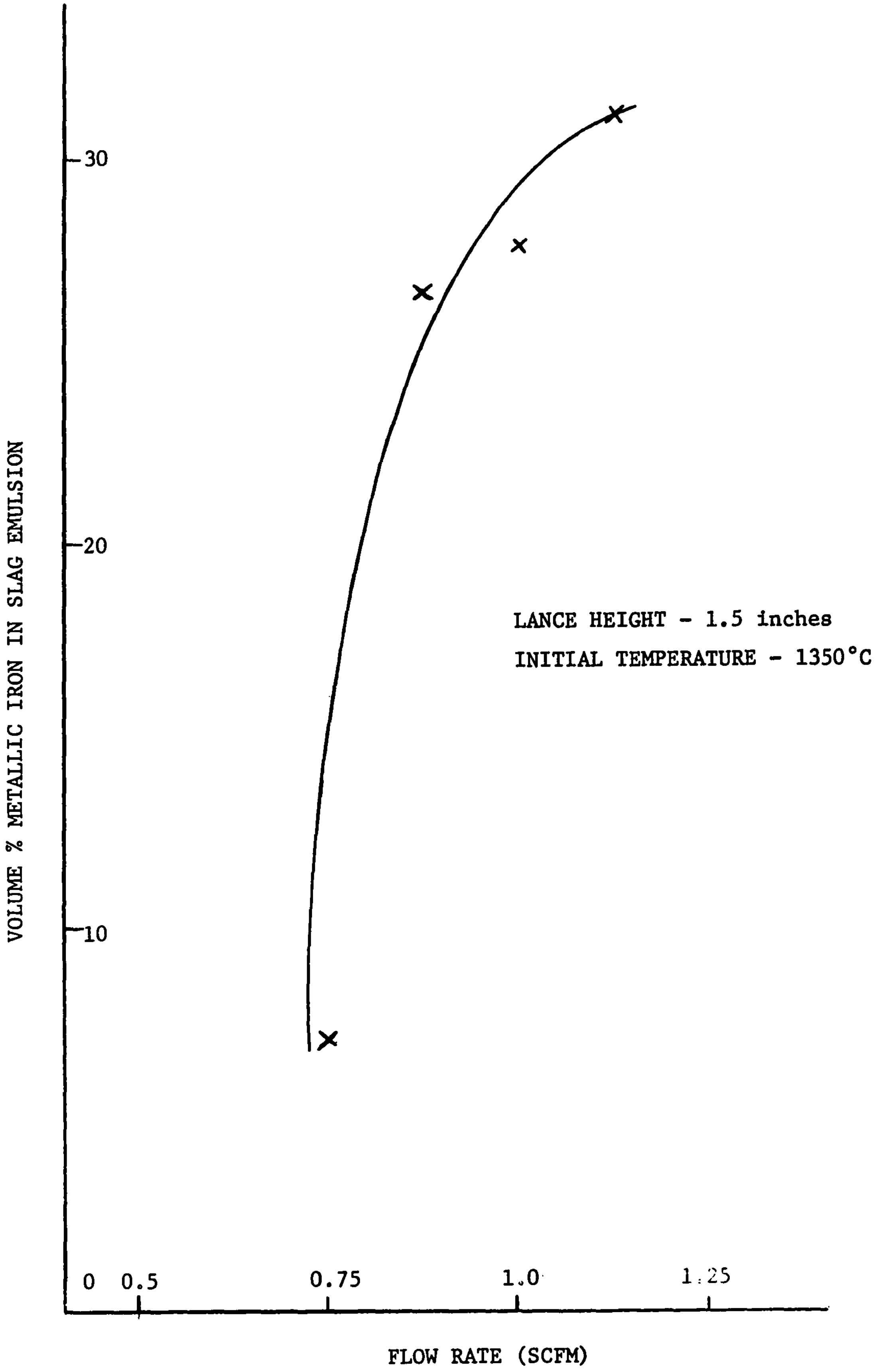

Figure 6.11 Degree of Emulsification of Iron in Slag vs Flow Rate.

CHAPTER 7

7.0 DISCUSSION

The experimental results have shown that reaction between reactive gas and liquid can take place at three locations:

a) at the liquid-gas interface of the cavity beneath the gas jet.

b) between drops ejected from the cavity and the gas above the liquids.

c) between ejected drops and reactive gas and slag of the slag foam.

It is the purpose of this section to discuss the dynamic behaviour of the experimental systems from the point of view of cavity behaviour, droplet ejection, and emulsion formation and to evaluate the rates and mechanisms of reactions in the locations as described above.

7.1 Mechanisms Explaining Reaction Rates in Room Temperature Model

The clear walls of the perspex container permitted easy inspection of the dynamic behaviour of the liquids and clearly revealed the formation of a gas cavity which penetrated through the oil layer into the lower liquid layer. The depth of this cavity was observed to increase with increasing gas flow rate and decreasing lance height (Table 5.4). The absorption of HCl at the gas cavity was observed visually when methyl red indicator added to low concentration $NaHCO_3$ solutions showed the cavity surface to be red in colour.

Quantitative results showed the rate of HCO_3^- removal to increase with increasing gas flow and decreasing lance height (Figures 5.8 and 5.14). This behavour can be explained by:

a) increased cavity gas-liquid interfacial area

b) increased rate of droplet ejection and hence increased droplet-gas surface area.

with increased flow rate and decreased lance height.

7.1-1 Cavity Behaviour

Visual observation indicated that the cavity beneath the gas jet was extremely unstable and that droplets of the lower phase were periodically ejected. A high speed (500 fps) cine-film revealed a regular oscillation of the cavity, where the gas cavity cyclically reached a maximum penetration and then returned to a minimum. It was also observed that on returning to a minimum there was an ejection of lower phase into the upper atmosphere. The behaviour of the gas cavity is shown schematically in Figure 7.1 and a droplet ejection is shown in Figure 7.2.

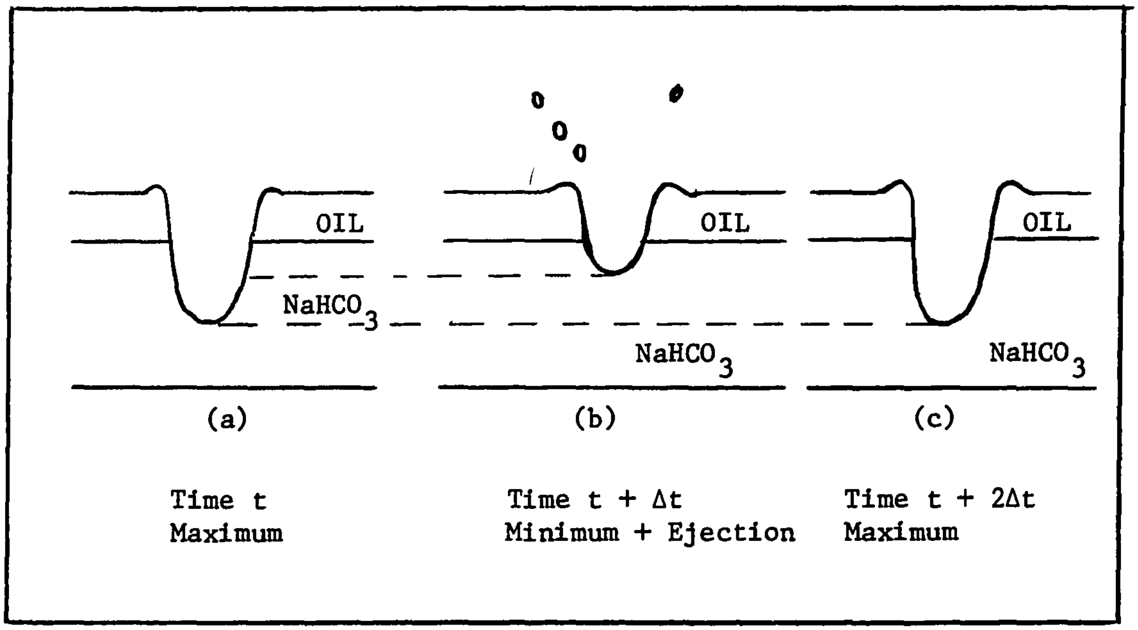

Figure 7.1 Sequence of events leading to droplets being splashed from lower liquid into atmosphere.

Figure 7.2 16 mm film frame from 500 fps cine-film showing minimum cavity penetration and accompanying droplet ejection. ($Q = 120\ cm^3 sec^{-1}$, $h = 2.5$ cm, $d = .15$ cm)

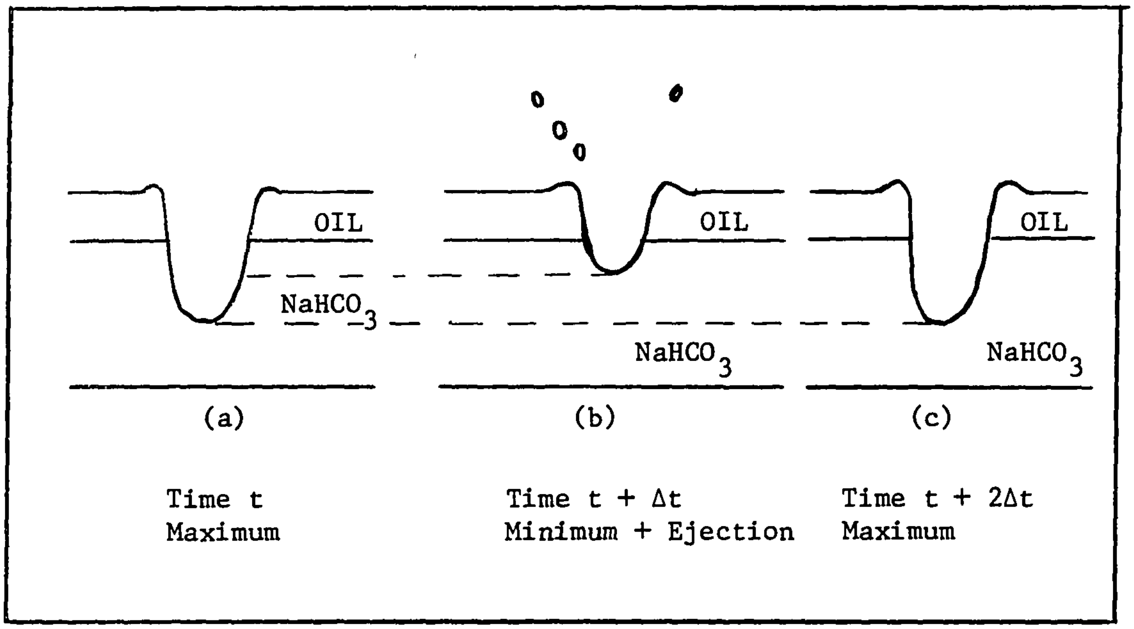

Figure 7.1 Sequence of events leading to droplets being splashed from lower liquid into atmosphere.

Figure 7.2 16 mm film frame from 500 fps cine-film showing minimum cavity penetration and accompanying droplet ejection. ($Q = 120$ cm^{3}sec^{-1}, $h = 2.5$ cm, $d = .15$ cm)

Measurements of the gas cavity displacement from the cine-film, showed, the oscillation to be sinusoidal, satisfying:

$$y = A \sin \omega t \quad . \ . \ . \ . \ . \ . \ . \ . \ . \ . \ 7.1$$

Where: y - distance of cavity bottom above maximum penetration in cm.

A - distance between maximum and minimum cavity penetration in cm.

ω - number of cavity oscillations per second, where one oscillation is counted after each maximum penetration rev sec^{-1}.

t - time in seconds.

The values obtained for A and ω were (.62 ± .1) cm and (7.5 ± 1) rev sec^{-1} respectively, for the following experimental conditions:

Flow rate - 120 $cm^3 sec^{-1}$
Lance height - 2.5 cm
Lance diameter - .15 cm
Oil depth - .84 cm (Volume 70 ml, viscosity 21 cstks)
Solution depth - 2.5 cm (volume 222 ml, 4% HCO_3^-)

Equation 7.1 becomes:

$$y = (.62 \pm .1) \sin (7.5 \pm 1)\, t \quad . \ . \ . \ . \ . \ 7.1a$$

The droplets which are ejected from the aqueous layer are at a lower HCO_3^- concentration than the bulk of the solution due to their being exposed to the oxidizing power of the gas jet. In addition the aqueous droplets rise and fall through an atmosphere of HCl, thus ejected droplets return to the aqueous layer at a lower concentration than that of the bath itself. This is illustrated by plots of $\%HCO_3^-$ in the bath and in the emulsified layer as a function of time (Figures 5.6 and 5.12).

An indication of the relative rates of liquid ejection is given by the amount of aqueous solution emulsified in the oil layer (liquid properties being held constant). Figure 5.11 and 5.17 both show, decreased lance height and increased flow rate lead to increased amounts of emulsification.

The increased rate of droplet formation is due, most likely, to an increase in distance of cavity oscillation and an increase in return gas velocity up the cavity surface.

7.1-2 Reaction Rate Mechanism

The experimental investigations with the room temperature model have shown that the mechanisms for the rate of reaction are as follows:

1) HCl gas is absorbed at the point of impingement of the gas jet after the formation of a gas cavity which extends into the aqueous phase. The rate of HCO_3^- removal depends upon the surface area of the gas cavity which is in turn dependent upon gas flow rate, lance height and lance diameter.

2) The sinusoidal oscillation of the depression results in a regular ejection of aqueous solution (already at a lower HCO_3^- concentration than the normal lower layer concentration due to HCl absorption) into the above atmosphere where it further reacts with the HCl of the atmosphere. The ejected droplets return to the aqueous layer via the oil layer.

3) The shearing and stirring action of the gas jet particularly at the gas-aqueous-oil junction causes the lower liquid to be emulsified in the upper layer in the form of small droplets. Mass transport of aqueous phase by rising bubbles may also contribute to emulsification. During their period of stay in the upper phase, the drops may react with the HCl dissolved in the oil layer and also with the HCl in the gas phase of the foam. The amount of aqueous phase dispersed into the

upper layer and the residence time depends upon the gas flow rate, lance height, oil viscosity, oil layer thickness and the surface activity of the oil.

In the following sections an attempt will be made to evaluate the relative importance of each mechanism upon the rate of reaction in the room temperature model.

7.1-3 Mechanism 1 - Gas Absorption at the Gas Cavity

A Cavity Shape and Size

A mathematical interpretation of the dynamic behaviour of the jet cavity can be obtained by considering that the depth of the cavity is determined by a balance between the kinetic energy of the gas jet and the potential energy of the liquid medium. The velocity of the gas stream as it leaves the lance is given by:

$$v_m = \frac{4}{\pi}\frac{Q}{d^2} \quad \ldots\ldots\ldots\ldots\ldots \quad 7.2$$

Where: v_m - velocity at lance tip cm $\sec^{-1}$.

Q - gas flow rate $cm^3 \sec^{-1}$.

d - lance diameter cm.

The decay in center-line velocity of the gas jet is given as [11].

$$\frac{v_x}{v} = K \frac{d}{x} \quad \ldots\ldots\ldots\ldots\ldots \quad 7.3$$

Where: v_x - center-line velocity at a distance x cm from the lance tip cm $\sec^{-1}$.

K - constant $= 8.6$ at $Re \sim 10^4$.

Referring to Figure 7.3, a stagnation pressure analysis is applied at point O where the center-line velocity is reduced to zero.

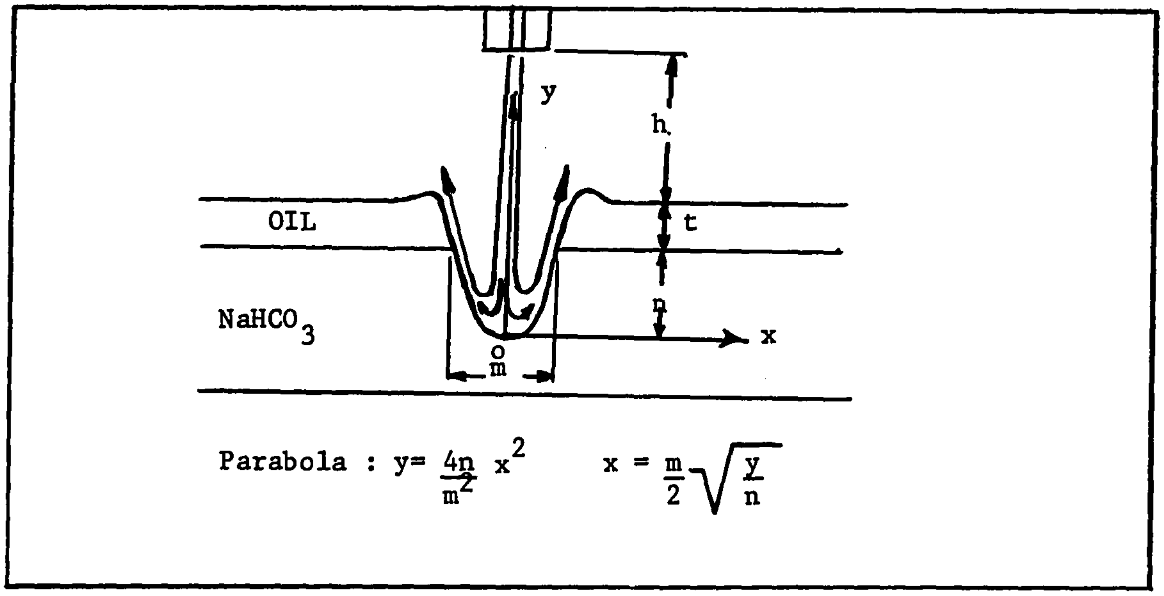

Figure 7.3 Schematic diagram of cavity, showing stagnation point O.

$$\rho_s gt+\rho_m gn = 1/2\rho_g v_o^2 \quad . \ . \ . \ . \ . \ . \ . \ . \ . \ . \ . \ . \quad 7.4$$

Velocity v_o is given by Equations 7.2 and 7.3 with $x = h+t+n$:

$$v_o = \frac{34.4 \ Q}{\pi d(h+t+n)} \quad . \ . \ . \ . \ . \ . \ . \ . \ . \ . \ . \ . \ . \ . \quad 7.5$$

Substituting Equation 7.5 into 7.4 yields:

$$\rho_s gt+\rho_m gn = 1/2 \ \rho_g \left(\frac{34.4Q}{\pi d(h+t+n)} \right)^2 \quad . \ . \ . \ . \ . \ . \ . \ . \ . \ . \quad 7.6$$

Where: ρ_s, ρ_m, ρ_g - slag, metal and gas densities in gm cm^{-3}.

g - gravity constant 981 cm sec^{-2}.

t - thickness of slag layer in cm.

n - depth of cavity penetration into lower liquid in cm.

Equation 7.6 was solved with the help of an IBM 360-50 computer. Values of n calculated from Equation 7.6 are compared with experimentally observed maximum cavity depressions for the low temperature system in Table 7.1.

TABLE 7.1

Flow Rate Q (cm^3 sec^{-1})	Lance Height h (cm)	Measured cavity diameter m (cm)	Measured cavity depth n (cm)	Calculated cavity depth n (cm)	Error %
100	3.5	1.10	1.054	0.884	-16.1
100	3.0	1.20	1.238	1.082	-12.6
100	2.5	1.20	1.408	1.302	-7.5
100	2.0	1.40	1.579	1.544	-2.2
100	1.5	1.50	1.789	1.807	+1.0
120	2.5	1.50	1.935	1.722	-11.0
110	2.5	1.30	1.589	1.514	-4.7
100	2.5	1.20	1.336	1.302	-2.5
90	2.5	1.10	0.901	1.086	+20.5

B Surface Area of Gas Cavity

One of the important factors determining the rate of gas-liquid reaction is the area of the jet cavity, calculation of which requires values for bath cavity depth (n) and cavity width (m). Since only n has been calculated from first principles (Equation 7.6), a value of m must be assumed, and is taken to be equal to n as indicated by Table 7.1.

In the calculation of surface area of the gas cavity, its shape can be assumed to be an ellipse of revolution or a parabola of revolution. Wakelin[11] used a parabola of revolution to approximate the form of the gas cavity and showed that areas calculated according to Equation 7.7 yielded areas in error by about 5% (the calculated area being smaller). Figure 7.4 illustrates the terms used in Equation 7.7.

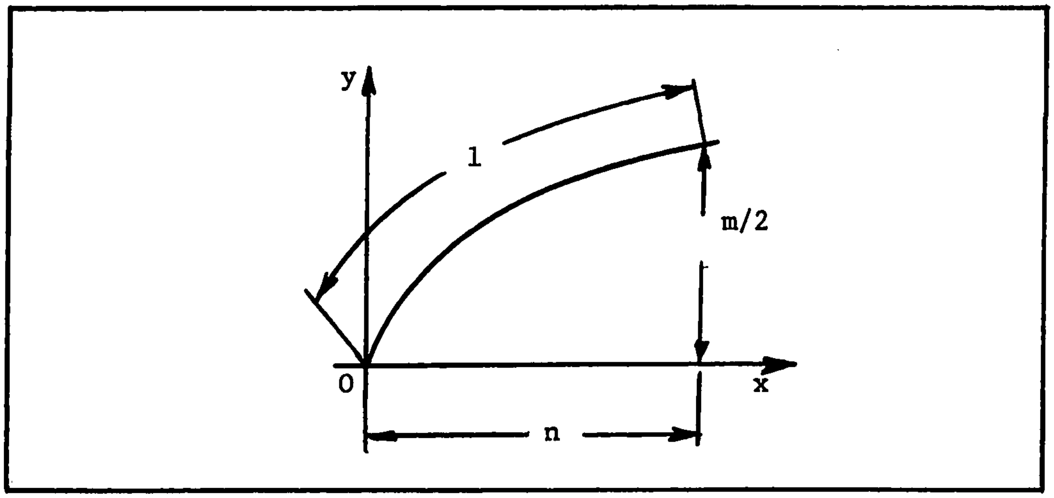

Figure 7.4 Criteria defining a parabola.

$$A = \frac{\pi m^4}{96n^2} \left[\left(1 + \frac{16n^2}{m^2}\right) - 1 \right] \quad . \; . \; . \; . \; . \; . \; . \quad 7.7$$

The equation defining the length of the arc of a parabola is given by Equation 7.8.

$$l = 1/2\sqrt{4n^2 + m^2/4} + \frac{m^2}{16n} \ln \frac{2n + \sqrt{4n^2 + m^2/4}}{m/2} \quad . \; . \quad 7.8$$

The equation defining the volume of a paraboloid of revolution is:

$$V = 1/8\pi m^2 n \quad . \; . \; . \; . \; . \; . \; . \; . \; . \; . \; . \; . \quad 7.9$$

C. Reaction Rate at the Cavity

Prediction of the size of the gas cavity permits estimation of the surface area present for mass transfer between the aqueous liquid and the absorbing gas. The rate of mass transfer can be estimated on the basis of the Higbie or penetration model. In the model it is assumed that an element of the aqueous solution approaches the cavity at position A (Figure 7.5) and that the element is drawn up the surface of the cavity by the upward deflected gas jet. The packet of fluid at position A begins to lose dissolved HCO_3^- by chemical reaction with the gas jet until it reaches position B, as shown in Figure 7.5.

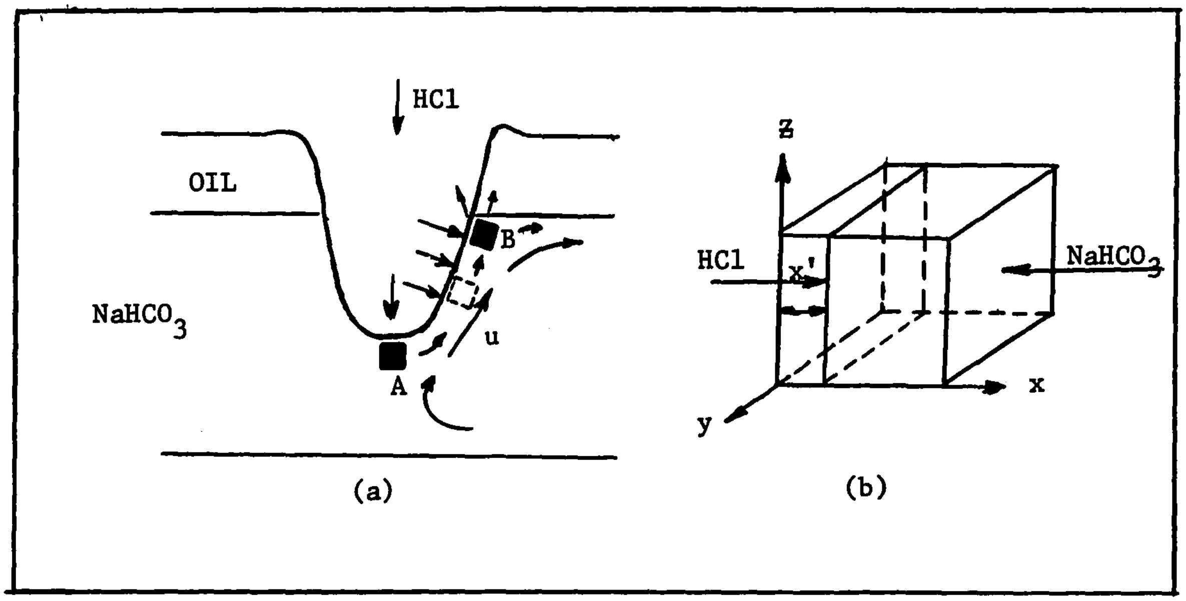

Figure 7.5 (a) Sketch showing motion of packet of fluid at velocity u

(b) An expanded packet of fluid is shown.

The reaction scheme is assumed to be as follows:

a) HCl is absorbed into the aqueous solution through the gas-liquid interface, x=0. HCO_3^- ions diffuse toward the surface from the bulk of the aqueous solution.

b) HCl and $NaHCO_3$ react instantaneously to completely destroy the reactants.

The HCl - Ar gas mixture is assumed to be perfectly mixed in the turbulent gas jet. The effect of diffusion in the gas phase is discussed in detail in Section D.

The situation of HCl diffusion outward from the interface and HCO_3^- diffusion outward plus instantaneous reaction between the diffusion species leads to the condition of a plane parallel to the liquid-gas interface at a distance x' from it. This plane separates the region containing no HCl from that containing no $NaHCO_3$. The distance x' is a function of t, since the boundary between HCl and $NaHCO_3$ retreats as $NaHCO_3$ is used up in the chemical reaction. The HCO_3^- ion in the HCl region is converted into H_2CO_3 which decomposes to dissolved CO_2.

The differential equations describing the system are:[60]

$$\frac{\partial C_o}{\partial t} = D_o \frac{\partial^2 C_o}{\partial x^2} \quad \ldots\ldots \quad 0<x<x'(t) \quad \ldots \quad 7.10$$

$$\frac{\partial C_c}{\partial t} = D_c \frac{\partial^2 C_c}{\partial x^2} \quad \ldots\ldots \quad x'(t)<x<\infty \quad \ldots \quad 7.11$$

c refers to HCO_3^- and o refers to HCl.

The solutions to the above differential equations are:

$$\frac{C_o}{C_{oi}} = b1 + b2 \operatorname{erf} \frac{x}{\sqrt{4D_o t}} \quad \ldots\ldots\ldots \quad 7.12$$

$$\frac{C_c}{C_{ci}} = b3 + b4 \operatorname{erf} \frac{x}{\sqrt{4D_c t}} \quad \ldots\ldots\ldots \quad 7.13$$

Where: C_{oi} is the interfacial liquid phase concentration of HCl and C_{ci} is the initial bulk concentration of HCO_3^-.

At the reaction surface Equation 7.12 reduces to

$$C_c(x',t) = 0 \quad \ldots\ldots\ldots\ldots\ldots \quad 7.14$$

The perfect differential of Equation 7.14 gives:

$$dC_c = 0 = \left(\frac{\partial C_c}{\partial x}\right)_t dx' + \left(\frac{\partial C_c}{\partial t}\right)_{x'} dt \quad \ldots\ldots \quad 7.15$$

the solution of which is

$$\frac{dx'}{dt} = \frac{-(\partial C_c/\partial t)_{x'}}{(\partial C_c/\partial x')_t} \quad \ldots\ldots\ldots\ldots \quad 7.16$$

Substituting Equation 7.12 into 7.16 yields:

$$\frac{dx'}{dt} = \frac{x'}{2t} \quad \ldots\ldots\ldots\ldots\ldots \quad 7.17$$

which integrates to:

$$x' = \sqrt{4at} \quad \ldots\ldots\ldots\ldots\ldots \quad 7.18$$

where 'a' is an integration constant. A total of five constants a, b1, b2, b3, b4 must be determined. The following initial and boundary conditions are used:

I.C.	at	$t=0$	$C_c=C_{ci}$	7.19
B.C.1	at	$x=0$	$C_o=C_{oi}$	7.20
B.C.2	at	$x=x'\ (t)$	$C_o=0$	7.21
B.C.3	at	$x=x'\ (t)$	$C_c=0$	7.22
B.C.4	at	$x=x'\ (t)$	$-D_o\frac{\partial C_o}{\partial x} = D_c\frac{\partial C_c}{\partial x}$	7.23

The last boundary condition is the stoichiometric condition that one mole of HCl consumes one mole of $NaHCO_3$. The five boundary conditions allow us to get the five integration constants. The constant a is given implicitly by:

$$1-\mathrm{erf}\sqrt{\frac{a}{D_c}} = \frac{C_{ci}}{C_{oi}}\sqrt{\frac{D_c}{D_o}}\ \mathrm{erf}\sqrt{\frac{a}{D_o}}\ \exp\left(\frac{a}{D_o} - \frac{a}{D_c}\right) \quad \ldots\ldots \quad 7.24$$

The remaining constants are:

$$b1 = 1 \quad \ldots\ldots\ldots\ldots\ldots \quad 7.25$$

$$b2 = -\left(\mathrm{erf}\sqrt{\frac{a}{D_o}}\right)^{-1} \quad \ldots\ldots\ldots\ldots \quad 7.26$$

$$b3 = 1-\left(1-\mathrm{erf}\sqrt{\frac{a}{D_c}}\right)^{-1} \quad \ldots\ldots\ldots\ldots \quad 7.27$$

$$b4 = \left(1-\mathrm{erf}\sqrt{\frac{a}{D_c}}\right)^{-1} \quad \ldots\ldots\ldots\ldots \quad 7.28$$

The instantaneous rate of mass transfer at the interface is calculated from:

$$\dot{N}''_o\Big|_{x=o} = -D_o \frac{\partial C_o}{\partial x}\Big|_{x=o} \quad \text{. . . . .} \quad 7.29$$

$$= \frac{C_{oi}}{\text{erf}\sqrt{\frac{a}{D_o}}}\sqrt{\frac{D_o}{\pi t}} \quad \text{. . . . .} \quad 7.30$$

The average rate of absorption up to time t is

$$\dot{N}''_o \text{ av.} = \frac{1}{t}\int_o^t \dot{N}''_o dt$$

$$= \frac{2\ C_{oi}}{\text{erf}\sqrt{\frac{a}{D_o}}}\sqrt{\frac{D_o}{\pi t}} \quad \text{. . . . .} \quad 7.31$$

It is interesting to note that the value of $\text{erf}\sqrt{\frac{a}{D_o}}$ works out to be very nearly 1 and hence Equation 7.31 reduces to:

$$\dot{N}''_{o,av.} = 2\ C_{oi}\sqrt{\frac{D_o}{\pi t}} \quad \text{. . . . .} \quad 7.32$$

which is the same rate of absorption as predicted by the unsteady state diffusion into an infinite sheet with zero initial concentration of HCl in the liquid[61]. The time of exposure of the packet of fluid in travelling from the bottom of the gas cavity to the liquid-liquid interface is given by:

$$t = \frac{1}{u} \quad \text{. . . . .} \quad 7.33$$

Where: u - fluid velocity next to crater in cm sec^{-1} (fluid velocities in the region of the crater have been taken from the work of Wakelin[62]).

1 - one half the length of the arc of a parabola in cm given by Equation 7.8.

$$1 = 1/2\sqrt{4n^2+m^2/4} + \frac{m^2}{16n} \ln \frac{2n+\sqrt{4n^2+m^2/4}}{m/2} \quad . \quad . \quad . \quad 7.8$$

The total surface area of exposed lower liquid is given by Equation 7.7:

$$A = \frac{\pi m^4}{96n^2}\left[\left(1 + \frac{16n^2}{m^2} \right) - 1 \right] \quad . \quad . \quad . \quad . \quad . \quad . \quad . \quad . \quad 7.7$$

Combining Equations 7.32, 7.8, 7.7 gives an average rate of HCO_3^- removal at the gas cavity by HCl absorption. Table 7.2 lists the concentrations, and constants which have been used to calculate the molar flux. Table 7.2 also shows the calculated rates of decarburization as compared to the measured rates.

TABLE 7.2

$D_o = 4.0 \times 10^{-5}\ cm^2 sec^{-1}$ [54]

$D_c = 1.5 \times 10^{-5}\ cm^2 sec^{-1}$ [54]

$a = 8.36 \times 10^{-3}\ cm^2 sec^{-1}$
(integration constant)

$C_{oi} = 0.001$ moles cm^{-3}
(gas 10%HCl - 90% Ar)

$C_{ci} = 6.8 \times 10^{-4}$ moles cm^{-3}

$U \approx 10\ cm\ sec^{-1}$

Bath Volume = 222 cm^3

h	Q	A	l	t	x^1	$\dot{N}''_o$	% HCO_3^- min^{-1}		Calculated % of Measured
cm	$cm^3 sec^{-1}$	cm^2	cm	sec	cm	$\frac{moles}{cm^2\ sec}$	Calculated	Measured	
3.5	100	2.64	1.24	.124	.064	2.03×10^{-5}	.085	.216	39.4
3.0	100	3.35	1.43	.143	.069	1.89	.100	.313	31.9
2.5	100	3.75	1.57	.157	.072	1.80	.107	.417	25.7
2.0	100	4.93	1.78	.178	.077	1.69	.132	.622	21.2
1.5	100	5.94	1.99	.199	.082	1.60	.151	.765	19.7
2.5	120	6.38	2.12	.212	.084	1.55×10^{-5}	.157	.898	17.5
2.5	110	4.56	1.76	.176	.077	1.70	.123	.665	18.5
2.5	100	3.58	1.51	.151	.071	1.84	.104	.417	24.9
2.5	90	2.31	1.12	.112	.061	2.13	.078	.050	156.0

When the packet of fluid reaches position B in Figure 7.5 it takes one of three possible routes: it is ejected into the above atmosphere, it is stirred into the slag as emulsion droplets or it continues in the aqueous phase along the oil-water interface. Nucleation of dissolved CO_2 occurs at the foamy oil-water interface and on small oil particles ejected into the aqueous layer. An illustration of this occurrence is given in Figure 7.6. The region immediately surrounding the gas cavity was high in dissolved HCl as shown by the red colour of the gas cavity in a colour film taken of the system with methyl red indicator added. No CO_2 bubbles were observed in this region surrounding the cavity.

According to Table 7.2 the mechanism of gas absorption at the gas cavity represents about 25% of the total measured reaction rate. Noteable deviations occur at conditions of small cavity size and activity (low flow rate and/or high lance height) where reaction rates according to HCl gas absorption at the crater account for an increasing portion of the reaction mechanism. This was dramatically illustrated by the experiment at Q - 90 $cm^3 sec^{-1}$ and h - 2.5 cm where virtually no splashing was observed and reaction rate is completely governed by HCl absorption at the cavity.

In most cases HCl absorption at the gas cavity does not adequately explain the rate determining step in the room temperature model, suggesting the importance of another mechanism at conditions of high cavity activity.

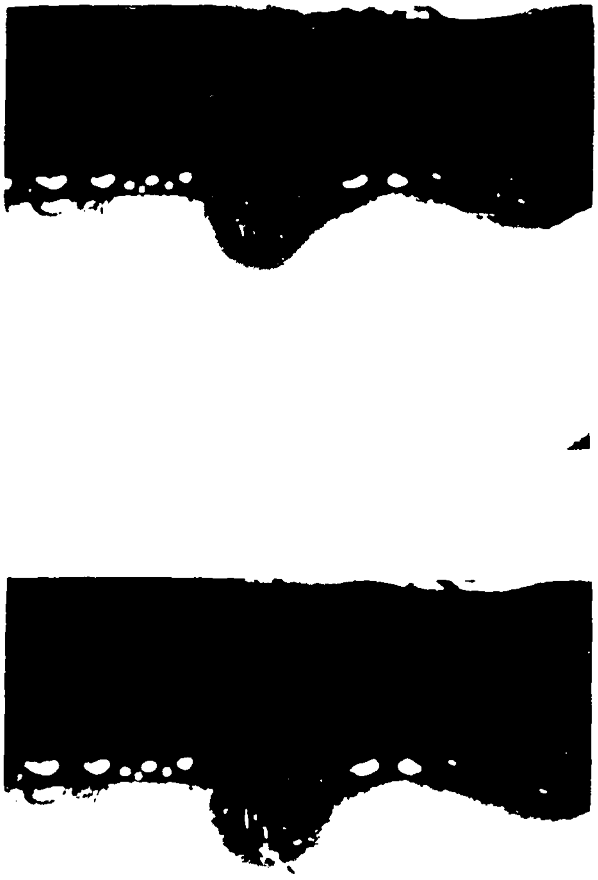

Figure 7.6 Single frames from 500 fps film (16 mm) showing bursts of CO_2 bubbles from the interface and gas evolution in lower phase.

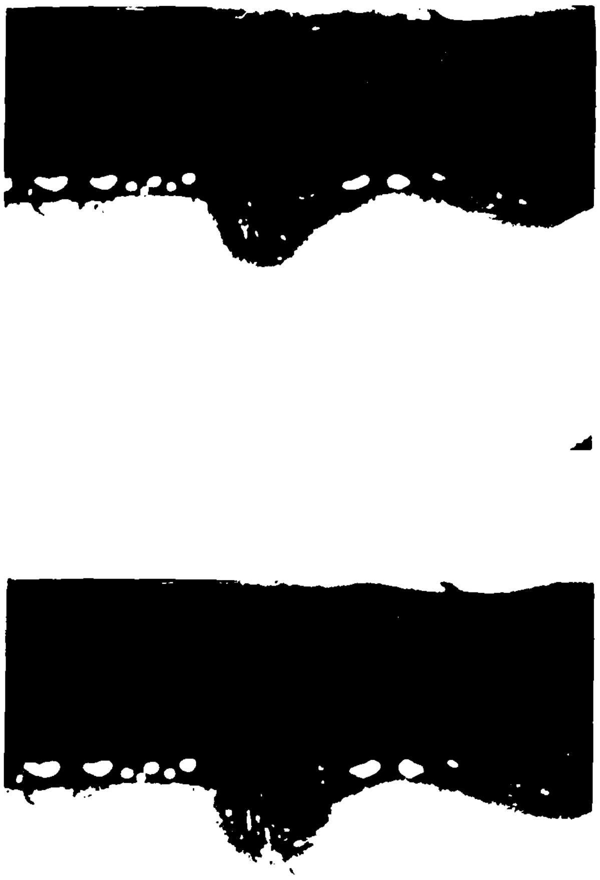

Figure 7.6 Single frames from 500 fps film (16 mm) showing bursts of CO_2 bubbles from the interface and gas evolution in lower phase.

D. Effect of Diffusion in the Gas Phase

In the derivation of mechanism 1 the gas phase was assumed to be completely mixed due to the turbulence of the gas flow. A derivation considering diffusion of HCl in the Ar-HCl mixture is now considered. Figure 7.7 shows the concentrations involved.

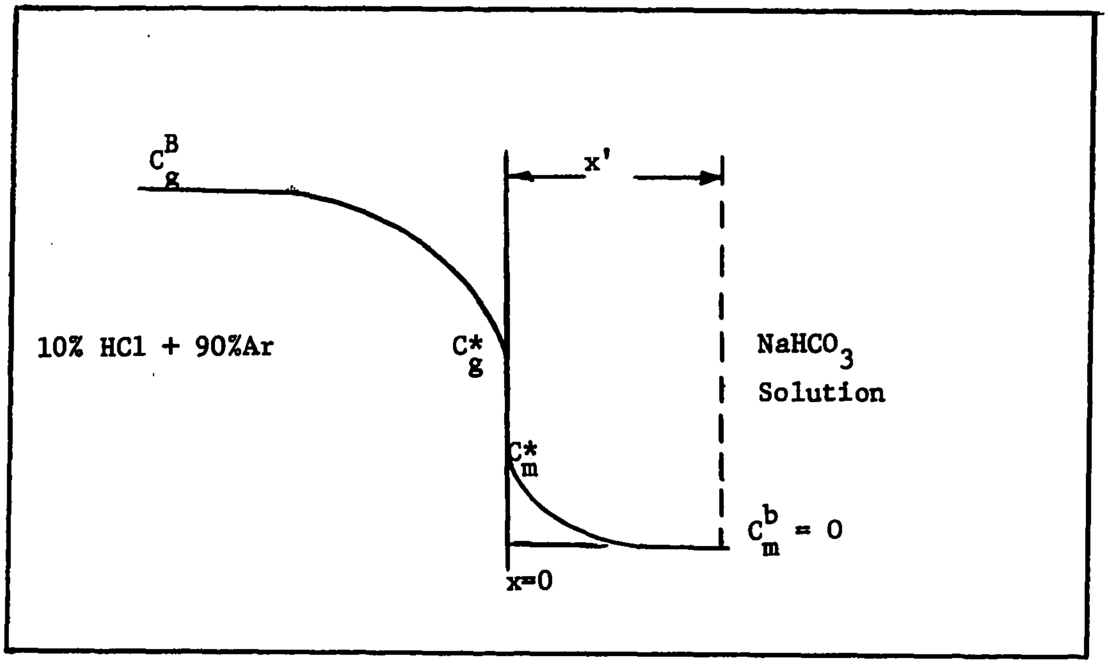

Figure 7.7 Effect of diffusion in gas phase on rate of HCl absorption.

The gas concentrations are:

$$C_g^* = \frac{k}{2.45\text{x}10^4} \quad \text{moles cm}^{-3} \quad = \quad .407\text{x}10^{-4}k$$

$$C_g^B = \frac{.1}{2.45\text{x}10^4} \quad \text{moles cm}^{-3} \quad = \quad .407\text{x}10^{-5}$$

Where k represents the mole fraction of HCl in the gas mixture at the interface.

The metal concentrations are:

$$C_m^* = .01k \text{ moles cm}^{-3}$$

$$C_m^b = 0$$

The equations describing the system are of the following form:

$$C_{g,x,t} = A + B \text{ erf } \frac{x}{\sqrt{4D_g t}} \quad \ldots\ldots\ldots \quad 7.34$$

$$C_{m,x,t} = F + E \text{ erf } \frac{x}{\sqrt{4D_m t}} \quad \ldots\ldots\ldots \quad 7.35$$

The following boundary conditions apply:

B.C.1 $x=0$ $C_g = C^*_g$
B.C.2 $x=0$ $C_m = C^*_m$
B.C.3 $x=x'(t)$ $C_m = C^b_m = 0$

B.C.4 $x= -\infty$ $C_g = C^B_g$
B.C.5 $x=0$ $-D_g \frac{\partial C_g}{\partial x} = -D_m \frac{\partial C_m}{\partial x}$
B.C.6 $t=0$ $C_m = C^b_m = 0$

The reaction interface is given in the same way as Equation 7.18 $x'(t) =$

$\sqrt{4at}$

Solving for the above boundary conditions give:

$$C_{m,x,t} = C^*_m - C^*_m \text{ erf } \frac{x}{\sqrt{4D_m t}} \quad \ldots\ldots \quad 7.34a$$

$$C_{g,x,t} = C^*_g + (C^*_g - C^B_g) \text{ erf } \frac{x}{\sqrt{4D_g t}} \quad \ldots\ldots \quad 7.35a$$

From B.C.5

$$C^*_m = \frac{D_g}{D_m} (C^B_g - C^*_g)$$

$$.01\ k = 1.45\text{x}10^2\ (.407\text{x}10^{-5} - .407\text{x}10^{-4}k)$$

$k =$ .037 mole HCl/mole gas at interface

Differentiating Equation 7.35a and using average flux.

$$\dot{N}''_{HCl} = 2\sqrt{\frac{D_g}{\pi t}}\ (C^B_g - C^*_g)$$

which for the conditions $Q = 120\ \mathrm{cm}^3\mathrm{sec}^{-1}$, $h = 2.5$ cm. ($1 = 2.12$ cm Table 7.2) becomes:

$$= 2\sqrt{\frac{.84}{\pi x.212}}\quad(4.07x10^{-6} - 4.07x10^{-5}x.037)$$

$$= 5.75x10^{-6}\qquad\frac{\text{mole HCl}}{\text{cm}^2\ \text{sec}}$$

It can be seen that in the case where the gas jet is completely stagnant, the rate of reaction in the region of the jet cavity would be reduced to approximately 1/3 the liquid controlled rate.

Conditions in the gas jet are violently turbulent, however, (Re jet $> 10^3$) and the gas phase diffusion resistance is not expected to be significant.

7.1-2 Mechanism 2 - Droplet Ejection from Gas Cavity

The ejection of liquid drops into the atmosphere was observed to occur as the depression moves from its maximum to minimum position.

The velocity in the impingement area of the depression is the main factor influencing the breakup of the liquid surface. The size of the gas cavity is important because the distance over which the shearing forces on the liquid surface act influences the critical velocity required for drop formation. The following dimensionless parameters may influence splashing:

$$\left(\frac{g\rho_1}{\gamma_1}\right)^{1/2} n_c = f\left(\frac{\rho_g}{\rho_1},\ \frac{\mu_g}{\mu_1},\ \frac{\gamma_1}{\rho_1 gh^2},\ \frac{g\mu_1^{\ 4}}{\rho_1\gamma_1^{\ 3}},\ \frac{\dot{M}}{\rho_1 gh^3}\right)$$

Where: n_c - critical depth of cavity for splashing, cm
ρ_1 - liquid density gm cm^{-3}
ρ_g - gas density gm cm^{-3}
μ_g - gas viscosity poise

μ_1 - liquid viscosity poise

γ_1 - liquid surface tension dyne cm^{-1}

h - lance height cm

$\dot{M}$ - momentum flux of gas jet dynes

The events leading to a droplet ejection can be explained by a momentary imbalance in the modified Froude Number ($\rho_g v^2/\rho_1 gl$) at the gas cavity whereupon the liquid buoyancy force causes an ejection.

It was observed that the gas cavity had a tendency to move in the horizontal direction as well as the vertical. As a consequence, buoyancy forces cause an ejection due to the apparent shift in position of the central axis of the gas jet. This is shown schematically in Figure 7.9 and in a film sequence in Figure 7.10.

If the liquids are incompressible and the position of the separating interface remains unchanged, then the volume of liquid ejected will be approximated by the shaded area in Figure 7.8(c). This volume represents the difference between gas cavity volume at maximum and minimum depths of penetration. At a flow rate of 120 $cm^3 sec^{-1}$, lance height 2.5 cm, and lance diameter .15 cm the difference between maximum and minimum cavity penetration was observed as .62(±.1) cm (Equation 7.1a). The cavity alternated between maximum and minimum penetration 7.5 (±1) times per second (Equation 7.1a).

The volume of lower phase ejected is given by:

$$V = 1/8\pi m^2 n - 1/8\pi m^2 (n-.62)$$

$$= 1/8\pi m^2 (0.62)$$

$$V = .078\pi m^2 \quad . \; . \; . \; . \; . \; . \; . \; . \; . \; . \; . \; . \; . \quad 7.36$$

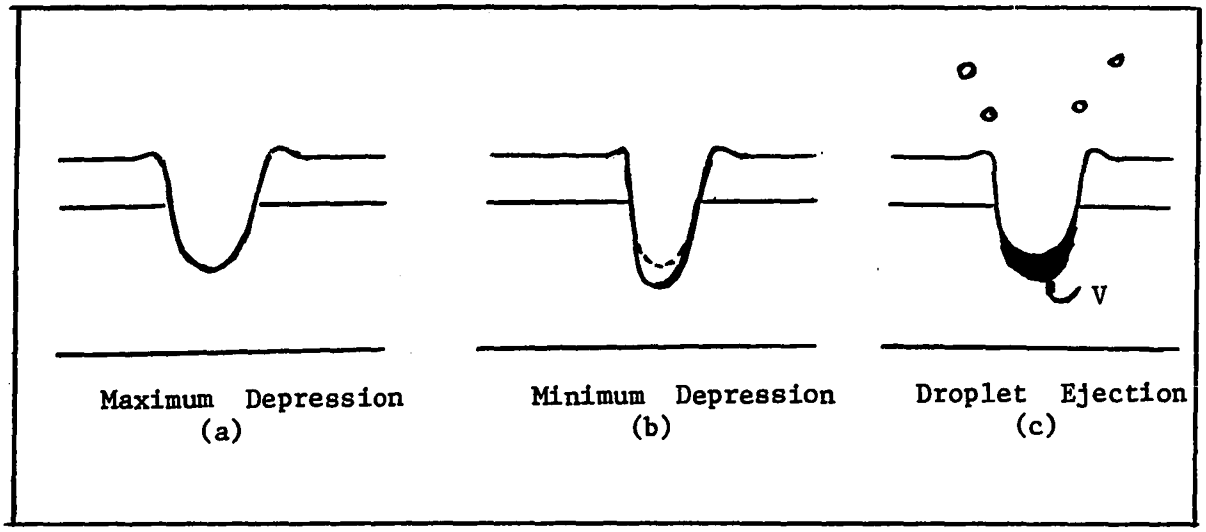

Maximum Depression
(a)

Minimum Depression
(b)

Droplet Ejection
(c)

Figure 7.8 Volume of liquid ejected at cavity minimum.

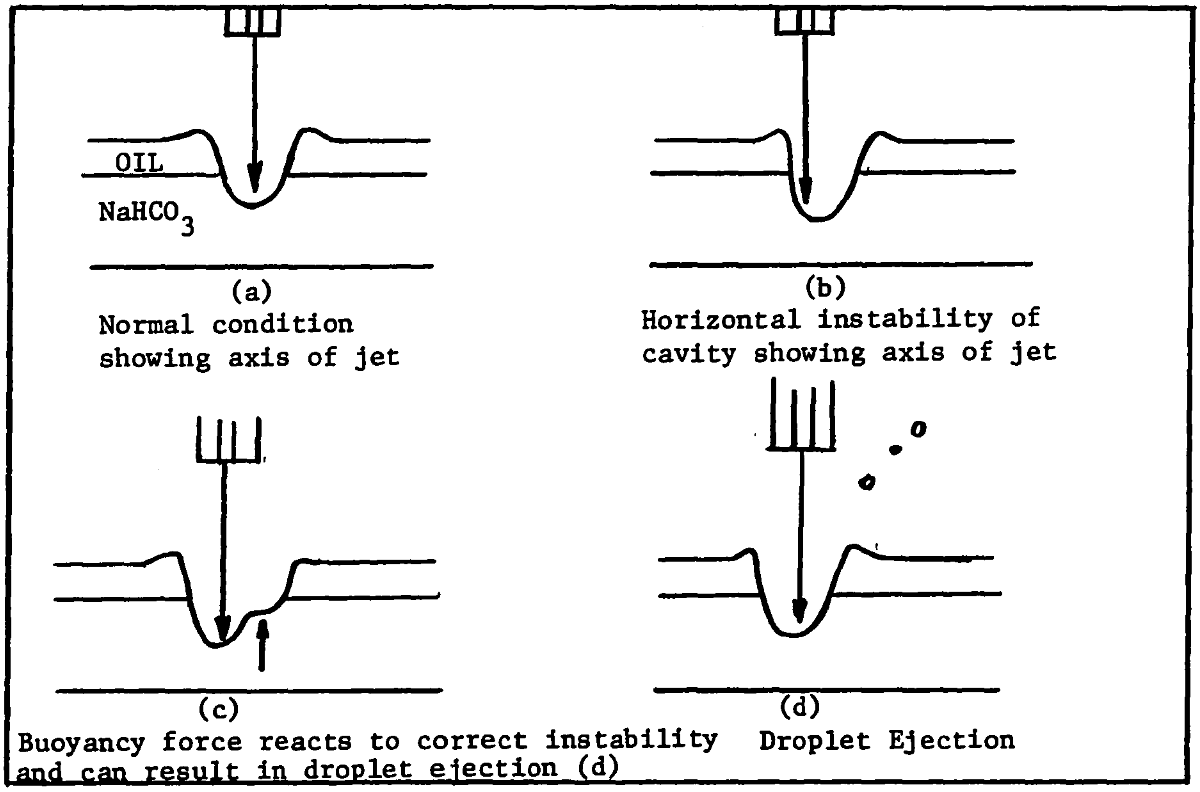

(a)
Normal condition
showing axis of jet

(b)
Horizontal instability of
cavity showing axis of jet

(c)
Buoyancy force reacts to correct instability
and can result in droplet ejection (d)

(d)
Droplet Ejection

Figure 7.9 Schematic showing droplet ejection due to horizontal instability of the gas cavity.

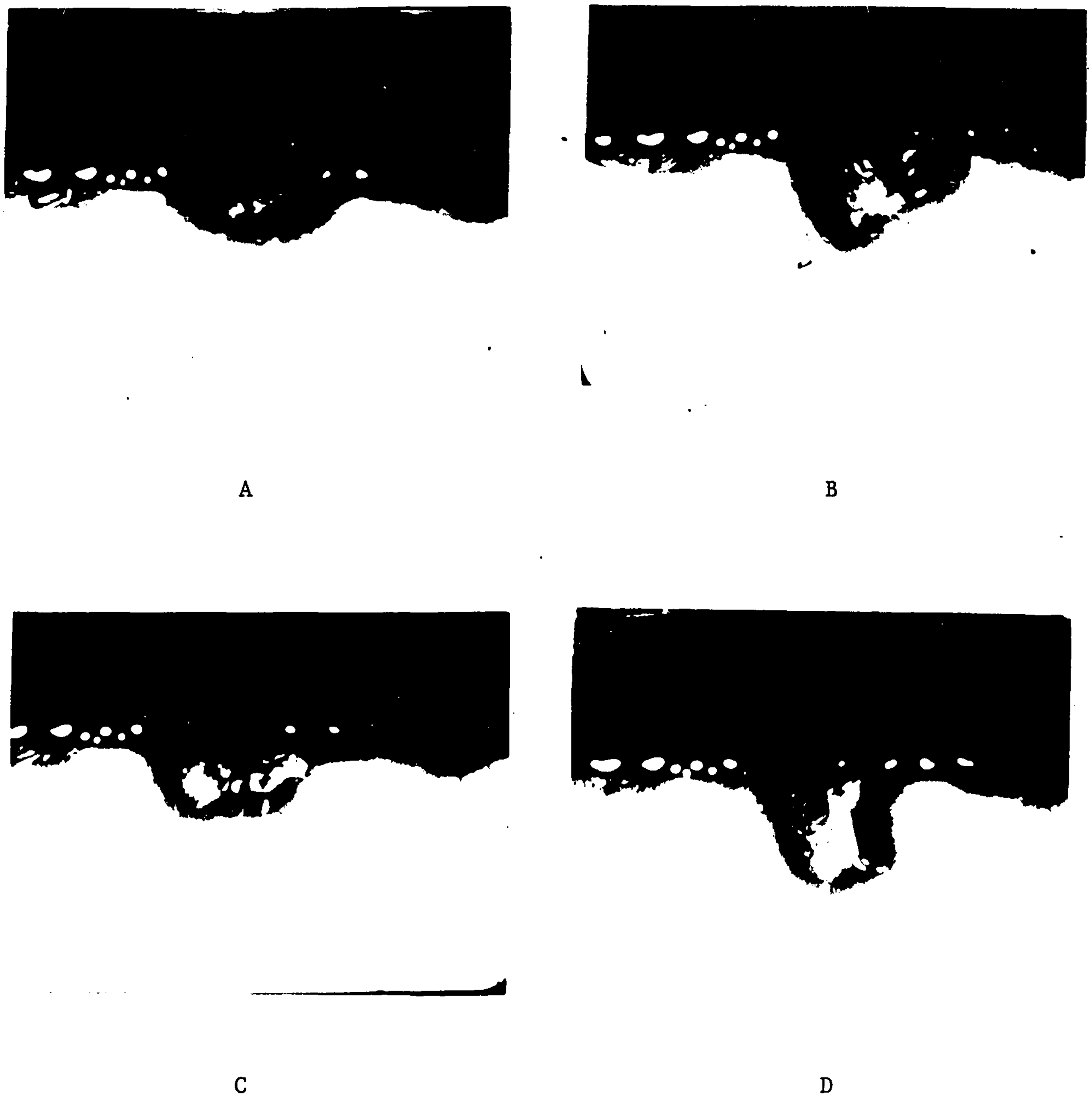

Figure 7.10 16 mm frames showing horizontal instability of the gas cavity resulting in droplet ejection.

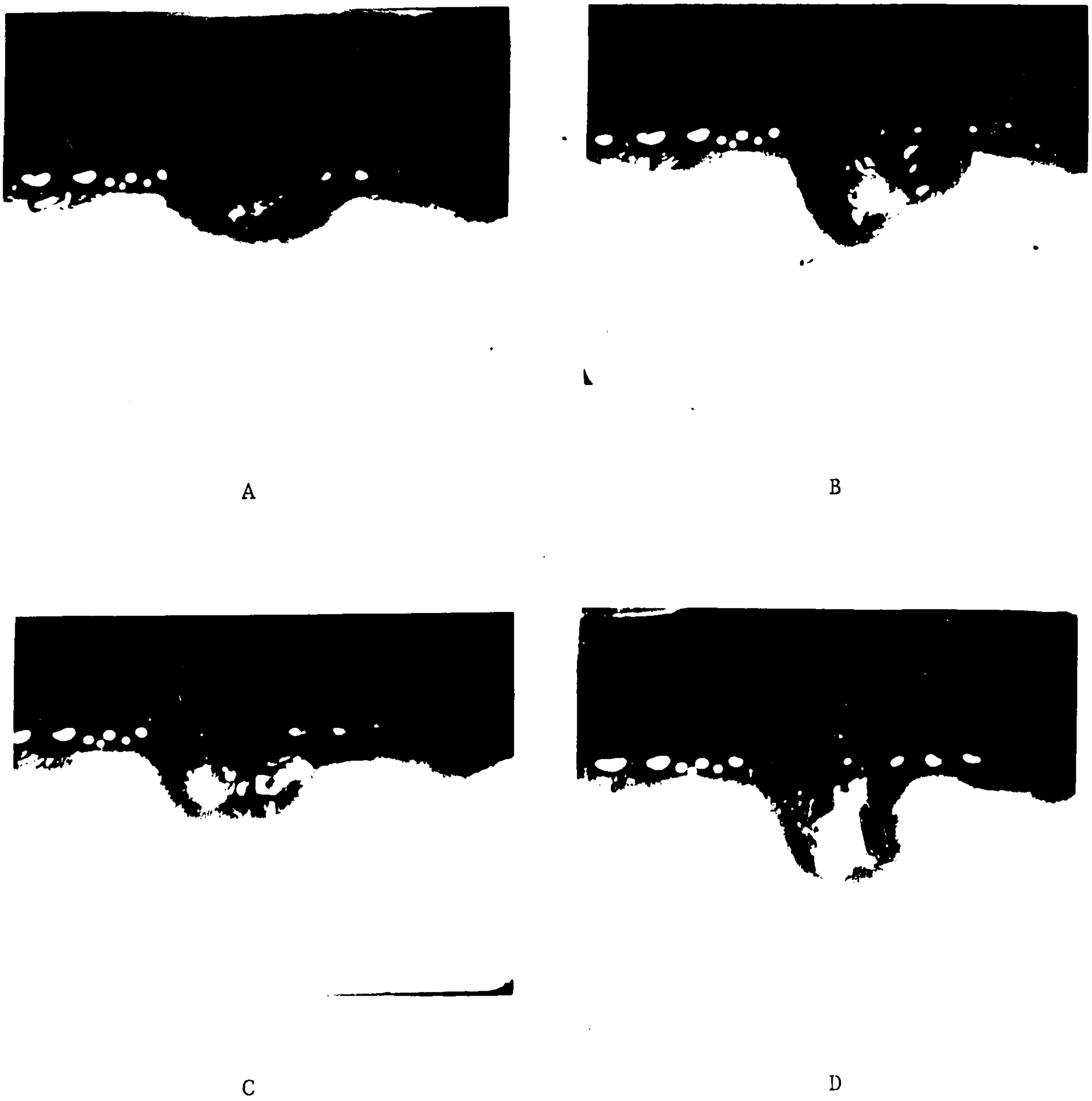

Figure 7.10 16 mm frames showing horizontal instability of the gas cavity resulting in droplet ejection.

If this volume is assumed to be ejected at each minimum of the gas cavity, then the amount of liquid ejected per unit time becomes:

$$\dot{V} = 7.5 \cdot 0.78\pi m^2$$

$$\dot{V} = .58\pi m^2 \quad \ldots\ldots\ldots\ldots \quad 7.37$$

At $Q = 120\ \mathrm{cm^3 sec^{-1}}$, $h = 2.5$ cm, $d = .15$ cm; $m = 1.5$ cm

$$\dot{V} = .58\pi(1.5)^2$$

$$= 4.1\ \mathrm{cm^3 sec^{-1}}$$

At a liquid density of 1.033 gm $\mathrm{cm^{-3}}$(Table 5.1) the circulating mass becomes:

$$\dot{m} = 4.2\ \mathrm{gm\ sec^{-1}}$$

Further measurements taken from the 16 mm film (500fps) of the cavity show that ejected drop sizes range in size between .10cm and .15cm in diameter while the average time of travel of a droplet through the atmosphere is .12 seconds.

The equation defining the unsteady state absorption of HCl by a sphere of aqueous $NaHCO_3$ solution is given by Crank[61] as:

$$\frac{M_t}{M} = 1-\frac{6}{\pi^2} \sum_{n=1}^{\infty} \frac{1}{n^2} \exp\left(\frac{-D\pi^2 n^2 t}{r^2}\right) \qquad 7.38$$

Where: M - represents the total amount of substance to effuse or diffuse.

M_t - represents the amount that has effused or diffused up to time t.

D - diffusion coefficient $\mathrm{cm^2 sec^{-1}}$.

r - radius of sphere cm.

t - time in sec.

For HCl absorption M is defined by $\frac{4\pi r^3}{3}(C_{oi}-C_o)$, C_{oi} represents the solubility of HCl in water (at a partial pressure of HCl = .1, C_{oi} = .001 moles $\mathrm{cm^{-3}}$.) and C_o will be zero.

The validity of this model, which considers only diffusion of HCl inward and HCO_3^- outward has been established previously for the planar interface by comparison between Equations 7.32 and 7.33. Equation 7.38 considers only inward diffusion of HCl but with the short exposure times involved (.12 sec) this equation should closely approximate the multi-component diffusion case. It is assumed that the drop moves quickly enough to be in continual contact with an atmosphere containing 10% HCl.

Applying Equation 7.38 to the droplet as it falls through the oxidizing atmosphere, allows the HCO_3^- loss to be calculated based on an initial concentration of 4%HCO_3^-.

At diameter .10 cm ΔC_c = .84%HCO_3^-

diameter .15 cm ΔC_c = .57%HCO_3^-

The rate of HCO_3^- loss in the lower layer due to ejection of liquid droplets into the oxidizing atmosphere can be calculated from the following equation:

$$M \frac{dC_c}{dt} = 60 \Delta C_c \dot{m} \quad . \; . \; . \; . \; . \; . \; . \; . \; . \; . \; . \; . \quad 7.39$$

Where: M - mass of lower layer in gm
(222 ml x 1.033 gm cm^{-3} = 229.3 gm - 43.4gm of emulsified lower layer = 185.9 gm)

$\frac{dC_c}{dt}$ - rate of HCO_3^- loss in lower layer in %HCO_3^- min^{-1}

ΔC_c - loss of HCO_3^- while drop exposed to atmosphere %HCO_3^- (given above)

$\dot{m}$ - circulating mass of liquid gm sec^{-1} (4.2 gm sec^{-1})

Substituting these values into Equation 7.39 gives reaction rates of:

At diameter .10 cm $\frac{dC_c}{dt}$ = 1.18 %$HCO_3^-min^{-1}$

diameter .15 cm $\frac{dC_c}{dt}$ = .79 %$HCO_3^-min^{-1}$

The comparable rate of reaction in the bath was .89 $\%HCO_3^- min^{-1}$ and ΔC_c was .58 $\%HCO_3^-$ (Figure 5.12), for identical values of Q-120 $cm^3 sec^{-1}$ and h-2.5 cm.

The observed values for ΔC_c (HCO_3^- content in bulk aqueous phase - HCO_3^- content in emulsified droplets) and rates of HCO_3^- removal from the system are in reasonable agreement with those calculated by Equation 7.38 and Equation 7.39. Table 7.3 shows the comparison of HCO_3^- removal rates for each location and the cumulative rate as compared to the measured removal rates.

TABLE 7.3

Drop Diameter	ΔC_c measured $\%HCO_3^-$	ΔC_c cal'd $\%HCO_3^-$	Calculated $\frac{dC_c}{dt}$		Measured $\frac{dC_c}{dt}$
			cav.	drop eject.	$\%HCO_3^- min^{-1}$
.10 cm		.84		1.18	
.15 cm		.57		.79	
	.58		.16		.90

The lower observed rate may be attributed to the fact that all the liquid between maximum and minimum cavity depth is not ejected into the atmosphere and that most of the ejected drops may be of the larger size.

7.1-3 Mechanism 3 - Metal-Slag Reaction in Foam and Emulsion

The transport of aqueous solution into the oil layer in the form of small droplets is a function of the stirring power of the gas jet. Observed directions of flow which lead to emulsification are shown in Figure 7.11. Transport of aqueous phase into the oil layer by CO_2 bubbles rising from nucleation sites at the bottom of the vessel was observed[63]. It is also suspected that small CO_2 bubbles nucleate at the oil-water interface and carry droplets of the aqueous layer into the oil.

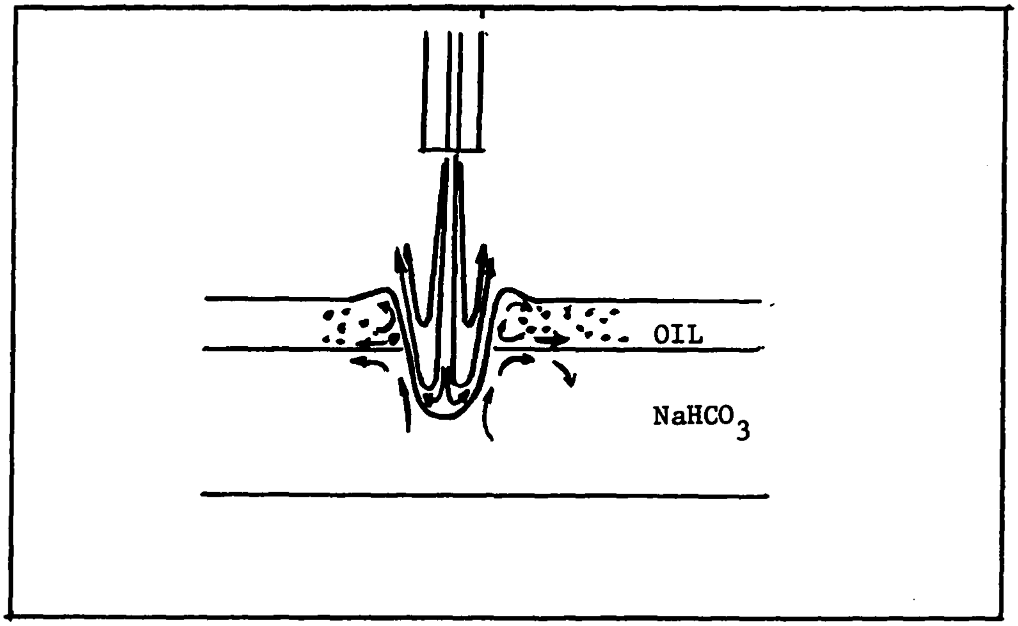

Figure 7.11 Stirring power of gas jet causing emulsification.

The forces favouring emulsion formation and preventing their destruction have been reviewed in Chapter 3.

When a surface active agent was added to the oil, foaming was induced to a great extent and the amount of aqueous phase in the water/oil emulsion rose to values of 80 volume %. The reaction between the gas of the foam and the aqueous droplets was significant as shown by the high rate of reaction in the emulsion of $1.1\%HCO_3^-\ min^{-1}$ compared to value of $.75\ \%HCO_3^-\ min^{-1}$ for the aqueous layer. Rates under comparable conditions in the case of no surface active agent additions are .86 %HCO_3^- min^{-1} in the emulsion and 0.90 %$HCO_3^-$$min^{-1}$ in the aqueous layer (Figure 5.24).

The lower rate of reaction in the aqueous layer than observed under normal conditions is due to the effective increase in lance height as the lower liquid was emulsified into the oil. The higher emulsion reaction rate in the surface active agent case is further confirmation of increased amount of foam - droplet reaction.

The loss of dissolved impurity from the emulsion droplet to the oil layer depends on the size of the droplet and its time of residence in the upper layer. The reaction between the suspended emulsion droplets and the oil medium or the gas of the foam could not be estimated in the room temperature model. However, the low molar flux $\check{N}''=4 \times 10^{-8}$ moles HCl $cm^{-2}sec^{-1}$ measured for transfer of HCl between quiescent layers of oil and sodium bicarbonate solution (section 5.4-6) as compared with molar fluxes of 10^{-5} moles HCl $cm^{-2}sec^{-1}$ for gas liquid reaction suggest that this mechanism is of lesser importance in this system.

7.2 Mechanisms Explaining Reaction Rates in High Temperature Model

In the iron-slag system at starting temperatures of 1350°C, decarburization in the emulsion droplets was more drastic than in the room temperature model. The high temperature system was characterized by a foamy slag which acted as a blanket on the iron melt, holding in the oxidizing gases. At times during the blow, the slag covered the lance tip, sealing off any exit for the exhaust gases, until the pressure build up beneath burst a hole in the foam covering. This phenomenon is pictured in Figure 7.12.

At higher flow rates splashing is more prominent and the slag foam was not able to so easily blanket the system. Splashing and droplet ejection are pictured in Figure 7.13.

Analysis of the high temperature system on the basis of the reaction locations proposed for the room temperature model results in the following three mechanisms:

1) Oxygen gas is absorbed at the point of impingement of the gas jet after the formation of a gas cavity which extends into the iron layer. The rate of decarburization at the point of impingement is dependent upon the surface area of the gas cavity which is in turn dependent upon gas flow rate, lance height and lance diameter.

2) As in the low temperature system, the high temperature cavity was seen to eject iron drops into the oxidizing atmosphere at regular intervals. The exposed droplets undergo decarburization and then settle through the slag layer.

3) Iron droplets suspended in the foaming slag undergo decarburization due to reaction with the oxygen of the slag and with the oxygen gases of the foam.

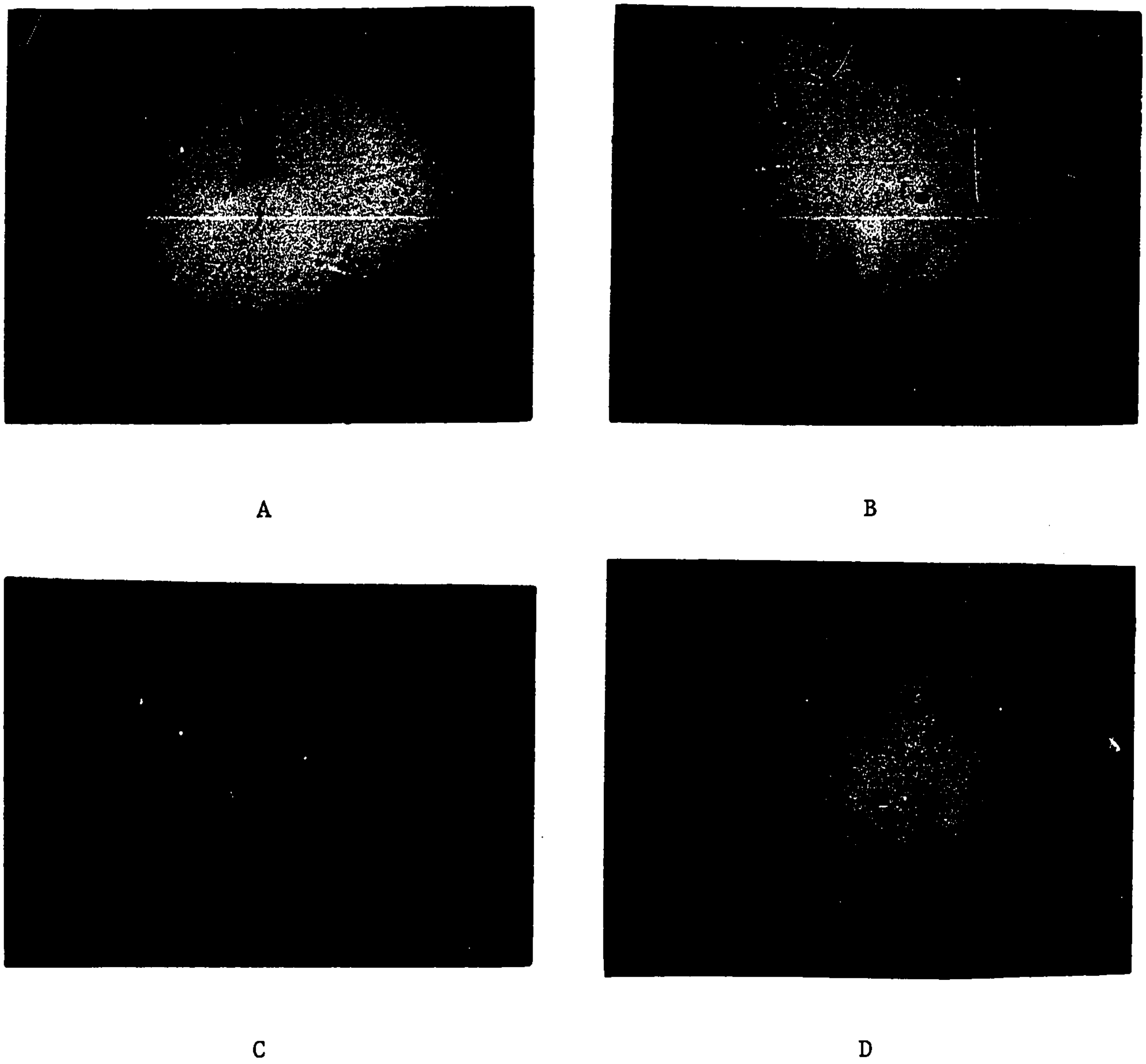

Figure 7.12 Sequence of 16 mm movie frames (64 frames per second)

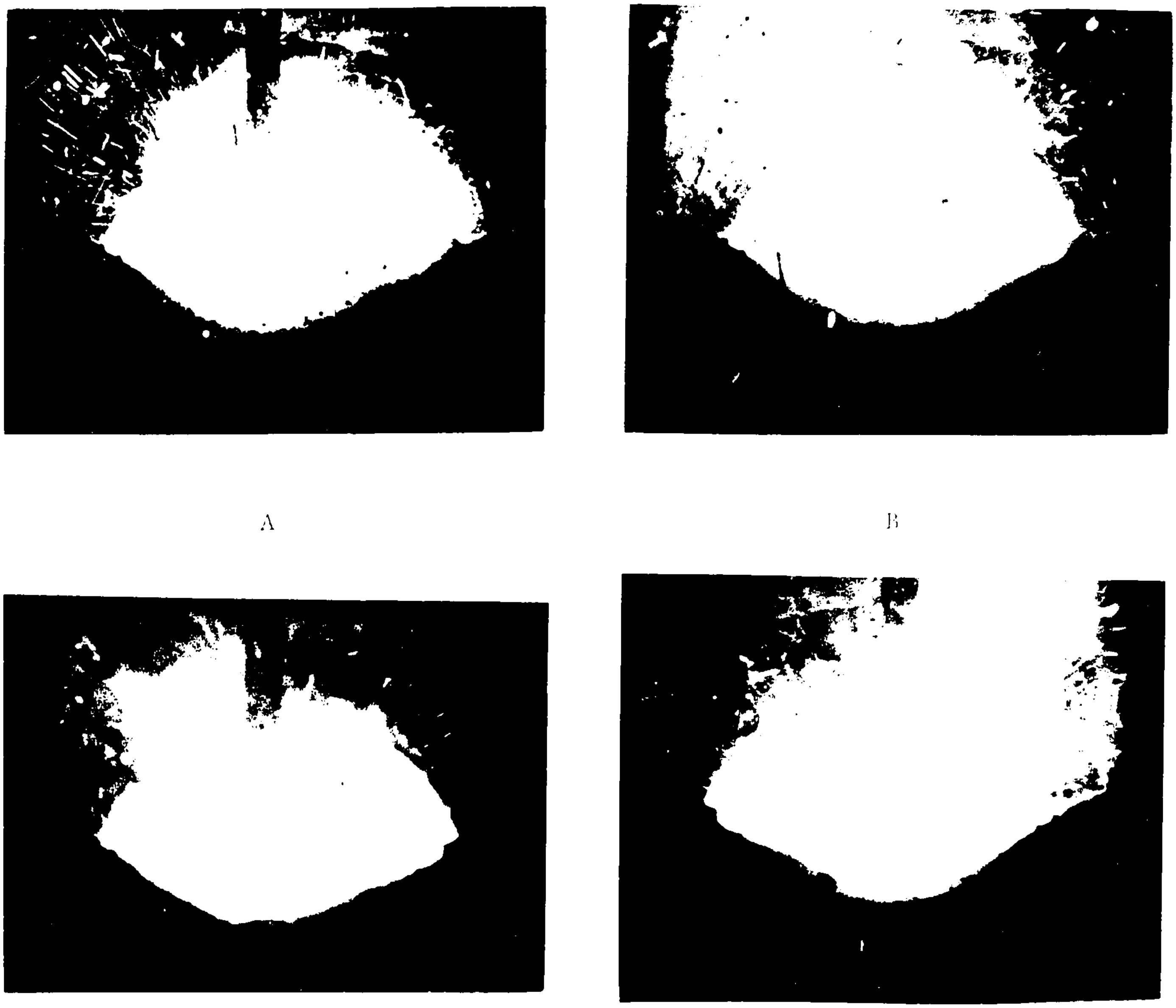

A

B

C

D

Figure [illegible]

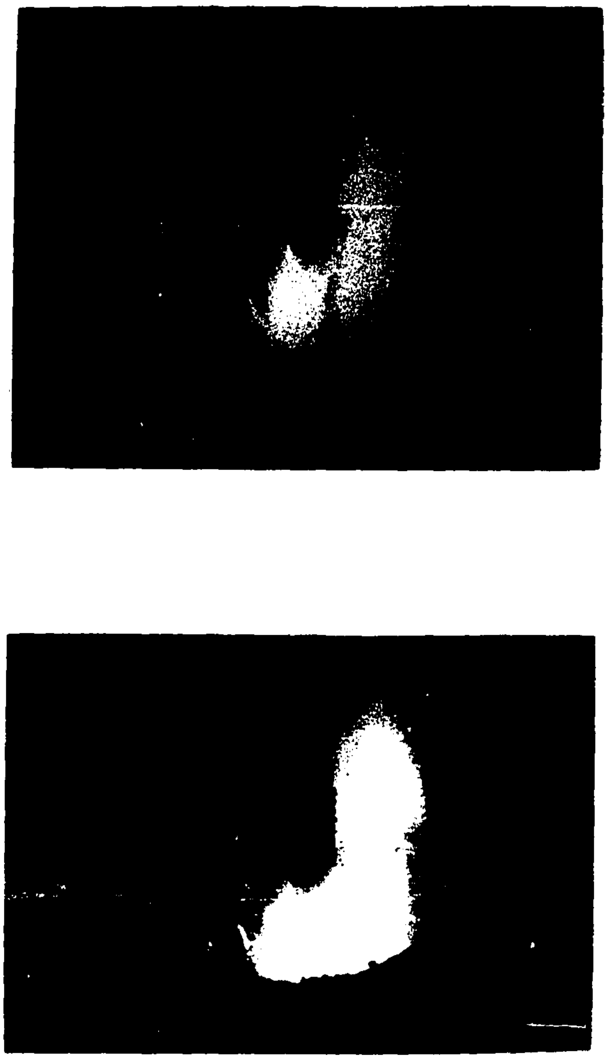

Figure 7.13 16 mm frames (200 fps) showing splashing and droplet ejection.

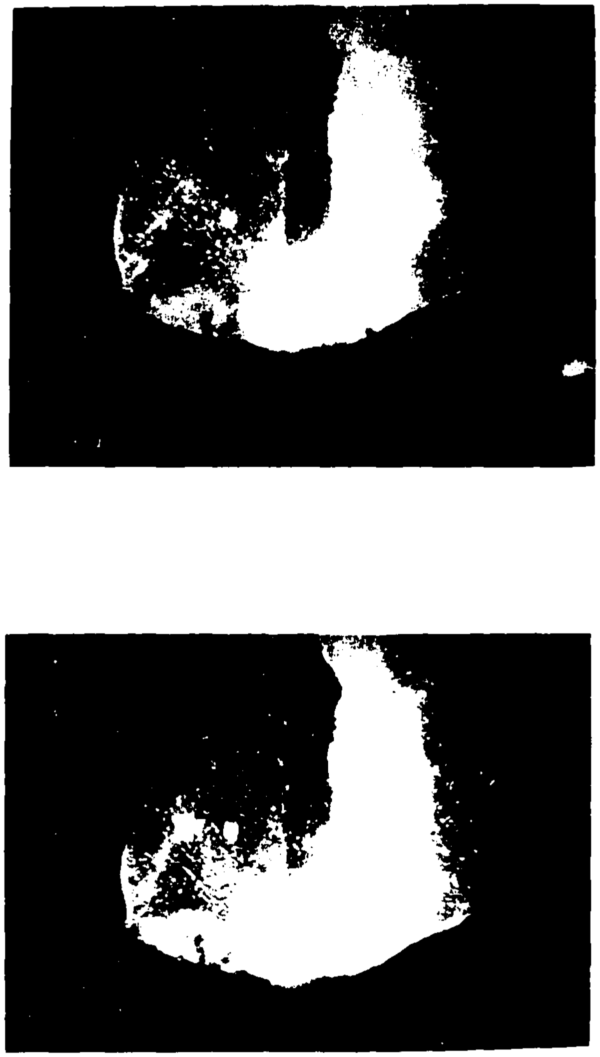

Figure 7.13 16 mm frames (200 fps) showing splashing and droplet ejection.

7.2-1 Mechanism 1 - Gas Absorption at the Cavity

Mass transfer rates at the gas-liquid interface of the gas depression in the high temperature system can be calculated by the Higbie model as proposed in Section 7.1-1. However, in the iron-carbon system, carbon can be eliminated from the iron in two ways: carbon effuses from the bulk metal to the gas-liquid interface, reacting with oxygen to form CO gas; oxygen diffuses into the metal bulk to supersaturation, but CO is not able to nucleate into a bubble until it reaches the slag layer.

A typical element of iron is shown in Figure 7.14. The unsteady state diffusion of carbon into the gas cavity is first considered. The concentration of carbon C as a function of time t and distance x from the gas-

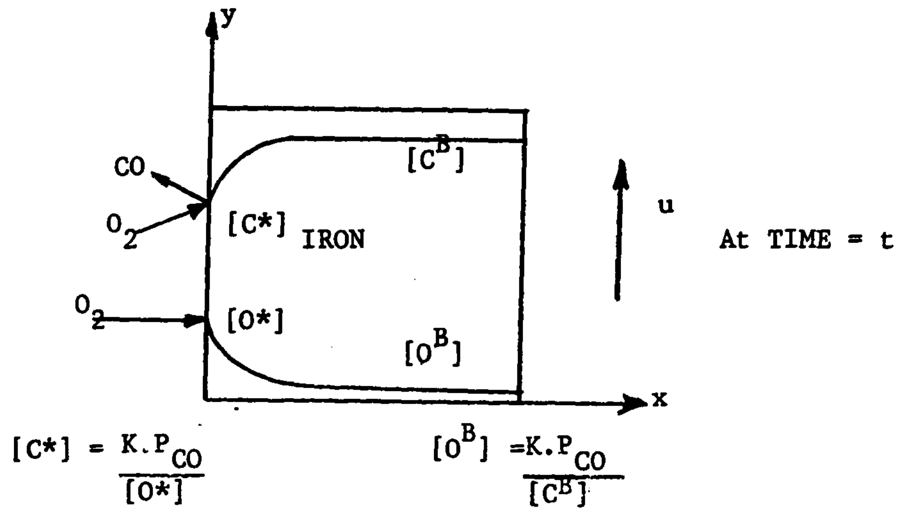

Figure 7.14 Iron element showing oxygen and carbon concentrations.

liquid interface is given by:*

$$[C]_{x,t} = A + B\,\mathrm{erf}\,\frac{x}{\sqrt{4D_c t}} \quad . \; . \; . \; . \; . \; . \; . \; . \quad 7.40$$

A, B are constants and D_c is the diffusion coefficient for carbon in molten iron. The boundary conditions for Equation 7.40 are:

B.C.1 $x=0$ $\quad [C]_{0,t} = [C^*]$ $\quad$ 7.41

B.C.2 $x=0$ $\quad [C]_{x,0} = [C^B]$ $\quad$ 7.42

In the above boundary conditions [C*] represents the concentration of carbon in equilibrium with the saturation solubility of oxygen (i.e. with FeO) at the interface [O*] (moles cm^{-3}) and is governed by:

$$[C^*][O^*] = 6.08 \times 10^{-8} P_{CO} \quad . \; . \; . \; . \; . \; . \; . \; . \quad 7.43$$

64

Where: $[O^*] = .23$ wt% or 1.035×10^{-3} moles cm^{-3} at 1600°C

P_{CO} - carbon monoxide gas partial pressure in atmos.(1 at, or less)

In boundary condition 2, $[C^B]$ represents the bulk carbon content in moles cm^{-3}. The final form of Equation 7.40 becomes:

$$[C]_{x,t} = [C^*] + ([C^B] - [C^*])\,\mathrm{erf}\,\frac{x}{\sqrt{4D_c t}} \quad . \; . \; . \; . \; . \; . \quad 7.40a$$

The instantaneous carbon flux $\overset{\circ}{N}{}''_c$ at the gas-liquid interface is given by:

$$\overset{\circ}{N}{}''_c \Big|_{x=0} = -D_c \frac{\partial C_c}{\partial x}\Big|_{x=0} \quad . \; . \; . \; . \; . \; . \; . \; . \; . \quad 7.44$$

Differentiating Equation 7.40a and multiplying by $-D_c$ yields:

$$\overset{\circ}{N}{}''_c = \sqrt{\frac{D_c}{\pi t}}\,([C^*] - [C^B]) . \quad . \; . \; . \; . \; . \; . \; . \quad 7.45$$

---

* The convention [ ] representing in metal and ( ) representing in slag will be used.

The average rate of absorption up to time t is:

$$\overset{\circ}{N}''_{c\ av.} = \frac{1}{t}\int_{0}^{t} \overset{\circ}{N}''_{c}dt = 2\sqrt{\frac{D_c}{\pi t}} \quad ([C^*] - [C^B]) . \quad . \quad 7.46$$

If the same principles are applied to the unsteady state diffusion of oxygen into the iron, then the governing equation will be:

$$\overset{\circ}{N}''_{o\ av.} = 2\sqrt{\frac{D_o}{\pi t}} \quad ([O^*] - [O^B]) \; . \; . \; . \; . \; . \; . \; . \quad 7.47$$

Where: $[O^B]$ is given by:

$$[C^B][O^B] = 6.08 \times 10^{-8} P_{CO} \; . \; . \; . \; . \; . \; . \; . \; . \; . \quad 7.48$$

$[O^B]$ is assumed to be given by the equilibrium between $[C^B]$ and a CO pressure of 1 atmosphere, i.e., the starting pig iron is assumed to have been able to evolve carbon and oxygen to the P_{CO} level of 1 atmosphere during melting. The oxygen flux described by Equation 7.41 cannot effectively remove dissolved carbon until CO nucleation occurs.

The maximum depth of depression of the gas jet is calculated according to Equation 7.6. It is assumed that the diameter of the depression is equal to its depth in order to calculate the area and arc length of the cavity from Equations 7.7 and 7.8. The calculated results are tabulated in Table 7.4.

TABLE 7.4

h = 1-1/2 inches			
Q (SCFM)	n (cm)	A (cm^2)	l (cm)
1.125	.844	1.610	.971
1.000	.627	0.888	.710
0.875	.412	0.383	.455
0.750	.200	0.091	.213

If the liquid flow velocity at the cavity boundary is assumed to be the same as in the low temperature model due to kinematic similarity, then $u \approx 10$ cm sec^{-1}. Using Equations 7.33, 7.8, 7.7, 7.46, 7.47 to calculate the degree of carbon desorption and oxygen absorption at the gas cavity enables the construction of Table 7.5.

TABLE 7.5

$D_o = 10^{-4}$ cm^{2}sec^{-1}

$D_c = .5 \times 10^{-4}$cm^{2}sec^{-1}

$U \simeq 10$ cm sec^{-1}

[O*]= .23 wt% 1.035x10^{-3} moles cm^{-3}

[C^B]= 4.0% .024 moles cm^{-3}

Bath Weight - 15 lb = 6820 gm

Q	A	1	t	$\dot{N}''_c$	$\dot{N}''_o$	Total $\dot{N}''_c$	%C min^{-1}	
(SCFM)	(cm^2)	(cm)	(sec)	moles/(cm^{2}sec)	moles/(cm^{2}sec)	moles/(cm^{2}sec)	Calculated	Measured
1.125	1.610	.971	.097	6.13x10^{-4}	3.76x10^{-4}	9.89x10^{-4}	.0168	.258
1.000	.888	.710	.071	7.17	4.39	11.56	.0108	.173
0.875	.383	.455	.046	8.90	5.45	14.35	.0058	.111
0.750	.091	.213	.021	13.18	8.07	21.25	.0020	.061

7.2-2 Mechanism 2 - Droplet Ejection from Gas Cavity

The ejection of liquid droplets into the atmosphere is assumed to occur as the gas cavity moves from its maximum to minimum position. If iron droplets are ejected in the same manner as water droplets in the low temperature system, the frequency of oscillation of the gas cavity can be calculated by counting the ejections pictured on a 16 mm film over a timed interval. The depth of the maxima and minima of the depression into the iron layer can only be estimated. The volume of ejected iron droplets can be obtained from the values of amplitude and frequency of oscillation by Equation 7.36.

The amplitude of oscillation in the low temperature model was .62 cm for a gas cavity of 1.935 cm depth (in aqueous layer) plus .84 cm (oil layer thickness). The depth of penetration in the high temperature system was .84 cm and the slag depth was 1.27 cm (Q = 1.125 SCFM and h = 1 1/2 inch). Since the two systems are kinematically similar, a calculation of the high temperature cavity oscillation by comparison with the low temperature system is possible.

$$\frac{A'' \rho''_{Fe}}{n'' \rho''_{Fe} + t'' \rho''_{s}} = \frac{A' \rho'_{w}}{n' \rho'_{w} + t' \rho'_{o}} \quad . \; . \; . \; . \; . \quad 7.49$$

Where A" is the amplitude in the high temperature system and A' is the amplitude in the low temperature system. Insertion of the data into Equation 7.49 gives a high temperature oscillation of .35 cm.

For the high temperature model Equation 7.1a would be:

$$y = (.35 \pm .1 \text{ cm}) \sin (5.8 \pm 1) \text{ rev sec}^{-1}) \, t \quad . \; . \; . \; . \; . \quad 7.50$$

The amount of liquid ejection can be assumed as in Section 7.1-2 to be the volume which lies between the maximum and minimum penetration of the gas jet. Using Equation 7.32 with A = .35 cm

$$V = 1/8\pi m^2 x.35$$

$$= .043\,\pi\,m^2 \; . \; . \; . \; . \; . \; . \; . \; . \; . \; . \; . \; . \quad 7.51$$

This volume is supposed to be ejected at each minimum of the gas cavity, so the amount of liquid ejected per unit time becomes:

$$\dot{V} = 5.8x.043\pi\,m^2 \; . \; . \; . \; . \; . \; . \; . \; . \; . \; . \; . \quad 7.51a$$

Assuming m=n then m=.84 (Table 7.3) and $\dot{V}$ will be:

$$\dot{V} = 5.8x.043\,\pi\,(.84)^2$$

$$= .55\ cm^3\ sec^{-1}$$

At a liquid density of 7.2 gm cm^{-3} the circulating mass becomes:

$$\dot{m} = 4.0\ gm\ sec^{-1} \; . \; . \; . \; . \; . \; . \; . \; . \; . \; . \quad 7.52$$

Further measurements taken from the 16 mm film (200fps) of the high temperature blow suggest that ejected drops range in size between .4 cm and .5 cm diameter in good agreement with the Holden and Hogg[12] estimate of .3 cm diameter. The average time of travel of a droplet through the oxidizing atmosphere is .25 seconds.

The same principles used to derive Equation 7.46 and 7.47 will be applied to the spherical drop. It is assumed that the amount of carbon which will be removed from the droplet during its flight in the oxygen phase is the sum of the carbon effusion rate plus the oxygen absorption rate. Actual carbon removal by the absorbed oxygen will not take place until nucleation occurs, most likely as the droplet falls into the slag.

The equation defining the unsteady state diffusion of carbon from a sphere of iron or the unsteady state absorption of oxygen by a sphere of iron is given by Equation 7.38. In the case of oxygen diffusion M is defined by $\frac{4\pi r^3}{3}$ ([O*]- [O^B]), [O*] representing the saturation oxygen solubility at t=0, and [O^B] represents the concentration of oxygen in equilibrium with the bulk carbon according to Equation 7.48. The value of M for carbon effusion would be $\frac{4\pi r^3}{3}$ ([C^B] - [C*]), [C^B] representing the original carbon content and [C*] represents the carbon content at the surface as defined by Equation 7.43.

It is assumed that, in rising and falling through the oxygen atmosphere, the drop is always in contact with fresh gas. Any deviation from this assumption will result in a lower value for [O*]. Applying Equation 7.38 to the droplet as it rises and falls through the atmosphere enables the calculation of carbon loss based on concentrations and diffusion coefficients given in Table 7.5.

At diameter .4 cm ΔC_c = .25 %C

diameter .5 cm ΔC_c = .20 %C

The rate of carbon loss in the lower layer due to the ejection of liquid droplets into the oxidizing atmosphere can be calculated from Equation 7.39 in which M=6600 gm (taking into account emulsified iron), $\dot{m}$=4.0 gm sec^{-1}, and ΔC_c = .20%C or .25%C. Substitution of these values into Equation 7.33 gives decarburization rates of:

At diameter .4 cm $\frac{dC_c}{dt}$ = .009 %C min^{-1}

diameter .5 cm $\frac{dC_c}{dt}$ = .007 %C min^{-1}

The measured rate of reaction in the bath was .258 %C min^{-1} and ΔC_c = 1.8 %C (Figure 6.11).

7.2-3 Mechanism 3 - Metal-Slag Reaction in Foam and Emulsion

The crushing of the slag samples resulted in a flattening out of many iron droplets, changing their diameter. An accurate sizing analysis could not be done by sieving because of the slag particles present. Optical analysis, however, showed many particles to be in the range 2-3 mm diameter. A large number of fine <.1 mm diameter iron beads were also observed in the slag samples, but these small diameter beads accounted for less than 5% by weight of the metallic portion of the emulsion. Figure 7.15 shows the typical range of droplet sizes obtained in an emulsion sample. Several droplets were seen to have a crater at their surface, probably where a CO bubble had nucleated at the surface as the drop enters the slag (Figure 7.16). This attached gas bubble will impede the normal settling of the iron bead through the slag to the iron bath.

The mechanisms by which iron beads are suspended in the slag are depicted in Figure 7.17. The forces aiding the formation of metallurgical foams and emulsions as well as their stabilities have been reviewed in Chapter 3.

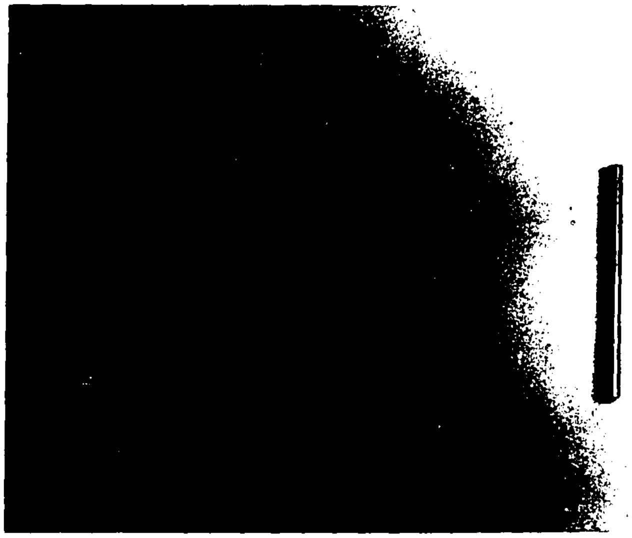

Figure 7.15 Typical emulsion sample after crushing and removal of attached slag.

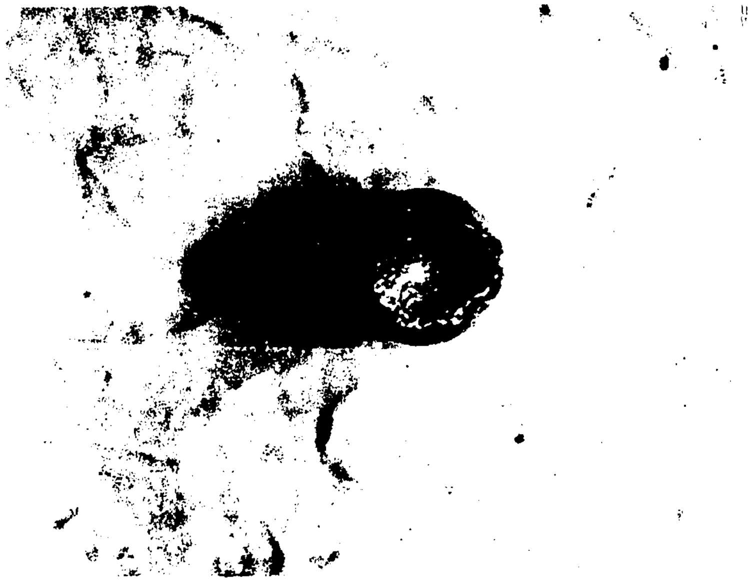

Figure 7.16 Close-up of an emulsion droplet which had a CO bubble nucleate at its surface (30X).

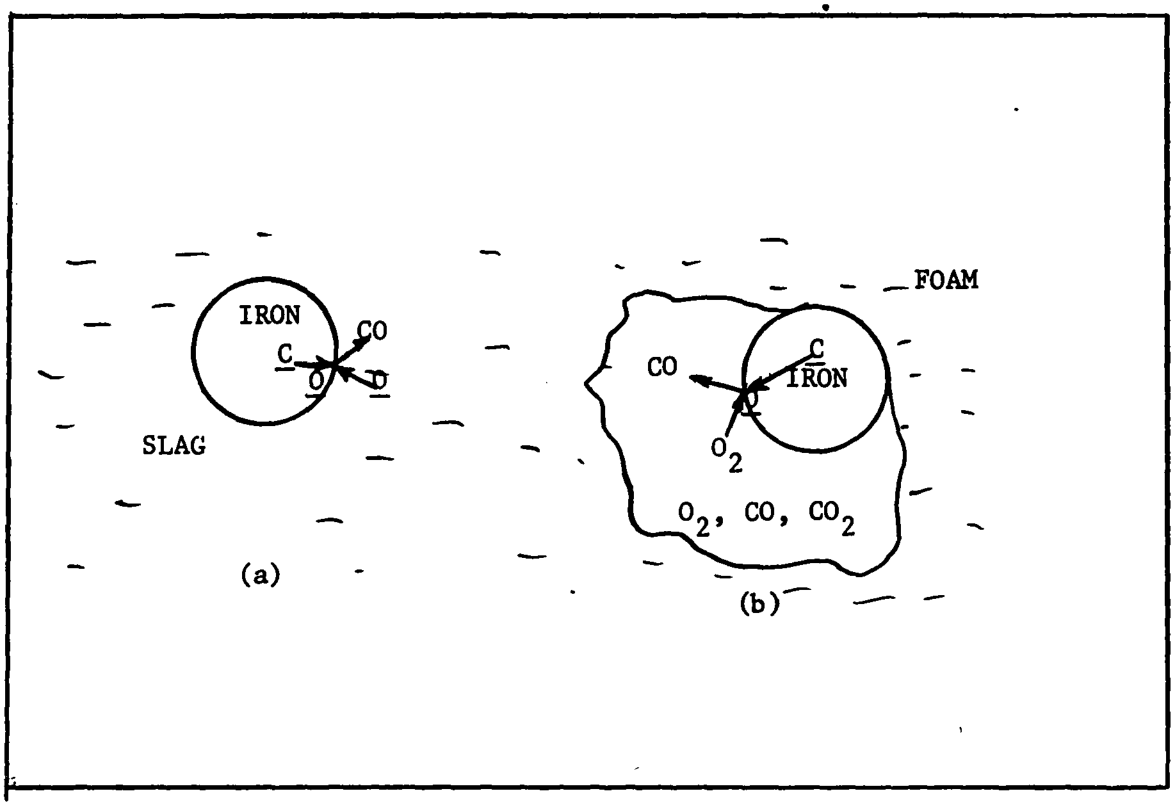

Figure 7.17 Two ways in which iron droplets can exist in slag. (a) Totally immersed in liquid slag. (b) Clinging to film of slag foam and therefore having a large gas-liquid interface.

Figure 7.16 Close-up of an emulsion droplet which had a CO bubble nucleate at its surface (30X).

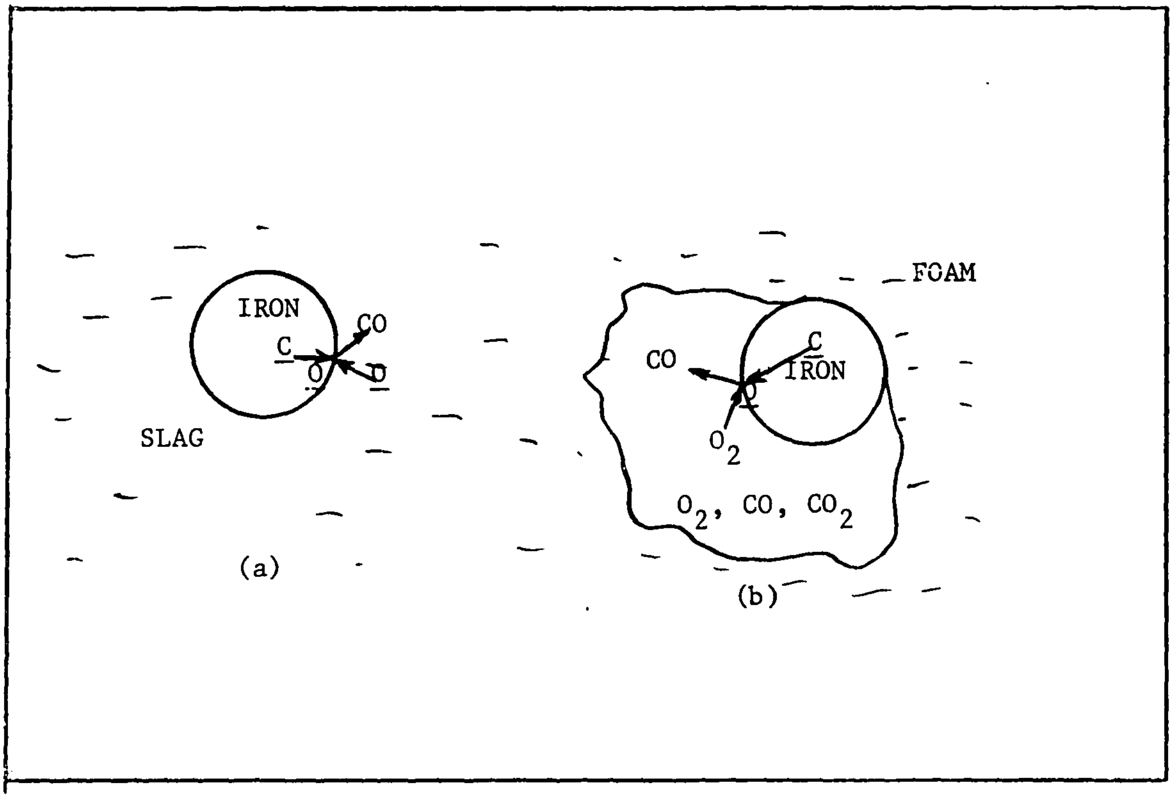

Figure 7.17 Two ways in which iron droplets can exist in slag. (a) Totally immersed in liquid slag. (b) Clinging to film of slag foam and therefore having a large gas-liquid interface.

A. Reaction with Slag

The reaction rates of iron droplets suspended within the liquid slag are predicted by unsteady state molecular diffusion of FeO to the droplet surface and reaction with dissolved carbon to form CO gas. Simultaneous FeO diffusion in slag and carbon diffusion in the droplet was not treated due to the complexity of the diffusion equations.

Carbon diffusion in the iron droplet has been shown to be rapid (Figures 7.18 and 7.19) and hence it does not significantly influence the decarburization rate.

An iron drop completely surrounded by slag can be simplified as in Figure 7.20, where r2 must equal ∞ to be exact, but may be finite if the oxygen content at r2 is close to $(O^B)^*$.

---

* Note particularly that ( ) refers to slag and [ ] refers to metal.

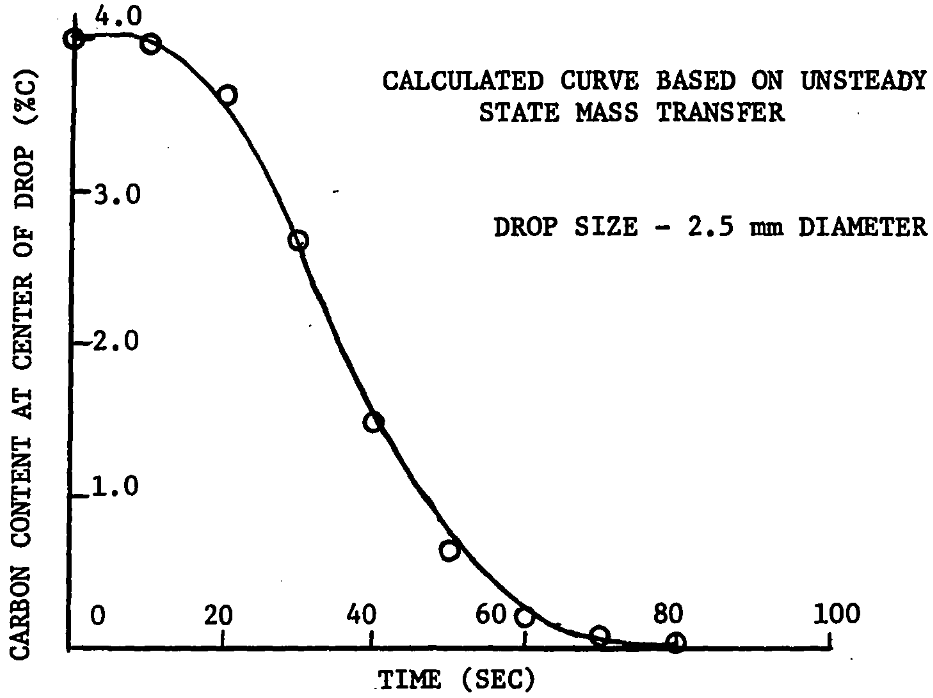

Figure 7.18 Emulsion Drop in Slag ($a_{FeO} = 0.29$)

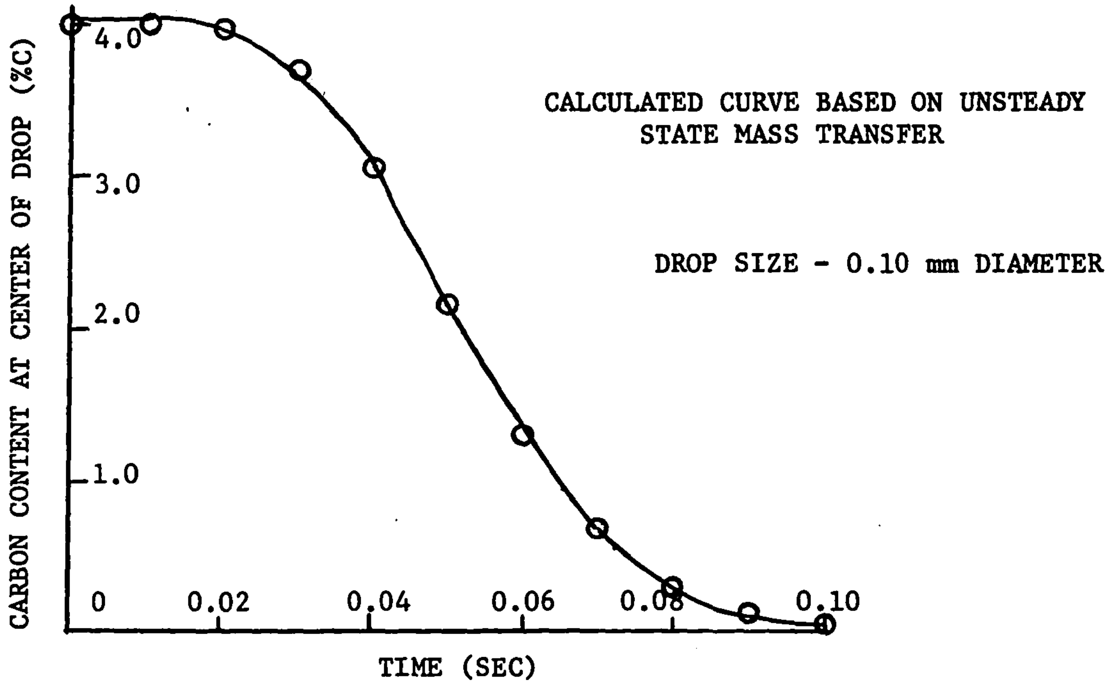

Figure 7.19 Emulsion Drop in Slag ($a_{FeO} = 0.29$)

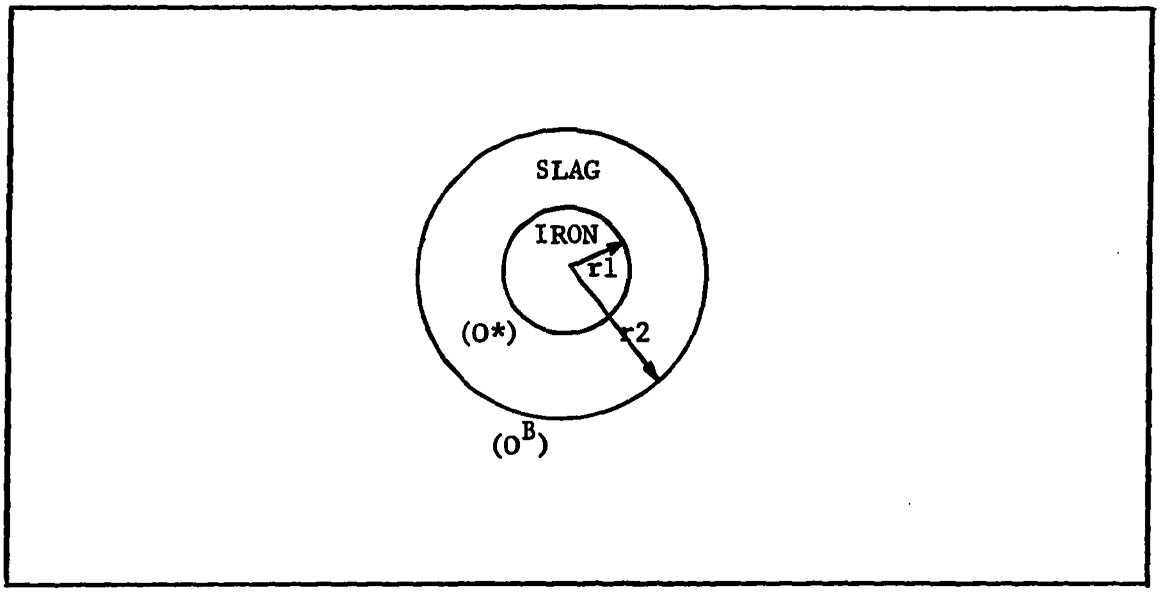

Figure 7.20 Diagram showing simplified iron droplet in slag diffusion controlled decarburization mechanism.

The equation defining the system has been derived by Barrer[65]:

$$\frac{-\dot{N}''_O}{D_O} = \left.\frac{\partial(O)}{\partial r}\right|_{r=r1} = \frac{-(O^*)}{r1} + \frac{(O^B)r2 - (O^*)r1}{(r2 - r1)\,r1}$$

$$+ \frac{2}{r2 - r1}\sum_{n=1}^{\infty} \frac{(O^B)r2\cos n\pi - (O^*)r1}{r1}\ \exp\left(\frac{-D_o\pi^2 n^2 t}{(r2-r1)^2}\right)$$

$$- \frac{2(O^B)}{r2 - r1}\sum_{n=1}^{\infty} \frac{r2\cos n\pi - r1}{r1}\ \exp\left(\frac{-D_o\pi^2 n^2 t}{(r2 - r1)^2}\right). \quad . \quad . \quad 7.53$$

The oxygen concentrations are calculated in terms of the number of moles of FeO per cm^3 of slag using a slag density of 3.5 gm cm^{-3}. Thus $(O^B) = .016$ moles cm^{-3} ($(FeO^B) = .016$ moles cm^{-3}) corresponds to $a_{FeO} = .29$ in the experimental slags (see Section 6.2). (O^*) is defined by a_{FeO} at the surface of the iron drop according to Equation 7.54,

$$(FeO) + [C^*] = [Fe] + CO \quad . \quad . \quad . \quad . \quad . \quad . \quad . \quad . \quad . \quad . \quad 7.54$$

and $$\frac{a_{Fe}\cdot P_{CO}}{a_{FeO}\cdot a_C} = K = 1.58 \times 10^4 \qquad (1600^\circ C) \quad . \quad . \quad . \quad . \quad . \quad . \quad . \quad 7.55$$

The activity of iron a_{Fe} is taken as 1 and the pressure of the forming carbon monoxide is taken as 1 atmosphere. a_c represents the activity of carbon at the drop surface and in the assumed case of rapid carbon diffusion will be a_C in the bulk of the droplet. At a $[C^B]$ of 4%C the activity of carbon is 0.86[64] and the calculated value of (O*) is 3.94×10^{-6} moles cm^{-3}. This value of (O*) is a minimum possible value and hence the calculated FeO diffusion rate is the maximum rate.

The solution of Equation 7.53 is very difficult due to the reluctance of this equation to converge quickly. An approximation to Equation 7.53 can be obtained from a similar approach as was employed to develop Equation 7.47 in this case using the area of the drop as the area of diffusion. The equation which would apply here would be:

$$\dot{N}''_{o,av.} = 2\sqrt{\frac{D_o}{\pi t}}\left((O^B) - (O^*)\right) \quad . \; . \; . \; . \; . \; . \; . \; . \quad 7.56$$

D_o represents the diffusion coefficient of oxygen as FeO in the slag $D_o = 10^{-6} cm^2 sec^{-1}$[9].

Equation 7.56 will best approximate 7.53 at small values of (r2-r1). Equation 7.56 has been solved for two typical droplet sizes of 2.5 mm and .1 mm diameter for the emulsion situation and the results are reported in Figures 7.21 and 7.22.

Figures 7.18 and 7.19 are presented to show that if carbon diffusion in the droplet were the rate controlling step, the rate of decarburization (Equation 7.38) would be some 10^2 to 10^3 times faster than that calculated for FeO transfer in the slag (assumed conditions $[C^B]$ = 4%C = 0.24 moles cm^{-3}; [C*] = .036%C = 2.2×10^{-4} moles cm^{-3} in equilibrium with a_{FeO} =.29, P_{CO}=1 atmosphere, a_{Fe}=1 calculated using Equation 7.55). This 2-3 order of magnitude difference confirms that carbon diffusion will not appreciably effect the decarburization rate.

B Reaction with Oxygen in Foam

Calculations of rates of decarburization of an iron drop by the oxygen gases of a foam can be made for the case of carbon effusion, using Equation 7.38, where CO nucleation is assumed to occur at the droplet surface in the foam. In absence of information with regard to the composition of the foam gas, composition of the gas has been assumed to be pure oxygen.

In this case the concentrations of the diffusing species are:

$[C^B] = 4\%C = .024$ moles cm^{-3}

$[C^*]$ (Equation 7.43) $= 6 \times 10^{-5}$ moles cm^{-3}

Results of calculations using Equation 7.38 are plotted in Figures 7.21-7.24.

The outstanding feature of the graphs resulting from these slag-metal and slag-foam calculations is the high rate of decarburization of iron droplets, especially those of small diameter. This occurrence is proved important when referring to Figure 6.11, where the difference in carbon content of the emulsified droplets and the bulk iron layer (approximately 1.8%C) is much greater than that predicted by droplet ejection (.20-.25%C).

It is also apparent that decarburization takes place much more quickly in the oxygen foam than in the slag medium itself. It must be realized, however, that the oxygen in the foam will quickly be depleted and diluted by CO as it evolves at the surface of the metal droplet. Thus the gas-metal reaction may rapidly decrease and the foam may consist principally of CO.

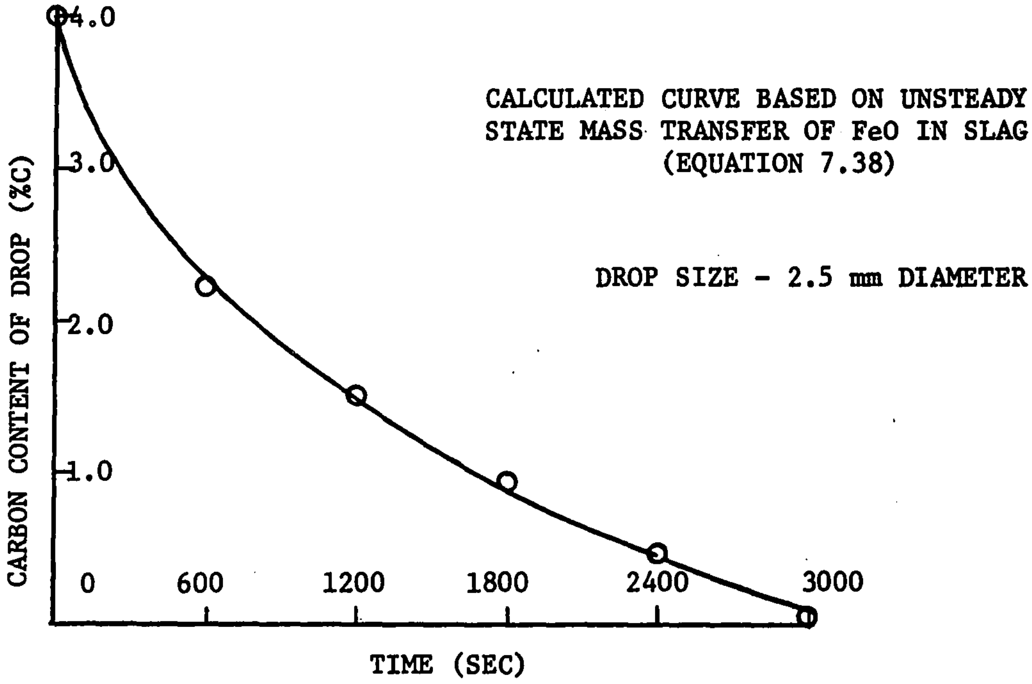

Figure 7.21 Emulsion Drop in Slag ($a_{FeO} = 0.29$)

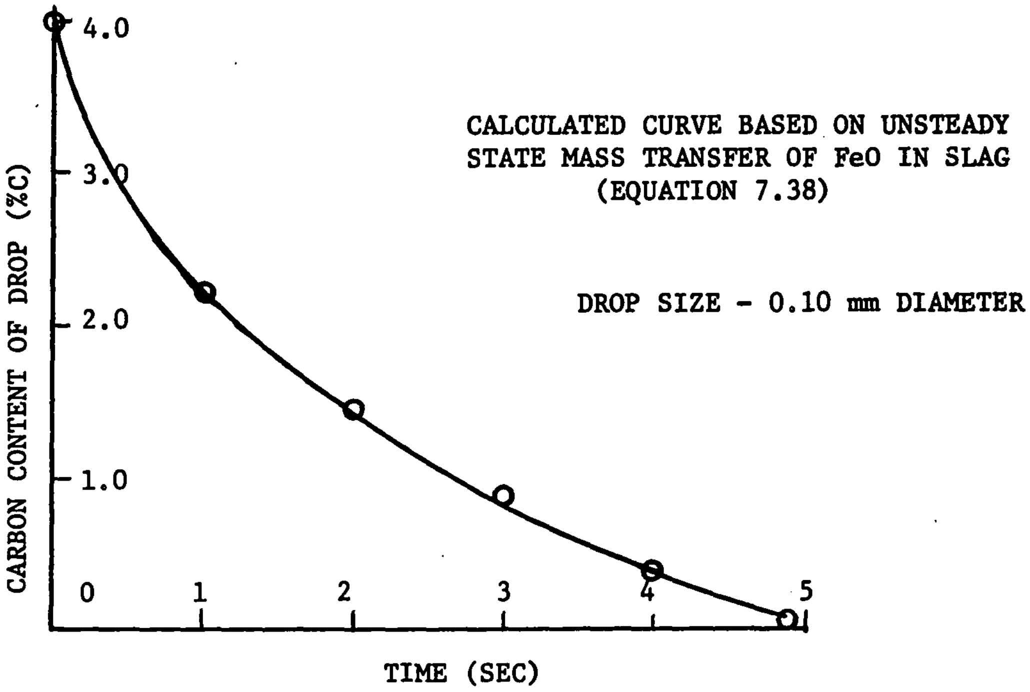

Figure 7.22 Emulsion Drop in Slag ($a_{FeO} = 0.29$)

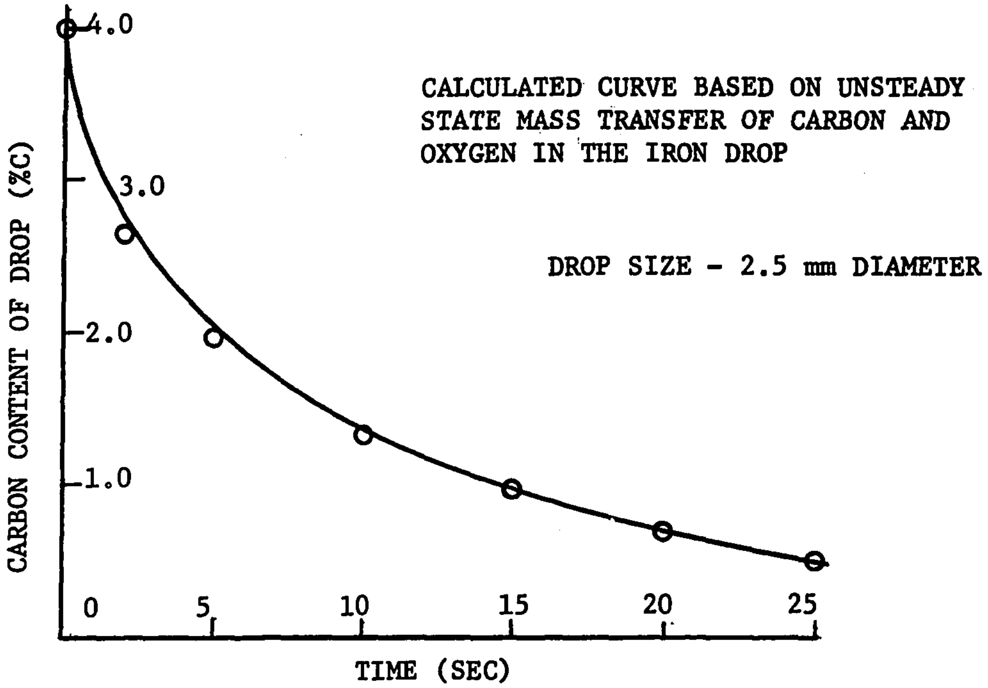

Figure 7.23 Iron Drop in Oxygen Gas of Foam.

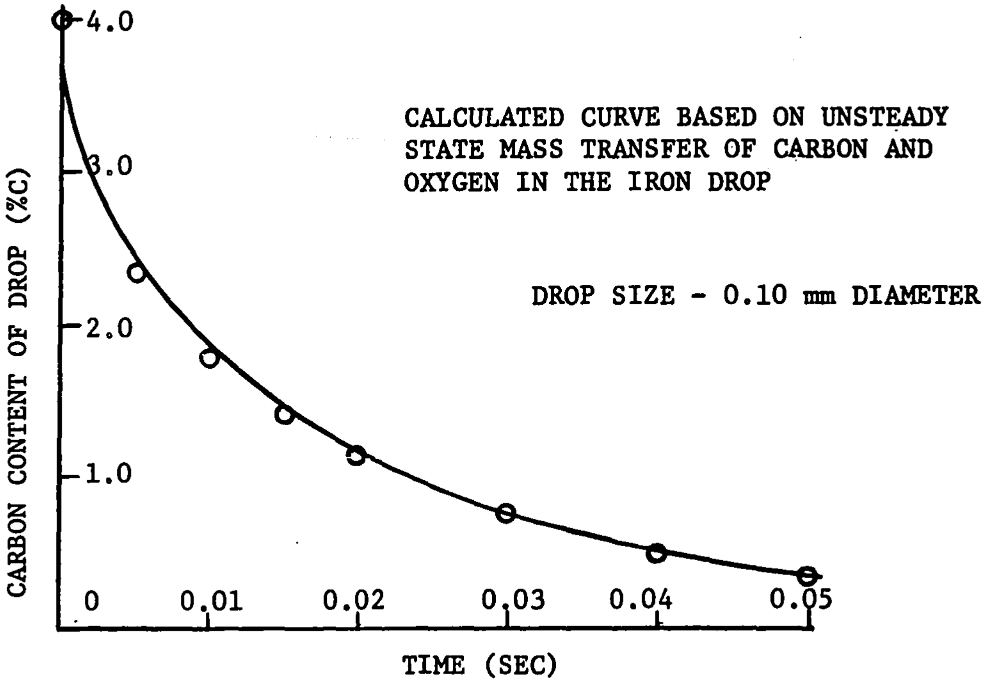

Figure 7.24 Iron Drop in Oxygen Gas of Foam.

C Turnover of Droplets in Slag

The droplet decarburization data can be used to estimate the rate of turnover of iron droplets in the slag foam and metal/slag emulsion by employing Equation 7.39. If each drop is assumed to be completely decarburized before returning to the iron layer, the ΔC_c will be given by the bath carbon content less the amount of decarburization of the drop in the above atmosphere. Initially ΔC_c would be 4%C - .25%C = 3.75%C. The resulting circulation rate of iron droplets would be:

$$\overset{\circ}{m} = \frac{dC_c}{dt} \; \frac{M}{60\Delta C_c} \quad . \; . \; . \; . \; . \; . \; . \; . \; . \; . \; . \quad 7.39a$$

$$= \frac{.258 \times 6600}{60 \times 3.75}$$

$$= 7.5 \text{ gm sec}^{-1}$$

Thus 7.5 gm of iron, which is equivalent to .1% of the total metallic iron, must enter and leave the slag every second to account for the observed reaction rate of .258%C min^{-1}.

This value compares well with the rate of 4.0 gm sec^{-1} predicted on the basis of cavity oscillations (Equation 7.38). Further droplet formation might possibly arise from direct stirring of metal into the slag.

The relative importance of each mechanism is tabulated in Table 7.6 for the test (Q = 1.125 SCFM, h = 1 1/2 inch)

TABLE 7.6

Mechanism and Location	Rate of Reaction	Rate of Carbon Removal from the bath.
Cavity beneath jet - oxygen absorption - carbon effusion Total	moles $cm^{-2} sec^{-1}$ 3.8×10^{-4} 6.1×10^{-4} 9.9×10^{-4}	.017 %C min^{-1}
Drops Ejected into the atmosphere by Cavity oscillation (total C effusion and O_2 absorption)	48-60%C min^{-1}	.008 %C min^{-1}
Drops in Emulsion (Slag-metal reaction)	.08-48.7 %C min	-
Drops in Foam (O_2-metal reaction)	7.2-52.1 %C min^{-1}	-
Observed overall Bath Decarburization Rate		.258 %C min^{-1}

Table 7.5 summarizes the high temperature results and shows very clearly that the principle route of reaction is between slag and metal in emulsion form and/or between gas and metal in foam form. In fact under experimental conditions 90% of the rate must be attributed to reaction in the slag emulsion or foam.

7.3 Summary of Experimental Findings

Examination of Table 7.2 which compares measured $NaHCO_3$ reaction rate with the rate predicted by HCl absorption at the gas cavity, shows this mechanism to be relatively unimportant (20-25% of total rate) except at conditions of low flow rate or high lance height. At these conditions, the depth of penetration into the aqueous layer is very small and the amount of splashing is also very small. However, at higher flow rates and lower lance heights this mechanism plays a secondary role and splashing of $NaHCO_3$ solution droplets into the HCl atmosphere accounts for the major portion of the reaction rate as demonstrated in Section 7.1-2.

Table 7.5 reveals a similar phenomenon in the high temperature system as was observed in the low temperature case. Decarburization rates as predicted by oxygen absorption and carbon effusion at the gas cavity predict rates which are 3-6% of the measured values.

The second mechanism, involving droplet ejection into the oxidizing atmosphere, predicts a decarburization rate of .009 %C min^{-1} as compared to a measured rate of .258%C min^{-1} for the test Q=1.125 SCFM, h=1 1/2 inches. This mechanism thus accounts for approximately 3% of the total reaction rate.

The relatively small importance of the first two mechanisms in determining the rate of decarburization leads to the conclusion that mechanism 3, which involves the reaction of emulsified droplets with the slag and with the gas of the slag foam, is the most important mechanism. The high rate of decarburization of small iron droplets under these conditions, as shown in Figures 7.21-7.24, substantiates this theory.

An important step in validating this theory would be measurement of the rate of continuous creation of emulsion droplets and the rate of return of reacted droplets to the iron bath. These emulsification rates have not been directly measured, but calculations based upon measured decarburization rates indicate that the turnover rates are in the order of 6% of the metal bath per minute of lancing.

The speed at which the iron drops leave the slag region depends upon emulsion and foam stability. The stability can be altered by changing the slag composition, and surface active nature and hence, to some extent at least, the residence time of iron droplets in the slag can be controlled.

Control of slag composition will, therefore provide a means of controlling the decarburization rate.

CONCLUSIONS

1. A gas cavity, which penetrates through the slag layer into the metal, was observed beneath the jet in both low and high temperature systems.

2. The cavity in the low temperature model was unstable, in both the horizontal and the vertical plane.

3. An emulsion and foam are formed by the force of the gas jet upon the two liquid system, which can be stabilized by the addition of surface active agents. The degree of emulsion formation increases with increasing flow rate and decreasing lance height.

4. Slags contain chains and rings which can produce stable foams and emulsions in a steelmaking system. The most important surface active agents in slags appear to be silicate and phosphate chains.

5. Reaction rates have been shown to increase with increasing nozzle diameter at constant gas velocity, with increasing flow rate and decreasing lance height.

6. Gas utilization efficiency increases with increasing lance diameter at constant gas velocity, with increasing flow rate and decreasing lance height.

7. The low temperature gas cavity was observed to attain a regular maximum and minimum penetration, the minimum penetration terminating with ejection of lower liquid in the form of droplets. Regular drop ejection was observed in the high temperature system indicating a similar regular maximum and minimum penetration mechanism as in the low temperature system.

8. Ejected drops react quickly with the atmosphere due to the high surface to volume ratio of a sphere. In the absence of reaction in the upper layer, the drop-atmosphere reaction can account for most of the total reaction.

9. Reactions between metal drops and oxidized slag and the gas of slag foams are extremely important mechanisms in the decarburization process. The high temperature experiments have shown that up to 90% of the total reaction can be between droplets and slag or foam.

10. Metal turnover through the slag in the order of 6% of the bath per minute can account for the observed industrial reaction rates.

APPENDICES

APPENDIX I

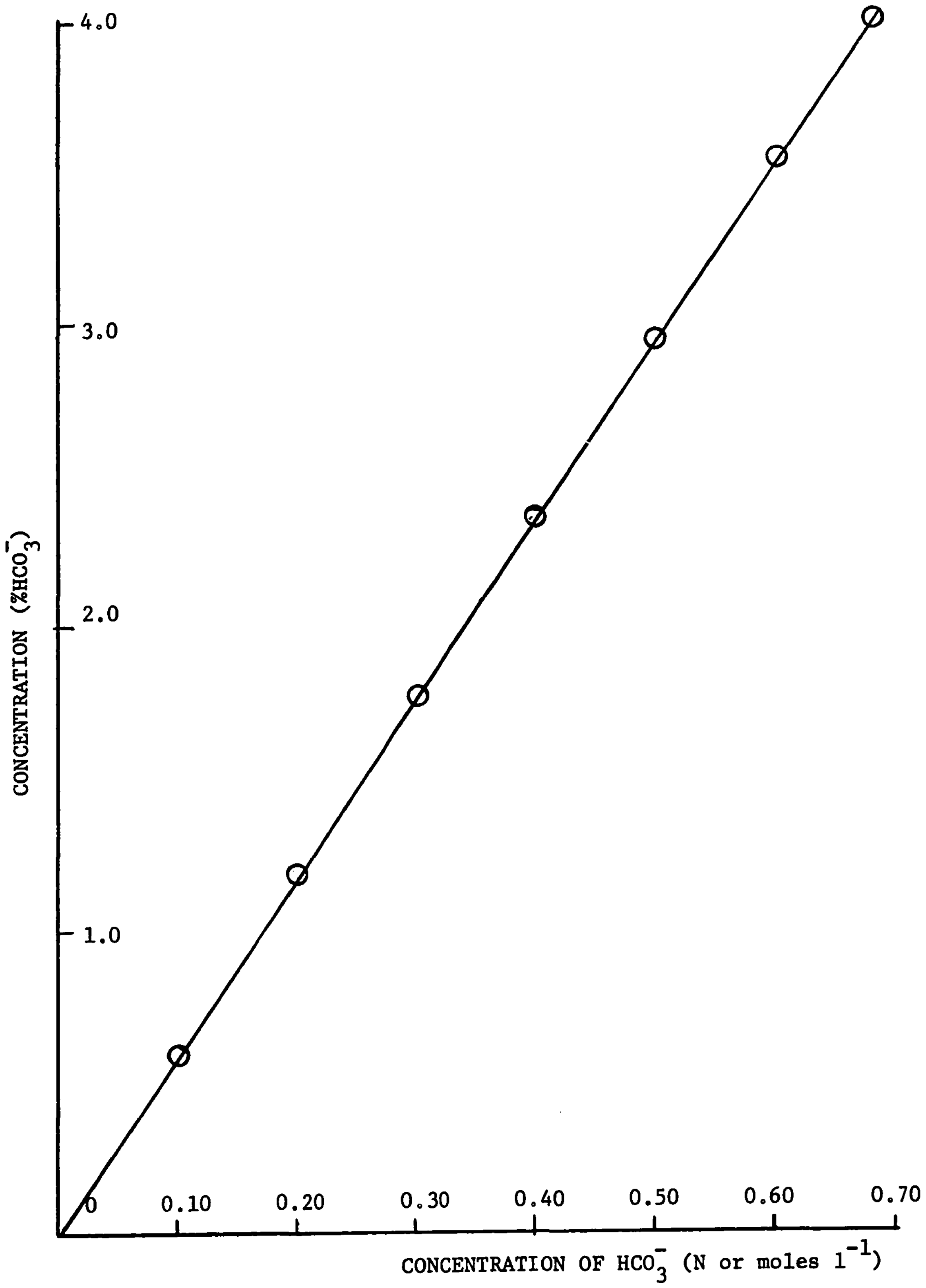

Figure A.1 Curve Relating %HCO$_3^-$ to Normality Concentration.

A.2 Reaction Rate as a Function of Lance Height

Q = 100 $cm^3 sec^{-1}$ d = .15 cm μ = 21 centistokes h = 1.5-3.5 cm

Lance height h (cm)	Time (min)	Bath Conc. (%HCO_3^-)	Emulsified Phase Conc. (%HCO_3^-)	Volume % water in emulsion
3.5	0	4.00		
	4	3.28	2.83	15.0
	6	3.16	2.93	13.6
	9	2.38	1.93	15.8
	18	0.38	0	18.9
		slope-.22	slope-.22	Av15.8
3.0	0	4.00		
	1	3.72	3.46	17.4
	2	3.44	3.06	13.0
	3	2.98	2.64	20.0
	4	2.70	2.02	20.3
	5	2.53	2.20	17.2
	8	1.37	1.06	20.1
	10	1.13	0.85	24.8
	12	0.13	0	-
		slope-.31	slope-.30	Av19.0
2.5	0	4.00		
	1	3.75	3.31	19.1
	2	3.26	2.79	19.6
	3	2.86	2.28	27.6
	4	2.50	1.96	21.2
	5	2.39	1.56	27.2
	6	1.88	1.47	27.7
	7	0.93	0.48	31.2
	8	0.43	0	30.4
		slope-.42	slope-.42	Av25.5
2.0	0	4.00		
	1	3.55	2.59	18.5
	2	3.35	2.27	24.1
	3	2.24	1.67	29.9
	4	1.64	1.11	27.1
	5	0.85	0.31	32.0
	6	0.21	0	27.0
		slope-.62	slope-.57	Av26.4
1.5	0	4.00		
	1	3.40	2.87	26.8
	2	2.71	2.11	32.8
	3	1.99	1.56	40.5
	4	1.10	0.65	38.6
	5.5	0		
		slope-.77	slope-.69	Av34.8

A.3 Reaction Rate as a Function of Flow Rate

h = 2.5 cm d = .15 cm μ = 21 centistokes Q = 90-120 $cm^3 sec^{-1}$

Flow Rate ($cm^3 sec^{-1}$)	Time (min)	Bath conc. (%HCO_3^-)	Emulsified Phase Conc. (%HCO_3^-)	Volume % water in emulsion
90	0	4.00		
	2	3.88	3.70	16.5
	4	3.78	3.45	12.5
	6	3.57	3.34	15.7
	8	3.56	3.05	16.4
	15	3.31	2.88	15.7
	20	3.02	2.46	14.2
	25	2.63	2.32	18.0
		slope-.05	slope-.06	Av15.6
100	0	4.00		
	1	3.75	3.31	19.1
	2	3.26	2.79	19.6
	3	2.86	2.28	27.6
	4	2.50	1.96	21.2
	5	2.39	1.56	27.2
	6	1.88	1.47	27.7
	7	0.93	0.48	31.2
	8	0.43	0	30.4
		slope-.42	slope-.42	Av25.5
110	0	4.00		
	1	3.40	2.81	28.6
	2	2.96	2.42	23.4
	3	2.18	1.48	28.8
	4	1.45	0.81	26.9
	5	0.83	0.42	25.8
		slope-.67	slope.64	Av26.7
120	0	4.00		
	1	3.26	2.78	33.1
	2	2.43	1.93	36.5
	3	1.55	0.88	31.7
	4	0.56	0.08	48.8
		slope-.90	slope-.86	Av37.5

A.4 Reaction Rate as a Function of Oil Viscosity

$Q = 120\ cm^3 sec^{-1}$ d=.15 cm h=2.5cm μ=5.8-56.6 centistokes

Oil Viscosity (centistokes)	Time (min)	Bath Conc. ($\%HCO_3^-$)	Emulsified Phase Conc. ($\%HCO_3^-$)	Volume % water in emulsion
56.6	0	4.00		
	1	3.30	2.71	27.4
	2	2.52	1.96	33.8
	3	1.64	1.22	40.3
	4	0.73	0.19	39.2
		slope-.86	slope-.83	Av35.2
33.3	0	4.00		
	1	3.33	2.98	33.6
	2	2.62	1.96	34.9
	3	1.78	1.25	28.6
	4	0.80	0.12	34.4
		slope-.84	slope-.84	Av32.9
20.7	0	4.00		
	1	3.26	2.78	33.0
	2	2.48	1.76	36.6
	3	1.68	1.16	37.8
	4	0.56	0.38	40.1
		slope-.82	slope-.81	Av35.6
12.5	0	4.00		
	1	3.34	3.02	26.8
	2	2.39	2.39	31.1
	3	-	-	35.3
	4	0.71	0.31	35.4
	4	0.65	0	34.1
		slope-.86	slope-.82	Av32.6
5.8	0	4.00		
	1	3.38	2.74	23.8
	2	2.58	2.02	17.9
	3	1.76	1.08	18.2
	4	1.17	0.38	8.8
	5	0.16	0	10.0
		slope-.80	slope-.80	Av15.7

A.5 Oil Layer Thickness

Q=120 $cm^3 sec^{-1}$ h=2.5 cm d=.15 cm μ=21 centistokes

Oil Thick. (cm)	Time (min)	Bath Conc. (%HCO_3^-)	Emulsified Phase Conc. (%HCO_3^-)	Volume % water in emulsion
0.43	0	4.00		
	1	3.35	2.83	51.4
	2	2.01	1.73	52.6
	3 1/2	0.56	0.35	54.7
		slope-.97	slope-.93	Av51.7
0.68	0	4.00		
	1	3.25	2.78	36.0
	2	2.41	1.85	34.5
	3	1.52	1.08	46.3
	4	0.63	0.30	43.7
		slope-.88	slope-.82	Av40.1
0.86	0	4.00		
	1	3.26	2.78	33.0
	2	2.48	1.76	36.5
	3	1.68	1.16	37.8
	4	0.56	0.38	40.1
		slope-.82	slope-.79	Av35.6
1.11	0	4.00		
	1	3.41	2.95	18.3
	2	2.86	2.34	20.2
	3	2.11	1.44	20.8
	4	1.37	0.68	20.5
	5	0.98	0.31	21.1
	6	0.08	0	18.3
		slope-.66	slope-.69	Av19.9
1.30	0	4.00		
	1	3.68	3.36	17.3
	2	3.00	2.26	17.2
	3	2.71	1.78	20.8
	4	2.14	1.57	19.4
	5	1.54	0.82	26.8
	6	1.12	0.29	15.8
		slope-.51	slope-.49	Av19.6

A.6 The Effect of a Surface Active Solute on Reaction Rate

$Q=120$ $cm^3 sec^{-1}$ $h=2.5$ cm $d=.15$ cm $\mu=21$ centistokes

Surface active agent - IGEPAL soluble in oil

.2 volume % IGEPAL

Time (min)	Bath Conc. ($\%HCO_3^-$)	Emulsified Phase ($\%HCO_3^-$)	Volume % water in emulsion
0	4.00		
1	3.28	2.61	42.9
2	2.54	1.88	54.7
3	1.70	1.04	53.1
4	0.72	0.21	43.3
			Av48.5

.4% volume % IGEPAL

0	4.00		
1	3.30	2.71	49.3
2	2.56	1.56	78.5
3	1.80	0.51	80.6
4	0.28	0	80.0
			Av72.1

A.2-1f Reaction Rate with no Oil Layer

$Q = 100$ $cm^3 sec^{-1}$ $h=2.5$ cm $d=.15$ cm

Time (Min)	Bath Concentration ($\%HCO_3^-$)
0	4.00
1	3.29
2	2.55
3	1.83
4	1.07

APPENDIX II

High Temperature Results

Initial temperature T_i - 1350°C h=1.5 in d=3/32 in Q=.75-1.125SCFM

Flow Rate (SCFM)	Time (min)	Bath %C	Emulsified Phase %C	Weight % metal in emulsion	Volume % metal in emulsion
0.75	0	4.18			
	3	4.19	1.39	13.4	7.8
	6	4.12	2.07	10.9	6.3
	9	4.08	-	-	-
	12	3.92	1.63	12.7	7.4
	15	3.65	1.97	15.2	8.9
	18	3.56	1.88	8.9	5.0
		slope-.061		Av12.2	Av7.1
0.875	0	4.19			
	3	4.05	1.57	28.5	17.9
	6	3.68	1.98	21.20	12.8
	9	3.38	1.86	48.6	34.1
	12	3.01	1.64	56.3	41.3
		slope-.111		Av38.7	Av26.5
1.00	2	3.96	0.96	56.0	41.0
	4	3.55	1.34	35.5	23.1
	6	3.27	0.98	35.5	23.1
	8	2.69(8 1/2)	0.97	52.2	32.4
	10	2.61	0.87	22.6	13.7
		slope-.173		Av40.4	Av27.7
1.125	0	3.92			
	1 1/2	3.86	1.70	24.6	15.2
	3	3.40	1.21	52.6	37.7
	4 1/2	2.95	1.20	27.4	17.1
	6	2.67	1.05	77.0	64.7
	7 1/2	2.29	0.96	32.3	20.7
		slope-.258		Av42.8	Av31.1

LIST OF SYMBOLS

k_i - mass transfer coefficient of species i in cm sec^{-1}

V - volume of bath cm^3

MWi - gm molecular weight of i

$\dot{N}_i$ - flux of i moles cm^{-3}

$\gamma_{w/A}$ - surface tension of water in contact with air dynes cm^{-1}

$\gamma_{o/A}$ - surface tension of oil in contact with air dynes cm^{-1}

$\gamma_{w/o}$ - water-oil interfacial tension dynes cm^{-1}

S - spreading coefficient dynes cm^{-1}

Γ_i - surface excess of species i in moles cm^{-2}

μ_i - chemical potential of species i cal $mole^{-1}$

a_i - activity of species i

T - temperature absolute degrees

R - universal gas constant

θ - contact angle degrees

ρ_g - gas density gm cm^{-3}

ρ_l - liquid density gm cm^{-3}

v_m - exit gas velocity of jet cm sec^{-1}

g - gravity

t - slag (oil) thickness cm

h - lance height

μ_m - metal viscosity centipoise

μ_s - slag viscosity centipoise

η_m - metal kinematic viscosity centistokes

η_s - slag kinematic viscosity centistokes

ρ_m - molten metal density gm cm^{-3}

ρ_s - molten slag density gm cm^{-3}

d - lance diameter

γ_m - liquid metal surface tension dynes cm^{-1}

γ_s - liquid slag surface tension dynes cm^{-1}

$\gamma_{s/m}$ - slag-metal interfacial tension dynes cm^{-1}

Q - gas glow rate $cm^3 sec^{-1}$ or SCFM

D - vessel diameter cm or inches

$\dot{M}$ - momentum flux of gas jet dynes

n - depth of depression of gas cavity below metal-slag interface cm

m - diameter of gas cavity at metal-slag interface cm

A - surface area of parabola of revolution cm^2

C_o - HCl concentration in water moles cm^{-3}

C_c - HCO_3^- concentration in water moles cm^{-3}

D_o - diffusion coefficient of HCl in water $cm^2 sec^{-1}$

D_c - diffusion coefficient of $NaHCO_3$ in water $cm^2 sec^{-1}$

x' - reaction interface distance from solution-gas interface in cm

u - liquid velocity next to crater cm sec^{-1}

C_g - concentration of HCl in HCl-Ar mixture %

C_m - concentration of HCl in water moles cm^{-3}

$\dot{V}$ - drop ejection rate $cm^3 sec^{-1}$

$\dot{m}$ - drop ejection rate gm sec^{-1}

r - drop radius cm

A - amplitude of cavity oscillation cm

ω - frequency of cavity oscillation rev sec^{-1}

y - distance of cavity bottom above maximum penetration cm

t - time in sec

v_x - center-line velocity at a distance x from the lance tip cm sec^{-1}

x - distance from lance tip cm

K - center-line decay constant

l - half length of parabola arc cm

M - weight of liquid in lower layer gm

$[C]$ - concentration of carbon in iron mole cm^{-3}

$[O]$ - concentration of oxygen in iron moles cm^{-3}

$\dot{N}''_i$ - flux per unit area of species i moles $cm^{-2} sec^{-1}$

(O) - concentration of oxygen in slag as FeO moles cm^{-3}

ACKNOWLEDGEMENTS

Sincere appreciation is extended to Professor W. G. Davenport who supervised this work and whose suggestions helped solve many problems.

Thanks are due to Professor W. M. Williams, Chairman, Department of Metallurgical Engineering, McGill University and Professor R. L. Guthrie for their interest and encouragement.

The author wishes to extend his thanks to Mr. M. Knoepfel for his technical assistance and to Mr. C. Henry for his help with the photography.

The author is indebted to the International Nickel Company for providing financial assistance.

REFERENCES

1. Kosmider, H., et al,Stahl Eisen, 77, (1957), 1277-1283

2. Rellermeyer, H., et al,Stahl Eisen, 77, (1957), 1296 - 1303

3. Meyer, H.W., W. F. Porter, G. C. Smith and J. Szekely,
   J. of Met. A.I.M.E. July, 1968, 35-42.

4. Kozakevitch, P., J. of Met., A.I.M.E., July, 1969, 57-68

5. Darken, L.S., "Kinetics of Metallurgical Reactions with
   Particular Reference to the Open Hearth", "The
   Physical Chemistry of Steelmaking", J.F. Elliot
   Editor, 1958.

6. Morgan, D.W., and J.A. Kitchener, Trans. Faraday Soc.,
   50, 51 (1954)

7. Schwedtfeger, K., TMS A.I.M.E., 239, (1967), 134-137

8. Brower, T.E. and B.M. Larsen, TMS A.I.M.E., 172, (1947),164

9. Basic Open Hearth Steelmaking, 3rd Edition, "Physical
   Chemistry of Steelmaking Committee A.I.M.E.",
   Edited by G. Derge, New York, 1951, p611

10. Flinn, R.A., R.D. Pehlke, D.R. Glass and P.O. Hays,
    TMS A.I.M.E. 239, (1967), 1776-1791

11. Wakelin, D.H., PhD Thesis, London Univ., 1966

12. Holden, C. and A. Hogg, J.I.S.I., 196, (1960), 318-332

13. Newton, J., "Extractive Metallurgy", J. Wiley & Sons,
    New York, 1959, P147.

14. Fuji, T. and S. Ura, Tetsu-to-Hagane, 1962, 1372-1374

15. Li, K., D. A. Dukelow, and G. C. Smith, TMS A.I.M.E.
    230, (1964), 71-76

16. Smith, G.C. and D.A. Dukelow, J. of Met. A.I.M.E.
    April 1964, 357-361

17. Newby, M.P., J.I.S.I. 162, (1949), 452-456

18. Perbix, G.W., J. of Met., A.I.M.E. July 1966, 824-831

19. Ogryzkin, Ye.M., (Dnepropetrovsk), Docklady Akad. Nauk. S.S.S.R., 3, (1964), 24-36 (Translation)

20. McBride, D.L., J. of Met., A.I.M.E., July, 1960, 531-537.

21. Kootz, T., J.I.S.I., 196, (1960), 253-259

22. Holmes, B.S. and M.W. Thring, J.I.S.I., 196, (1960),259-261

22. Hasimoto, H., Tetsu-to-Hagane, 44, (1958), 222-223

24. Turkdogan, E.T., Chem. Eng.Sc.,21, (1966), 1133-1144

25. Chedaille, J., and M. Horvais, Centre Doc. Sid. Circ. Inf. Techn. 19, (1962), 361-366.

26. van Langen, J.M., J.I.S.I., 196, (1960), 262-264

27. Red'ko, A.N., V.A. Frolov, J.B. Frolova and I.V. Melent'ev, (Tula), Docklady Akad. Nauk. S.S.S.R., 5,(1966),15-17 (Translation)

28. Dubrawka, E., Open Hearth Proc., 44, (1959), 388-390

29. Cooper, C.F. and J.A. Kitchener, J.I.S.I., 193, (1959), 48-55.

30. Cooper, C.F. and C.L. McCabe, "Some Considerations on the Nature of the Surface of Silicate Melts", "Physical Chemistry of Process Metallurgy Part I", Met. Soc. Conf., A.I.M.E., Pittsburgh 1959, Edited by G.R. St. Pierre, Interscience Publishers, New York, 1961.

31. Kozakevitch, P., "Formation and Destruction of Foams and Emulsions in Iron and Steelmaking", "The Physical Chemistry of Steelmaking", J. F. Elliot, Editor, 1958.

32. Alexander, J., "Colloid Chemistry", D. Van Nostrand, New York, 1924, p 102.

33. Clayton, W., "Theory of Emulsions", 4th Edition, The Blakiston Co., Philadelphia, 1943, pl.

34. Encyclopedia Brittanica, 14th Ed. 8,416

35. Hatschek, E., "Introduction to the Physics and Chemistry of Colloids", P. Blakistons Son & Co., Philadelphia, 1926.

36. Sutheim, G., "Introduction to Emulsions", Chemical Publishing Co., Brooklyn, 1946, pl.

37. Schulz, G., "Emulsions and Emulsifiers", O.T.S Report PB 98002, Department of Commerce, Washington, 1949, p2.

38. McBain, J.W., "Solubilization", Academic Press, 1955, pxi

39. "Emulsions", Carbide and Carbon Chemicals Corp., 6th Ed., 1937, p8

40. Webster's New Collegiate Dictionary, G & C. Merriam Co.

41. Becher, P., "Emulsions: Theory and Practice", 2nd Ed. Reinhold Publishing Corp., New York, 1965.

42. Ross, S., E.S. Chen, P. Becher and H.J. Ranuto, J. Phys. Chem., 63 (1959), 1681.

43. Harkins, W.D., "The Physical Chemistry of Surface Films" Reinhold Pub. Corp., New York, 1952, 83-91

44. Schulman, J.H., and J. Leja, Trans. Faraday Soc., 50 (1954), 598

45. Sokolov, O.K., (Moscow), Docklady Akad. Nauk. S.S.S.R. 5(1964),44-45

46. Richardson, F.D., "Oxide Slags-A Survey of our Present Knowledge", "Physical Chemistry of Steelmaking", Editor J.F. Elliot,1956

47. Bockris, J. O'M, J.A. Kitchener and J.D. Mackenzie, Trans. Faraday Soc. 51, (1955), 1734-1748

48. Bockris, J.O'M, J.A. Kitchener and S. Ignatowicz, Trans. Faraday Soc., 48, (1952), 75

49. Toop, G.W. and C.S. Samis, TMS A.I.M.E. 224, (1962), 878-887

50. Toop, G.W. and G.S. Samis, Can. Met. Quart., 1, (1962), 129-152

51. Majdič, A. and S.K. Tiwary, Rudarsko-Metalurški Zbornik, 1, (1968), 23-44

52. Birkhoff, G, and E.H. Zarantonello, "Jets, Wakes and Cavities", Academic Press Inc., New York, 1957

53. Johnstone, R. E. and M.W. Thring, "Pilot Plants, Models, and Scale-up Methods in Chemical Engineering", McGraw-Hill, London, 1957.

54. Weast, Handbook of Chemistry and Physics, 49th Ed., The Chemical Rubber Corp. 1969-1969.

55. Harkins, W.D. and F. E. Brown, J. Am. Chem. Soc., 41, (1919), 499

56. Belcher, R. and A. J. Nutten, "Quantitative Inorganic Analysis", 2nd Ed., Butterworths, London, 1960

57. Hoppner, Dtsch. Zucherindustr, 61, (1936), 361

58. Hathaway, J.M., J. of Met., A.I.M.E., March, 1967, 67

59. Kinson, K., J.E. Dickeson and C.B. Belcher, Anal. Chim. Acta., 41, (1968), 107-112

60. Bird, R.B., W.E. Stewart and E.N. Lightfoot, "Transport Phenomena", J. Wiley & Sons, Inc., New York, 1960

61. Crank, J., "The Mathematics of Diffusion", Oxford Univ. Press, London, 1956

62. Davenport, W.G., D.H. Wakelin and A.V. Bradshaw, "Interaction of both Bubbles and Gas Jets with Liquids", Heat and Mass Transfer in Process Metallurgy, The Institude of Mining and Metallurgy 1967.

63. Poggi, D., R. Minto, W. G. Davenport, J. of Met., A.I.M.E. Nov. 1969, 40-45.

64. Elliot, J.F., M. Gleiser, V. Ramakrishna, "Thermochemistry for Steelmaking" Vol II, Addison Wesley, Reading, Mass.,1963.

65. Barrer, R.M., Phil. Mag. 35, (1944), 806

66. Trentini, B., TMS A.I.M.E., 242, (1968), 2377-2388

67. Berthet, A., J. Rouanet, P. Vayssière and B. Trentini, J.I.S.I. June 1969, 790-797.